AN ABSTRACT OF THE DISSERTATION OF

Shane Daly for the degree of Doctor of Philosophy in Mechanical Engineering presented on
June 13, 2018.

Title: Rational Fuel Design for Low Temperature Internal Combustion Engines

Abstract approved: _____

Christopher L. Hagen

This work introduces a new methodology to design transportation fuels offering improved efficiency
and reduced emissions, aimed to complement both traditional and emerging engine technologies.
Many of these emerging technologies are centered around exploiting low temperature combustion
(LTC) strategies that offer improved efficiency and reduced emissions. However, a standardized fuel
does not exist to effectively operate in a LTC mode. Through engine simulations, supervised machine
learning, and multivariate optimization, this work provides a tool to create fuels tailored to a specific
LTC engine application. Engine simulations in this work characterize the LTC performance for
hundreds of fuel samples, quantified by a fuel performance metric called the LTC index. Supervised
machine learning provides correlations between measured fuel infrared absorbance spectra to various
fuel performance metrics: the LTC index, Research Octane Number (RON) and Motor Octane
Number (MON). The predictive models of these metrics circumvent the need for costly and time
consuming engine experiments to explore the performance of uncharacterized fuels.

The success of this work is heavily reliant on the ability of the models to make accurate predictions of the fuel performance metrics, viz. the LTC index, which is assessed through two efforts. The
first effort is generating a robust validation data set to benchmark model predictive performance.
Here, multivariate optimization is also used to create surrogates for the FACE gasolines. These
surrogates are paired with engine simulations to determine the true LTC index and compare to predicted values. LTC indices of most FACE gasolines are found to be accurately predicted within 3
units, and at worst within 6. The second effort toward predictive model validation is a novel experimental campaign, measuring first and second-stage fuel-spray ignition delays in a constant volume

combustion chamber (CVCC). The novelty comes by using ultra-short injections to enhance mixing prior to ignition phenomena, quantified by a state-of-the-art optical diagnostic—developed in this work—that images spatiotemporal fuel-spray concentrations. The mixture data are compared to a spray-ignition model with simplified fluid mechanics, found to capture spray mixing exceedingly well. The validated spray physical model is paired with a comprehensive chemical mechanism to predict and compare to experimentally-obtained spray-ignition onsets, thereby establishing a novel way to assess the accuracy of chemical mechanisms and surrogate fuels.

The validated LTC index predictive model is finally paired with multivariate optimization techniques to design a fuel tailored to a dual mode engine. In theory, this engine would operate in LTC mode where possible for efficiency improvements, and switch to traditional spark-ignition where needed. The tools developed in this work simultaneously point fuel and vehicle technology in a unique direction for designing high efficiency, next-generation combustion systems.

Rational Fuel Design for Low Temperature Internal Combustion Engines

by

Shane Daly

A DISSERTATION

submitted to

Oregon State University

in partial fulfillment of
the requirements for the
degree of

Doctor of Philosophy

Presented June 13, 2018
Commencement June 2018

Doctor of Philosophy dissertation of Shane Daly presented on June 13, 2018.

APPROVED:

_____

Major Professor, representing Mechanical Engineering

_____

Director of the School of Mechanical, Industrial, and Manufacturing Engineering

_____

Dean of the Graduate School

I understand that my dissertation will become part of the permanent collection of Oregon State University libraries. My signature below authorizes release of my dissertation to any reader upon request.

_____

Shane Daly, Author

ACKNOWLEDGEMENTS

their time and expertise on my PhD committee.

CONTRIBUTION OF AUTHORS

This work contains five published or in preparation manuscripts. The following breaks down author contributions for each manuscript.

Paper I: Kyle Niemeyer, and William Cannella provided technical advice and reviewed manuscripts for several iterations.

Paper II: Kyle Niemeyer, and William Cannella provided technical advice and reviewed manuscripts for several iterations. Kyle Niemeyer located literature and stimulated the direction towards numerically formulating fuel surrogates for the FACE gasolines.

Paper III: Kyle Niemeyer, and William Cannella provided technical advice and reviewed manuscripts for several iterations. Kyle Niemeyer provided Python code to post-process HCCI simulations to calculate LTC index. Khang Tran converted previously developed HCCI simulation code to work with server resources to expedite LTC index studies; Khang also executed LTC index studies and collected IR spectra for a large portion of the fuels used in training the IR-LTC index predictive model.

Paper IV: Emre Cenker, Lyle Pickett and Scott Skeen provided technical advice and reviewed manuscripts for several iterations. Emre Cenker helped set-up and conduct the experiments. Lyle Pickett performed adiabatic mixing calculations to provide data that is required to post-process extinction measurements. Julien Manin calculated the scattering and absorption optical cross sections for C70-fullerene.

Paper V: Noud Maes, Emre Cenker, Lyle Pickett and Scott Skeen provided technical advice and reviewed manuscripts for several iterations. Noud, Emre and Scott accelerated the process of setting-up, troubleshooting, and executing experiments. Noud and Emre assisted in recording high-speed images during experiments.

TABLE OF CONTENTS

TABLE OF CONTENTS (Continued)

LIST OF FIGURES

LIST OF TABLES

LIST OF APPENDIX FIGURES

Chapter 1: Introduction

1.1 Background and Motivation

Combustion of hydrocarbon fuels will maintain their status as the United States's leading source of energy between now and 2040, supplying 80 percent of the nation's energy needs by 2040 (increasing dependence) [1]. Society continues to rely on internal combustion engines (ICEs) for transportation, commerce, and power generation. As a result, the demands to reduce emissions and improve efficiency in these systems are significant to lessen the growing environmental and economic impacts. Therefore, there is motivation to seek out alternative, eco-friendly fuels and to move away from traditional combustion strategies in favor of advanced, next-generation systems that are cleaner and more efficient. This work answers this call to action by providing a tool that can rationally design high efficiency fuels tailored to next-generation combustion systems.

Since the inception of the ICE, harmful pollutants such as particulate matter, nitrogen oxides, unburned hydrocarbons, and carbon dioxide have been expelled into the atmosphere. These pollutants can cause serious adverse health effects and negatively impact the environment [2, 3]. Emissions have been managed by exhaust after-treatment strategies and by inherently improving the efficiency of the combustion process within the engine. Fuel efficiency steadily improved over the years due to increasing compression ratios, downsizing, and turbo-charging resulting in increased thermal efficiency [4]; in addition, increased electric hybridization led to reduction in overall fuel use [5]. Recent governmental regulations including the CAFE 2025 standards mandate reaching 54.5 mpg within the next 10 years—a significant engineering effort to accomplish in such a short time frame. Solving this challenge will be aided by continued electric hybridization, but it is projected that by 2025 only 11% of total vehicles in the U.S. will be registered as a hybrid vehicle [5]. Clearly, there is motivation to further improve upon the reciprocating internal combustion engine for public transportation to meet increasingly stringent standards.

Low temperature combustion (LTC) engines implement a non-traditional combustion strategy, and offer higher efficiencies and lower emissions that could satisfy CAFE standards. This engine

operation strategy is still of current research interest and requires further development to become a viable option. LTC engine research and development has many facets, but this work focuses on designing a fuel to operate in this environment—LTC is highly fuel sensitive (e.g., gasoline, diesel, etc.).

Fuel performance metrics provide insight to how a fuel will perform in ICEs. Traditional metrics require time consuming and expensive physical experiments to determine, and have had little success in describing how a fuel will perform in a LTC engine. In order to facilitate fuel design for LTC engines, a fuel performance metric characterizing LTC performance is needed. Additionally, the parameter space demanded for fuel design is immense, so a means to determine such a metric rapidly would accelerate the process. This body of work is a parallel effort to address these issues. The author reviews traditional and newly proposed fuel metrics, and select a metric that best indicates how a fuel will perform in a LTC engine.

1.2   Core Principles

First, a brief overview of the workings of the classic reciprocating ICEs will be introduced, along with a discussion of current areas for improvement and where past and current research efforts bring us. Second, next-generation engine concepts will be introduced with a discussion on the benefits they offer over the classic ICE strategies. Third, fuel performance metrics will be discussed that give useful insight into how particular fuels will perform in their respective ICEs, and will be a primary topic of this work as it is mostly concerned with fuel design. Fourth, with a given LTC engine fuel performance metric, the methodology to rapidly predict this metric is introduced through supervised machine learning techniques. A reader familiarized with the four aforementioned topics can skip the following subsections without any loss in continuity.

1.2.1   CI and SI operation

Diesel engines are capable of operating at high thermal efficiencies due to high compression ratios, lean mixtures (therefore higher isentropic exponent), and unthrottled operation (i.e., high volumetric efficiency). However, due to the complex heterogeneous combustion of the high molecular weight diesel fuel, large amounts of soot form. Therefore, diesel engines are thermodynamically efficient but not considered clean. On the other hand, SI engines combust a homogeneous, stoichiometric

charge of reactants and thus produce low amounts of soot. At the same time, the higher combustion temperatures produce NOx, requiring three-way catalysts to reduce the pollutant emissions. Thus, SI engines are considered clean but not as efficient as diesel engines. Advanced combustion engines are an attempt to operate in a regime that both minimizes emissions and increases efficiency by reducing the combustion temperatures. This idea is called low temperature combustion (LTC), and is the topic of the next section.

1.2.2   Low Temperature Combustion Engines

LTC engines are an attempt to unify the benefits of SI and CI engines, using a lean fuel-air mixture (to keep temperatures low and isentropic exponent high) in the piston-cylinder chamber and ignited through compression [6]. High fuel concentrations (fuel rich) are avoided due to significant, and potentially damaging, in-cylinder pressure rise rates. Homogeneous charge compression ignition (HCCI) engines implement the LTC concept with a lean, well-mixed (homogeneous) charge of fuel (e.g., gasoline, diesel, or viable hydrocarbons) and air. This cycle is thermodynamically similar to the Otto cycle, but offers higher compression ratios. With this, it is possible to offer the efficiency closer to that of or higher than a diesel engine, but with low emissions of particulates, CO2, and NOx without the need for expensive exhaust after-treatment [7]. However, the homogeneous charge coupled with compression ignition leads to control issues (e.g., rapid heat-release, ignition timing) due to the fuel-air mixture igniting all at once, coupled with ignition timing being chemistry controlled and not by a physical process. Other methods, such as reactivity controlled compression ignition (RCCI), leverage multiple fuels and injection strategies to operate in the LTC regime with fewer control issues than HCCI [6]. There are other variants of LTC engines, and interested readers are guided to Yao et al. [8] for a more comprehensive survey.

1.2.3   Fuel Performance Metrics

1.2.3.1   Gasoline Spark Ignition (SI) Engines

In ICEs, the higher the geometric compression ratio used, the higher the thermal efficiency achieved for an Otto cycle [9]. The limitation on the compression ratio for SI engines is dictated by the onset of engine knock that is itself influenced by the combination of fuel chemistry and operating conditions—higher compression ratios in general increase the propensity for knock. Knock is the result of rapid

chemical heat release, and can cause engine damage. Since particular fuels are more resistant to withstanding knock higher compression ratios can be achieved. It is therefore useful to define the ignition quality of gasoline fuels as the propensity to withstand knock (e.g., octane requirement). The Anti Knock Index (AKI)—the value at the gas pump—assigns a performance metric to the gasoline auto-ignition quality, and is defined by the arithmetic average of the Research Octane Number (RON) and Motored Octane Number (MON). The two octane numbers are determined in an experimental facility using a Cooperative Fuels Research (CFR) engine via the ASTM-CFR standard testing procedures D2700-14 and D2699-13b [10, 11]. Fuels are combusted in the engine while the compression ratio is increased, until the fuel starts to exhibit significant cyclic variation (instability) or auto-ignition. Each test has specific operating points, the primary difference being air-fuel charge temperature regulation and engine speed [10, 11].

1.2.3.2 Diesel Compression Ignition (CI) Engines

Diesel engines are capable of operating at higher thermal efficiencies due to the high compression ratios, lean mixtures (therefore higher isentropic exponent), and unthrottled operation (i.e., high volumetric efficiency). High compression ratios are achievable because the diesel fuel is introduced into the piston-cylinder chamber when it is desirable to ignite the fuel, and not along with the air during the intake stroke as is done with SI engines (with the exception of direct injected SI—also known as stratified SI, which is not yet widely adopted). When the diesel is injected, there is a finite time delay until auto-ignition occurs. Since knowing the delay time is significant to ensure optimal combustion timing, and therefore efficiency, the cetane number (CN) corresponds to this ignition delay. CN can be thought of as the antithesis of sorts to AKI. That is, resistance to autoignition results in a high AKI, but low CN. The values are determined in a similar manner to that of RON and MON with a Cooperative Fuels Research (CFR) engine, where instead the compression ratio is increased until a set ignition delay time is achieved [12].

1.2.3.3 LTC Engines

LTC engines currently do not have any sort of accepted standard to quantify fuel performance, although some significant efforts focused in this area can be found in the work of Kalghagti et al. [13], Urushihara et al. [14], Rapp et al. [15], and Truedsson et al. [16–20]. These efforts, while

partially successful at describing combustion behavior for gasoline-like fuels, have little relation to realistic engine performance such as fuel economy. It would be helpful if a metric could rank the performance of fuels in such a way that gave insight to potential performance gains from use in LTC engines, in addition to identifying how the fuel will chemically behave in the LTC engine. A LTC fuel performance metric should be able to help designers avoid potentially damaging auto-ignition/knock, but also indicate how efficient the fuel is in HCCI. This metric could then also be used to identify attractive fuels for LTC engine operation based on the potential performance gain associated by using that fuel in addition to containing information on combustion behavior.

A novel LTC index which rates fuels by their potential fuel savings in order to capture useful engine performance from HCCI operation was developed. Niemeyer et al. [21] introduced this index (OSU-Chevron LTC index) based on operating envelopes—engine speeds and loads that can be achieved with a given fuel governed by attributes such as auto ignition timing, knock constraints, fuel conversion efficiency, etc.—and comparing the HCCI results to useful operating conditions. The definition of the OSU-Chevron LTC-index is as follows:

$$I_{LTC} = \frac{m_{f,SI} \; \epsilon(HCCI)}{m_{f,SI}} * 100\% \tag{1.1}$$

where m_f presents the mass of fuel used, and subscripts SI and HCCI refer to the IC modes. The numerator represents the mass of fuel that HCCI operation could potentially replace, and the denominator that of the entire driving cycle: the ratio of the two is a mass weighting of sorts that encapsulates potential fuel savings achieved using bi-modal operation of HCCI-SI over its 100% SI counterpart. The (useful) operating envelopes are those required for realistic operating and driving conditions, determined from transient driving cycle simulations. A fuel with poor performance has an operating envelope that is not within realistic conditions. If a fuel cannot achieve realistic operating conditions via HCCI, governed by combustion constraints, then there are no potential fuel savings and therefore a low LTC index assigned. This LTC index is distinct from prior efforts in developing a fuel rating index for HCCI due to the real-world impact on fuel economy that is represented within the index, in addition to the combustion constraints that are held to define viable HCCI operation.

1.2.4 Machine Learning

Machine learning is a broad field that uses statistical techniques to "learn" a specified task. This work uses supervised learning, a machine learning technique that maps an input to an output by inferring a linear or non-linear function. For this work, the inferred function maps a vector "X" to a scalar "Y", mathematically similar to standard regression procedures. A matrix of X examples and corresponding Y values, referred to as training data, are fed into a supervised learning algorithm. The algorithm uses the training data to "learn" the best mapping function, i.e., solving for the best function that minimizes prediction errors of Y provided X. The model training procedure also entails ensuring the model is robust, meaning the function can be applied to new examples outside the training data set. A separate test data set with X and corresponding Ys—not used to train the model—are fed into the model; the predicted Y values are compared to the true Y values and the model error is assessed. A robust mapping function can then take unseen X values to predict a corresponding Y.

1.3 Chapter and Document Organization

Utilizing machine learning, this work showcases a correlation between measured fuel infrared spectra to the LTC index: a fuel performance metric characterizing low temperature combustion performance. The predictive model validity is assessed through two efforts. The first is generating a robust validation data set to benchmark model predictive performance. Second, a novel experimental campaign measures various combustion parameters in a constant volume combustion chamber (CVCC) apparatus for an array of fuels, using state-of-the-art optical diagnostics. With the accuracy of the LTC index predictive model assessed, LTC indices of fuel mixtures are rapidly predicted using procured fuel infrared spectra, mitigating the need for costly and time-consuming engine experiments. The predictive model is paired with multivariate optimization techniques to design a novel fuel. This work delivers a fuel offering improved efficiency and reduced emissions for a specific vehicle platform and LTC engine. The following sections outline each chapters structure, as well as key contributions in the order of document appearance.

1.3.1 Chapter Layout

The core body of work is organized into six chapters, five of which contain a published or in preparation manuscript. Information presented in the first five chapters stand alone, and serve as building blocks towards the overall goal of this work. The goal is to develop a tool to rationally design a next-generation fuel promising increased efficiency; this is outlined in the sixth chapter, not containing a manuscript. Chapters with manuscripts are preceded with introductory remarks as to how the manuscript ties into the overall body work, highlighting contributions toward rational fuel design. These prefaces provide the logical progression of this work and summarize key findings. This allows you to skip over the detailed manuscripts while retaining readership, yet gain an in-depth understanding by reading the manuscripts if desired.

1.3.2 Document Layout

Chapter 2 demonstrates that chemical functional groups, represented by infrared absorbance spectra, can be related to fuel octane rating (SI engine fuel performance metric) with machine learning. Neat hydrocarbons and simple fuel mixtures (a combination of up to six neat hydrocarbon components) are shown to sufficiently train a model to accurately predict the octane rating of complex fuels that comprise thousands of components.

Machine learning requires a large data set for predictive model training, testing, and validation. Developing a computational tool to aid data-set generation preceded creating the predictive model for LTC fuel performance. This was required for cascading reasons. The LTC performance metric in this work is a computationally determined metric (LTC index), and validating the model to predict complex refinery-grade samples requires simulating "true" values. However, it is not yet possible to directly simulate refinery-grade fuels in combustion models. Instead, simple fuel mixtures are designed to emulate the thermochemical attributes of the complex fuels, known as "fuel surrogates". Surrogates can be used in engine simulations to establish "true" LTC fuel performance for the complex fuel sample they represent. Chapter 3 presents the formulated computational tool to design fuel surrogates.

Chapter 4 builds upon the data and tools created in Chapters 2 and 3 to create a predictive model for LTC index. The validation data-set (true LTC index values of complex fuels) is created

from the surrogate fuel compositions from Chapter 3. The LTC index predictive model is created using the same methodology as Chapter 2.

The engine simulations used in determining LTC index are simplistic, potentially giving incorrect trends between fuel mixtures. If the developed predictive model for LTC index were founded on an erroneous data set then non-physical trends are predicted. In an effort to validate the LTC index data set, a novel experimental campaign is conducted to measure various combustion parameters in a constant volume combustion chamber (CVCC) apparatus. The experimental campaign is split into three parts. The first part develops a novel optical diagnostic to quantify spatiotemporal spray mixing in a high pressure and temperature environment, outlined in Chapter 5. The second part, outlined in appendix D, uses the developed diagnostic in a brief study to quantify spray mixing. Using an ultra-short injection duration is found to reduce unfavorable concentration gradients within the fuel spray, serving to reduce physical complexity. Simplistic 1-D modeling efforts are shown to accurately represent spray-mixing processes. The third and final part in the experimental campaign is outlined in chapter 6. Here, a short-injection spray-ignition study optically resolves low- and high-temperature ignition phenomena for fuels with varying thermochemical properties. The experimental results are compared to a 1-D spray-ignition model, where large errors are found at a few thermodynamic conditions. This lead to the conclusion that there are errors in the chemical mechanism used in the simulations. These findings provide an indirect measure to the accuracy of the training, test, and validation LTC index data-sets used for predictive model development.

Chapter 7 embeds the fuel performance predictive models developed in Chapters 2 and 4 into the multivariate optimization routine from chapter 3. The tool automates the design of novel fuels tailored to a specific vehicle application. The author attempts to design a single fuel that can potentially operate in a hybrid SI/HCCI engine. Portions of the engine operation that can be achieved with HCCI are leveraged for efficiency improvements, and where not possible supplemented with traditional SI—offering improvements in fuel efficiency and emissions. The tool designed in this work could stimulate market production of LTC engine strategies. Lastly, the body of work is summarized in Chapter 8.

Chapter 2: Machine Learning to Predict SI Engine Fuel Performance

This chapter creates a correlation between measured fuel infrared spectra to the Research Octane Number (RON) fuel performance metric. With this tool, RON is rapidly and accurately predicted using procured fuel infrared spectra, mitigating the need for costly engine experiments to do so. The model developed in this work is novel since the training methodology is historically different from literature.

RON values for a wide array of hydrocarbons and complex fuel mixtures are available in literature, providing an expansive data set to create a robust predictive model. On the other hand, LTC index values are not provided in literature and must be simulated through exhaustive time-consuming simulations. Creating a LTC index data set large enough to inform a predictive model is computationally expensive. This RON study establishes the efficacy of using fuel infrared (IR) spectra to correlate and predict fuel performance. The study is low-risk, since the training, test, and validation data, i.e., RON for many fuels, are available in literature. The IR spectra of these fuels are experimentally obtained by the author.

The RON correlation study proves two concepts: (1) chemical functional groups, represented by infrared absorbance spectra, can be related to fuel performance; and (2), neat hydrocarbons and simple fuel mixtures (a combination of up to six neat hydrocarbon components) are sufficient to train a model that accurately predicts the performance of complex fuels comprising thousands of components. Proving these points informed and motivated the development of a LTC index data set to create a robust LTC index predictive model. The following sections outline the novel RON correlation work, adapted from:

Daly, Shane R., Kyle E. Niemeyer, William J. Cannella, and Christopher L. Hagen. "Predicting fuel research octane number using Fourier-transform infrared absorption spectra of neat hydrocarbons." *Fuel* 183 (2016): 359-365.

Predicting fuel research octane number using Fourier-transform infrared absorption spectra of neat hydrocarbons

Shane R. Daly, Kyle E. Niemeyer, William J. Cannella, Christopher L. Hagen

2.1 Introduction

Research octane number (RON), determined by ASTM-CFR standard testing procedure D2699-15 [22], indicates a fuels' resistance to autoignition under specific engine operating conditions. RON and the other ASTM 4814 fuel specifications dictate several attributes necessary to operate in the installed fleet of vehicles. In 2014, 136.78 billion gallons of gasoline were consumed in the US [23]—all of which need to meet those quality specifications. Determining the RON of fuels using a Cooperative Fuels Research (CFR) engine costs over $200,000 for the capital investment (among considerable lab modifications) takes 20 minutes, and also requires trained technicians/operators.

In an effort to reduce this testing burden, researchers sought out more cost-effective and faster noninvasive optical techniques for determining RON, among other fuel specifications, by way of statistical analysis. Vibrational spectroscopy, such as infrared absorption (IR) and Raman spectroscopy, has proved to be a reliable method for fuel characterization. The work of Kiefer [24] highlights current technical advances in the context of fuel characterization, overviews fundamental theory, and discusses advantages/ disadvantages of the various techniques currently in use today. Now, a brief sequential overview of literature utilizing vibrational spectroscopy in conjunction with statistical analysis will be discussed.

Kelly et al. [25] determined 10 ASTM specifications including RON, Motor Octane Number (MON), vapor pressure, specific gravity, bromine number, and contents of aromatic, alkene, saturate, sulfur, and lead using a short wavelength near infrared (SW-NIR) scanning spectrophotometer (660–1215 nm) and multivariate analysis to correlate the spectra to the performance metrics. For example, the group showed that RON of gasolines can be predicted to a standard error within 0.4–0.5 [25], which is better than the ASTM RON test itself at ± 0.7 [22]. The original work of Kelly et al. [25] inspired other investigations to enhance their technique, consider alternate fuels, or to predict other fuel performance metrics. To briefly touch on these alternate studies, Williams et al. [26] instead leveraged FT-Raman spectra (3200–600 cm^{-1}) to predict cetane index and cetane number to ± 1.22 and 2.19, respectively. Cooper et al. [27] applied a similar methodology as Williams et al. (using Raman spectra at wavenumber ranges of 2510–3278 cm^{-1} and 196–1851 cm^{-1}) to predict MON, RON, and pump octane number to within ± 0.415, 0.535, and 0.410, respectively. Litani atmzilai et al. [28] combined near-IR (700–1000 nm) and laser-induced fluorescence (250–500 nm third and

fourth harmonic) spectra to predict 10 physical specifications; e.g., RON and MON were predicted to within ± 0.33 and 0.27, respectively. The more recent work of Kardamakis and Pasadakis [29] presents an efficient multivariate analysis technique that predicts RON within ± 0.26 using a limited data set in comparison to previous studies; this work also provides a succinct history of efforts in this field. There are many additional studies to the short list previously mentioned that consider various optical and multivariate analysis techniques to predict performance parameters of fuels [30–38].

Various commercial devices utilize these principles to rapidly predict relevant properties of gasoline and diesel fuels based on optical characteristics. For example, the Zeltex ZX 101C octane analyzer [39] passes radiation from light emitting diodes through optical filters and gasoline samples (14 static wavelengths ranging from 893–1045 nm). The light is collected on a photodetector and processed for absorbance at the wavelengths of interest, with a total measurement time of 20 s and accuracy of ± 0.5 RON units [39]. The IROX Miniscan IRXpert gasoline/diesel analyzer takes a similar approach based on FTIR spectroscopy, collecting a broad absorption spectrum and generating information at 12,900 wavelengths. This allows the prediction of 16 total ASTM specifications, and predicts RON with an accuracy of ± 0.5 within 80 s [40]. This equipment costs less than half of a CFR engine and does not require expert technicians/operators.

All the previous approaches using multivariate analysis to predict fuel attributes [25–38] used existing, real-world fuel samples (i.e., existing gasoline, diesel, jet fuels) as the training data set to predict performance attributes of those specific fuels. This work used hydrocarbons—neat or combined as mixtures for gasoline surrogate fuels including up to five neat components—to provide model input for predicting RON of the Fuels for Advanced Combustion Engines (FACE) gasolines designed by the Coordinating Research Council (CRC) and manufactured by ChevronPhillips Chemical Co [41]. With this novel approach, a sensitivity analysis can then target neat hydrocarbons and classes (i.e., functional groups) to develop and optimize spectroscopic surrogates for the FACE gasolines. These spectroscopic surrogates most simply represent the bulk auto-ignition behavior (through statistics) of the FACE gasolines. Researchers and industry alike can then predict RON for future fuels (e.g., new, alternative, regarding advanced engines) that may otherwise not be accurately represented spectroscopically by traditional fuels used today. Here, the statistical models created are robust in that they are informed on a fundamental level. This mitigates the issue of creating a model informed by existing fuels that may be physically and spectroscopically

different to future fuels—inaccurate prediction of the future fuel would result.

This work uses the FACE gasoline for the fuel and RON to represent the fuel performance parameter. RON is readily obtained for neat hydrocarbons, surrogate and research-grade gasolines, and has previously been shown extensively in literature to correlate well with optical data of quantified gasoline samples. We test our model by predicting RON for the 10 FACE gasolines and 12 additional blends with ethanol; these represent candidate fuels for advanced internal combustion engines (i.e., future fuels) [41].

The structure of the paper is as follows. Section 6.2 presents the methodology of the approach. This section includes the neat hydrocarbons and surrogate gasoline mixtures considered in this work, the FTIR spectra collection method, and the development of the statistical model. Section 6.3 provides the results and discussion of the predicted RON values of FACE gasoline samples from the developed statistical model. Lastly, Section 6.4 summarizes the findings of this study.

2.2 Methodology

In the current approach, hydrocarbon components (neat or mixtures of up to five components) informed a statistical model rather than characterized gasoline samples as in prior efforts. First, the training data set—i.e., the pure hydrocarbon components and mixtures considered to train the statistical model—is discussed. Second, IR absorbance spectra collection methods and the statistical methodology used in this work are covered. Lastly, with the statistical model created, the methodology to validate the model is discussed.

2.2.1 Neat hydrocarbons considered

Promoted by the literature [19, 42, 43] as components most relevant to simple fuel surrogates, we primarily considered mixtures of n-heptane, isooctane, toluene, ethanol, methylcyclohexane, and 1-hexene. These six hydrocarbons will be referred to as the "primary" hydrocarbons used in this study. In brief, the first two components are used to measure RON (also called the primary reference fuels, or PRFs) and represent the straight and branched alkane functional groups, respectively. Toluene and ethanol represent aromatics and oxygenates, while methylcyclohexane and 1-hexene represent cycloalkane (naphthene) and alkene (olefin) classes, respectively. This study used the aforementioned neat hydrocarbons in addition to the 134 blends taken from the literature [19, 20,

42, 43]. These blends are mixtures of the six hydrocarbons in various combinations ranging from two to five components, primarily consisting of isooctane, n-heptane, and a third component; see the supplemental material for the full list.

In addition to the six primary neat hydrocarbons, we also considered hydrocarbons found within the FACE gasolines via detailed hydrocarbon analysis [41]. Table 2.1 lists these additional 28 pure components, referred to as the "additional" hydrocarbons in this work; they will be used to supplement the "primary" hydrocarbons. The hydrocarbon classes of these additional species overlap with the classes from the primary set. However, an outcome of this study demonstrated that the primary set—common components in gasoline surrogate mixtures [19, 42, 43]—was not sufficient to physically and spectroscopically represent the FACE gasolines, and species from the additional set were needed (see Section 6.3).

2.2.2   IR absorbance spectra collection

Absorption spectra were collected using a ThermoFisher Nicolet iS10 FTIR with a single-bounce, Attenuated Total Reflectance (ATR) smart accessory (650–4500 cm^{-1} at 2 cm^{-1} resolution, crystal type: diamond with ZnSe lens, part number: 222-24700). A Norm-ject 1 mL latex-free (VWR-53548-001) disposable syringe was used to transfer a few drops of the liquid sample directly onto the ATR crystal. Prior to spectrum collection of the sample, the FTIR was purged with nitrogen to remove any water vapor contamination. With the collected light intensity, absorbance was calculated with the following relation (the Beer-Lambert law shown for completeness [52]):

$$A(\nu) = \ln \left(\frac{I_o}{I} \right)_\nu = \sigma_\nu cL \, , \tag{2.1}$$

where I_o and I are reference and measured light intensity, respectively, σ_ν is molar absorption coefficient (mol^{-1}cm^2), c is concentration (mol cm^{-3}), and L is path length of the attenuating medium (cm). No path length or dispersion effects were accounted for in the ATR absorbance results; we found correcting ATR spectra made no difference for the statistical model performance, as discussed next.

Measurements were also made using a more involved transmission approach by way of a Spectra-Tech EZ-fill™ precision path length optical cell with 3 mm KBr optical slides. These data were

Fuel name	Formula	RON	Class
n-heptane	nC_7H_{16}	0	straight alkane
isooctane	C_8H_{18}	100	branched alkane
toluene	$C_6H_5CH_3$	113 [19]	aromatic
ethanol	C_2H_5OH	108.5* [43–45]	alcohol
methylcyclohexane	C_7H_{14}	74.1 [42]	cycloalkane
1-hexene	C_6H_{12}	74.9 [42]	alkene
2-methylbutane	C_5H_{12}	92 [46]	branched alkane
2-methylpentane	C_6H_{14}	73.4 [47]	branched alkane
3-methylpentane	C_6H_{14}	74.5 [47]	branched alkane
2-methylhexane	C_7H_{16}	42* [47, 48]	branched alkane
3-methylhexane	C_7H_{16}	52* [47, 48]	branched alkane
2,4-dimethylpentane	C_7H_{16}	83.1* [47, 48]	branched alkane
2,3-dimethylpentane	C_7H_{16}	91.1* [47, 48]	branched alkane
2,5-dimethylhexane	C_8H_{18}	55.3* [47, 48]	branched alkane
2,4-dimethylhexane	C_8H_{18}	65.2* [47, 48]	branched alkane
3-ethyl-2-methylpentane	C_8H_{18}	87.3* [47, 48]	branched alkane
xylene	C_8H_{10}	114 [49]	aromatic
1,2,3-trimethylbenzene	C_9H_{12}	100.5 [47]	aromatic
4-ethyl-m-xylene	$C_{10}H_{14}$	100.6 [47]	aromatic
2-ethyl-p-xylene	$C_{10}H_{14}$	100.6 [47]	aromatic
1,2,4-trimethylbenzene	C_9H_{12}	101.4 [47]	aromatic
cumene	C_9H_{12}	102.1 [47]	aromatic
1,3,5-trimethylbenzene	C_9H_{12}	106 [47]	aromatic
1,2,3,4-tetrahydronaphthalene	$C_{10}H_{12}$	96.4 [47]	aromatic
2-propyltoluene	$C_{10}H_{14}$	100.3 [47]	aromatic
1,2,3,4-tetramethylbenzene	$C_{10}H_{14}$	100.5 [47]	aromatic
cyclopentane	C_5H_{10}	100.1 [47]	cycloalkane
cyclohexane	C_6H_{12}	80.7 [10]	cycloalkane
butylcyclohexane	$C_{10}H_{20}$	63.8 [50]	cycloalkane
1-pentene	C_5H_{10}	90 [49]	alkene
2-methyl-2-butene	C_5H_{10}	97.3 [47]	alkene
2-pentene	C_5H_{10}	98 [46]	alkene
2-methyl-1-butene	C_5H_{10}	100.2 [47]	alkene
diisobutylene	C_8H_{16}	103.8 [51]	alkene

Table 2.1: Pure hydrocarbon species considered in this work. Infrared absorption spectra for all species were acquired via Attenuated Total Reflectance FTIR spectroscopy. * indicates average of multiple values.
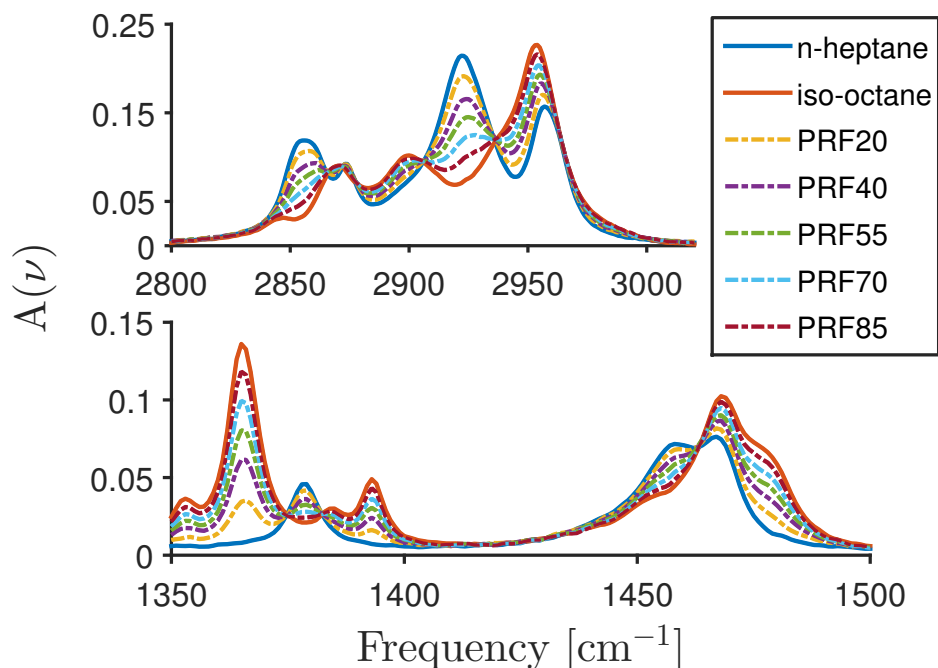
Figure 2.1: FTIR-ATR absorbance spectra of n-heptane, isooctane, and their mixtures (PRFX, where X indicates volume % of isooctane). The two axes show subsets of the optical frequencies considered where these samples absorb strongly.

post-processed via the Beer-Lambert law and baseline corrected with the optical constant method guided by literature [53–57]. We found that when using the same FTIR, no difference resulted in the performance of our approach between using uncorrected ATR (qualitative) or corrected transmission (quantitative) data. The use of ATR appeared to introduce an instrument function to the data which cancelled when ratioing the incident and transmitted light; as a result, this did not affect the statistical post processing. Spectra can be collected via ATR an order of magnitude faster than by transmission, in addition to simpler post processing, and thus we chose ATR over transmission-based methods for the current application. Figure 2.1 shows a representative subset of the collected ATR absorption spectra, for mixtures of n-heptane and isooctane.

2.2.3 RON model development

The IR absorbance spectra were correlated to RON by way of principle component regression (PCR). PCR identifies patterns in multi-dimensional data and correlates these to an explanatory variable, i.e., a variable that may correlate to the patterns found in the chemical data [58]. The authors used PCR as the statistical method, and implemented it via MATLAB software with the built-in
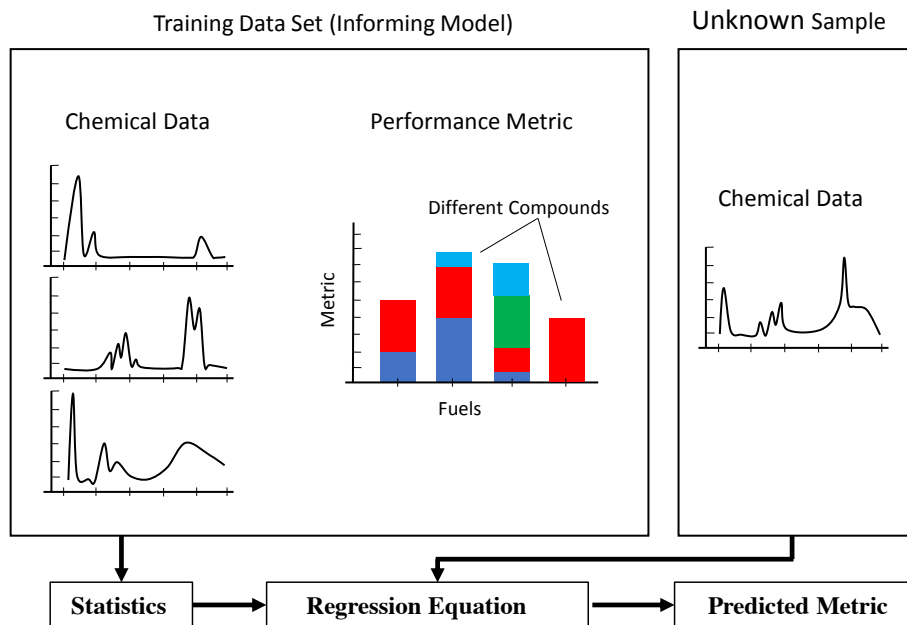
Figure 2.2: Flowchart depicting the multivariate analysis process.

function `pca`. All principal components were used for each training data set. Figure 2.2 shows a diagram illustrating this process.

A training data set informed the statistical model, which included a set of IR absorbance spectra and RON. Figure 2.1 shows a representative subset of the collected ATR-IR absorbance spectra used with the training data set; shown are isooctane and n-heptane neat and as mixtures (PRFX). The training data set limits the predictive capabilities of the model: the larger and more varied it is, typically the better the model. The final result is a regression equation, which uses IR absorption spectra as an input and returns a prediction for RON.

To validate the created statistical models, RON was predicted for gasoline samples with known RON. The fuels studied are the 10 FACE gasolines and 12 FACE gasoline mixtures blended with ethanol [41]. These include 22 well-documented fuels statistically designed with chemical and ASTM performance variations for researchers to investigate in advanced internal combustion engines. This bounded the task of creating a model to predict real gasoline fuels that contain hundreds of various hydrocarbons.

2.3 Results and discussion

In order to test how subsets of the fuels considered in this work affect the model predictive performance—i.e., the RON prediction of FACE gasolines, not that of the fuels used to inform the model—we selectively and additively included neat hydrocarbons and surrogate fuels in the model and observed the effect on the residual (residual = actual RON − predicted RON, where the average, max, and min were analyzed). A limited sensitivity analysis with the neat hydrocarbons was performed first by selectively including them in the model.

The sensitivity study first informed a model with a baseline data set consisting of the six primary neat hydrocarbons and the 134 mixtures, then a prediction of RON for all FACE gasolines. Next, we selectively included one new neat hydrocarbon in the model (i.e., baseline fuels plus one hydrocarbon) from the additional neat hydrocarbons and observed how the predicted RON of the FACE gasolines were affected. Here it was learned definitively that the branched alkane and aromatic classes were not satisfactorily represented by isooctane and toluene. When the model was informed with more neat hydrocarbons representing these classes, the predictive performance changed by up to 40 RON for many of the FACE gasolines. When including alkanes or aromatics, the average residual improved by 9.0 and 9.7 RON units, respectively. However, the alkene and cycloalkane classes were sufficiently represented by 1-hexene and methylcyclohexane, respectively; species in these classes respectively improved the residual by 0.4 and 0.7 on average.

Following the sensitivity study, fuels were additively included to inform the model. Figure 2.3 shows the performance of the model as a function of fuels considered in the training data set. Moving along the horizontal axis indicates fuels (or fuel sets) additively included in the model (e.g., at the third horizontal axis location, the model includes six neat hydrocarbons plus the Truedsson et al. [19] n-heptane, isooctane, toluene, and ethanol fuel blends). The vertical axis indicates the RON residual, where a box-and-whisker plot shows the distribution of RON predicted by each training data set—the magnitudes of the maximum and minimum residuals are indicated with error bars ("whiskers"), with outliers beyond a normal distribution indicated with symbols.

First, only four neat hydrocarbons were used: n-heptane, isooctane, toluene, and ethanol. This attempt at modeling resulted in predictions of RON within 22.7±24.8 (residual average ±standard deviation), and with an error of 48.5 RON in the worst case. Next, neat hydrocarbons methyl-
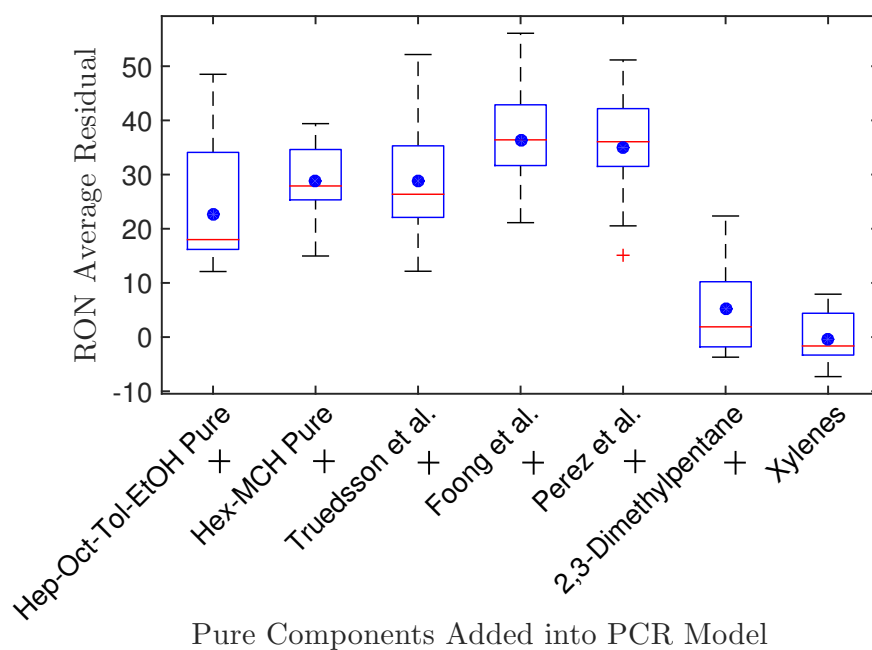
Figure 2.3: Model performance indicated by average residual for prediction of FACE gasoline RONs as a function of training data set. For each data set, the middle line (red) indicates the median, the circle is the mean, the edges of the box the 25th and 75th percentiles, the whiskers extend to minimum and maximum values not considered outliers, and the outliers are indicated with plus signs. "Pure" indicates that the spectra of the pure individual components were used, and "Hep," "Oct," "Tol," "EtOH," "Hex," and "MCH" refer to n-heptane, isooctane, toluene, ethanol, 1-hexene, and methylcyclohexane, respectively.

cyclohexane and 1-hexene were added—Perez et al. [42] considered these as components in fuel surrogates—which resulted in prediction within 28.8±29.4 RON, with a worst-case error of 39.5 RON. Following this, we investigated the effect of adding mixtures to the model performance, meaning the absorption spectra and published RONs from literature [19, 42, 43]. We learned that mixtures affected model predictions of RON for many of the FACE gasolines. Residuals still reached 50 for many of the fuels. Subsequently, two additional neat hydrocarbons were added—indicated by the sensitivity study to have the largest impact on model performance—representing the branched alkane (2,3-dimethylpentane) and aromatic (xylenes) classes. The performance of the RON model for all research gasolines converged with the addition of these, resulting in predictions within 0.3±4.4 RON, with a maximum error of 7.9. Adding additional neat hydrocarbons—whether they represent alkanes, aromatics, cycloalkanes, or alkenes—did not improve the model further. This indicates that only a few hydrocarbons representing the branched alkane and aromatic classes are required to improve the model, and further inclusion of hydrocarbons resulted in diminishing returns with little effect. All the additional neat hydrocarbons (see Table 2.1) were included in the model yielding 0.1±4.8 and 9.7 RON in the worst case. Figure 2.4 illustrates the first (only four of the primary neat hydrocarbons) and the final model performance (all six primary neat hydrocarbons, 28 additional neat hydrocarbons, and the 134 mixtures considered).

The first training data set (recall this included four of the primary neat hydrocarbons) is believed to poorly inform the model as they do not represent the many spectral attributes seen in the FACE gasolines. Figure 2.5b depicts FTIR-ATR absorbance spectra (650–$950\,\mathrm{cm^{-1}}$) of these four neat hydrocarbons and the FACE gasolines. It is evident that additional functional groups need to be included to better represent the FACE gasolines spectroscopically. In particular, none of the neat hydrocarbons exhibit the absorption peaks of the FACE gasolines at 741, 768, 805, and $909\,\mathrm{cm^{-1}}$ (shown by the arrows in Figure 2.5a).

The effect of changing the order in which hydrocarbons were additively included in the model was also investigated, as seen in Figure 2.6. For example, 2-methylbutane was investigated as a candidate to replace 2,3-dimethylpentane—recall this was originally added as the *first* neat hydrocarbon to the study in Fig. 2.3 after the baseline (which yielded 5.1±9.5, max residual = 22.3). 2-Methylbutane improves the model (7.2±9.6, max residual = 18.1) in nearly the same way that 2,3-dimethylpentane originally had. Following that, we added 1,2,3,4-tetrahydronaphthalene to the model guided by
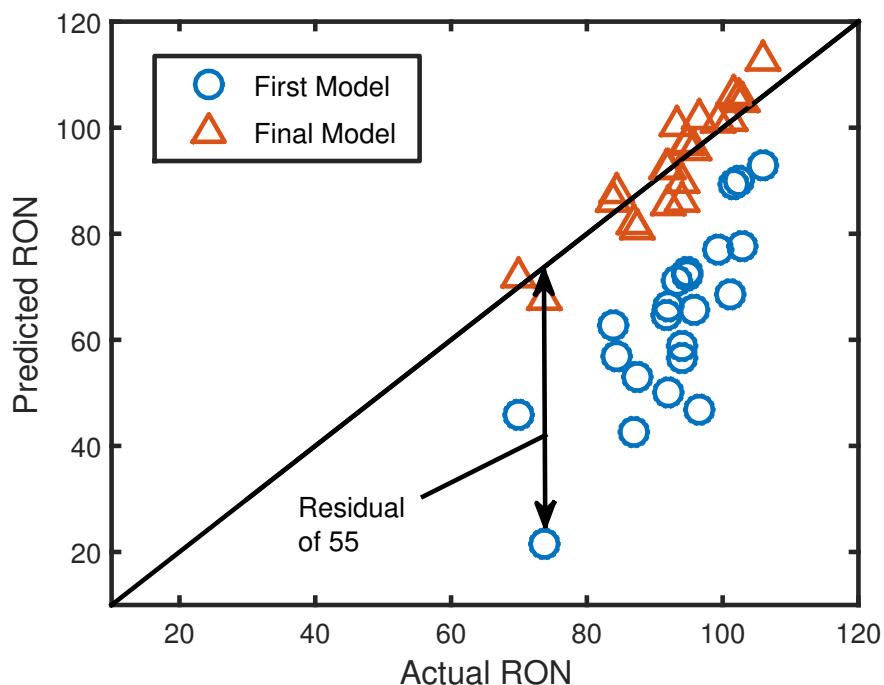
Figure 2.4: Statistically predicted RON compared with actual RON for the first model (four neat hydrocarbons) and the final model (all neat hydrocarbons and the 134 mixtures considered in this work). Predicted RON values shown are for the FACE gasolines and blends with ethanol. Example residual indicated in figure is actual RON − predicted RON.

the sensitivity study—recall that this highlighted hydrocarbons with the most impact on model performance. This hydrocarbon represents the aromatics class, and its addition results in improved model performance (3.1 ± 5.6, max residual = 13.1). However, this addition is not as significant as that provided by xylene, the second pure component added to the model (0.3 ± 4.4, max residual = 7.9). Moving to the right in Fig. 2.6, the addition of 2,3-dimethylpentane or xylene no longer dramatically affects the model performance when added after other hydrocarbons; albeit, the model does improve with its addition.

Here we demonstrated that adding pure components from one class can affect the model sensitivity to hydrocarbons from others, and that alternative hydrocarbons representing the branched alkane and aromatic class may be used in lieu of the original 2,3-dimenthylpentane and xylenes considered. This could be due to shared IR absorbance features at particular optical frequencies. For example, the fundamental C−H stretch frequency from one class overlapping with hydrocarbons from other classes. This results in spectroscopically redundant information being added to the model, and may explain why some hydrocarbons classes can somewhat inform the statistical model
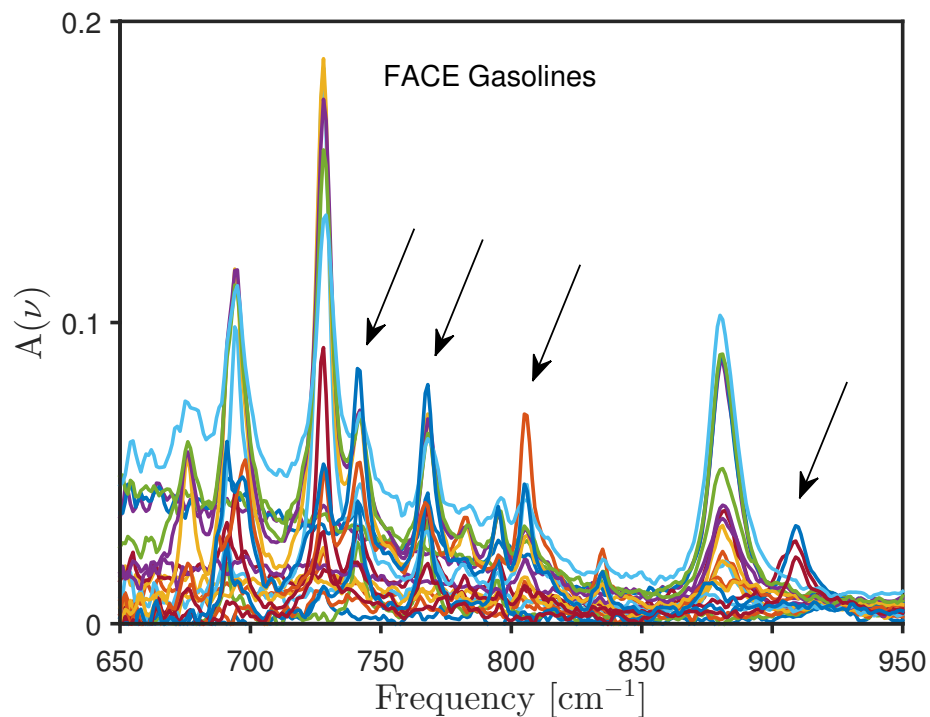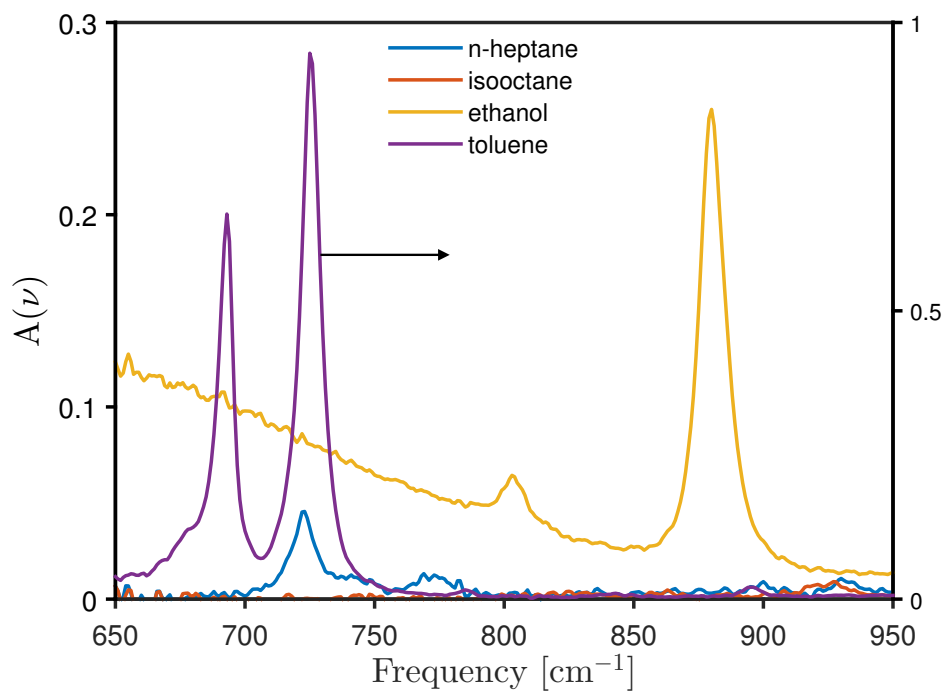
Figure 2.5: (a) FTIR-ATR absorption spectra for the 10 FACE gasolines and 12 FACE gasoline mixtures blended with ethanol, and (b) initial set of four neat hydrocarbons. Arrows in (a) indicate absorbing frequencies not found in the pure components shown. Right vertical axis in (b) indicates toluene absorbance.
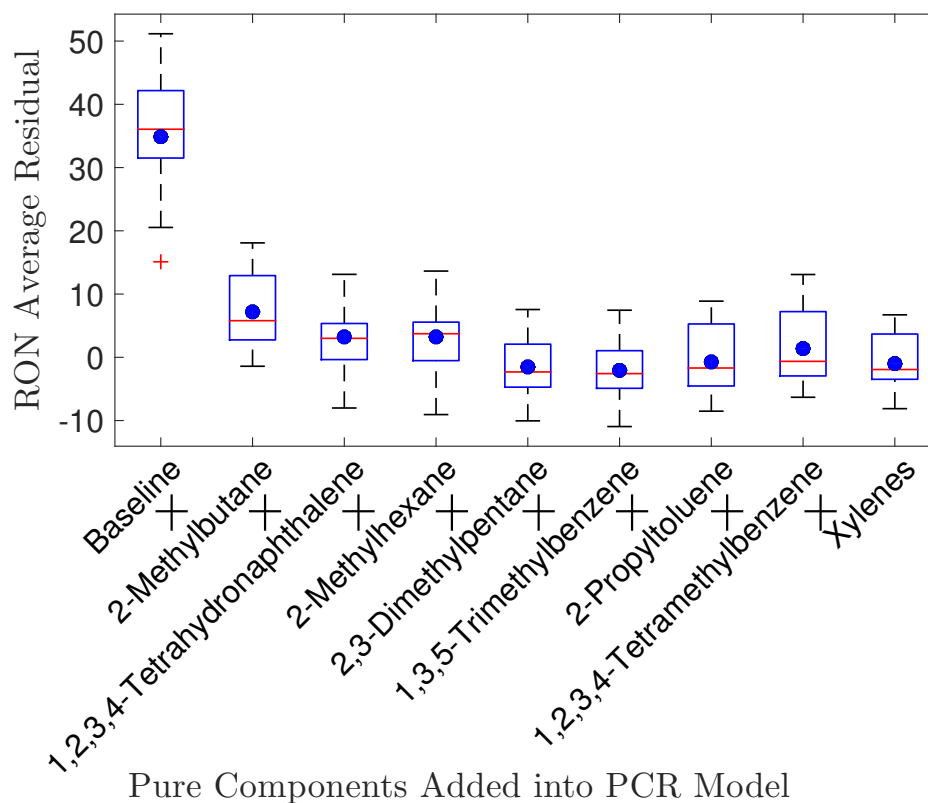
Figure 2.6: RON residual for all FACE gasolines and blends as a function of neat hydrocarbons added into the model (in a different order than in Fig. 2.3. "Baseline" indicates all species added in Fig. 2.3 up to the Perez et al. [42] fuels. For each dataset, red line indicates the median, blue circle the mean, the edges of the box the 25th and 75th percentiles, the whiskers extend to minimum and maximum values not considered outliers, and the outliers are indicated with red plus signs.

in the same way as other hydrocarbons classes. Further parametric investigation is needed to fully optimize component choice.

We also explored removing the 134 mixtures from the training data set to observe the effect of only leveraging neat hydrocarbons. The previously determined (best) performance (0.3±4.4, max residual = 7.9 RON) could not be achieved with pure components alone; the maximum residuals reached 25 RON for many of the predicted FACE gasolines. We believe mixtures are necessary to inform the model due to non-linear blending effects of RON and the IR spectra with mixtures— this may be attributable to solvation effects. For example, ethanol particularly introduces these non-linear blending effects for RON [43] and the absorbance spectra [59]. In general, it is suggested that alcohols interact with hydrocarbons in various ways by means of van der Walls forces, and the molecular structures formed (e.g., double-bonded dimer, linear polymer, water-like structure, etc.) are a function of the alcohol concentration. These various interactions thereby alter the original molecular structure of the hydrocarbons and therefore their absorbing characteristics [60, 61]. This highlighted that mixtures are equally as important as the neat components alone for model robustness. This may indicate the possibility of increasing model performance further by including mixtures containing additional branched alkane and aromatics which improved the model alone.

2.4   Conclusions

The approaches of Kelly et al. [25] and other work in this area [26–38] used real-world fuel samples to inform the optics-based statistical models. This work instead used neat hydrocarbons—six of them are primarily utilized as constituents in gasoline surrogates, and 28 being the primary constituents in the FACE gasolines—as well as mixtures that contain the primary six components. The six primary pure components and 134 mixtures of these pure components predicted RON poorly (34.8±36.1 on average and 51.2 RON in the worst case). However, the addition of two neat hydrocarbons, one to each represent the branched alkane and aromatic classes, resulted in model improvement: predicted RON within 0.3±4.4 and 7.9 RON in the worst case, respectively. This performance could be achieved with various neat hydrocarbons representing these classes. Additional parametric investigation is required for ideal fuel selection. This, however, would be difficult to determine due to the many possible combinations and results to likely change when considering additional hydrocar-

bons. More importantly and simpler to implement, mixtures containing these two additional pure components should be investigated for their effect on the model, primarily because the six primary neat hydrocarbons proved to be important in mixtures as they are individually.

This work shows that the ignition quality of gasolines can be represented by as few as eight hydrocarbon spectra. With this information, the most impactful fuels (neat or otherwise) can be targeted to inform spectroscopic surrogates to predict performance of complex fuels, in this case the FACE gasolines. We developed a model informed by simple fuel surrogates and neat hydrocarbons to predict RON of the FACE gasolines. Therefore, this work builds upon previous efforts by creating models that are irrespective of the fuels we wish to predict performance attributes of. The primary benefit being predicting fuel performance without the need to gather a training data set that uses those particular fuels to inform the model—e.g., using ATR-FTIR spectra and known RONs of characterized gasolines to inform the model to predict RON for an unknown gasoline sample from its measured ATR-FTIR spectra. In addition, the results may support using computationally determined performance metrics for the training data set. This is to say, fuel performance metrics of real fuels—burdensome to accurately model due to complex chemical mechanisms—can be predicted with a computationally modeled data set of neat-hydrocarbons and surrogate fuels, which are relatively simple and computationally more efficient to model. This model would predict real fuel performance (e.g., RON or alternative metrics) informed by computational simulations and FTIR-ATR absorption spectroscopy.

Chapter 3: Emulating Complex Fuel Thermochemical Attributes

The previous chapter outlined techniques demonstrating that fuel infrared spectra can be correlated to RON. The RON model was informed by pure hydrocarbons and fuel mixtures containing few hydrocarbon components. The model is simple by nature, yet it is capable of predicting complex refinery grade gasoline samples, reinforcing that infrared spectra correlate well to fuel performance. The complex fuel samples predicted are the FACE gasolines (Fuels for Advanced Combustion Engines), well-characterized gasoline fuels used in the research community. Predicting RON of the FACE gasolines and comparing to their true RON values from literature served as a robust validation procedure.

In order to validate a LTC index predictive model in the same manner as the RON model, the LTC indices of the FACE gasolines must be known. Since the LTC-index is computationally based, the FACE gasoline LTC indices then have to be simulated to create the validation data set. However, due to the FACE gasolines comprising hundreds of hydrocarbon species, and therefore highly complex, it is not yet possible to directly simulate at this time. Instead, researchers create simpler fuels that are a mixture of a few pure hydrocarbon components that emulate the theromchemical properties of the complex fuels. These simple fuels are known as "surrogates", and serve as a means to represent and benchmark the performance of the complex fuel in combustion simulations.

At the time of this work there were only surrogates available for 2/10 of the FACE gasolines ("A" and "C") in literature [62, 63]. The remaining surrogates had yet to be created. Surrogate fuel creation for the FACE gasolines is the topic of this chapter. This chapter outlines an automated procedure to numerically blend pure hydrocarbon components into a surrogate fuel. This work has a novel aspect to it, in that the methodology leverages the developed predictive RON model from Chapter 2. The following sections outline the work to create the FACE gasoline surrogates, adapted from:

Daly, Shane R., Kyle E. Niemeyer, William J. Cannella, and Christopher L. Hagen. "FACE gasoline surrogates formulated by an enhanced multivariate optimization framework." In review with *Energy and Fuels*.

FACE gasoline surrogates formulated by an enhanced multivariate optimization framework

Shane R. Daly, Kyle E. Niemeyer, William J. Cannella, Christopher L. Hagen

3.1 Introduction

Combustion of hydrocarbon-based fuels accounted for approximately 84% of US energy consumption in April 2017 [64], and some projections show this remaining at $82–84\%$ through 2050 [65]. Society continues to rely on internal combustion engines for transportation, commerce, and power generation. Vehicle fuel economy has steadily improved over the years due to increasing compression ratios, downsizing, and turbocharging, resulting in increased thermal efficiency [4]; in addition, increased electric hybridization has helped reduce overall fuel consumption. However, simultaneously evolving fuel compositions and combustion strategies challenge further improvements to ICE performance—both are being adapted to meet high efficiency, low emission government mandates. These recent governmental regulations, namely the Corporate Average Fuel Economy 2025 standards, propose reaching 54.5 mpg within the next eight years, although they are currently under review. Continued electric hybridization will help solve this challenge, but projections suggest personal and fleet hybrid vehicles will comprise only 4.6% of on-road vehicles in the United States by 2025 [66]. Reducing the environmental impact of these systems motivates research into further reduction of emissions and improvements in efficiency.

The chemical composition of a fuel significantly affects engine-out emissions and performance [20, 67–69]. Gasoline presents challenges to studying the influence of fuel composition since it contains hundreds of various hydrocarbon species [70]. The methodology proposed in this work will accelerate the process of studying complex gasoline samples by formulating fuel surrogates. Surrogates blend a small number of well-characterized hydrocarbons to represent real fuels (like refinery-grade gasolines) by emulating their thermophysical and chemical kinetics properties. By representing these real fuels—comprised of near-continuous spectra of component hydrocarbons—as discrete mixtures of components, surrogates can be modeled with validated chemical kinetic models and enable simulations of combustion technology. Additionally, experiments with surrogate fuels can provide insight into fuel-composition effects on engine-out performance and emissions. Experimental and computational research using surrogates designed with the proposed algorithm will help inform researchers to effects of fuel composition and thermochemical properties on internal combustion engine performance.

Our work builds upon the diesel surrogate formulation framework developed by Mueller et

al. [71]. They demonstrated that physical properties and fuel performance metrics relevant to internal combustion engine performance—composition based on carbon nuclear magnetic resonance spectra, distillation curve, cetane number, and density—can be targeted to formulate surrogates that mimic the behavior of the real diesel fuel properties. Their work helped overcome the challenge of automating the design of a mixture containing a small number of hydrocarbon species (eight, in this case) to broadly represent the performance of complex fuels. Their method weights individual fuel properties and combines these into a single objective function, then designs a surrogate by minimizing this objective via changing the relative component amounts.

Ahmed et al. [72] extended the diesel surrogate formulation framework to gasoline fuels: Fuels for Advanced Combustion Engines (FACE) gasolines A and C. The FACE gasolines are a matrix of research gasolines designed by the Coordinating Research Council (CRC) and manufactured by ChevronPhillips Chemical Co. [41]. Ahmed et al. efforts incorporated fuel performance metrics more relevant to gasoline fuels; e.g., research octane number (RON) in lieu of cetane number. Later, Sarathy et al. [73] presented multiple surrogates for FACE gasolines F and G, using the method of Ahmed et al. [72] with additional target properties like motor octane number (MON). Multiple surrogates were presented for FACE gasolines F and G based on species palette selection restrictions and a RON/MON calculation methodology. After which, Javed et al. [74] used the refined methodology of Sarathy et al. [73] to formulate surrogates for FACE I and J. Shankar et al. [75] also formulated surrogates for low octane sensitivity gasolines FACE A, C, I and J, mainly to investigate the application of using primary reference fuels as surrogates specifically for pre-mixed, low-temperature combustion engine applications.

3.1.1   Octane model review

Here, we outline the various methodologies to develop surrogates whose RON and MON attempt to match those of the target gasoline in the aforementioned efforts [72–74], while highlighting the challenges and areas for improvement. Following that, we present an alternative approach to calculate RON and MON.

Ahmed et al. [72] correlated RON to simulated constant-volume ignition delay times. Their approach requires an autoignition simulation for every iteration in the surrogate formulation framework. This step can be time-consuming, especially with detailed chemical models containing thou-

sands of species, since the computational time increases exponentially with the number of component species considered for the surrogate—and hundreds of iterations may be required to formulate a surrogate. Ahmed et al. also considered a simpler linear-by-mole correlation and formulated alternate surrogates based on this less-expensive computational approach [72].

Sarathy et al. [73] added octane sensitivity (S = RON-MON) as a target parameter when formulating surrogates for FACE gasolines F and G [73]. They correlated octane sensitivity to the slope of the negative temperature coefficient (NTC) region of simulated constant volume ignition delays—a significant computational hurdle, compared with a single ignition delay calculation (see Mehl et al. [76] for more detail on this correlation). To alleviate computational effort, Sarathy et al. also formed alternative surrogates for FACE gasolines F and G based on another linear-by-mole blending formula [73]. The linear-by-mole equation, while simple, was developed and verified only for toluene reference fuels (TRFs: mixtures of toluene, n-heptane, and isooctane). Sarathy et al. extended the application to non-TRF mixtures by replacing toluene, n-heptane, and isooctane as the aromatic, n-paraffin, and isoparaffin species in the linear-by-mole equation with other species being considered. This is to say, predicting RON or MON of a fuel mixture containing 1,2,4-trimethylbenzene, n-butane, and 2-methylbutane, would be achieved by using the respective mole fractions directly in the equation originally developed for only TRFs. As such, errors using the equation in this manner may be significant. Despite this, Sarathy et al. did this to investigate an approach requiring minimal computational effort in comparison to the other, computationally-heavy method.

Javed et al. replaced the TRF linear-by-mole relationship with the more detailed octane blending model of Gosh et al. [77] in formulating FACE J. This relation accounts for non-linear blending effects at the level of the total paraffins, total olefins, total naphthenes, etc., but not at the individual molecule level [77]. Here, model interaction parameters that represent blending effects between hydrocarbon classes were trained using gasoline samples. After, the trained model was validated against other refinery-grade gasoline samples, and proved to produce excellent results. While this octane model does return individual pure component octane ratings for neat hydrocarbons, it is not validated toward simpler surrogate mixtures where molecule-molecule interactions can be more prominent.

The RON/MON calculation approaches used in previous gasoline surrogate formulation ef-

forts [72, 73, 78] are either not very accurate (the TRF linear-by-mole relationship), do not account for molecule-molecule octane blending, or computationally expensive (the NTC-sensitivity correlation based on multiple autoignition simulations). In the current study, we explored improved options that require less computational effort and are capable of predicting quantities for a wide array of hydrocarbons. Initially, we attempted to extend the correlation of simulated ignition delay approach of Ahmed et al. [72] to calculate MON, since they only developed a correlation for RON. The coefficient of fit for our MON model was sufficient, but the RON and MON models in combination could not accurately capture sensitivity. More recently, Singh et al. [79] used regression tools to find the initial temperature and pressure conditions at which RON and MON best correlate with the simulated ignition delay times; it is applicable to mixtures of n-heptane, isooctane, toluene, 1-hexene, and 1,2,4-trimethylbenzene.

We instead implemented novel models that correlate attenuated total reflectance, Fourier-transform infrared (ATR-FTIR) spectra of a fuel to RON and MON. These models alleviate the extensive computational effort of auto-ignition simulations—decoupling the need for complex chemical kinetic models—and provide accurate predictions for robust mixtures of various hydrocarbons, as well as more complex fuels like the FACE gasolines. Daly et al. [80] provide such a model developed through principal component regression (PCR), informed by neat hydrocarbons and low-component fuel mixtures. The model can predict RON for various pure components and their mixtures, as well as the higher-complexity FACE gasolines. The model takes a fuel's IR spectra, whether it is a pure component, mixture of pure components, or a refinery-grade gasoline sample, and predicts the RON. Here, we use this technique to create a separate MON correlation, and also improve the predictive capability of the original RON correlation provided by Daly et al. [80].

The surrogate formulation algorithm, updated with the IR-octane models, is used to generate surrogates for the 10 FACE gasolines A–J. Table 3.1 list the measured properties of these fuels [41]. We next describe the IR-octane models and the surrogate formulation algorithm.

3.2   Methodology

We first discuss the general workings of the IR-RON model from Daly et al. [80]. Following that, we outline how the current work improves upon the existing model and create a new MON correlation. The predictive capability of these models are presented thereafter. Next, we discuss the

Target property	FACE gasolines									
	A	B	C	D	E	F	G	H	I	J
RON	83.9	95.8	84.3	94.2	87.4	94.4	96.8	86.9	70.2	73.8
MON	83.5	92.4	83.0	87.0	81.1	88.8	85.8	79.8	69.5	70.1
Density [kg/m^3]	685	697	690	743	725	707	760	759	697	742
H/C ratio	2.29	2.21	2.27	1.88	2.04	2.13	1.83	1.72	2.26	1.92
% Volume distilled	Temperature [K]									
10	329	337	331	338	335	346	350	334	343	346
20	344	352	341	354	342	351	363	349	354	368
30	357	364	350	366	348	357	378	363	359	376
40	365	371	359	374	354	363	394	373	362	380
50	368	374	366	379	359	370	411	382	364	384
60	370	376	372	384	365	376	426	390	366	390
70	372	378	376	390	371	382	439	401	368	401
80	374	381	382	413	379	387	447	417	371	417
Carbon type	Fractional %									
1	54.5	56.4	53.1	41.3	33.2	43.2	35.4	27.5	46.1	32.8
2	22.7	15.2	24.6	18.4	19.1	18.2	13	22.4	32.3	32.8
3	16.6	16.6	14.6	5.2	8.2	12.1	6.5	3	13.4	4.5
4	0.8	0	0	0.2	21.7	11.5	10.5	9.5	1.8	1.1
5	0.4	0	0	0	1	0.1	0.8	0.8	0.7	0.6
6	0	0	0	0	0	0	0	0	0	0
7	0.5	4.1	2	20.7	8.3	5.3	18.4	24.8	1.1	18.1
8	0.1	1.8	1.3	9.3	2.7	2.3	10.8	9.1	0.2	9.9
9	0	0	0	0	0	0	0	0	0	0
10	0	0	0	0.2	0.3	0	0.5	0.5	0	0.1
11	4.4	5.8	4.4	4.7	1.9	4.2	1.8	0.5	2.3	0
12	0	0	0	0	1.3	1.5	0.3	0.3	1	0
13	0	0	0	0	1.9	1.5	1.3	1.1	1	0
14	0	0	0	0	0.4	0	0.6	0.6	0	0.1

Table 3.1: FACE gasoline target properties [41], including carbon bond (C–C) type relative amounts (rounded to nearest tenth); nomenclature for C–C is defined in the Methodology section.

gasoline surrogate formulation framework of Ahmed et al. [72], and introduce some alterations to their methodology, including the performance parameter evaluation and additional considerations for determination of final surrogate mixtures. Lastly, we list the neat hydrocarbon components considered for the surrogate palette.

3.2.1   ATR-FTIR octane model

Here, our work improves upon the predictive capability of the RON correlation developed by Daly et al. [80]. We also present a new MON correlation, created by following the same methodology as the new RON model, using PCR to correlate fuel ATR-FTIR spectra to octane ratings. The models were further improved by extending the original training dataset to include the FACE gasolines. Because of this addition, the performance of the model cannot be judged by how well the FACE gasolines are predicted, as originally done by Daly et al. [80].

Instead, model performance (foresight) will be measured by its ability to predict 25 TRF fuel mixtures from Knop et al. [81]. We also provide a comparison of the IR model's predictive capability to seven octane correlations (specific to TRF mixtures) proposed in the literature [81]. We performed this extra step to show that the IR-RON model of Daly et al., although not made specifically for TRF mixtures, can predict octane numbers of TRF mixtures at least as well as the TRF-specific correlations used by Sarathy et al. [73]. We now outline the calculation methodology with the updated IR-octane models.

In this approach, PCR assigns a weighting coefficient to each absorbance value (for all wavenumbers), and the dot product of these weightings with a fuel's ATR-FTIR absorbance spectra, plus a constant offset factor, yields the octane rating. In equation form, this is given by

$$\mathrm{ON} = \sum_{\nu} W_{\nu} A_{\nu} + b \,, \tag{3.1}$$

where: ON = RON or MON; W_{ν} and A_{ν} are the weighting coefficients and absorbance spectra associated with a particular wavenumber ν, respectively; and b is an offset. The summation is performed over the applicable wavenumber range. The spectral weightings and offset for the RON and MON correlations can be found as supplemental material. The absorbance spectra of a gasoline,

neat hydrocarbons, or mixtures of neat hydrocarbons may be attained by using an ATR-FTIR[1], with ν ranging 650–$3580\,\text{cm}^{-1}$ in increments of $1\,\text{cm}^{-1}$ (See Daly et al. [80] for more details on spectra collection methodology). Mixtures of neat fuels are assigned an IR spectra based on the molar-weighted sum of the individual components:

$$A_b = \sum_{\nu} \sum_{j=1}^{n} X_j A_{j,\nu} \, , \tag{3.2}$$

where A_b is the resulting linearly blended spectra of mixture b, X_j is the mole fraction of each component j, A_j is component js spectra, and the summation is performed over the n components in the mixture. The mole-weighted summation is carried out over all wavenumbers ν. In this manner, a small database of neat hydrocarbon spectra can be used to numerically create fuel spectra.[2]

We evaluate the newly developed models by their ability to predict the octane numbers of the TRF mixtures referenced in Knop et al. [81]. Our updated RON and new MON correlations predicts RON, MON, and sensitivity of the TRF dataset as well as TRF model (designated here as "K-3") and better than the other six correlations investigated by Knop et al. [81] Figure 3.1 shows the global error for RON, MON, and S for Knop et al. models ("K-1" to "K-7") and our models ("IR"). The global error measures the average root-sum-square error of RON, MON, and sensitivity (S) over all 25 TRFs—lower values are better.

The IR correlations accurately predict quantities of TRF fuel mixtures as well or better than other proposed TRF-specific correlations in the literature [81]. As of now, the model is proven for TRF fuel mixtures, the 34 pure hydrocarbon components outlined in Daly et al. [80], fuel mixtures with various proportions of n-heptane, isooctane, toluene, methylcyclohexane, 1-hexene, and ethanol [16, 42, 43], and the FACE gasolines [41]. Based on this evidence, we believe the IR models to be valid for the hydrocarbons (and mixtures thereof) studied in this work.

In the next section, we incorporate these RON and MON models into the surrogate formulation framework and develop surrogates for the 10 FACE gasolines. At the time of writing this, surrogates for four of these have not yet been published by any researchers. The surrogates are benchmarked

---

[1]Here we used a ThermoFisher Nicolet iS10 FTIR with a single-bounce, Attenuated Total Reflectance (ATR) smart accessory (650–$4500\,/\text{cm}^{-1}$ at $2\,\text{cm}^{-1}$ resolution, nitrogen purged, and crystal type: diamond with ZnSe lens, part number: 222-24700).

[2]Alcohols, such as ethanol, exhibit nonlinear IR blending due to solvation effects, [60, 61] so precautions are needed to include alcohols. See the work of Corsetti et al. [59] for a relevant analysis of this phenomena.
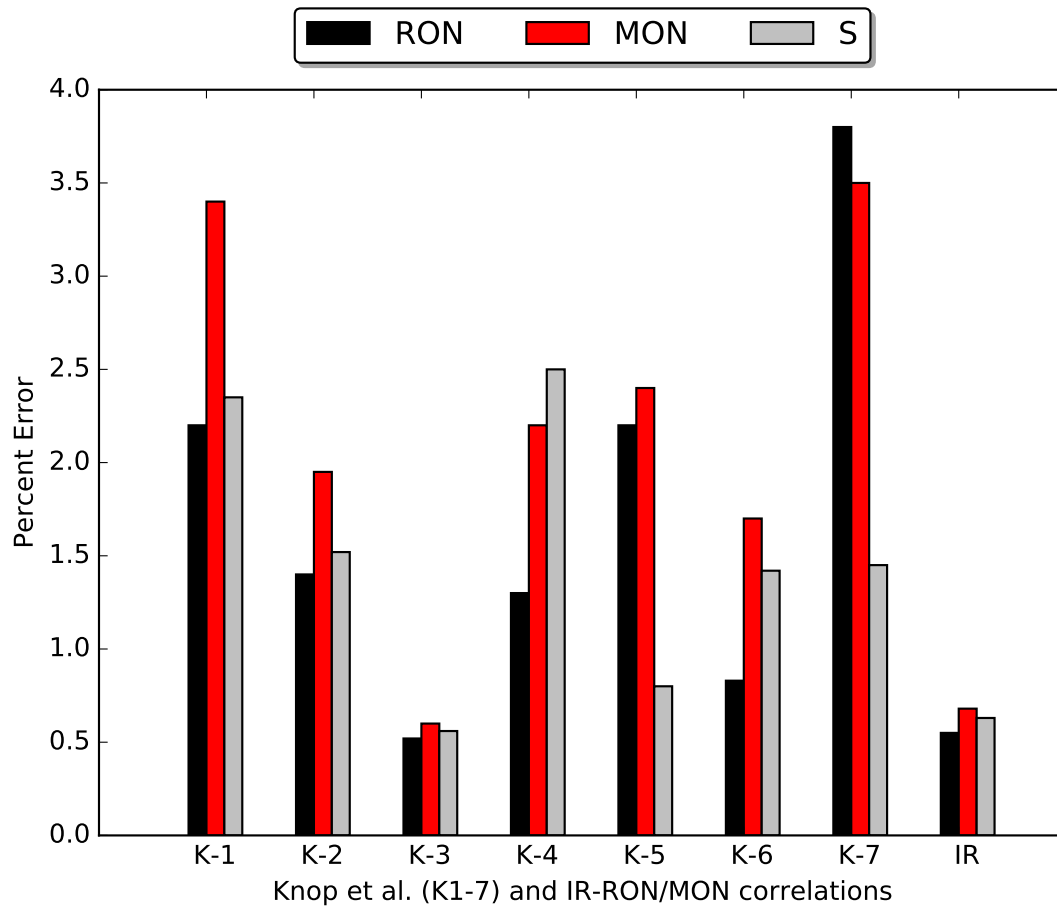
Figure 3.1: Global error of the Knop et al. [81] and current correlations for RON, MON, and sensitivity for the TRF dataset.

by their ability to match the measured properties of the FACE gasolines (see Table 3.1). We then compare formulated FACE gasoline surrogates A, C, F, G, I and J with established surrogates from the literature [72–74, 78] (found in Tables 3.6–3.11).

3.2.2 Framework for formulating surrogate fuels

The framework for formulating surrogate fuels builds on that of Ahmed et al. [72], although our approach uses an open-source software stack based on Python. We used Cantera [82] to handle all chemical Kinetic property evaluations and as the basis for simulating autoignition delay (used for the preliminary ignition delay-octane correlation study). Our approach does still rely on NISTs non-open REFPROP [83] software for evaluation liquid density and distillation curves. We accessed REFPROP via Python using an established interface developed by Thelen [84]. We now outline the objective function, and the methodology to calculate various performance parameters for it.

We use the objective function, the performance variables, and each variable's respective weighting factor given by Ahmed et al. [72], which Table 3.2 shows. However, we add MON to our objective function, with the same weight as RON. Again, these are calculated based on the FTIR-octane models, as outlined in the previous subsection. The objective function, f, sums weighted errors in performance variables of a given surrogate with respect to the target fuel:

$$f = \sum_{j=1}^{n} \beta_j E_j \,, \tag{3.3}$$

where β_j is the weight of parameter j, E_j is the relative error in parameter j between the surrogate and the target fuel, and n is the number of performance parameters (six, in this case). Ahmed et al. chose weighting factors according to each optimization parameter sensitivity, which signifies the respective reduction of error per unit increment of the weighting factor. High sensitivity parameters, such as RON, require a larger weight to minimize surrogate error.

	RON	MON	Density	Distillation	C–C	H/C
Weight (β)	10^4	10^4	10^3	10^2	10^2	1

Table 3.2: Weights for each performance parameter considered in the objective function, taken from Ahmed et al. [72] (except MON, which matches RON here).

In addition to RON and MON, the objective function requires four additional performance

parameters: hydrogen-to-carbon (H/C) ratio, distillation points (temperature at 10-80% volume recovered), density, and carbon–carbon (C–C) bond types. Ahmed et al. [72] provide more details on the calculation methodology for these parameters, though we briefly describe them here for completeness.

H/C ratio, the overall proportion of hydrogen to carbon atoms in the mixture, is calculated via the molar-weighted sum of each component species's ratio. The distillation curves and fluid density calculations are determined in the same manner as Ahmed et al. [72]. For a given fuel mixture, REFPROP approximates the mixture fluid density and determines the distillation curve by simulating thermodynamic vapor-liquid equilibrium states, described in detail by Mueller et al. [71] We consider neat hydrocarbons not represented in default REFPROP database; as such, they were incorporated into the software with guidance from the developers. [85] This required creating reference files containing thermodynamic properties for these species, which REFPROP uses in evaluating the Peng–Robinson equation of state, as well as polynomial fits for specific heat with temperature [83]. These hydrocarbons not included in REFPROP are summarized in Table 3.3, and the associated thermodynamic files are available openly [86]. Our distillation calculations produce advanced distillation curves (ADC), known to be quantitatively different from those produced from typical ASTM-D86 experimental procedures, as laid out by the works of Bruno et al. [87–89]. Advanced distillation curves are only available for six of the ten FACE gasolines [90]. For consistency between formulating all ten FACE surrogates, we use the complete ASTM-D86 distillation data [41] for our study. Future efforts will address sensitivity in formulated surrogate compositions to using ADC versus ASTM-D86 data. Lastly, we assigned the 14 C–C bond types in the same manner as Sarathy et al. [73], including their nomenclature for numbering the types:

1   *n*-CH$_3$ - primary carbon

2   *n*-CH$_2$ - secondary carbon

3   *iso*-CH - tertiary carbon

4   *naphthene* - CH$_2$ - secondary carbon

5   *naphthene to alkyl* - tertiary carbon

6   *naphthene to naphthene* - tertiary carbon

7   *aromatic* CH - tertiary carbon

8   *aromatic to alkyl* C - quaternary carbon

9   *aromatic to naphthene* C - quaternary carbon

10   *aromatic to aromatic* C- quaternary carbon

11   *aliphatic* C - quaternary carbon

12   *primary* C=C double bond

13   *secondary* C=C double bond

14   *tertiary* C=C double bond

Table 3.1 lists the amounts of each C–C bond type for the FACE gasolines, based on the detailed hydrocarbon analysis (DHA) by gas chromatography-flame ionization detector [41]. The general gasoline formulation framework approach will now be explained.

The surrogate formulation framework's task, given a user-defined species palette, is to determine a set of optimal mole fractions that minimize the objective function; i.e., numerically blend species to closely match the fuel properties of the target fuel. This requires iteration, where each iteration is a new set of mole fractions that dictate the bulk fuel properties. For example, in the case of calculating RON/MON, linear-blended spectra (by mole) based on each species in the palette is first determined; then, the spectra is fed to the FTIR-octane models to calculate RON/MON. The errors between the predicted RON/MON and the target fuel RON/MON contribute to the overall objective function value. To find the global minimum of the objective function, we used a constrained multiobjective optimization routine from the SciPy library (`scipy.optimize.minimize()`) [91], with a constrained quasi-Newton method (L-BFGS-B) [92]. We also found, in agreement with Ahmed et al. [72], that the optimization algorithm could get "stuck" in many local minima of the objective function. To resolve this, we fed 100 randomized initial conditions (i.e., mixture mole fractions) into the optimization routine, then chose as the final result the designed surrogate (out of 100) with the lowest objective function value. We acknowledge that other optimization routines may be more efficient than this ad-hoc solution, such as a basin-hopping routine (e.g., `scipy.optimize.basinhopping()`), but our approach requires minimal computational effort to redundantly evaluate the objective function, so we did not see much reason to pursue alternatives.

In the optimization algorithm, we constrain the mole fractions for each constituent species in the surrogate palette between zero and a species-dependent value less than one. The upper bound of each species is dictated by its respective hydrocarbon class and the relative proportion of that class within the target fuel, as per the DHA. For example, if the target fuel has 20% by mole of n-paraffins, and the surrogate palette has two n-paraffins such as n-pentane and n-heptane, then the upper mole-fraction bound of both species is 0.2. This seemed a reasonable bound to expedite the surrogate design as opposed to setting the bound to one. However, if the algorithm designs a final surrogate with a species at its upper bound, then the bound is increased and the optimization repeated to (potentially) yield a better solution. We also ensured that species mole fractions summed to one by applying a penalty function to the objective (multiplying by 10^8) when

violating this constraint.

We also imposed additional logic at the end of the optimization routine to further simplify surrogates: if the number of species in the palette is greater than seven, and if any these species are present at less than 4% by mole, then a new surrogate palette is generated without these minor species. This threshold of 4% was arbitrary and deemed to quantify a "minor" amount. We recognize that the threshold method could possibly cause any given hydrocarbon class containing only "minor" species to be completely eliminated for the reduced palette. We did find that this does occur, but with no penalty to the objective function score for the "reduced" formulated surrogate. We then re-execute the surrogate formulation framework with this reduced palette, and again with 100 new randomized fuel mixture initial conditions. We repeat this process until no minor species remain in the final surrogate—we present this result as a "reduced" surrogate, versus the "full" surrogate before this process is applied. This was performed in anticipation of future efforts that will require reduced chemical kinetic models for these FACE surrogates; the kinetic model of Sarathy et al. [73], which incorporates 2315 species and 10,079 reactions, is extensive—fewer components in the final surrogate mixture will result in a simpler reduced kinetic model.

Table 3.3 shows the palette species chosen. We chose the species palette constrained to three criteria. First, we utilize hydrocarbons included in prior surrogate research [72–74, 76, 78]. Next, we only considered species available in comprehensive chemical kinetic models, so that surrogates may be readily used for computational studies; the comprehensive model of Sarathy et al. [73] includes a wide array of species. This kinetic model has additional species not included in past surrogate research. Lastly, we selected species present in the training dataset of the IR-octane correlation used in this work; i.e., the species that informed the PCR model and whose properties we expect to be adequately predicted. See Daly et al. [80] for the complete list of fuels used in the training data set. One exception to this is pure n-pentane, which is not present in the training dataset directly as a pure component for the IR-octane models. The FACE gasolines themselves are included in the training dataset in this work, and contain 0.06–15.06% by mole n-pentane as per the DHA. As such, we expect fuels with less than 15% by mole of n-pentane to be adequately predicted; prediction error may increase for fuels with more than 15% of n-pentane. The pure component spectra of n-pentane was collected after the IR-RON/MON model training phase, and will be included in future efforts. N-butane was not able to be included in the species palette, as with literature surrogates [72, 73],

since we could not procure the ATR-FTIR spectra. This is primarily due to limitations in the spectra collection methodology, which require the substance measured to be solid or liquid at room conditions.

Based on our constraints, the final fuel palette extends previous efforts containing n-pentane, 2-methylpentane, 1-pentene, cyclohexane, and o-xylene. These species broaden the range of molecular weights and hydrogen to carbon ratios for each PIONA class, present to varying extents within the FACE gasolines. Indeed, many of these species are not prevalent in most of the FACE gasolines individually. However, guided by the work of Daly et al. [80], blended octane ratings are highly sensitive and non-linear to additions of these species. As such, incorporating these species extends the range of blended octane rating combinations, and we expect better convergence to target octane ratings. We limit the parameterization of our current study by omitting some candidate species, such as m-/p-xylenes or 2-pentene; these will be investigated in future efforts. Although, as we will show, there are marginal benefits to leveraging an expansive species palette as opposed to a reduced sub-set.

Palette species	CAS #	Formula	Class (PIONA)	T_b [K]	MW [g/mol]	REFPROP
n-pentane	109-66-0	nC_5H_{12}	paraffin	309.2	72.14	✓
n-heptane	142-82-5	nC_7H_{16}	paraffin	371.5	100.20	✓
2-methylbutane	78-78-4	C_5H_{12}	isoparaffin	300.9	72.14	✓
2-methylpentane	107-83-5	C_6H_{14}	isoparaffin	333.3	86.17	✓
2-methylhexane	591-76-4	C_7H_{16}	isoparaffin	363.4	100.21	✗
2,2,4-trimethylpentane	540-84-1	C_8H_{18}	isoparaffin	372.3	114.22	✓
1-pentene	109-67-1	C_5H_{10}	olefin	304.0	70.13	✗
1-hexene	592-41-6	C_6H_{12}	olefin	337.0	84.15	✗
cyclopentane	287-92-3	C_5H_{10}	naphthene	322.0	70.13	✓
cyclohexane	110-82-7	C_6H_{12}	naphthene	353.8	84.15	✓
toluene	108-88-3	C_7H_8	aromatic	383.7	92.13	✓
o-xylene	95-47-6	C_8H_{10}	aromatic	417.5	106.16	✓
1,2,4-trimethylbenzene	95-63-6	C_9H_{12}	aromatic	442.4	120.19	✗
1,3,5-trimethylbenzene	109-67-1	C_9H_{12}	aromatic	437.8	120.19	✗

Table 3.3: Species palette for FACE surrogates. T_b is the normal boiling point, and "REFPROP" indicates whether the species was represented in the software. Species not included in the default REFPROP database were manually added.

3.3 Results and discussion

First, we present the surrogates developed here for FACE gasolines A–J. These surrogates were generated from the full, original species palette with 8–13 species (depending on the target FACE gasoline). We also developed simpler surrogates containing 4–7 species from a reduced species palette. The supplemental material contains tables and figures comparing the full- and reduced-palette surrogates, describing in detail how well the surrogate matches respective target properties. Finally, we compare the surrogates for FACE gasolines A, C, F, G, I and J with other proposed surrogates from the literature.

3.3.1 Full-palette FACE surrogates

Table 3.4 presents the full-palette FACE gasoline surrogates. A molar amount of zero indicates that the species was considered but the algorithm converged on that value, while a blank entry indicates the species was not considered.

The FACE gasoline surrogates, on average, match the array of target properties within 5 %. This demonstrates that our framework can create gasoline surrogates for the wide range of gasoline target properties the FACE gasolines represent—given the species palette utilized. In contrast to the other surrogates generated, the FACE G surrogate exhibits high prediction errors in density (5.3 %) and H/C ratio (16.8 %). This may result from the relatively high weighting factors used to (successfully) match RON and MON with low errors. At the same time, the species mole fractions were not strictly constrained to enforce matching the target H/C, C−C types, or density; as a result, the algorithm was free to depart from these target properties to minimize the objective function. To match the high octane sensitivity of FACE G—11, the highest of the FACE gasolines—the optimization algorithm selected large amounts of olefins (high sensitivity) and low amounts of n-paraffins (low sensitivity); no other options were available based on the species present in the palette. We conclude that the the IR-octane models should be updated with additional high-sensitivity fuel mixtures for greater model robustness, as it should be possible to design a high sensitivity fuel with proper n-paraffin, isoparaffin, olefin, naphthene, and aromatic proportions. This means the IR-octane model training procedure revisited by including additional high-sensitivity fuel mixtures, potentially adding new components to the surrogate species palette that the IR-octane model is updated with, followed

by repeating the surrogate formulation. The surrogates for the remaining, lower-sensitivity FACE gasolines (ranging 0–8) adequately capture the target properties; for example, the FACE D surrogate matches all performance attributes within 3 %.

3.3.2   Reduced-palette FACE surrogates

Table C.1 presents the simpler FACE surrogates, with four to seven species, designed using reduced species palettes. Interestingly, though these surrogates contain fewer components, they capture the properties of the target fuels better, or nearly as well as the larger, full-palette surrogates. The minor species removed from the "full" palette did result in some hydrocarbon classes being completely eliminated. For example "reduced" surrogates for FACE A and B no longer have n-paraffins, and the objective function score was further minimized (indicating a better surrogate). The reduced-palette surrogates, on average, predict RON, MON, and distillation curve slightly better, and density and H/C ratio slightly worse than the full-palette surrogates. Overall, the reduced-palette FACE surrogates achieved better objective function evaluations than their full-palette counterparts—meaning they better-match the real gasoline. Based on the overall similarity in performance between the two sets of surrogates, satisfactory surrogate fuels may be obtained without requiring an ever-larger palette of potential components.

This result is counter intuitive. We expect that as components in the surrogate palette and their relative proportions approaches that of the target fuel the objective function would be best-minimized (approach zero). We suggest that modeling artifacts causes much of the "reduced" surrogates to outperform the "full". The overall accuracy of predicted fuel properties could be reducing as the species palettes grows. Larger species palettes also bring the increased possibility that the optimization routine is not guaranteed to return a global minimum. Additionally, weighting factors for the objective function may also need to be tuned on a per-surrogate basis, due to the large variability in the species palette and therefore parameter sensitivity. These intricacies and their impact on modeling results were not investigated in this work, but should be investigated in future efforts.

Unfortunately, limiting the palette exacerbates some errors for the worse-performing full-palette surrogates. For example, FACE G reduced-palette surrogate captures H/C ratio worse at 15.7 %, although density, RON, and MON still closely match those of the full-palette surrogate. The

Parameter	A	B	C	D	E	F	G	H	I	J
RON	83.9	95.1	84.1	93.7	87.4	93.6	95.9	86.7	70.2	72.7
MON	83.6	93.2	83.2	87.7	81.2	88.2	86.7	80.1	69.5	71.0
Density (kg/m^3)	697	709	703	762	734	734	803	771	716	748
H/C	2.23	2.15	2.16	1.83	2.00	2.03	1.57	1.76	2.12	1.90

% Volume distilled	Temperature [K]									
10	338	339	336	347	337	345	348	344	343	352
20	344	346	341	354	342	350	358	349	348	360
30	352	355	348	361	346	356	372	355	354	368
40	360	365	355	370	352	363	389	364	360	375
50	367	372	363	378	358	369	406	374	367	381
60	370	375	370	387	365	374	418	387	370	388
70	371	377	374	395	371	380	423	399	373	400
80	372	380	378	405	379	387	426	413	378	422

Carbon type	Fractional %									
1	54.8	55.4	51.8	38.9	33.3	42.5	24.1	27.5	41.4	33.6
2	21.5	14.9	21.5	14.3	18.9	15	14.8	17.4	27.9	25.8
3	11.9	12.1	11.4	7.4	6.7	8.5	0.3	2.8	7	3.1
4	0	0	0	3.1	19.4	11.9	6.6	14.2	7.9	7.2
5	0	0	0	0	0	0	0	0	0	0
6	0	0	0	0	0	0	0	0	0	0
7	3.4	6.9	6.7	23.6	9.4	9.5	28.1	23.3	7.3	13.2
8	1	3.1	2.8	10	4	4.7	17.1	10.8	3.3	9.9
9	0	0	0	0	0	0	0	0	0	0
10	0	0	0	0	0	0	0	0	0	0
11	7.4	7.7	5.8	2.7	3.1	5.6	0.3	1.2	4.2	2.5
12	0	0	0	0	2.6	1.2	4.4	1.3	0.5	2.4
13	0	0	0	0	2.6	1.2	4.4	1.3	0.5	2.4
14	0	0	0	0	0	0	0	0	0	0

Species	Molar %									
n-pentane	6.4	0.0	5.9	0.3		0.0		5.3	13.0	3.0
n-heptane	5.1	1.7	5.3	4.1	1.3		3.9	9.4	15.0	21.8
2-methylbutane	20.0	24.0	18.6	9.8	10.2	9.4	0.0		7.7	2.3
2-methylpentane	1.0	4.2	13.3	20.4	1.0	0.1	0.5	7.8	4.2	1.9
2-methylhexane	10.6	3.3	6.5	3.1	12.6	10.4		2.8	7.0	
2,2,4-trimethylpentane	51.8	54.9	40.0	18.9	19.9	38.9	1.8	8.3	28.5	18.1
1-pentene					4.8		11.2	5.0	0.6	8.4
1-hexene					12.1	8.3	20.1	4.0	3.0	8.6
cyclopentane				4.3	15.6	16.5	9.3	18.6	0.0	
cyclohexane					8.0			0.5	9.0	8.5
toluene	3.4	1.9	4.3	8.8	4.1			13.6	5.1	3.4
o-xylene	1.7	9.9	5.0	30.1	9.6	16.4	38.9	14.9	3.3	5.0
1,2,4-trimethylbenzene			1.5	0.3			14.4	9.8	3.7	15
1,3,5-trimethylbenzene					0.8					

| Objective Function | 1.61 | 2.85 | 1.25 | 3.12 | 0.30 | 1.91 | 10.5 | 3.29 | 3.05 | 6.95 |

Table 3.4: Full palette, formulated FACE gasoline surrogates. A blank entry indicates that the species was considered in the work, but was not included in the palette for the particular FACE gasoline. A zero (0) indicates the species was in the palette, but not chosen by the optimizer.

supplemental material contains surrogate-specific target property changes between the full- and reduced-palette formulations. In general, the C−C bond types are the hardest properties to predict with the reduced palette.

3.3.3 Comparison with literature surrogates

This section compares the surrogates developed in the current study with surrogates proposed in the literature for FACE gasolines A [72, 78], C [72, 78], F [73], G [73], I [74] and J [74]. For now, we omit comparing to the FACE A, C, I and J primary reference fuel (PRF) surrogates from Shankar et al. [75], as they only considered RON/MON in their formulation methodology. While these PRF surrogates are well-validated to emulate combustion behavior for these FACE gasolines at pre-mixed conditions, the surrogates may not be applicable to more complex physical environments including spray, mixing and diffusion. As such, we only consider the literature surrogates that targeted both physical and chemical properties, specifically: hydrocarbon classes, C−C bond type proportions, distillation characteristics, H/C ratios, density, and octane ratings. Tables 3.6–3.11 compare the new surrogates with previous surrogates in terms of target properties.

3.3.3.1 FACE A

Table 3.6 compares the performances of the full-palette, eight-component and reduced-palette, four-component surrogates developed in the current study for FACE gasoline A along with the five-component surrogates developed by Sarathy et al. [78] and Ahmed et al. [72]. For clarity, Ahmed et al. presents three FACE A surrogates; however, one of them is from Sarathy et al. [78] for comparison. Figure 3.2a shows that the full-palette surrogate well-matches the n-paraffins and isoparaffins hydrocarbon classes in FACE gasoline A. The aromatic content of this surrogate surmounts to the the combined content of olefins, naphthenes, and aromatics. The proposed surrogates from the literature match well, but do not account for the aromatics, olefins, or nephthenes. The reduced-palette surrogate comprises only isoparaffins and aromatics, where the n-paraffin content has been replaced by isoparaffins. Figure 3.2b shows the C−C bond type proportions; both surrogates developed in the current study closely match FACE A in all groups, despite the differences in overall hydrocarbon class makeup. Our surrogates better match the distillation characteristics of FACE A, with a higher T_b above 60 % distillate than the literature surrogates as Figure 3.2c shows. We attribute

Parameter	A	B	C	D	E	F	G	H	I	J
RON	83.8	95.1	84.4	93.9	87.4	94.4	96.3	86.9	70.1	73.2
MON	83.7	93.1	82.9	87.3	81.1	88.9	86.8	79.9	69.5	70.2
Density (kg/m^3)	700	718	698	761	731	732	802	775	710	761
H/C	2.22	2.11	2.20	1.83	2.05	2.03	1.54	1.75	2.15	1.86

% Volume distilled	T [K]									
10	337	341	334	344	339	346	352	348	341	360
20	343	349	340	352	342	351	363	354	347	368
30	352	360	348	362	346	357	374	362	353	374
40	361	371	358	373	351	363	387	372	360	379
50	368	376	367	382	357	369	404	382	364	384
60	371	378	372	389	364	374	419	391	367	391
70	372	380	375	395	372	379	424	400	368	401
80	375	385	378	404	382	386	426	417	369	419

Carbon type	Fractional %									
1	54.4	54	53.7	38.6	35.4	43.1	23.7	27	44	30.8
2	21	14.3	21.7	13.9	18.4	15.5	17.7	16.4	28.4	24.6
3	13.5	11.8	11.5	6.6	7.8	8.4	0	2	9.1	2.3
4	0	0	0	4.9	20.9	10.3	0	16.6	4.2	10.2
5	0	0	0	0	0	0	0	0	0	0
6	0	0	0	0	0	0	0	0	0	0
7	3.4	8.4	4.3	23	7.3	9	28.6	22.8	8.4	14.6
8	1.7	4.2	2.1	9.8	3.6	4.5	17.4	10.9	1.7	10.5
9	0	0	0	0	0	0	0	0	0	0
10	0	0	0	0	0	0	0	0	0	0
11	6	7.3	6.6	3.2	3.5	5.9	0	2	4.2	2.3
12	0	0	0	0	1.6	1.7	6.3	1.2	0	2.4
13	0	0	0	0	1.6	1.7	6.3	1.2	0	2.4
14	0	0	0	0	0	0	0	0	0	0

Species palette	Molar %									
n-pentane									11.0	
n-heptane			13.0	8.6				16.5	11.6	23.7
2-methylbutane	26.1	23.3	28.2	16.2	8.8	9.4			12.8	
2-methylpentane			5.5	7.7						
2-methylhexane	25.9	9.1		0.0	19.2	7.5			20.0	
2,2,4-trimethylpentane	42.1	52.4	45.9	22.5	22.5	41.5		13.9	28.5	16.4
1-pentene							9.5	8.0		8.5
1-hexene					10.3	11.6	35.7			8.7
cyclopentane				6.9	27.3	14.3		22.8		
cyclohexane									4.7	12.3
toluene				8.1				15.0	11.4	
o-xylene	5.9	15.2	7.4	30.0	11.9	15.7	40.0	11.1		15.0
1,2,4-trimethylbenzene							14.8	12.7		15.4

Objective Function	1.21	2.11	0.60	2.19	0.48	0.66	12.2	2.98	1.87	4.02

Table 3.5: Reduced palette FACE gasoline surrogates. A blank entry indicates that the species was considered, but was not included in the palette for the particular FACE gasoline. A zero (0) indicates the species was in the palette, but not chosen by the optimizer. The reduced species palette was generated using an iterative, auto-reduction strategy based on a low-amount species threshold.

Parameter	FACE A[41]	Full	Reduced	Sarathy[78]	Ahmed[72]	
RON	83.9	83.9	83.8	84.0	86.6	85.6
MON	83.5	83.6	83.6	84.0		
Density [kg/m^3)	685	697	699.8	686	694	691
H/C	2.29	2.22	2.22	2.28	2.28	2.26

% Volume distilled	Temperature [K]					
10	329	337	336	335	321	351
20	344	343	343	347	337	360
30	357	352	352	356	351	365
40	365	360	361	362	361	368
50	368	367	368	366	366	369
60	370	370	371	368	368	370
70	372	371	372	369	369	370
80	374	372	375	370	369	370

Species	Molar %					
n-butane				7.0	7.7	5.0
n-pentane		6.4	0			
n-heptane		5.1	0	7.0	10.0	5.0
2-methylbutane		20.0	26.1	15.0	12.0	5.0
2-methylpentane		1.0	0			
2-methylhexane		10.6	25.9	11.0	10.3	15.0
2,2,4-trimethylpentane		51.8	42.1	60.0	60.0	70.0
toluene		3.4	0	0	0	0
o-xylene		1.7	5.9			
1,2,4-trimethylbenzene		0	0			

Table 3.6: The full- and reduced-palette FACE gasoline A surrogates compared with literature surrogates and the real FACE A properties. A blank entry indicates the species/parameter was not considered. A zero (0) indicates the species was in the palette, but not chosen by the optimizer.

this to the higher boiling components, which other proposed surrogates do not contain. We find matching higher T_b comes at the expense of more error with formulated PIONA, since our aromatic composition in the surrogate are larger than the combined aromatic, olefin, and naphthenes of the target fuel. Future efforts will investigate if this is due to ADC modeling artifacts, discrepancies in ADC to ASTM-86 methods, and if it is preferential to match PIONA versus higher T_b targets in the surrogate formulations. Lastly, Figure 3.2d shows the error between the remaining target properties—recall that the development of surrogates proposed by Ahmed et al. [72] for FACE A did not consider MON. The current surrogates match RON better than the literature surrogates, but at the expense of matching H/C and density. The full-palette surrogate slightly outperforms the reduced-palette surrogate in these four final metrics.

3.3.3.2 FACE C

Parameter	FACE C[41]	Full	Reduced	Sarathy[78]	Ahmed[72]
RON	84.7	84.1	84.4	84.0	85.3
MON	83.5	83.2	82.9	84.0	
Density [kg/m^3]	690	703	698	686	696
H/C	2.27	2.16	2.20	2.25	2.23
% Volume distilled			Temperature [K]		
10	331	336	334	325	329
20	341	341	340	341	344
30	350	348	348	354	357
40	359	355	358	363	365
50	366	363	367	367	368
60	372	370	372	369	370
70	376	374	375	370	372
80	382	378	378	370	374
Species			Molar %		
n-butane				17.0	18.4
n-pentane		5.6	0		
n-heptane		5.2	13.0	11.0	12.5
2-methylbutane		18.6	28.2	8.0	7.0
2-methylpentane		13.3	5.5		
2-methylhexane		6.5	0	5.0	4.7
2,2,4-trimethylpentane		40.0	45.9	56.0	54.6
toluene		4.3	0	3.0	4.8
o-xylene		5.0	7.4		
1,2,4-trimethylbenzene		1.5	0		

Table 3.7: The full- and reduced-palette FACE gasoline C surrogates compared with literature surrogates and the real FACE C properties. A blank entry indicates the species/parameter was not considered. A zero (0) indicates the species was in the palette, but not chosen by the optimizer.
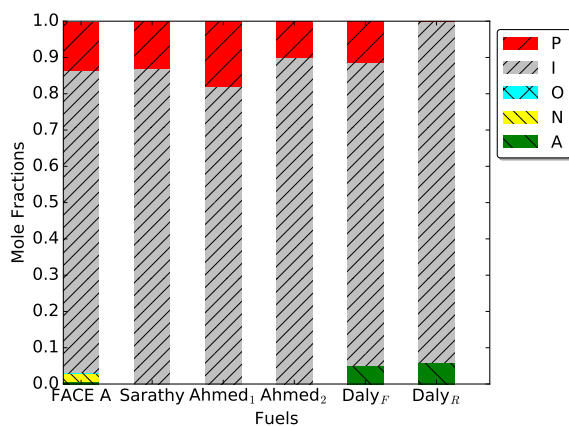
(a) Hydrocarbon class proportions
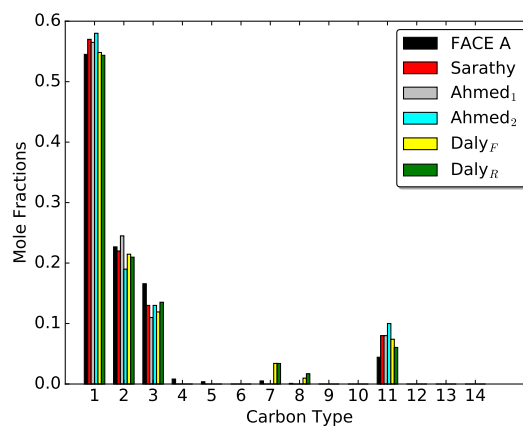
(b) C–C bond type proportions
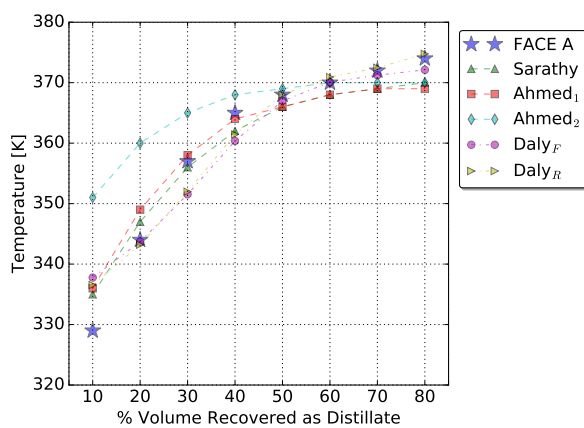
(c) Distillation curve
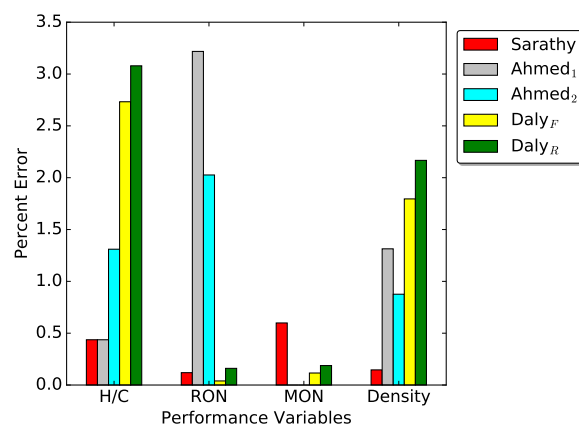
(d) Error in H/C, RON, MON, and density

Figure 3.2: Target property comparisons for FACE A and surrogates. Shown are surrogates developed in this work and past literature efforts. Ahmed et al. [72] did not consider MON in their surrogate formulations for FACE A

Table 3.7 compares the FACE gasoline C surrogates with the six-component surrogates of Sarathy et al. [78] and Ahmed et al. [72]. Again, Ahmed et al. presents two FACE C surrogates but one of them is from Sarathy et al. [78] for comparison. Our full palette consists of a nine-component surrogate, as well as a reduced four-component version. It can be seen in Figure 3.3a, that the full- and reduced-palette surrogate has less n-paraffins and more aromatic content than those by Ahmed et al. The reduced-palette surrogate, in comparison with the reduced surrogate for FACE A, retains n-paraffins content. The C−C bond type proportions are again seen in Figure 3.3b, showing a trade-off with all surrogates for the C−C groupings; no surrogate matches all groups perfectly. The C−C proportions remain similar, with a small trade-off between bond groups such as 1 and 7, in congruence with PIONA. Figure 3.3c presents the distillation curves. The current surrogates show higher T_b, relative to literature surrogates, above 60 % distillate to better match FACE C. We attribute this to higher compositions of the higher boiling components over the other surrogates. Again, we find that matching higher T_b comes at the expense of an arguably less-optimal solution for PIONA. As discussed with FACE A surrogates, future efforts aim to investigate these findings in more detail. Interestingly, the reduced surrogate matches the target curve best at all distillate percentages out of all surrogates (except at 10 %). Lastly, Figure 3.3d shows the error between the remaining target properties—recall surrogates proposed in Ahmed et al. [72] for C did not consider MON. We can see that the RON are better-matched in both new surrogates, but at the expense of H/C and density.

3.3.3.3   FACE F

FACE gasoline F surrogates are compared in Table 3.8 with those presented in Sarathy et al. [73], which utilized eight and seven components. We present a seven-component surrogate with alternate isoparaffins and additional aromatics to those in Sarathy et al. [73], as well as a reduced six-component version. It can be seen in Figure 3.4a, that the full surrogate has no n-paraffins, more aromatics, and similar olefinic and naphthenic content than FACE F. The PIONA of the full surrogate are similar to that of Sarathy et al. [73], with the exception of n-paraffins. The surrogates lacking n-paraffins are likely attributable to the IR-RON/MON correlation attempting to match octane sensitivity. As found with the FACE C surrogates, Figure 3.4b shows a trade-off with all surrogates for the C−C groupings, and no surrogate matches all groups completely. Once again, the

(a) Hydrocarbon class proportions
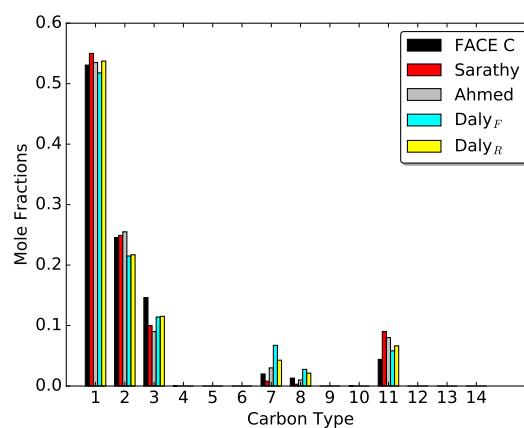
(b) C–C bond type proportions
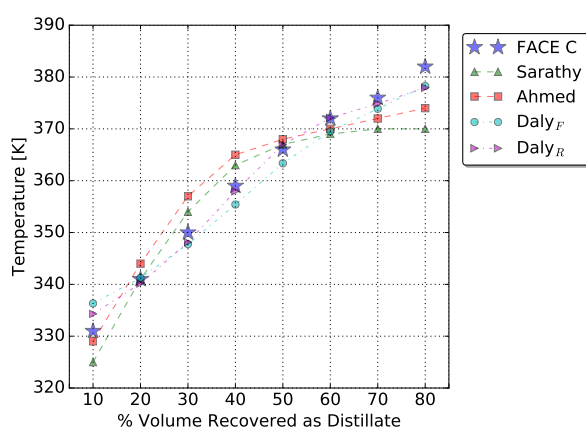
(c) Distillation characteristics
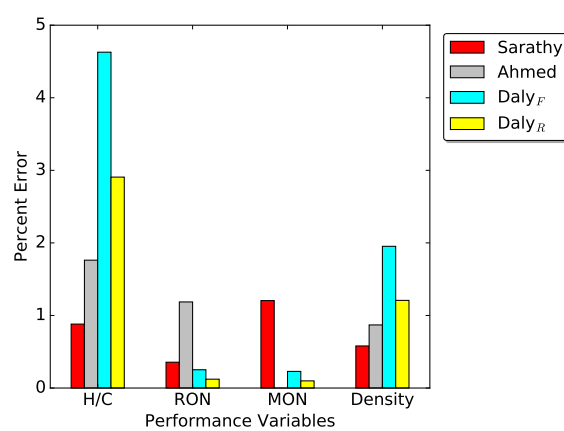
(d) Error in H/C, RON, MON, and density

Figure 3.3: Target property comparisons for FACE C and surrogates. Shown are surrogates developed in this work and past literature efforts. Ahmed et al. [72] did not consider MON in their surrogate formulation for FACE C

| Parameter	FACE F[41]	Full	Reduced	KAUST[73]	LLNL[73]
RON	94.4	93.6	94.3	93.6	93.8
MON	88.8	88.2	88.7	88.9	89.5
Density [kg/m^3]	707	734	731.8	707	712
H/C	2.13	2.03	2.03	2.12	2.06
% Volume distilled	Temperature [K]				
10	346	345	346	350	353
20	351	350	351	356	356
30	357	356	357	361	358
40	363	363	363	366	361
50	370	367	369	370	364
60	376	375	374	374	366
70	382	380	379	378	369
80	387	387	386	383	371
Species	Molar %				
n-butane				6.9	0
n-pentane		0	0		
n-heptane		0	0	0	7.0
2-methylbutane		9.4	9.4	9.8	0
2-methylpentane		0.1	0		
2-methylhexane		10.4	7.5	7.0	0
2,2,4-trimethylpentane		38.9	41.5	43.7	53.0
1-pentene		0	0		
1-hexene		8.3	11.6	8.4	14.0
cyclopentane		16.5	14.3	15.8	14.0
cyclohexane		0	0		
toluene		0	0	0	12.0
o-xylene		16.4	15.7		
1,2,4-trimethylbenzene		0	0	8.4	0

Table 3.8: The full- and reduced FACE F surrogates compared with literature surrogates and the real FACE F properties. A blank entry indicates the species/parameter was not considered. A zero (0) indicates the species was in the palette, but not chosen by the optimizer.

C−C proportions remain similar in accordance with PIONA for both surrogates. Figure 3.4c shows the Daly surrogates have higher T_b above 60 % distillate to better match FACE F. We attribute this to the increased amount of higher boiling components in comparison to the other surrogates. Both full and reduced surrogates have nearly the same distillate curve with little error in comparison to the target fuel. Lastly, Figure 3.4d shows the error between the remaining target properties— Sarathy's surrogates for [73] FACE F did consider MON. We can see that the reduced surrogate outperforms the full surrogate across the board, and better-matches RON and MON in comparison to all other surrogates. Both our full and reduced surrogates do not match H/C or density as well as those from Sarathy et al. [73].

The octane ratings of the LLNL FACE F surrogate, as predicted by our FTIR-octane model, surmount to a RON of 91.4 and MON of 86.0. These are not in agreement with the reported values of 93.8 and 89.5 for RON and MON, respectively. Sarathy et al. did not perform auto-ignition or RON/MON tests for the LLNL surrogates [73] (but did for KAUST surrogates), so at this time the octane correlation discrepancies are left unresolved and a study for future efforts. As previously discussed, we cannot evaluate the KAUST surrogates because our FTIR-octane model does not incorporate n-butane.

3.3.3.4   FACE G

In Table 3.9, FACE gasoline G surrogates are compared with those presented in Sarathy et al. [73]. This work presents a full palette eight-component surrogate, as well as a reduced four-component version. It can be seen in Figure 3.5a, that the full surrogate has more aromatics and olefins than FACE G, with less naphthenes, isoparaffins and n-paraffins. PIONA of the full surrogate are dissimilar to those proposed by Sarathy et al. [73], which match the PIONA of FACE G very well. The reduced surrogate is composed only of olefins, naphthenes, and aromatics, with the olefinic content mostly replacing the n-paraffins and isoparaffins. Figure 3.5b shows the C−C groupings for the current surrogates being relatively large for carbon types 7 and 8, due to the high olefins and aromatics, with a low amount of carbon type 1, from lack of n-paraffins and isoparaffins. Figure 3.5c shows the new surrogates match FACE G T_b from 10 to 70 % evaporated, better than the other surrogates. However, all surrogates fail to capture the high T_b above 70 %, as a result of all surrogates lacking enough proportions of higher boiling components. Logically, it seems advisable to
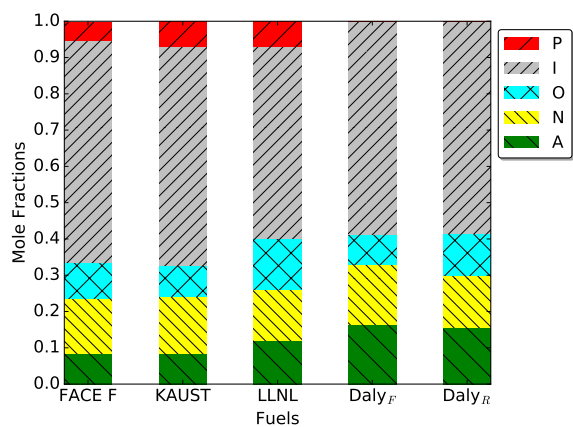
(a) Hydrocarbon class proportions
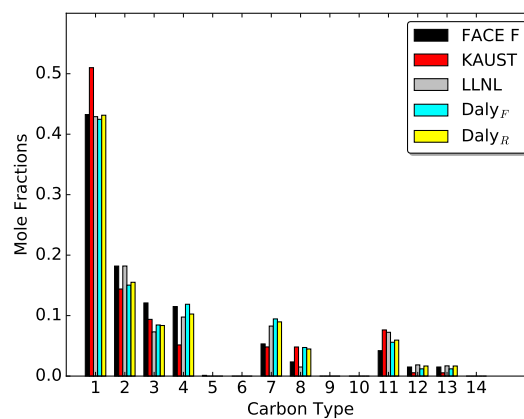
(b) C–C bond type proportions
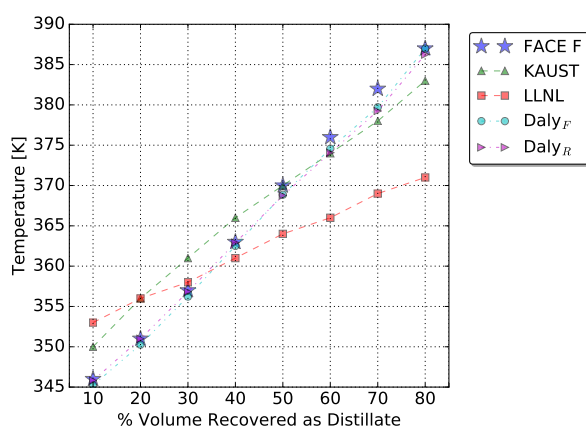
(c) Distillation curve
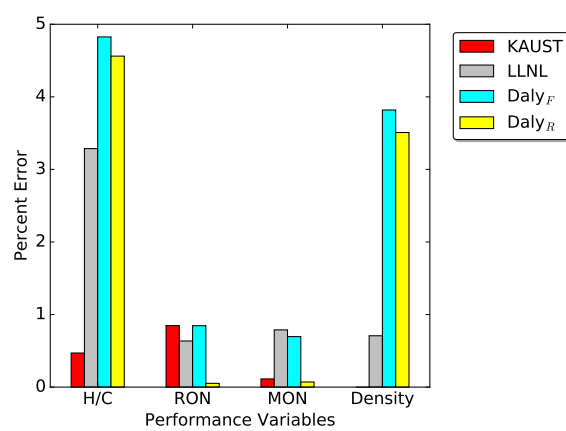
(d) Error in H/C, RON, MON, and density

Figure 3.4: Target property comparisons for FACE F and surrogates. Shown are surrogates developed in this work and past literature efforts.

| Parameter	FACE G[41]	Full	Reduced	KAUST[73]	LLNL[73]
RON	96.8	95.9	96.3	95.2	96.4
MON	85.8	86.7	86.8	87.9	85.5
Density [kg/m^3]	760	803	802	742	751
H/C ratio	1.83	1.57	1.54	1.85	1.87
% Volume distilled			Temperature [K]		
10	350	348	352	345	361
20	363	358	363	351	366
30	378	372	374	359	371
40	394	389	387	367	378
50	411	406	404	376	385
60	426	418	419	386	393
70	439	423	424	397	405
80	447	426	426	417	426
Species			Molar %		
n-butane				7.6	0
n-pentane		0	0		
n-heptane		3.9	0	0	8.0
2-methylbutane		0.0	0	9.5	0
2-methylpentane		0.5	0		
2-methylhexane		0	0	9.8	0
2,2,4-trimethylpentane		1.8	0	18.0	38.0
1-pentene		12.1	9.5		
1-hexene		20.1	35.7	8.1	9.0
cyclopentane		9.3	0	15.3	14.0
cyclohexane		0	0		
toluene		0	0	10.6	0
o-xylene		38.9	40.0		
1,2,4-trimethylbenzene		14.4	14.8	21.1	31.0

Table 3.9: The full- and reduced FACE G surrogates compared with literature surrogates and the real FACE G properties. A blank entry indicates the species/parameter was not considered. A zero (0) indicates the species was in the palette, but not chosen by the optimizer.

reformulate these surrogates for FACE G with additional constraints to use the higher boiling 1,2,4-trimethylbenzene, as opposed to o-xylene. However, it is seen that the other surrogates proposed in literature, which do include 21-31% of this molecule, do not match this distillation region either. We can see, in Figure 3.5d, that the current surrogates have high H/C and density errors, but low errors for RON and MON.

FACE G was particularly challenging to formulate a surrogate for. The contributing factors are: 1) the optimization routine not being strictly constrained to follow hydrocarbon class proportions to match the target fuel, 2) the IR-octane models converging to high olefinic contents in order to formulate a high octane sensitivity fuel, and 3) the objective function highly weighting octane more-so than H/C or density. In short, the optimization routine blended a high sensitivity fuel (by way of high olefinic content), at the expense of properly matching H/C, density, and hydrocarbon class proportions. To support this, we evaluated the LLNL FACE G surrogate with our FTIR-octane model to ensure their surrogate would not provide a high octane sensitivity fuel. Indeed, we found the RON to be 90.2 and MON of 89.9, in contradistinction to the reported values of 96.4 and 85.5. We conclude that the formulation framework utilizing the IR-octane models, in their current state, and the components chosen for the palette are inadequate to match fuels having S > 10, H/C > 1.8, and density $<760\,\mathrm{kg/m^3}$—in other words, low olefinic content fuels with high octane sensitivity. The flexibility in species bounds was found necessary to match octane of FACE G with the IR models. Future efforts will involve improving the IR model so tighter species constraints can be made to better-match PIONA and octane simultaneously.

3.3.3.5   FACE I

In Table 3.10, FACE gasoline I surrogates are compared with those presented in Javed et al. [74]. This work presents a full palette twelve-component surrogate, as well as a reduced seven-component version. It can be seen in Figure 3.6a, that the full surrogate has more textit{n-paraffins, aromatics, and naphthenes than FACE I, with less olefins and isoparaffins. The reduced surrogate is a closer match for napthenes, still a relatively high proportion of aromatics, no olefins, but with a closer match for n-paraffins and isoparaffins. PIONA of those proposed by Javed et al. [74] match the PIONA of FACE I very well. Figure 3.5b shows the C−C groupings for the current surrogates being relatively large for carbon types 7 and 8, due to the high napthenes and aromatics. Figure 3.6c
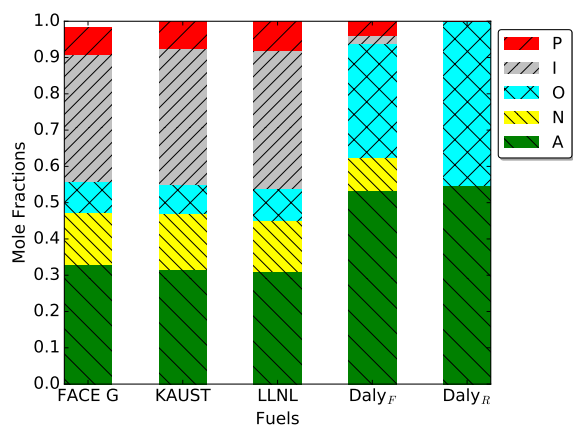
(a) Hydrocarbon class proportions
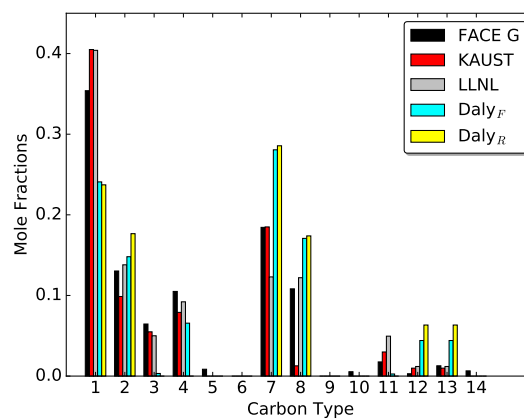
(b) C–C bond type proportions
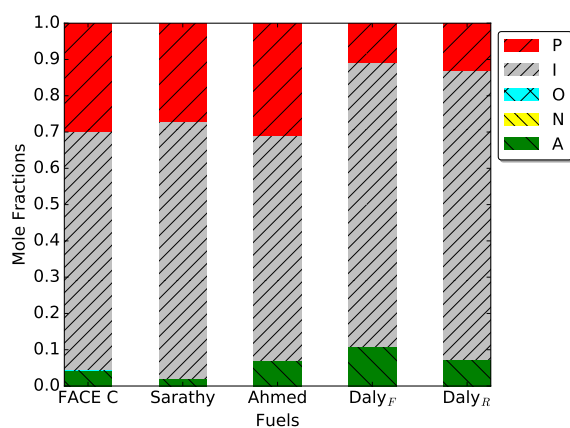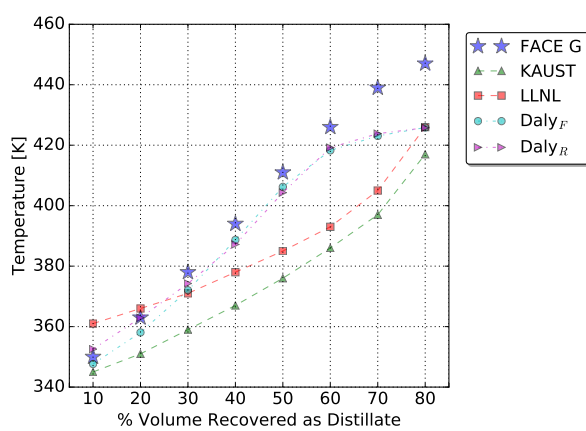

(c) Distillation Characteristics
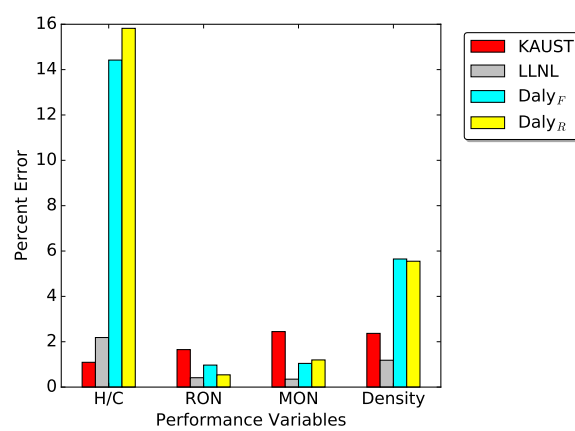
(d) Error in H/C, RON, MON, and density

Figure 3.5: Target property comparisons for FACE G and surrogates. Shown are surrogates developed in this work and past literature efforts.

| Parameter	FACE I[41]	Full	Reduced	Javed[74]
RON	70.2	70.2	70.1	70.7
MON	70.1	69.5	69.5	68.4
Density [kg/m^3]	697	716	710	706
H/C ratio	1.92	2.12	2.15	2.22
% Volume distilled	Temperature [K]			
10	343	343	341	350
20	354	348	347	354
30	359	354	353	358
40	362	360	360	361
50	364	367	364	363
60	366	370	367	365
70	368	373	368	366
80	371	378	369	367
Species	Molar %			
n-butane				
n-pentane		13.0	11.0	
n-heptane		15.0	11.6	12.0
2-methylbutane		7.7	12.8	11.0
2-methylpentane		4.2		
2-methylhexane		7.0	20.0	27.0
2,2,4-trimethylpentane		28.5	28.5	34.0
1-pentene		0.6		
1-hexene		3.0		6.0
cyclopentane		0.0		6.0
cyclohexane		9.0	4.7	
toluene		5.1	11.4	
o-xylene		3.3		
1,2,4-trimethylbenzene		3.7		4.0

Table 3.10: The full- and reduced FACE I surrogates compared with literature surrogates and the real FACE I properties. A blank entry indicates the species/parameter was not considered. A zero (0) indicates the species was in the palette, but not chosen by the optimizer.

shows our surrogates are generally out-performed across the majority of distillate temperatures. We can see, in Figure 3.6d, that our current surrogates have relatively high H/C and density errors, with less errors for RON and MON.

Applying the FTIR-octane correlation to the Javed et al. FACE I surrogate, we predict a RON of 70.0 and MON of 69.8. These values are in better agreement to the target values than reported by Javed et al., who used the TRF linear-by-mol octane model. When using our FTIR-octane model, the Javed et al. surrogate then outperforms our surrogates across all performance metrics. Indeed, the objective function is further minimized (0.59) over our proposed full (3.05) and reduced (1.8) surrogates. Clearly, our optimization routine did not find the global minimum of the objective function, suggesting our framework could benefit from additional parameterization of the species palette and initial mole fraction guesses—likely non-specific to FACE I. Fortunately, this finding serves to validate the application of the FTIR-octane correlation, since the experimentally-validated surrogate of Javed et al. returned an objective function of nearly zero.

3.3.3.6   FACE J

In Table 3.11, FACE gasoline J surrogates are compared with the surrogate of Javed et al. [74]. Our work presents a full palette eleven-component surrogate, as well as a reduced seven-component version. It can be seen in Figure 3.7a, that the full surrogate has more olefins and napthenes than FACE J, with less isoparaffins and n-paraffins; the reduced surrogate has similar PIONA to the full surrogate. The Javed et al. [74] surrogate does not include the minor proportions of olefines and napthenes, but matches the isoparaffins, n-paraffins, and aromatics. Figure 3.5b shows the C$-$C groupings for the current surrogates being relatively large for carbon types 4, 12, and 13 due to the high olefins and napthenes, with a low amount of carbon type 2, from lack of n-paraffins and isoparaffins. Figure 3.7c shows our reduced surrogate for FACE J T_b from 20 to 80 % evaporated is similar to the Javed et al surrogate, which match the target characteristics very well. Our full surrogate tends to under-predict values across this distillate range. We can see, in Figure 3.7d, that our full component surrogate has lower H/C, RON, and MON errors, with higher density error. On the other hand, our reduced surrogate has lower errors only for RON and MON.
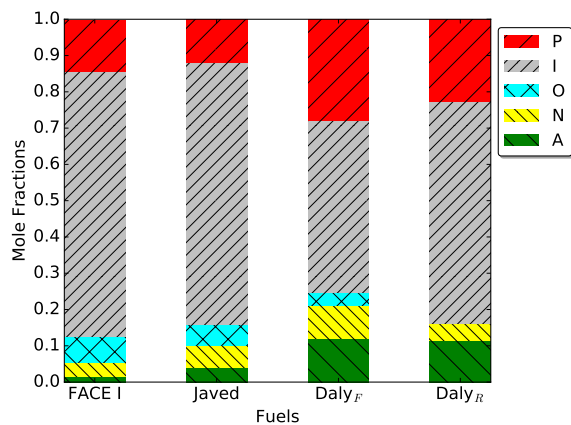
(a) Hydrocarbon class proportions
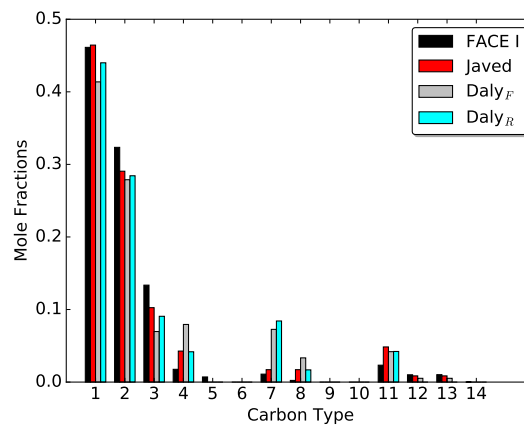
(b) C–C bond type proportions
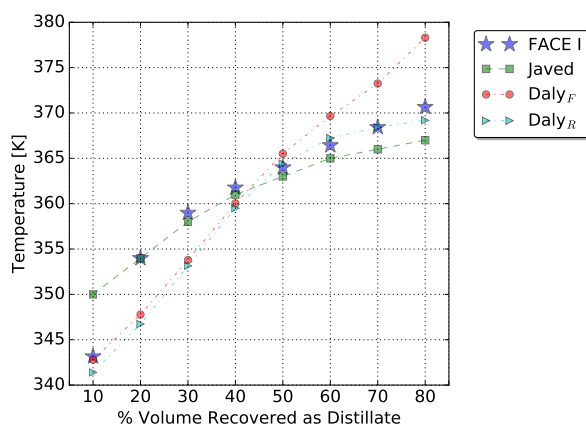
(c) Distillation Characteristics
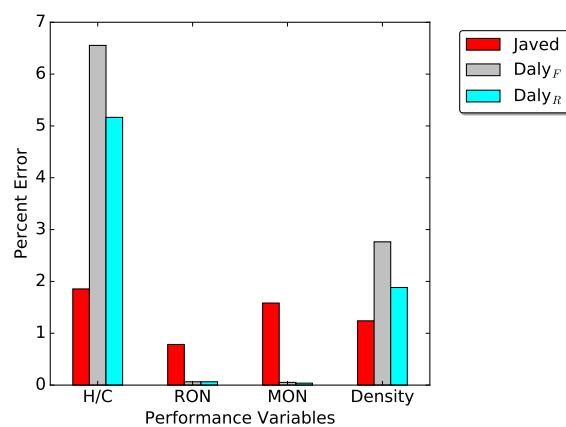
(d) Error in H/C, RON, MON, and density

Figure 3.6: Target property comparisons for FACE I and surrogates. Shown are surrogates developed in this work and past literature efforts.

Parameter	FACE J[41]	Full	Reduced	Javed[74]
RON	73.8	72.7	73.2	70.6
MON	70.1	71.0	70.2	66.5
Density [kg/m^3]	742	748	761	740
H/C ratio	1.92	1.90	1.86	1.95
% Volume distilled	Temperature [K]			
10	346	352	360	353
20	368	360	368	372
30	376	368	374	379
40	380	375	379	383
50	384	381	384	387
60	390	388	391	393
70	401	400	401	404
80	417	422	419	422
Species	Molar %			
n-butane				10.5
n-pentane		3.0		
n-heptane		21.8	23.7	24.5
2-methylbutane		2.3		
2-methylpentane		1.9		
2-methylhexane				23.0
2,2,4-trimethylpentane		18.1	16.4	12.0
1-pentene		8.4	8.5	
1-hexene		8.6	8.7	
cyclopentane				
cyclohexane		8.5	12.3	
toluene		3.4		
o-xylene		5.0	15.0	
1,2,4-trimethylbenzene		15	15.4	30.0

Table 3.11: The full- and reduced FACE J surrogates compared with literature surrogates and the real FACE J properties. A blank entry indicates the species/parameter was not considered. A zero (0) indicates the species was in the palette, but not chosen by the optimizer.
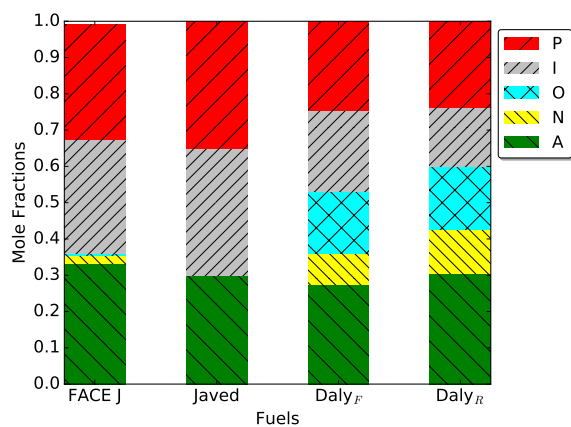
(a) Hydrocarbon class proportions
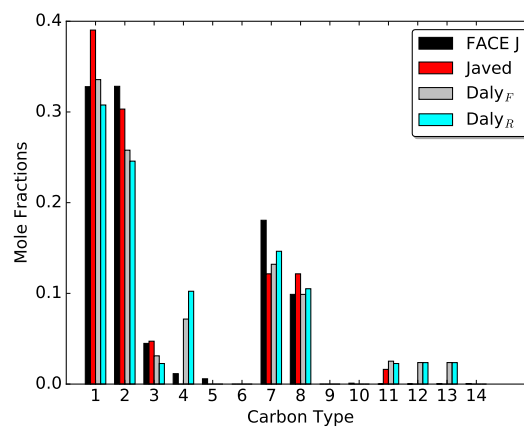
(b) C–C bond type proportions
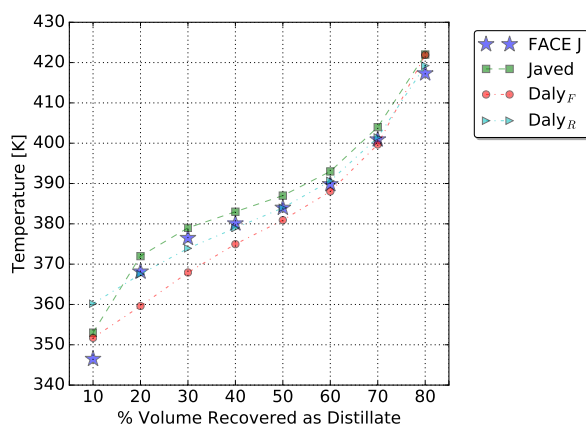
(c) Distillation Characteristics
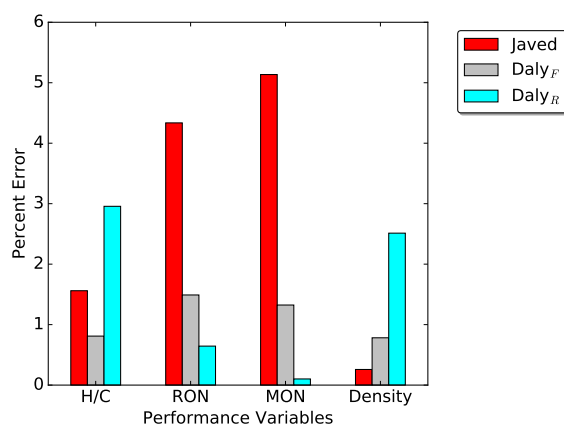
(d) Error in H/C, RON, MON, and density

Figure 3.7: Target property comparisons for FACE J and surrogates. Shown are surrogates developed in this work and past literature efforts.

3.4 Conclusions

An existing gasoline surrogate formulation algorithm was further enhanced by incorporating novel chemometric models. These models use attenuated total reflectance, Fourier transform infrared (ATR-FTIR) spectra of hydrocarbon fuels to predict research and motor octane numbers, alleviating the need for time-consuming auto-ignition simulations. This work developed surrogates from a palette of 14 hydrocarbon species for the Fuels for Advanced Combustion Engine (FACE) gasolines. The palette includes candidate component species not previously considered in the literature: *n*-pentane, 2-methylpentane, 1-pentene, cyclohexane, and *o*-xylene. Furthermore, reduction in the number of components in surrogates was automated based on a mole fraction threshold. As such, the ability to match the properties of the 10 FACE gasoline was evaluated.

This technique yields surrogates for gasoline fuels that accurately match target properties. On average, our "full" (7–12 species) and "reduced" palette (4–7 species) surrogates match all the target properties of the FACE gasolines within 5 %. RON, MON, and distillation curves were matched within 1 %, with H/C and density within 2.5 % and 4.8 %, respectively. FACE G presented the only challenge to create a surrogate for. This seems to be due to the high octane sensitivity (S=11) coupled with low H/C (1.83) and high density ($760\,\text{kg/m}^3$), attributable to low olefins with high aromatics and paraffins present in this fuel. This was a challenge due to three contributing factors: 1) the optimization routine not being strictly constrained to follow hydrocarbon class proportions to match the target fuel, 2) the IR-octane models converging to high olefinic contents in order to formulate a high octane sensitivity fuel, and 3) the objective function highly weighting octane more-so than H/C or density. In short, the optimization routine blended a high sensitivity fuel (by way of high olefinic content), at the expense of properly matching H/C, density, and hydrocarbon class proportions. We conclude that the formulation framework utilizing the IR-octane models, in their current state, are not completely adequate to match fuels having a combination of sensitivity greater than 10, H/C ratio greater than 1.8, and density less than $760\,\text{kg/m}^3$—in short, low olefinic-content fuels with sensitivity over 10. With that said, the other nine FACE gasoline surrogates adequately matched all target properties. We suggest using the "full" palette surrogates since PIONA proportions are better met with these surrogates, in addition to the other target properties. However, if a study requiring minimal computational expense is desired, the formulated "reduced"

palette surrogates can be used (at the expense of matching PIONA).

In some cases, the "reduced" surrogates has a lower objective function value, indicating a more optimal fuel mixture over the "full" surrogate. This result is counter intuitive. We expect the objective function to be zero as the components in the surrogate palette approaches those contained in target fuel, and also blended in the correct proportions by the optimization routine. We suggest that modeling artifacts causes the "reduced" surrogates to outperform the "full". The overall accuracy of predicted fuel properties could be reducing as the species palettes grows. Larger species palettes also bring the increased possibility that the optimization routine is not guaranteed to return a global minimum. We found this to be the case with FACE I, where the established surrogate from Javed et al. [74] provided a lower objective function value over both our formulated surrogates. Because of this, the fuel palette selection logic should be revisited. Additionally, weighting factors for the objective function may also need to be determined on a per-surrogate basis, due to the large variability in the species palette that could influence parameter sensitivity. These intricacies and their impact on modeling results were not investigated in this work, and should be considered in future efforts.

The surrogates created in this work were compared to literature [72–74, 78]. Our surrogates, on average, better-match RON, MON, and distillation characteristics at 0.46, 0.65, and 0.93 % error, respectively, with literature surrogates at 1.2, 1.1, and 1.8 % error. Although, we worse-match density and hydrogen-to-carbon ratio at 3.31 and 6.81 % error with literature surrogates at 1.3 and 2.3 %. We also find that our molar quantities of carbon–carbon bond types deviate at 2.66 molar% with literature at 1.9 molar%.

Surrogates from the literature used vastly different approaches to predict RON, MON, or S. Those approaches were either computationally expensive, not valid for the hydrocarbons considered in this work, or not designed with the intent to predict fuels where molecule-molecule interactions are more prevalent—the methodology in this work simultaneously minimized computational effort and is applicable over the wide range of fuels considered. We evaluated the RON/MON with our FTIR-octane models for three proposed surrogates from literature including FACE F, G and I; these do not include n-butane in the species palette, a restriction our octane model requires. For the LLNL FACE F and G surrogates [73], RON and MON were found to have large discrepancies between our calculated values to those provided by the computationally-heavy, ignition delay to

octane correlation. The FACE I surrogate of Javed et al., with RON and MON based on the TRF linear-by-mol blending formula, agreed with our FTIR-octane predictions when evaluating this surrogate. Further investigations are warranted to verify the foresight of our FTIR-octane model more specific to low-component surrogate fuels seen during optimization. In this manner, a definitive conclusion could be made as to which octane model performs best in predicting surrogate mixtures.

The surrogates proposed in this work ultimately need to be validated by experimental efforts, such as those in literature [72–74, 78]. Based on the attractive results for many of the generated surrogates in this work, we aim to follow up with experimental validation efforts. The altered gasoline surrogate formulation framework generates surrogates in an expedited, and possibly a more accurate manner; it should be considered for further refinement and adoption. Alternately, this methodology could be extended to formulating diesel and jet-fuel surrogates. It should be possible to extend the methodology of Daly et al. [80] to create an IR-cetane number model to use in conjunction with the formulation framework.

Chapter 4: Machine Learning to Predict LTC Engine Fuel Performance

This chapter marries the two bodies of work outlined in Chapters 2 and 3. The methodology presented in Ch. 2 is extended to instead predict the Low Temperature Combustion Index (LTC index). Model robustness is validated by predicting the true values of LTC indices for the FACE gasoline surrogates, developed in Ch. 3. Presented hereafter is a *letter* draft (three journal page limit), presenting a model capable of predicting LTC index of complex fuel samples.

Predicting fuel low-temperature combustion performance using Fourier-transform infrared absorption spectra of neat hydrocarbons

Shane Daly, Khang Tran, Kyle Niemeyer, William Cannella, Christopher Hagen

4.1 Introduction

Low temperature combustion (LTC) engines are capable of offering low NOx and particulate emissions and gross indicated thermal efficiencies reaching 60% in transportation engines. Indeed, replacing traditional spark-ignition engines with LTC engines promotes fuel economy improvement efforts. However, research challenges currently prevent practical implementations of LTC strategies: poor combustion efficiency at light loads, difficulty operating at high loads, issues with controlling combustion phasing, and incomplete understanding of fuel composition effects [93]. In this work, we primarily address the fuel composition aspect by introducing a method to rapidly predict fuel LTC performance.

We describe an approach that couples our earlier techniques [68, 80, 94]. Niemeyer et al. [68, 94] introduced the LTC index, which quantifies the overall performance of a fuel in LTC engine operation. Daly et al. [80] used multivariate analysis to correlate Fourier-transform infrared (FTIR) spectra of a liquid fuel to its research octane number. We aim to predict the LTC index of fuels based on their FTIR spectra.

In this letter we describe the model training and validation process, the objective being to accurately predict LTC indices of refinery-grade gasoline samples. This work predicts LTC indices of the FACE (Fuels for Advanced Combustion Engines) gasolines—ten fuels designed to encapsulate the broad range of gasoline thermochemical properties [41]. By predicting the FACE gasolines we establish the efficacy of the developed model.

4.2 Methodology

The techniques used to correlate fuel spectra to engine performance will first be discussed. Next, we introduce the pure hydrocarbon components and mixtures considered to simulate for LTC index. Lastly, the model validation methodology is discussed.

4.2.1 IR spectra to LTC index model development

This work uses support vector machine regression (SVMR) to correlate IR spectra to LTC index. SVMR was implemented with a machine learning package `scikit-learn` [95] written in the Python programming language. The SVMR model training procedure was guided by literature [96, 97]

and the online `scikit-learn` documentation. We performed grid-search optimization studies for selecting the best kernel function type, function constants, and spectra pre-processing strategies. We imposed k-fold cross validation [98–100] to avoid model over-training; k was varied (3–20) and selected based on minimizing prediction error of the validation data set. The Gaussian type function with no data post-processing offered the best cross validation scores irrespective of k, with k = 20 yielding the best validation score (k > 20 did not improve model performance).

Our model is trained using 313 fuels relevant to advanced engines as guided by literature [16–20, 42, 43, 80]. This includes mixtures containing *n*-heptane, 2-methylbutane, 2-methylhexane, 2,2,4-trimethylpentane, methylcyclohexane, toluene, xylene(s), and ethanol. There are two reasons behind informing the model with neat hydrocarbons and simple mixtures as opposed to complex gasoline samples. First, the resulting statistical models are believed to be robust because they are informed on a fundamental level, namely, information from individual molecules and simple blends are exclusively used. This mitigates the issue of creating a model trained using existing, complex fuels that may be physically and spectroscopically different to future fuels, which could result in inaccurate predictions. Second, the LTC index is determined computationally, thereby limiting the number of hydrocarbon components that can be simulated due to chemical kinetic model size constraints. The full development and description of the procedure for determining LTC index is given by Niemeyer et al. [68, 94].

Due to the complex nature of the FACE gasolines [41], at best only surrogate[1] representations can be simulated such as those provided in literature [72, 73, 101]. With these surrogates, "exact" LTC index values were calculated for FACE gasoline surrogates A–J [101] using the kinetic model of Sarathy et al. [73]. We predict LTC indices of FACEs A–J with their actual spectra, and compare to the "exact" (surrogate) values to validate the model. The IR absorbance spectra collection methodology was carried out in the same manner, and using the same equipment, as described by Daly et al. [80]. See the appendices for additional SVMR and fuel details: fuel mixture compositions and LTC indices with utilized chemical mechanisms [73, 102–106] are in Appendix C), and SVMR model constants in Appendix E).

---

[1]Here, surrogate refers to a mixture of a few pure components that mimics performance attributes of the complex, real fuel.

4.3 Results and discussion

The IR-to-LTC index model has a coefficient of fit of 0.99 for the 313 fuels that trained the model. Fig.4.1 shows the LTC index predictions for FACE gasolines A–J, with an inset box-and-whisker plot of the residual errors.
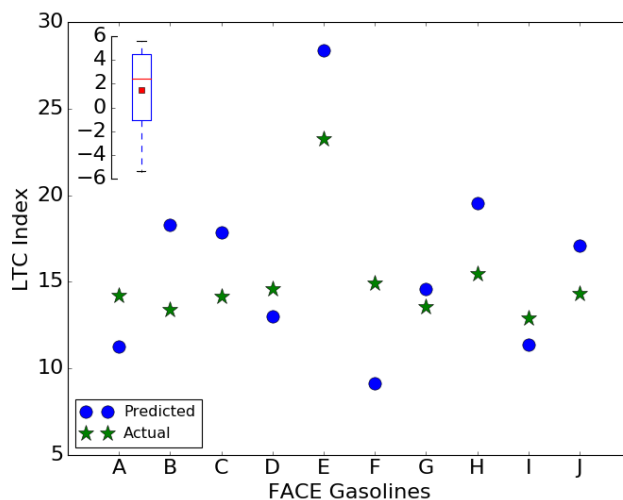
Figure 4.1: IR-to-LTC-index model validation with FACE gasolines. Inset shows box and whisker plot of residual errors.

Most FACE gasolines are predicted within 3 units ($\pm 0.67\sigma$), and at worst within 6 ($\pm 2.7\sigma$). The moderate success could be due to the IR absorbance spectra being non-linearly related to the LTC index, necessitated by the non-linear Gaussian kernel function. One possible reason for this finding is most of our fuel mixtures create an LTC index vastly different than the sum of their individual parts. The moderate prediction errors likely stem from spectral features that are present in the FACE gasolines that are not represented within the simple training data set.

4.4 Conclusions

The IR-to-LTC index model can be readily applied to predict LTC indices of fuels closely resembling those within our training data set. Predictions are reasonable for the FACE gasolines, indicating the model is applicable to refinery-grade fuels. Future efforts will include fuels with spectral features characteristic of the FACE gasolines that our current fuels lack [80], in an effort to improve model foresight. The current tool can predict LTC index of surrogate gasoline fuels or investigate functional groups that improve LTC index, providing researchers and practitioners with the means to design

fuels tailored to evolving combustion technologies.

Chapter 5: Spatiotemporal Fuel Mixture Fraction Measurements

The previous chapter delivered a predictive model for LTC index, founded upon a data set of simple fuels and validated by the FACE gasoline surrogates. Each LTC index value is determined by thousands of HCCI simulations. As such, the LTC index accuracy is dictated by the HCCI simulation accuracy. With HCCI simulation inaccuracies, i.e. results not in agreement with reality, then the generated LTC index data set is not informative of trends that would be observed in reality. As a result, the IR-to-LTC index predictive model utility could be compromised. This work aims to investigate the accuracy of low-fidelity combustion modeling in a novel way, which could in turn be used to validate the utility of the LTC index predictive model if proved a viable strategy. This process involves comparing combustion simulations to experimental results.

Ideally, one could compare simulated LTC index values to experimentally determined values. Unfortunately, determining LTC index for fuels directly with engine experiments would be unreasonable as the time invested to do so would be immense (possibly the span of a decade). Instead, various various combustion parameters are measured in a constant volume, combustion chamber (CVCC) apparatus for an array of fuels. Facilitating experiments in a vessel will take less time and require a lower volume of fuel sample. In this manner, it is reasonable to perform a sizeable parametric study of ambient conditions and fuel mixtures in a controllable manner, while also facilitating advanced experimental techniques that pose significant challenges to employ in an engine.

The experimental effort is organized into segmented studies. First, a simple one-dimensional model is assessed in its ability to capture key spray-formation processes for direct fuel injection conditions. The 1-D spray model is coupled with the same reaction chemistry used in the HCCI (LTC index) simulations; although here, the 1-D combustion model is used to predict spray-ignition onsets. As this work will show, the accuracy of this 1-D combustion model is found to vary with ambient conditions and fuel composition, implicating potential inaccuracies from the chemical mechanism.

Prior to the main experimental campaign (outlined in Chapter 6), the feasibility of using the combustion chamber apparatus to fundamentally study ignition phenomena of gasoline-like fuels is investigated. CVCCs require directly injecting the fuel into a high pressure and temperature

reactive gas mixture, a process that is high in thermal-fluid complexity. Fuel is subject to mass and momentum exchange with the environment, potentially followed by low-temperature heat release depending on the fuel, and subsequent ignition. That is, non-uniform fuel/air mixture compositions and temperature distributions as the spray mixes at timings relevant to ignition. This poses some challenges, primarily that any results derived from such experimental efforts could be too complex to predict with simple combustion models.

Again, this work will investigate the accuracy of simplistic combustion models used in generating the LTC index data set. Because of this, if the spray formation process is too complex and significantly influences ignition processes, a simplistic physical model to predict spray combustion behavior will be inaccurate. To investigate spray-mixing processes and the possibility of using simplified models to represent the mixing physics, the author develops a novel optical diagnostic to quantitatively measure fuel concentration.

This chapter presents a manuscript that introduces and validates a novel line-of-sight optical diagnostic towards quantifying air/fuel mixtures of a fuel spray in high temperature, high pressure environments. Information presented hereafter is a building block towards the overall scope for this body of work, but includes all pertinent information regarding the diagnostic. The following sections outlining the diagnostic are adapted from: "Visualizing fuel mixture fraction via high-speed extinction imaging of C70 Fullerene doped diesel sprays", published in the Western States Section of the Combustion Institute.

Visualizing fuel mixture fraction via high-speed extinction imaging of C70 Fullerene doped diesel sprays

Shane Daly, Christopher Hagen, Julien Manin, Emre Cenker, Lyle Pickett, Scott Skeen

5.1   Introduction

Direct-injection internal combustion and emissions performance is well Known to be affected by the mixture preparation between fuel and oxidizer. Until recently, the high-pressure and high-temperature conditions present within spray combustion applications posed unresolved challenges for optical diagnostics to quantitatively image air/fuel mixing physics. In this work we measure fuel-spray spatiotemporal concentrations with high-speed extinction imaging, made possible by dissolving optically-absorbent nanoparticles into the fuel. Manin et al. [107] provides a relevant history of efforts on quantifying air/fuel mixing physics, along with the strengths and weaknesses of the various experimental techniques used. Most reported attempts in the literature are either limited in spatial resolution and quantitative certainty from beam-steering or noise inherent with the technique, or the techniques lack sufficient time resolution due to hardware constraints. Westlye et al. [108] describes a diffuse back-illumination extinction imaging (DBIEI) setup for quantitative, high-temporal resolution line-of-sight extinction imaging in high-pressure and high-temperature environments. The use of a specifically designed diffuse illumination source abates line-of-sight errors caused by steep refractive index gradients, which alter perceived attenuation (i.e., beam steering). This application has been successfully applied to diesel spray soot quantification [108], and has many economical and performance benefits over those outlined in Manin et al. [107]. In this work, we extend the diagnostic towards spatiotemporal fuel-to-oxidizer mixture quantification. Hydrocarbons are optically transparent within the visible and into the ultraviolet (UV) frequencies, and the DBIEI technique is currently constrained to this range. As a result, fuel vapor imaged with DBIEI appears transparent. In this work, we dissolve nanoparticles of fullerene-C70 into the fuel, being optically absorbent in the visible-UV and soluble in many hydrocarbons. We present a work-in-progress, omitting rectification of accurate optical absorption and scattering (extinction) properties—further discussed in the Results and Discussion section. As such, derived fuel concentration maps qualitative in their current state are compared to predictions from a 1-D spray model [109] to assess diagnostic performance. We also investigate alleged extinction coefficients required to quantitatively match the 1-D spray model results. This work demonstrates that the diagnostic technique shows promise towards quantitative measurements of spatiotemporal fuel mixture fraction, with a nearly constant factor increase required with fullerene-C70 extinction characteristics for model and experimental

results to match.

5.2 Methodology / Experimental Setup

5.2.1 Vessel and injection system

Sprays of fuel doped with C70-fullerene were injected into an optically accessible constant-volume combustion vessel. C70-fullerene is soluble in many hydrocarbons, with highest solubility in aromatic compounds such as toluene [110, 111]. For this effort we used toluene as the fuel/solvent, in anticipation that we may require more fullerene than the solubility limits of diesel or n-dodecane. The vessel creates a high-pressure and high-temperatures environment with a combustible gas mixture tailored to provide the desired oxygen concentration after ignition. Heat transfer at the vessel walls cools the gas mixture over time, and we injected fuel at a predetermined time based on the vessel temperature/pressure history. In this case, an oxygen concentration of zero percent, a temperature of 900 K, and a pressure of 60 bar (22.8 kg/m^3). A detailed description of the facility is available in Ref. [112]. We used a heavy-duty Bosch 3-22 injector with single-hole, axial orifice belonging to the ECN family of "Spray D" injectors. The Spray D injector has a nominal orifice diameter of 191 μm and a k-factor of 1.5. The injector was mounted in the fuel-tube "down" position and a common rail was not used in our work. Omitting a common rail significantly reduces the amount of fuel required to purge the system. A syringe pump supplied the fuels at 150 MPa prior to injection. We supplied a 450 ramp 1050 μs hold electronic command with a Genotek driver to achieve a 2.5 ms hydraulic injection duration.

5.2.2 C70-fullerene / toluene preparation and properties

We procured fullerene-C70 (115383-22-7) through Sigma Aldrich at 98 % purity in powder form. Implementing proper safety precautions should be taken with fullerene, being an unbounded nano-particle with unknown long-term health effects. Fullerene-C70 was transferred with a metal scoopula to toluene contained in a 100 ml glass beaker. Taring the toluene and beaker prior to the adding fullerene, and weighing the beaker and solution thereafter determine the mass of the fullerene. The sample was ultrasonicated for five minutes to break up fullerene clusters and help dissolving them in the fuel. For significant spray optical extinction at our vessel conditions, we found it was necessary to add fullerene-C70 to toluene's solubility limit of 1.406 g/L [110, 111], appearing as

violet and opaque. We separately confirm optical properties of C70-fullerene in toluene, specific to near-UV (406 nm, 17 nm FWHM) light emitting diode (LED) source (140 ns pulses) and the 400 nm (25 nm FWHM) bandpass filter at standard room conditions. In this manner, we determined the frequency-integrated absorption coefficient specific to our experimental arrangement. Future efforts will aim at quantifying UV-visible optical properties of fullerene-C70 at elevated temperatures and pressures, which at the time of writing are unavailable in the literature. Fullerene near-visible spectra were collected at a concentration of 32.3 μg/ml in a 1 cm pathlength cuvette with a fiber optic spectrometer (Thorlabs) at integration times of 140 ms. Fig. 5.1 shows the raw intensity profile of the LED-filter-toluene-filled cuvette combination and after when fullerene is introduced. The molar extinction coefficient (σ) spectrum integrated between 385 and 414 nm is 13834.7 L/mole cm. For these preliminary efforts, we rely on these room-condition spectra for the upcoming signal quantification.
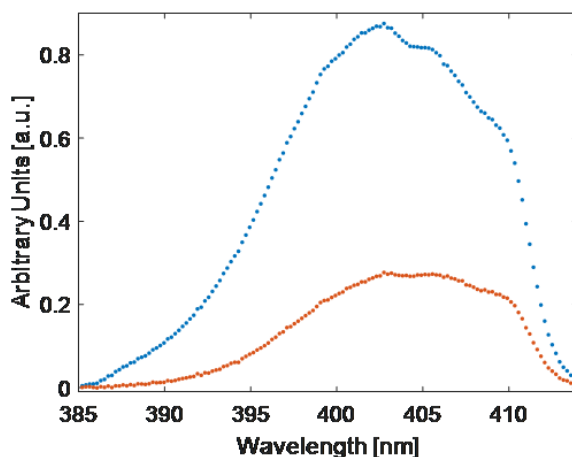
Figure 5.1: LED illumination distribution through a 1 cm quartz cuvette with toluene (blue), and with 32.3 μg/ml of fullerene added (red)

5.2.3 Diffuse Back-light Illumination Extinction Imaging (DBIEI)

The spatiotemporal spray-fullerene concentration is measured using a high-speed imaging extinction method. The main components of the high-speed extinction imaging setup shown in Fig. 5.2 consist of a high-output, ultra-fast LED (406 nm), a Fresnel lens, a large area (100 mm diameter) engineered diffuser, and a high-speed camera equipped with the appropriate lenses and optical filters. The illumination setup was designed to direct a bundle of diffused rays toward the object plane (central

spray axis) resulting in minimal perceived attenuation by density gradients (i.e., beam steering, schlieren effects). The engineered diffuser is 100 mm in diameter and converts collimated light into rays of constant intensity over a 15 degree solid angle and was placed three millimeters from the outer surface of the vessel window (75 mm optically from the central spray axis). The 150 mm diameter, f/1.0 Fresnel lens was placed 100 mm from the engineered diffuser and is used to collect and partially collimate the LED light. By placing the LED 40 mm beyond the Fresnel lens focal length, the light entering the diffuser slightly converges resulting in an angular profile in the periphery of the image plane better suited to the cameraâĂŹs collection angle. The high-speed camera is operated at 40,000 frames per second and is equipped with a 50 mm f/1.2 Nikkor lens, a 500D close-up lens, a 400 nm (25 nm FWHM) bandpass filter, and an OD 1.5 neutral density filter.
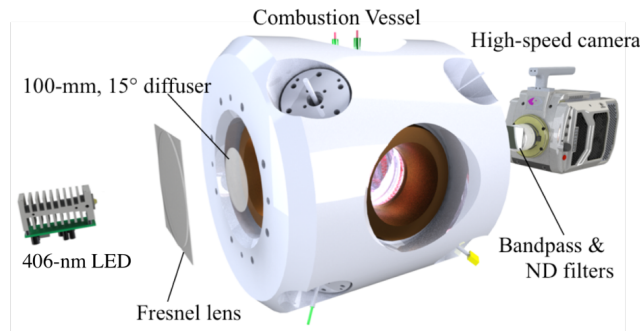
Figure 5.2: Schematic diagram of the combustion vessel and optical arrangement

The extinction images are converted into 2-D maps of optical thickness (KL) using the Beer-Lambert Law, $I/I_o = exp(KL)$, where I and I_o are the transmitted and incident illumination intensities, respectively, K is the dimensional extinction coefficient of fullerene, and L is the path length through the spray. KL images can be related to the volume fraction of fullerene in the chamber at each time step with knowledge of the dimensional extinction coefficient. Assuming an axisymmetric jet distribution, we used the Radon transform to convert the line-of-sight "KL" to a position-specific dimensional extinction coefficient, offering a three-dimensional perspective on mixing quantities. The molar extinction coefficient, σ, is used to solve (C=K/σ) for fullerene concentration, C. Molar extinction is a combination of molecular absorption, σ, and scattering, ϵ, components ($\sigma = \alpha + \epsilon$). The molar absorption is likely dependent on temperature and pressure, and scattering contributions dependent on fullerene clustering to larger particles (if present). For simplicity, we assume molar extinction is independent of the thermodynamic state with negligible

scattering, which is later discussed and accounted for in future efforts. We also assume the fullerene is distributed uniformly within the prepared fullerene/toluene solution such that we can calculate the toluene concentration based on the optically-derived concentration of fullerene-C70.

5.3   Results and Discussion

Fig. 5.3 shows select timings of false-color KL images, scaled between 0 to 2 absorbance (log base 10 of transmittance), showing ensemble averages of 5 sprays and the last image showing the time-average of the quasi steady period. The fullerene extinction map gives a clear representation of classic spray attributes, such as a distinct spreading angle and liquid length. When the toluene spray evaporates, the intermolecular forces binding the fullerene-C70 in solution vanish. Surrounded only by vapor-phase species, fullerene-fullerene collisions may be more likely leading to clustering. These clusters may remain as agglomerates or undergo aggregation. For example, Joutsensaari et al. [113] observed 40 to 150 nm fullerene particles in evaporating sprays having similar molarity and at lower ambient pressure conditions relative to the present work. In Ref. [113], in which fullerene-C60 was used, average particle sizes were smaller when the ambient temperature exceeded C60s sublimation temperature. Should clustering occur in the present work, these larger particles would remain as solid nanoparticles within the jet given that fullerene-C70 has a vapor pressure on the order of tenths of a Torr [114] at 900 K. Further discussion regarding the implications of fullerene-C70 clustering on the diagnostic technique under development here will be provided later.

Fig. 5.4 shows quasi-steady radial concentrations of toluene sprays at select axial positions, determined through tomographic reconstruction. The results are compared to a 1-D control-volume jet model, extended to 2-D by assuming the radial distribution follows the profile proposed by Abramovich, as discussed in Musculus et al. [109]. The experimental results (dashed lines) are individually scaled for a best fit with the modeled results (solid lines). This is done by increasing the extinction coefficient used in the high-pressure spray by a factor of 2.0 relative to the coefficient previously determined at standard conditions. After scaling, some deviation between the experimental and modeled radial profiles remains—with the largest difference observed at the farthest location from the injector outlet (6 cm). Nevertheless, assuming the physical source of the required scaling factor and the deviation in the radial profiles can be resolved, our methodology demonstrates promise as a quantitative diagnostic. The source of the required scaling factor and the deviation
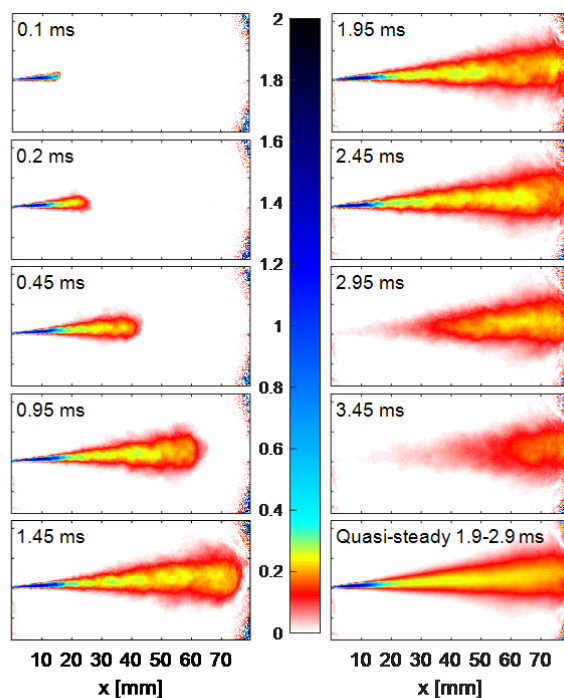
Figure 5.3: Select timings of false color scale, ensemble average of 5 spray recordings of C70-fullerene absorbance, "A", in a toluene/C70 spray at 900 K, 60 bar, 0 % oxygen ambient. Images scaled between 0 and 2 absorbance. Final image in sequence is a time-averaged image from 1.9 to 2.9 ms ASOI.
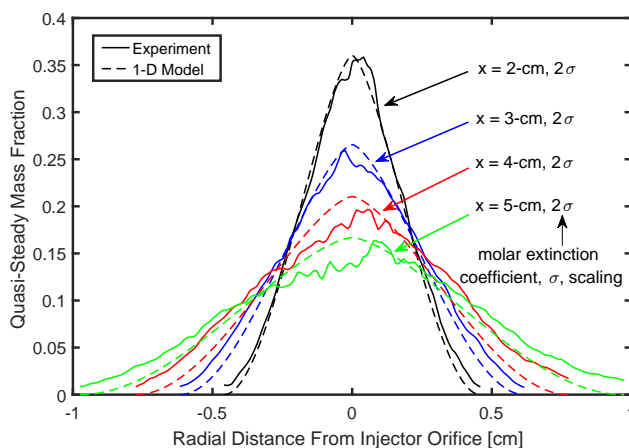
Figure 5.4: Model and experimental quasi-steady radial concentrations at various axial positions. Experimental profiles derived from fullerene molar absorption coefficient at standard room conditions, and experimental profiles derived from fullerene molar absorption coefficient at 2.0 times greater than the value at standard room conditions.

in the radial profile may be related to differences in the extinction characteristics of fullerene in a gaseous environment compared to that in solution, changes in α with temperature and pressure (spectral broadening), and/or C70 clusters resulting in larger and potentially spatially non-uniform particles influencing ϵ. Other sources of error in the radial profiles include insufficient averaging of turbulent structures with only five repeated sprays, the spray emanating at a slight angle from the injector causing asymmetric features, uncertainties with the one-dimensional Radon transform, or imperfect boundary condition inputs to the jet model, as discussed by Pickett et al. [115].

While a handful of studies report UV-visible spectra of C70 in various solvents or in the vapor phase at sub atmospheric and atmospheric pressure Refs [116–121], fullerene-C70 optical data in the visible spectrum at our high-pressure, high-temperature conditions is unavailable. Coheur et al. [121] investigated the effect of temperature on the gas-phase absorption spectra under high vacuum (10–6 Torr) and found that as temperature increases the fullerene-C70 absorption increases. At these conditions, the vapor fullerene-C70 absorption spectrum is double in magnitude and shifted to shorter wavelengths in comparison to fullerene/n-hexane solution at room conditions. In the present work, the influence of temperature may potentially be insignificant, illustrated by considering the change in the required σ scaling along the spray centerline. Modeling results indicate the spray centerline temperature varies from 625 K at 25 cm from the injector, to 750 K at 45 cm, yet the required σ does not reflect any correlation.

Under the conditions of the present work, clusters of fullerene-C70 are expected to form after toluene vaporization based on the results of Joutsensaari et al. [113]. As these clusters become larger, the contribution of scattering to the observed extinction would increase. In their spray-drying study, Joutsensaari et al. [113] found roughly spherical particles, averaging 100 nm in size at temperatures below 600 K, and averaging 40 nm above 600 K. Albeit, they used a fullerene mixture comprised of 15 % C70 and 85 % C60, where C60 is more volatile than C70. At temperatures above 600 K, C60 sublimes and, when dried, condenses to form the ultra-fine 40 nm particles [113]. Particles for pure C70 are likely normally distributed around 100 nm or larger, since C70 will not sublimate at these spray conditions, which is required to form ultra-fine particles. Future efforts aim to resolve fullerene clustering details specific to pure C70 at our thermodynamic conditions. To quantify the potential scattering contribution due to clustering as a source for the discrepancies found in extinction signal quantification, we performed Mie scattering calculations for spherical fullerene clusters of different

sizes. Scattering, absorption, and extinction cross-sections for fullerene C-70 particles ranging from 10 to 500 nm in diameter were computed, and the results are reported in Fig 5.5. The complex refractive index used for these calculations is: n = 2.1 + i0.7 [120].
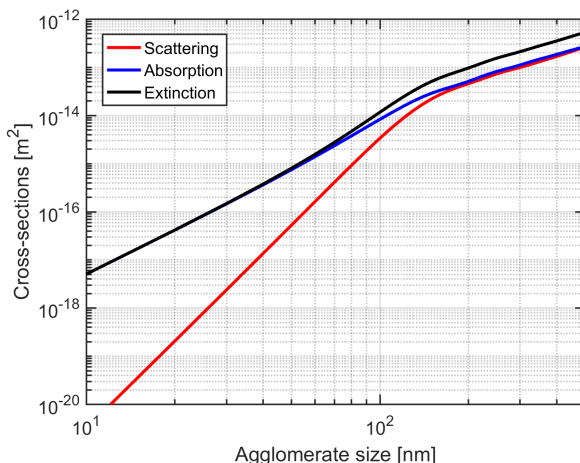
Figure 5.5: Scattering, absorption, and extinction cross-sections for fullerene C-70 as function of particle size

The cross-sections in Fig. 5.5 show, as expected, that absorption dominates extinction for small particles up to 80 nm. For larger particles on the other hand, scattering contributes to extinction, up to being of the same magnitude as absorption for above 150 nm in diameter. This means that if fullerene clusters when in the jet, while it does not in solution, then the extinction cross-section may increase by up to a factor two, over the simulated size range. It must be noted that these results are informative only, as fullerene is unlikely to exclusively cluster into sphere-like particles, which is one parameter of the Mie scattering calculation results presented in Fig. 5.5. Future work will consider more appropriate optical models to simulate the impact of scattering on measured extinction under agglomeration. In addition to the effect of scattering on extinction, the absorption coefficient may be different under the operating conditions: 900 K, 60 atm. We plan to measure the extinction coefficient of fullerene C-70 under the thermodynamic conditions and potential scattering of our experiments. As this requires the design of a dedicated optically-accessible high-pressure and high-temperature chamber with metered fuel delivery, it is an endeavor which will be completed during the next phase of this project.

5.4 Conclusions

We doped toluene with fullerene-C70, a nanoparticle being highly absorbent in the UV-visible spectrum and readily soluble in many hydrocarbons. Diffuse back-illumination extinction imaging was applied to record the line-of-sight extinction of the nanoparticles with high spatiotemporal resolution at high pressure and temperature. Quasi-steady vaporized fuel concentrations, derived from the extinction diagnostic, qualitatively match numerical results from a simple jet model, but do not quantitatively agree. We attribute disagreement to unresolved molar absorption coefficient dependence to the thermodynamic state, currently not available in the literature, as well as to different scattering efficiencies due to fullerene clustering. We find that the extinction coefficient required to quantitatively match the experimental results at various axial positions is 2 times greater than the quantity at room conditions. Future efforts will focus on characterizing the photo-physics of fullerene-C70 at engine relevant conditions to prove quantitative capability. If later proved quantitative, with the application of simultaneous camera views the diagnostic can resolve the entire spatiotemporal fuel spray distribution, which would be crucial in validating high-fidelity computational fluid dynamic data. Pending success, we aim to also investigate any influence on ignition characteristics the nanoparticles may have; in this manner, the diagnostic may be utilized directly with combusting sprays.

Chapter 6: Quantifying Spray-Ignition Toward Chemical Mechanism Development

The LTC-index predictive model is built upon a data-set informed by computational modeling. The utility of the predictive model therefore relies heavily on the accuracy of the HCCI (LTC index) simulations. A 0-D control volume has been shown to adequately represents the HCCI engine environment physics due to the reactive air/fuel charge being homegenous in reality; Niemeyer et al. provides a summary of literature on this subject [94]. With that said, 0-D modeling efforts are by no means a perfect representation of the complexities within an ICE, so errors are expected to be introduced, e.g., ignoring spatial thermal stratification that alters heat release rates [122]. Albeit, errors from the HCCI simulation are expected to be most influenced by the accuracy of the chemical mechanisms and surrogate fuels used, due to the established high sensitivity of LTC index to fuel composition.

This chapter outlines a novel experimental procedure to evaluate chemical mechanism accuracy and surrogate fuel performance. The works aims to encourage the many facilities around the world that have combustion vessels, traditionally developed to inform heavy-duty diesel applications, to participate in fundamental, ongoing data generation efforts. Namely, these data will serve to supplement ignition delay datasets by which modern combustion models are founded on, while simultaneously visualizing the spray formation process and its impact on the combustion behavior; the latter having practical implications for engines employing direct injection strategies. Success of this work will provide a methodology that could markedly expedite the study for many combustion technologies. The findings of the study will tie into this body of work by informing the accuracy of the chemical mechanism used in previous simulation efforts, performed to create the LTC index data set. If the methodology reveals promising results, the data could later be used to improve the reaction kinetics. With reaction kinetics more representative of reality, LTC index values could then be re-simulated and produce higher accuracy trends.

Using the diagnostic developed in Chapter 5, Appendix D outlines a brief quantitative spray

mixing study to investigate the applicability of using simpler zero- and one-dimensional modeling efforts to represent actual spray mixing. These simplified models assume homogenous distributions to some extent and ignore turbulence-chemistry interactions. The author hypothesized that a reduced injection duration would reduce fuel concentration and temperature gradients in the radial direction of the spray, serving to minimize complex turbulence-chemistry interactions, and potentially leading to homogeneous air/fuel mixture conditions prior to first stage ignition. When using ultra-short injections, featuring minimal spray penetration and prolonged mixing prior to ignition, concentration profiles in the radial direction are found to be fairly uniform at extended residence times (>1 ms after start of injection) while large gradients persist in the axial. Short-injections are expected to react uniformly in the radial, with significant stratification in the axial. Therefore, using 0-D modeling to predict and compare to experimentally derived ignition behavior would likely yield significant discrepancies, since spatiotemporal mixing is unaccounted for. The one-dimensional spray model of Knox et al [123] was found to accurately model the experimental fuel/air mixture distributions. A simple 1-D model can be efficiently paired with a detailed chemical mechanism. With trust in the spray-mixing model, the chemical mechanism accuracy can be benchmarked from reacting spray simulation—the topic of this chapter.

The author performs short-injection spray-ignition studies to resolve low- and high-temperature ignition phenomena. The experimental ignition results are compared to 1-D spray modeling efforts. In comparing these results it is possible to ascertain surrogate fuel and/or chemical mechanism performance. The study concludes that the chemical mechanism, the same mechanism used in LTC index simulations, may be a contributing factor to the observed spray-ignition simulation errors. Further spray-ignition studies with higher fidelity models should be conducted to ensure errors found in this effort are not from the simplified fluid mechanics of the 1-D spray model.

The following sections represent a manuscript covering the spray-ignition study, currently under Sandia National Laboratory internal review.

On the Low and high-temperature ignition delays for mixtures of n-heptane, iso-octane, toluene, and ethanol in an optically-accessible, direct injection constant volume combustion bomb

Shane Daly, Christopher Hagen, Emre Cenker, Noud Maes, Lyle Pickett, Scott Skeen

6.1   Introduction

Combustion strategies and fuel compositions are simultaneously evolving to meet high efficiency, low emission government mandates [124]. Researchers expedite these parallel efforts with computational modeling in the development of next-generation combustion systems. Models isolate key physical and chemical attributes of combustion systems. The physical portion includes the defining thermal-fluid-heat transfer physics intrinsic to the system—be it for traditional spark or compression ignition engines, low temperature combustion strategies such as HCCI engines, gas turbines, etc.— and the chemical portion describes fuel decomposition, energy release, and by-product formation. The chemical portion is fuel-specific, and the information contained in a "chemical mechanism". Computationally modeling refinery grade fuels, such as gasoline, is challenging since it contains hundreds of various hydrocarbon species [70]. Instead of trying to resolve the reaction kinetics of a mixture containing hundreds of various hydrocarbons, researchers typically characterize pure hydrocarbons. These well-characterized hydrocarbons are used individually or in combined mixtures to represent real fuels (like refinery-grade gasolines) by emulating their thermophysical and chemical kinetics properties into simpler fuels called surrogates. To summarize, real fuels are simplified to surrogates with reaction chemistry embedded in chemical mechanisms, and combined with a tailored physical model to permit timely simulations of combustion technology.

As we will show, chemical mechanisms and surrogate fuels require significant experimental and modeling efforts in their development. This work introduces an experimental methodology that can be used to characterize ignition behavior for a wide range of fuels used in conventional diesel-type compression ignition engines as well as gasoline compression-ignition operation. We then correlate and compare experimental results with a model that uses simplified fluid mechanics and mixing but full complex reaction chemistry. First, a brief introduction highlights challenges and reviews traditional and emerging approaches pertaining to fuel surrogate and combustion model development. Following, we extend on these efforts and explain potential benefits.

Accurate kinetic models are first founded for individual hydrocarbon components at application-relevant thermodynamic conditions. Multiple component kinetic models for surrogates are then founded as combinations of the single-component models, including any effect on kinetics as relative proportions of these hydrocarbons shift. Metrics such as ignition delay must be characterized

over a wide range of temperatures, pressures, hydrocarbon/oxidizer and hydrocarbon/hydrocarbon mixtures. Indeed, for this size of parametric study immense experimental efforts are required to obtain the necessary data to support chemical mechanism development. Separately, multi-component surrogates are computationally generated or leverage simplified computational models to some capacity in their design [71–73, 78]. Similar experimental efforts are used with fuel surrogates to ensure they represent the key ignition attributes of the actual fuel. As such, rapidly generated ignition quality of fuels and their surrogates along with modeling validation will expedite surrogate fuel design and their supporting chemical mechanisms. Historically, the combustion community has largely relied on fundamental homogeneous gas-phase ignition delay data from shock tubes, rapid compression machines, and jet stirred reactors for model assessment. Ultimately, these data are compared to simplified computational models that capture the key thermal-fluid-heat transfer physics at play, while using comprehensive, detailed chemical mechanisms. Holding the parameters of the physical model constant, the detailed reaction kinetics can be quantitatively tuned to match the experimentally obtained ignition characteristics, or vice-versa. In the same way, fuel surrogates are tested to validate its representation of the actual fuel, both experimentally and computationally.

Obtaining a single value of ignition delay with many shock-tube and RCMs require substantial time. Sequential tests can be cumbersome, and thus difficult to acquire statistically significant data sets. Results are further complicated from experimental uncertainties inherent in the methodology. For example, the work of Sarathy et al. [73] reported estimated uncertainties in their shock tube ignition delay measurements at 20% and rapid compression machine uncertainties at 10%; although, lower uncertainties have been achieved [125]. Newer methods that reduce experimental effort and time, while outperforming reported uncertainties will benefit the community. We first outline a few fundamental investigations proposing alternative methodologies that aim to address these issues.

To extend on traditional efforts, Fischer et al. [126] proposed using ignition data derived from a commercially available direct-injection constant-volume combustion chamber, similar to that of an ignition quality tester (IQT). This approach is different from traditional methods in that fuel is directly injected into an elevated temperature and pressure ambient. In this manner, the ignition quality of fuels can be rapidly tested with minimal amounts. They considered conditions around 660–770 K, 1–10 atm, and a global equivalence ratio of 0.63 for n-heptane. Here, the ignition delays were thought to be long relative to the spray fluid breakup and vaporization. They hypothesized that

the fuel/air mixture distribution reached homogenous conditions for most of the residence time prior to ignition. As such, the data were compared to modeled ignition delays from a constant-volume, adiabatic, perfectly stirred reactor. Unfortunately, in most cases the predicted ignition delay errors were unacceptable both quantitatively and qualitatively. They thought this to be from significant spray impingement on the vessel wall introducing physical complexities not represented in the simple 0-D modeling approach. The combustion model predictions and experimental data significantly mismatched, even when leveraging validated n-heptane kinetics, hindering the application as a chemical kinetic design tool. As a surrogate fuel validation tool, it is possible to compare ignition quality of the surrogate to actual fuel, but the fuel surrogates' representative chemical mechanism cannot be validated with the outlined modeling approach.

Alfazazi et al. proposed leveraging fuel spray ignition data from IQTs and constant volume combustion chambers (CVCC) of pre-burn type [127]. Unlike the approach of Fischer et al., the spray formation processes are highly complex for the CVCC conditions, where ignition delays occur during fuel injection. Despite the added physical complexity, Alfazazi et al. demonstrated that a 0-D, two-stage Lagrangian model can predict the CVCC ignition delays for n-dodecane and n-heptane across many conditions, highlighting that high-fidelity CFD simulations may not be required. However, their modeling approach yielded high errors for the IQT data in similar fashion to Fischer et al., though not as significant in magnitude. The long residence times within the IQT likely resulted in spray-wall interactions, and may again be the culprit for the challenges associated with predicting IQT data with simplified physical models. Their work demonstrated the feasibility of using pre-burn CVCC data for neat hydrocarbon or surrogate fuel chemical mechanism design, or in surrogate fuel validation.

Similarities between the study here and the previous work are investigating spray ignition behavior and assessing the feasibility of predicting it with a simplified model leveraging detailed reaction kinetics. We experimentally obtain first- and second-stage ignition delay timings with an optically accessible direct-injection CVCC of pre-burn type. We study ten fuels comprising neat n-heptane, and binary mixtures of n-heptane with isooctane, toluene, and ethanol. To the authors knowledge this is the first-time these lower-reactivity fuels have been investigated in a pre-burn CVCC. We subject the fuels to temperatures of 850 to 1300 K and a pressure of 40 atm, indicative of conditions in next-generation engines such as those employing LTC strategies.

Conventional direct fuel injections into the CVCC is high in fluid-thermal complexity as opposed to a pre-mixed experiment. Fuel is subject to mass and momentum exchange with the environment, potentially followed by low-temperature heat release depending on the fuel, and subsequent ignition. That is, non-uniform fuel/air mixture fractions and temperature distributions as the spray mixes and at timings relevant to ignition. Additionally, low-reactivity fuels will certainly impinge on the vessel walls prior to ignition, suffering from the issues present in an IQT. To further increase complexity, typical sprays are turbulent in nature, presenting steep species and temperature gradients which accelerate spray-ignition processes. According to R.N. Dahms et al. [128], these "turbulence-chemistry" interactions transport higher-temperature reactive species from the outer-edge of the spray—a result of low temperature reactions—radially inward to unreactive, high fuel concentration zones. The phenomenon dubbed the "cool-flame wave", stimulates low-temperature reactions in the core of the spray, serving to advance second-stage ignition. As a result, spray combustion simulations not incorporating turbulence-chemistry reactions, if present, may hugely overestimate ignition delays. The subsequent discussion offers a partial solution to this issue, and highlights practical limitations of our proposed approach.

We attempt to reduce the complexity associated with the spray formation process by favorably tailoring it to be simpler in nature. Ultra-short injections (200–250 μs) are employed, featuring minimal spray penetration and prolonged mixing after the end of injection and prior to ignition. We believe this reduces fuel concentration and temperature gradients within the radial direction of the spray, serving to minimize complex turbulence-chemistry interactions. Simpler zero- and one-dimensional modeling efforts—which assume homogenous distributions to some extent—should also be more representative of the actual conditions. Minimal spray penetration contains the fuel distribution within our optical diagnostics field of view for long residence times, key to study low-reactivity fuels with long ignition delays. The sprays also avoid wall impingement within the vessel, reducing unnecessary physical complexity. Furthermore, the ultra-short injections aim to minimize the physical ignition delay—the time required after the start of injection for the spray to sufficiently mix and reach elevated temperatures—to be small relative to the chemical ignition delay. Physical ignition delay timescales are expected to briefly outlast the length of the injection duration, leading to residence times of at least 250 μs prior to the spray reaching elevated temperatures, depending on mixing rates. Lastly, short injections minimize the fuel sample required for each experimental

run; 150-ml of fuel is sufficient to purge our fuel system and perform hundreds of injections.

A straightforward comparison to existing homogeneous ignition studies is unresolved. Spray physical ignition delay precedes chemical ignition delay and potentially in significant proportion, in contradistinction to homogenous studies which preclude physical ignition delays. As a result, measured ignition delays in this work are expected to be a combination of physical and chemical; even though our short injections aim to minimize physical ignition delay, chemical time scales for ignition can still be small relative to the physical. Subjecting fuels to high pressures and temperatures to force kinetic rates to be sufficiently high relative to physical mixing processes could resolve the physical ignition delay. Additionally, homogenous studies are at constant fuel/air mixture concentration, where sprays vary spatiotemporally, introducing more complexity. Analogous comparison of spray to homogenous ignition delays are left for future efforts. We direct our attention to comparing spray experimental to modeled results.

For modeling, we investigate the 1-D reactive spray model of Knox et al. [123], which allows the use of large, comprehensive chemical mechanisms. The reactive spray model proved to adequately replicate key combustion parameters for the Engine Combustion Network spray-H experimental data [123]. Predictions of vapor penetration, axial mixture fraction distribution, ignition delay, axial location of cool-flame reaction, and end-of-injection combustion recession agree reasonably well with experimental measurements. Knox et al. found the best agreement between experimental and modeled second-stage ignition delay oxygen concentrations of 15% and below, reasoned to be related to more-uniform mixture fraction distributions from prolonged mixing. Based on this, experiments at 15% oxygen concentration were performed, in conjunction with our ultra-short injections to further increase mixing times prior to ignition.

We aim to encourage the many facilities around the world that have combustion vessels, traditionally developed to inform heavy-duty diesel applications, to participate in fundamental, ongoing data generation efforts. Namely, these data will serve to supplement ignition delay datasets by which modern combustion models are founded on, while simultaneously visualizing the spray formation process and its impact on the combustion behavior; the latter having practical implications for engines employing direct injection strategies. Also, fuels and corresponding surrogates for computational modeling may be rapidly tested in a CVCC for surrogate fuel validation purposes. Similarly, as the combustion community begins to target novel alternative fuels and subject them to more

extreme operating conditions, CVCC can rapidly do so at potential ranges of 450 K to 1400 K, densities from 1 Kg/m^3 to 60 Kg/m^3, and pressures up to 350 atm—extending the limits of many homogenous facilities. Success of this work will provide a methodology that could markedly expedite the study for many combustion technologies.

Within the Methodology section we first present the fuels and select properties, the CVCC facility, and explain the optical diagnostics used to characterize the spray formation and ignition processes. We also provide example post-processed signals which define ignition behavior. After, the computational modeling strategy is further discussed; implementing proper boundary conditions are emphasized and a parametric study is outlined. Spray vapor penetration results are also presented here as they are used as boundary conditions for the modeling efforts. Next, the Results and Discussion section show time-sequenced images of spray formation and combustion for n-heptane at 900 K, 40 atm, and 15 % O2. Following, we present the optically derived first- (if any) and second-stage ignition delays for the ten fuel mixtures at temperatures ranging 850-1300 K at a constant pressure of 40 atm, 15 % O2. Lastly, the modeled ignition delay results are compared to the experimentally obtained values. Throughout the Result and Discussion section, we highlight the performance of our proposed methodology and compare to aforementioned works.

6.2   Methodology

6.2.1   Fuels

Fuels were selected to span a wide range of chemical attributes. These include pure n-heptane, and binary mixtures of n-heptane/isooctane (primary reference fuels, PRFs), n-heptane/toluene (HTs), and n-heptane/ethanol (HEs). Fuel composition and select chemical properties are presented in Table 6.1. The fuels considered here have various RON and stoichiometry, which will impact the residence time within the vessel prior to ignition. It is expected that high RON, low stoichiometric AFR fuels could over-mix and become too fuel-lean to ignite, even at 40 atm and the temperature conditions considered. As such, the selected fuels should benchmark methodology robustness at the desired ambient conditions as we move from reactive, fuel-rich mixtures to unreactive, fuel-lean mixtures.

ID	n-heptane (vol./mol. %)	isooctane (vol./mol. %)	toluene (vol./mol. %)	ethanol (vol./mol. %)	RON	Stoichiometric AFR (g/g)
H100	100/100				0.0	15.07
PRF20	80/81.88	20/18.12			20	15.06
PRF40	60/62.89	40/37.11			40	15.05
PRF70	30/32.63	70/67.37			70	15.04
H90T10	90/86.72		10/13.28		14.1	14.78
H80T20	80/74.37		20/25.63		27.7	14.51
H70T30	70/62.86		30/37.13		43.0*	14.27
H80E20	80/61.45			20/38.55	42.0*	12.71
H60E40	60/37.42			40/62.58	71.4	11.23
H40E60	40/20.99			60/79.01	94.4	10.23

Table 6.1: Fuels investigated in this effort: pure n-heptane, along with binary blends of n-heptane/ isooctane (PRFs), n-heptane/toluene (HTs), and n-heptane/ethanol (HEs). The "*" indicates RON values were estimated with the correlation of Daly et al. [80]

6.2.2 Facility

To supplement traditional approaches that study the impact of fuel chemistry on combustion performance, n-heptane, PRFs, HTs, and HEs were injected into a high-pressure and high-temperature environment within a constant-volume, pre-burn type combustion vessel. A combustible gas mixture tailored to provide the desired oxygen concentration after the pre-burn event, in this case fifteen percent, was ignited to generate 850—1300 K, 40 atm. Heat transfer at the vessel walls cools the gas mixture over time, and we injected fuel at a predetermined time based on the vessel temperature/pressure history. A detailed description of the facility is available in Siebers [129].

6.2.3 Injection Characteristics

We used a heavy-duty Bosch 3-22 injector with single-hole, axial orifice belonging to the ECN family of "Spray D" injectors. The Spray D injector has a nominal orifice diameter of 191-μm and a k-factor of 1.5. The injector was mounted in the fuel-tube "down" position and a common rail was not used in our work. The short injections employed are thought to not be influenced by pressure dynamics which a common rail dampens, and omitting it also significantly reduces the amount of fuel required to purge the system. A Teledyne 30D syringe pump supplied the fuels at 50 MPa prior to injection. We supplied an electronic command (ramp only) of 300±25 μs (11 to 21-A) to achieve the desired pilot-like injections of 250 μs. The electronic command had to be varied with differing fuels and

thermodynamic conditions. Although, this was probably due to random susceptibility of injector performance to the commanded ultra-short durations.

6.2.4 Optical Diagnostics

We used three high-speed cameras, simultaneously capturing Schlieren, natural luminosity, and OH* chemiluminescense. These diagnostics provide temporal- and spatially-resolved spray formation, along with first- and second-stage ignition processes, respectively. Formaldehyde planar laser induced fluorescence was originally utilized, but the measurement technique was not sensitive enough to resolve formaldehyde signal for the short injections in this work, and opted for natural luminosity measurements. The following sections outline diagnostic-specific details. Each section first provides relevant camera, lens, and filter specifications. Following, we explain the post-processing details for vapor penetration, first- and second-stage ignition—executed with MATLAB 2016b.

6.2.4.1 Schlieren

Transient spray penetration, low-temperature heat release (first-stage ignition) and second-stage ignition events for the entirety of the vessel field of view was provided by Z-type Schlieren imaging. A Phantom v2512 high-speed CMOS camera was used to capture the schlieren images (768 x 352 resolution, 80,000 fps, 1.2 μs exposure). The camera was outfitted with a 200 mm ($f/4$) Nikkor 219266 lens, with a 628 nm band pass (32 nm FWHM) and a neutral 0.1 OD filter, housed in a 52 mm Edmond optics 83340 filter holder. A custom 4-dye red (635 nm, 15 nm FWHM) LED operating at 11.5-V and 3-ns pulses, was synchronized with the high-speed camera to provide illumination for the schlieren setup. Using a short LED pulse further enhanced temporal resolution. A 50 mm condensing lens collected the LED emission and directed it through a 3 mm aperture prior to collimation by a 115 mm diameter, f/8 parabolic mirror. After passing through the combustion vessel, the collimated beam passed through a 70/30 beam splitter, and was then re-focused using a second parabolic mirror and a series of flat folding mirrors. The high-speed camera imaged the light source approximately 420 mm after the focal point, where a schlieren stop aperture of 12 mm diameter was placed to yield the desired contrast to density gradients. Similar to Pastor et al. [130], we sized aperture dimensions for best diagnostic performance. This reduces unwanted background schlieren caused by temperature gradients at the windows, and maximizes the contrast of softening

gradients during the low-temperature ignition event. Spray penetration is defined as the furthest downstream point of the spray head. We isolated the spray vapor signal by taking the standard deviation of three time-sequenced frames (i-1, i, i+1). The edge of the vapor as it propagates in the vessel provides a large standard deviation signal relative to the ambient and core of the spray. The MATLAB **bwmorph** function provides dilation and erosion filtering on this signal to provide a more-continuous spray border. Following, the filtered standard deviation signal is passed to the **bwboundaries** function, which finds a closed boundary of the spray border–the max position of this border is the penetration distance. Schlieren spray signal is dependent on the local refractive index, and mainly influenced by temperature and fuel particle size within the spray. Cool-flame activity, i.e., low temperature heat release (LTHR), causes the parent fuel to break down and slightly raises the local temperature. Picket et al. [131] demonstrated that cool-flame activity causes the refractive index to closely match the ambient, resulting in the spray schlieren signal to "vanish". As a result, the onset of LTHR can be visualized as the spray suddenly vanishing. LTHR we solely rely on natural luminosity measurements, discussed later.

6.2.4.2 OH* Chemiluminescence

OH* chemiluminescence can provide the onset and location of high-temperature reaction zones, i.e., second-stage ignition. We used a Photron SA-X2 camera, outfitted with a Lambert instrument HiCatt s20 lens-coupled intensifier (896 x 440 resolution, 20,000–60,000 fps, 8–43.5 μs exposure). Isolating the OH signal was achieved with a 312 nm band pass (16 nm FWHM, F16-213-UNB un-blocked filter). The intensifier was operated at a gain of 850V for the entirety of the parametric study; only the intensifier gate time was altered as needed to increase or decrease the OH* signal. We targeted the lowest shutter timing necessary to maximize the recording framerate. Framer-ates between 20,000 fps and 60,000 fps were achieved depending on the fuel reactivity and vessel conditions. We evaluated the image-integrated signal to produce a spray-integrated ignition delay. The integrated signal over time prior to any ignition event was processed to find the mean and standard deviation of the background noise. The time at which the OH* signal exceeded the mean plus ten times the standard deviation marked the onset of ignition, which is atypical of standard ECN procedure. Established routines focus to quantify axial-resolved ignition onsets from long fuel injections providing ample signal. In our work featuring ultra-short injections, the signal is low and

ignition is nearly homogenous. As such, we found our methodology better-characterized our ignition processes, and especially evident when compared to modeled results in comparison to traditional approaches. An example signal trace used to detect ignition can be found in Figure 6.1.

6.2.4.3   Natural Luminosity

Broadband luminosity images (hereafter referred to as natural luminosity) can visualize the onset and location of low temperature heat release (first-stage ignition). A Phantom v2512 high-speed CMOS camera captured the natural luminosity images (384 x 208 resolution, 20,000 fps, 43.5 μs exposure). We used a 50 mm ($f/12$) Nikkor 37540 with a 52 mm canon close-up 500-D lens. A 315–715 nm band pass (KG-3), 550 nm short pass (64664), and a 600 nm short pass 64665 filter were used to limit soot incandescence and schlieren light. We note the schlieren back-lighting is still present in the natural luminosity images, but is below the intensity originating from the low temperature heat release.

Limited by the optimum between camera framerate and exposure time, axially-resolving first-stage ignition was not feasible; as such, we provide spray-averaged first-stage ignition. With this experimental setup, the radiation caused by first-stage ignition was a mere 100 counts greater than the background noise, and in some cases a mere 10 counts higher than the Schlieren back-light penetrating the optical filters (dynamic range of camera is 3600 counts). Because of this, coupled with the background noise rising over time, the images were converted to binary based on an intensity threshold. We determined a threshold higher than the schlieren bleed-through and rising background, but less than the first-stage ignition signal. We finally arrive at a cropped-image signal of zeros (less than threshold) and ones (greater than threshold) integrated for each frame.

The onset of first-stage ignition is defined as the maximum peak ASOI and prior to saturated, second-stage ignition signal. The processed signal traces of OH* and luminosity from the images are presented in Figure 6.1 for a select run of n-heptane at 900 K, 40 atm, and 15 % O2. The natural luminosity imaging, for most of the ambient conditions studied, provides a clear signal of the first-stage ignition event. Based on our processing routine, the spray-averaged first-stage ignition is determined to be 0.71 ms. This is in accordance with the disappearance of the majority of schlieren spray signal at the core and head of the spray, and partial reasoning behind using the maximum of the luminosity signal as the onset of first-stage ignition. At higher temperatures or

reduced two-stage chemistry, the luminosity signal duration and magnitude decreases—the peak of the signal becomes the only distinguishing factor relative to the noise in these cases.
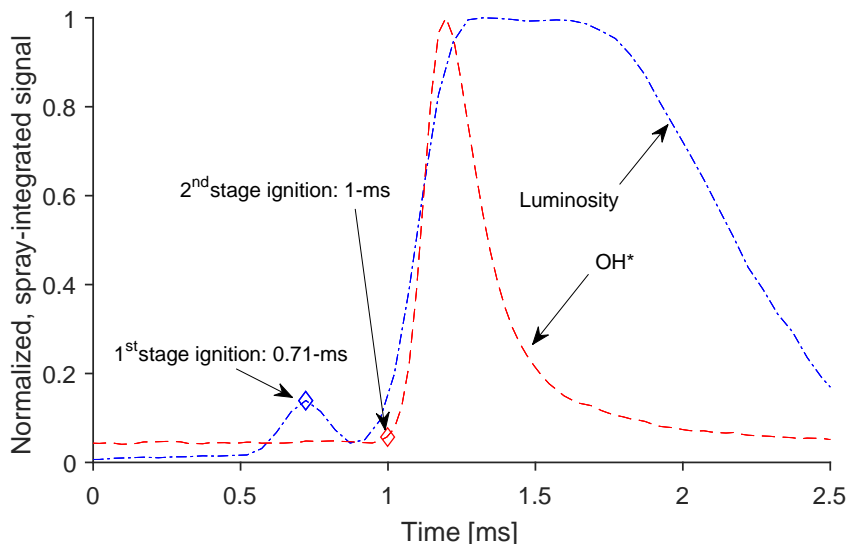
Figure 6.1: Processed signal traces of OH* and luminosity for a select run of n-heptane at 900 K, 40 atm, and 15 % O2

6.2.5   Modeling

We implement the 1-D reactive spray model of Knox et al.; details and equations governing the model are found in Ref. [123]. The proceeding discussion covers the importance of various model boundary conditions specific to our efforts. We focus attention to a few boundary conditions that influence spray formation—discharge coefficient, injection duration, and spreading angle. As outlined below, due to uncertainty in these values, we decide to perform a sensitivity study of modeled ignition delay to these boundary conditions. Following, we touch on chemical mechanism considerations.

Pickett and coworkers [115] demonstrated that when models capture experimental axial spray penetration, the mixture field was also well matched within the experimental uncertainty [115, 132, 133]. Because spray penetration is more easily quantified experimentally than fuel mixture fraction, it is convenient to rely entirely on penetration data to validate models. Prior to implementing reaction chemistry, we tuned/adjusted the model spreading angle to replicate the experimental vapor penetration. An iterative procedure was performed until we converge within two-standard

deviations of the mean.

The mean experimental penetration profiles for n-heptane are seen in Figure 6.2, with mean ignition delay onsets (squares) overlaid on respective profiles. The penetration rate during injection increases with ambient temperature, attributable to the reduction in ambient density to hold pressure constant. Penetration after 500 μs and prior to respective ignition events (square markers) do not follow this same trend. We attribute this to fluctuations in the hydraulic duration from shot-to-shot and between temperature cases upwards of 50 μs. Ignition seems to occur almost at the exact same penetration distance across the different temperatures. Sprays require time to adequately mix to ignitable conditions, hence a physical ignition delay, after which the chemical kinetics governs the total ignition delay. When the spray has reached roughly 4 cm, the mixing processes have completed their natural development and the spray is nearly stagnant, resulting in similar locational onsets regardless of the varying kinetic rates. The 1000 K case has a reduced penetration relative to the others at the time of ignition, a result of a shorter injection duration that randomly occurred during these runs.
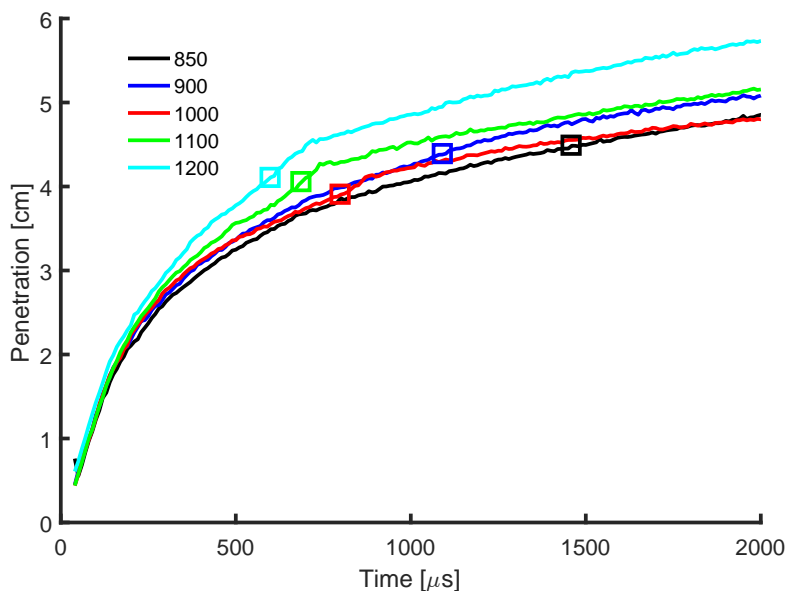
Figure 6.2: n-heptane experimental mean penetration trends at 850–1200 K, 40 atm, 15 % O2. Squares superimposed on the penetration curves indicate the mean, experimental ignition delay.

We found the task of matching the 1-D model to experimental penetration elusive for two reasons; the first reason is associated with our uncertainty in discharge coefficient. With our short injection durations, the injector may not be achieving steady-state flow performance, attributable to

transients required to fully-open (~100 μs) as well as close (~10 μs) as indicated by hydraulic force measurements [134]. This is a significant portion of the total injection duration (50 %), in addition to Spray D injectors requiring time (>250 μs) to reach steady-state performance [134, 135], attributable to the needle requiring time to fully open. As such, this casts doubt on using the reported value of 0.88, as it is derived from a long, quasi-steady injection relative opening and closing transients.

Figure 6.3 presents modeled penetration for n-heptane at 900 K and two discharge coefficients compared to the mean experimental penetration. We illustrate that when using the 0.88 value in literature the spreading angle must be 22-deg, which is greater than the actual spray (about 18-deg in this case). Musculus et al. claim that a reduced spreading angle, when compared to observed values, serves as a correction factor when assuming a constant velocity profile in modeling efforts [109]. The reduction in model spreading angle is typically around 0.66 of the experiential; e.g., knox et al. used a spreading angle of 15.5-deg to represent the experimental spreading angle of 23.0-deg [123]. In other words, when the experimental penetration is matched the model spreading angle should be smaller than reality—an experimental spreading angle of 18-deg informs the model spreading angle to be around 12.0-deg. In this work, using a discharge coefficient of 0.88 requires no correction factor to match penetration trends. Because of this and the latter reasoning, we decide to investigate significantly reduced discharge coefficients (C_d) of 0.66 and 0.5. For a C_d of 0.66, the model spreading angle is 15-deg to match penetration trends, which is only 0.83 of the experimental spreading angle, but a correction factor is still in place nonetheless. For a C_d of 0.5, the resulting spreading angle is 11-deg, which is 0.61 of the experimental spreading angle. Typical correction factors from literature, while a useful guideline, are also based on quasi-steady sprays. As such, there is no guarantee it is a physically reasonable value for the short injection sprays in this work. For now, we investigate the three mentioned discharge coefficients to quantify the impact on modeled ignition delay. We now continue to the next difficulty associated with matching experimental penetration.

In our short-duration sprays, penetration notably decelerates after the end of injection. Traditionally, forces acting on the spray head such as drag are small relative to the spray momentum during injection and are ignored in modeling efforts for typical sprays [123]. However, in our case of very short injections axial pressure gradients and shear stresses may be more significant and lead to this observed deceleration after the end of injection and prior to ignition. Guided by op-
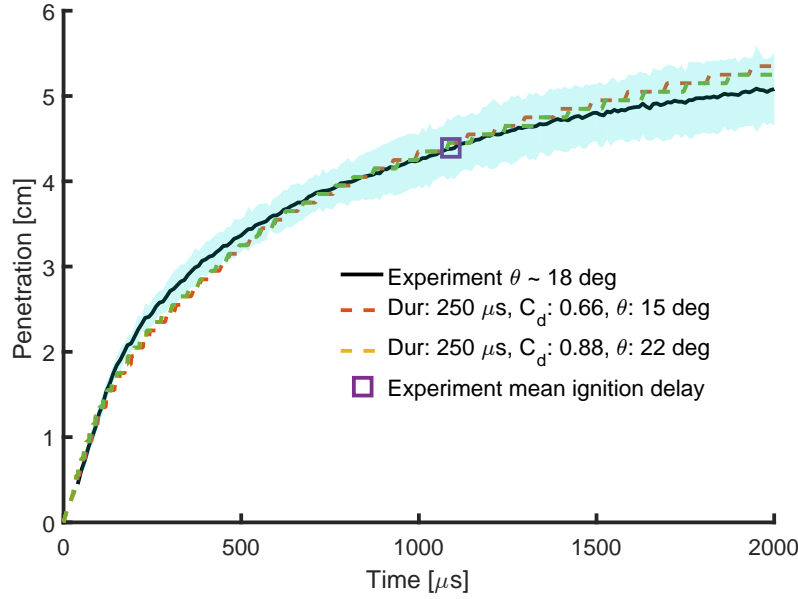
Figure 6.3: Simulated and experimental penetration for n-heptane, 900 K, 40 atm, 15 % O2. The transparent bands indicate two standard deviations about the mean for the 10 experimental repeat studies. The two discharge coefficients presented here illustrate the difference in spreading angle required to best-match experimental penetration. The discharge coefficient value of 0.5 is omitted here for brevity, but capable of having the same penetration trends with a reduced spreading angle.

tical observations of sprays expanding in a non-ideal fashion, published 1-D modeling efforts have implemented variable spray radial profiles which serve to accelerate or decelerate the spray as it progresses downstream [134]. In our case, this would give the desired result of achieving reduced downstream penetration velocities by enlarging downstream control volumes. In fact, at the head of the spray we do observe the spray width significantly enlarging after the end of injection. Executing this approach in the model may be a viable candidate to account for the spray head decelerating after the end of injection. The model of Knox et al. would need to be modified to incorporate this feature. For now, we model the spray with an ideal conical expansion, omit shear and axial pressure gradients, and best match experimental penetration with the current model. Like the previous discussion with uncertainties associated with discharge coefficient, we also have experimental uncertainty with injection duration of up to 50 μs between repeat studies. This significantly alters the total mass injected between injections, and evident in the differing penetration trends between repeat studies, visualized by the large uncertainty band in Figure 6.3. We choose to model two injection durations of 200 and 250 μs.

We settle on a parametric study of five cases between the three discharge coefficients and two

injection durations. This will bound the ignition delay sensitivity with our uncertainty in these two boundary conditions, and emphasize the attention to detail required when imposing boundary conditions. We constrain the five individual cases to have the same or as close as possible penetration curves. The values used in this study are found in Table 6.2.

Inj Dur (μs)	C_d (-)	850 (K)	900 (K)	1000 (K)	1100 (K)	1200 (K)
250	0.5	13	11	11	10	9
200	0.66	16	15	15	14	12
250	0.66	18	16	16	15	13
200	0.88	22	20	20	19	17
250	0.88	24	22	21	21	18

Table 6.2: Spreading angle (in degrees) required to match experimental penetration as a function of injection duration (Inj Dur) and discharge coefficient (C_d) for each vessel ambient temperature. We assigned priority to matching penetration around the time of experimentally-observed ignition

Knox et al. investigated two chemical mechanisms—one detailed and the other reduced—and found major discrepancy's in modeled ignition delays (at 15 % O2, spray-H conditions) of 10 and 100 percent error, respectively [123]. Utilizing a detailed chemical mechanism is evidently key. We limit the scope of our study to leveraging two detailed chemical mechanisms to evaluate the sensitivity on modeling results. The first being the comprehensive chemical mechanism of Princeton et al. [136–139], valid for n-heptane, iso-octane, toluene, and ethanol. The mechanism has been validated at various conditions which do depend on the relative proportions of species. For pure n-heptane, shock-tube experiments at temperatures between 750 to 1200 K and under 50 atm at stoichiometric equivalence ratios were validated [137], among other various validation techniques. We also use the detailed n-heptane mechanism (3.1) of Mehl et al. [140]. The mechanism of Mehl et al. has been extensively validated with shock tubes and rapid compression machines with conditions ranging from pressures of 3 to 50 atm, temperature from 650 to 1200 K, and equivalence ratios from 0.3 to 1.0 [140]. We define modeled ignition delays in this work by the temperature exceeding 400 K of the initial ambient temperature. Any portion of the spray exceeding this criterion marks the onset of second-stage ignition.

6.3   Results and discussion

Time-sequenced images for all diagnostics first illustrate n-heptane two-stage ignition, highlighting attributes of the short-injection spray events. After which, we summarize key findings regarding first-(if present) and second-stage ignition phenomenon. Lastly, we compare experimentally obtained second-stage ignition delays to our 1-D modeling efforts, and emphasize the success and limitations of our overall methodology toward chemical mechanism and surrogate fuel validation.

6.3.1   Reacting Sprays

As a representative example of the entire experimental set, schlieren, OH* chemiluminescence, and natural luminosity images are presented at select timings for n-heptane in a 900 K, 40 atm, 15 % O2 ambient in Figure 6.4. The first column is the schlieren imaging, the second natural luminosity, and third OH* chemiluminescence. The top left corner of each image shows the timings after start of injection, and the bottom right the image dynamic range.

As the fuel spray mixes with the ambient, the temperature of the mixture increases. By 0.49 ms, the schlieren reveals a softening of the spray, attributed to mixing with the ambient. However, by 0.69 ms, the spray rapidly begins to disappear—faster than that expected by mixing alone. Comparisons to non-reacting (0 % O2) sprays at this condition corroborate this. The natural luminosity indicates that there are low-temperature reactions taking place at this same time. By 0.89 ms, there is no longer any indication of LTHR with the natural luminosity; now, the spray is completely transparent in the schlieren. In support that the disappearance of luminosity and schlieren signals are evidence of LTHR, Curran et al. showed that first-stage ignition ends when increased temperatures shift the equilibrium of reactions until paths are shut-off [141]. At 1 ms the first evidence of second-stage ignition appears, as indicated by the faint darkening of the schlieren, and signal from OH* and natural luminosity. Significant heat release begins to take place immediately following this onset, as indicated by the rise in OH* signal. At these ambient conditions, all three diagnostics are synchronized for timings of first- and second-stage ignition events.

Indeed, we find that the schlieren signal for this n-heptane case provides spray penetration and, evidently, the onset of first- and second-stage ignition events. The schlieren reveals in high sensitivity that ignition occurs nearly everywhere in the spray radial at a given axial position.

This supports our hypothesis that the short injections enhance mixing to reduce concentration and temperature gradients in the radial—though gradients still exist in the axial direction, with evidence being ignition stratification occurring over a 300 μs period. Although, we find no significant ignition progression into the upstream portion, i.e., "tail", of the spray.

Combustion recession is not observed for the n-heptane case at 900 K, i.e., the spay tail does not ignite following the bulk of the spray. In typical long-injection sprays, ignition occurs downstream during fuel injection, manifesting to a quasi-steady flame lift-off position. After fuel injection, the spray tail section then mixes with the ambient and is engulfed by the pre-existing flame. In our short-injection sprays, the opportunity for ignition occurs after the end of injection. We believe the spray tail mixes rapidly relative to the downstream portion of the spray, which can cause unfavorable conditions for ignition depending on ambient conditions. Generally, as the fuel spray entrains hot ambient gases the mixture temperature favorably increases, and fuel concentration unfavorably decreases. During rapid mixing in the tail, the fuel has minimal residence time at favorable conditions that result in highest kinetic rates; instead, favorable conditions quickly transition to fuel-lean and near-ambient temperatures. Here, reaction rates are minimal, but heat is released nonetheless. Temperatures then typically rise from the minimal heat release, increase kinetic rates, in turn accelerating heat release. However, high inert ambient concentrations inhibit any sort of thermal runaway: where heat transfer losses and energy storage capacity of the inert ambient gasses combat the local heat release, serving to suppress temperature rises and therefore any chance for increasing reaction rates. As a result, over-mixed conditions can lead to undetectable ignition. We return to the ambient conditions and fuel combinations that lead to over-mixing in the bulk of the spray within the Ignition subsection.

(a) Schlieren   (b) Natural Luminosity   (c) OH*
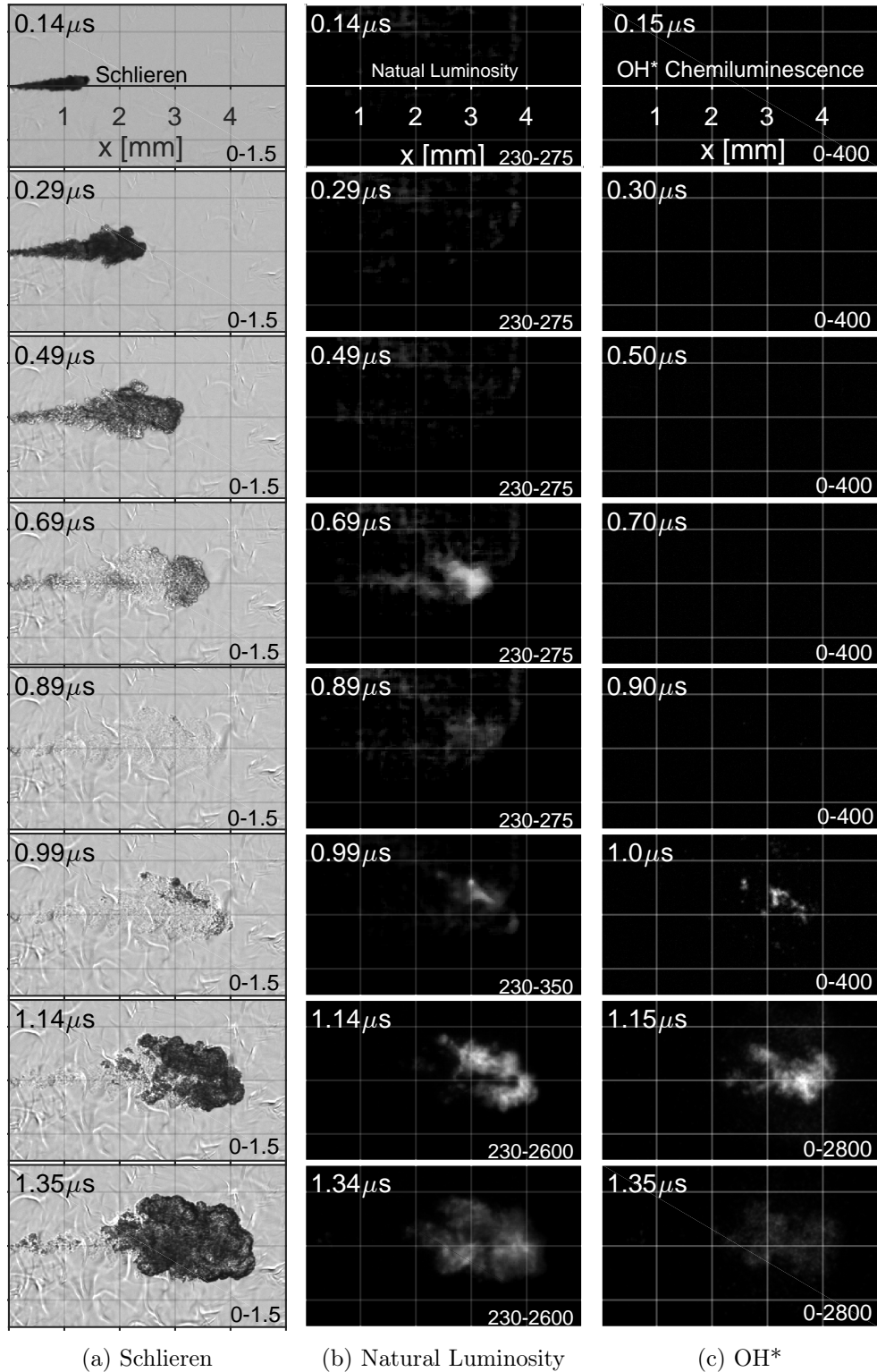
Figure 6.4: Select run of n-heptane at 900 K, 40 atm, 15% O2. Schlieren images are normalized by the first frame prior to the start of injection. OH* Chemiluminescence shown with dynamic range between 0 and 1000, with natural luminosity between 245 and 300. First-stage ignition initiates around 700 μs, with second-stage at 1000 μs.

6.3.2 Ignition Delay

6.3.2.1 n-heptane/isooctane fuels

(a) PRF first stage ignition

(b) PRF second stage ignition
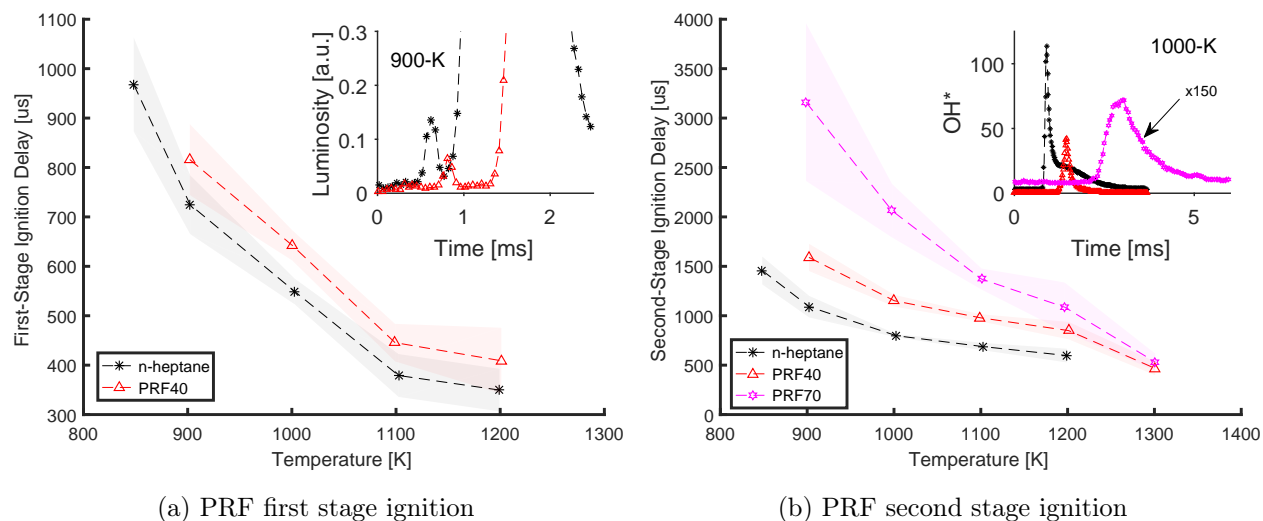
Figure 6.5: Ignition delays for first- and second-stage ignition for n-heptane and PRF fuels. First stage indicated by natural luminosity images, and second stage by OH* chemiluminescence.

Figure 6.5a portrays first-stage ignition delay for n-heptane and PRF40, with the inset axis being a single experimental run of luminosity signal at 900 K, also for n-heptane and PRF40. As can be seen, PRF40 first-stage ignition is delayed at 100 μs relative to n-heptane across all comparable temperatures. The luminosity signal decreases with increased iso-octane concentration, evidence of diminishing LTHR. PRF70 first-stage ignition is not detected due to limited diagnostic sensitivity to resolve the (expected) reduced LTHR, but likely present and with onset delayed relative to PRF40. Resolving first-stage ignition for PRF40 at 1300 K was also not possible due to insufficient camera framerate to distinguish first-stage from second-stage ignition.

Figure 6.5b shows second-stage ignition is delayed with increased isooctane concentration, in accordance to our first-stage ignition trends and to results derived from homogeneous gas-phase studies [79, 142]. The mean ignition delay of PRF70 disproportionately increases with octane rating at lower temperatures, e.g., 200 % longer ignition delays relative to PRF40 at 900 K, but only 30 % higher at 1200 K. Ignition delays are known to increase significantly at higher octane ratings at low-temperature ambient conditions [72], but may not exclusively explain trends. Increasing residence times with our sprays directly prolongs mixing, in turn reducing fuel concentrations. Reduced fuel

concentrations also increase chemical ignition delays [] or may inhibit ignition entirely if over-lean; we therefore expect further increases in ignition delays with lower reactivity fuels beyond that indicated by octane rating.

The inset axis of Fig. 6.5b shows select runs of OH* signal at 1000 K, corrected to account for differences in intensifier gate timings between fuel studies. To visualize the weak PRF70 signal we also scaled the values by 150. At this condition, peak OH* signal ranks in descending order with increasing fuel octane rating. Between these fuels, the fuel density and available energy contents are roughly equivalent, with penetration trends also nearly identical—combined, these indicate the total injected mass and therefore energy availability is similar and a non-contributing factor in decreasing OH* signal. Instead, decreasing OH* signal is attributable to combustion efficiency decreasing. As octane ratings increase, the residence time required within the vessel increases, and therefore prolonged mixing; again, this creates fuel-lean conditions that reduce kinetic rates and potentially inhibit thermal runaway if ambient dilution levels are high enough. Based on our observations with PRF70, residence times greater than 2 ms (prior to ignition) may be a practical limitation before over-mixing begins to occur; we return to more practical limitations later.

In addition to fuel-lean conditions from over-mixing, we also observe fuel-rich conditions at elevated temperatures. The inset axis reveals that n-heptane OH* signal lingers after the initial spike at 1000 K ambient. This is indicative of under-mixed conditions (fuel-rich) at the time of primary ignition, i.e., ambient entrainment for sufficient oxygen does not occur to completely burn the available fuel. Instead, additional mixing and entrainment of ambient oxygen after ignition is required to progress oxidation at these early ignition timings. We refer to this additional mixing time required as "burn-out"; to further illustrate the so-called "burn-out" period of OH*, n-heptane OH* traces for the temperatures tested are presented in Fig. 6.6a. As temperature increases, and residence times prior to ignition become less than 1 ms, OH* burn-out propensity and duration increases. Not visualized here, this also occurs for fuels of lower reactivity when the residence times are below 1 ms, such as PRF70 at 1300 K. Fig. 6.6b presents false-color images at select timings of n-heptane at 1200 K. Primary ignition is nearly homogenous throughout the spray periphery, stemmed from multiple ignition kernels. The OH* burn-out magnitude is near the local minimum at 1 ms, with minimal OH* signal in the spray tail and prolonged in the core and head of the spray. Around 1.3 and 1.5 ms as the spray minimally penetrates downstream, the head exhibits a recirculation

zone, induced from the primary ignition event. This recirculation zone of incomplete combustion products entrains the ambient, resulting in increased OH* signal until eventually quenched around 3 ms. Ignition delays prior to 1 ms occur in a fuel rich mixture; at around 1 ms ignition timings, ignition evidently occurs at more ideal compositions; ignition takes place in the fuel-lean at timings above 2 ms. Future efforts aim to resolve spatiotemporal fuel mixture fractions at these ignition timings to corroborate these hypotheses.

(a) n-heptane integrated OH* signal   (b) n-heptane OH* images

Figure 6.6: Ignition delays for first- and second-stage ignition for n-heptane and PRF fuels. First stage indicated by natural luminosity images, and second stage by OH* chemiluminescence.

For confounding reasons our experimental conditions made it difficult to quantitatively assess heat release propensity via pressure transducer measurements, be it during primary ignition or burn-out period. Primarily, the amount of injected mass is uncertain—required for quantitative assessment of combustion efficiency and for comparisons of heat release—due to uncharacterized injector performance at our short injections. Additionally, ignition occurring prior to 1 ms are violent, generating intense shock-waves registering as noise the same order of magnitude as perceived signals from heat release. With injected mass and combustion efficiency unknown, as well as large uncertainty in pressure transducer signals, only qualitative comparisons can be made. Although, we can analyze primary ignition versus burn-out heat release magnitudes for a specific case. Fig. 6.7 provides derived heat release profiles for the 1200 K n-heptane case, after applying extensive measures to filter noise. At this condition about 70 % of the heat is released from the primary ignition event, with remaining 30 % during the burn-out period. Extending this analysis to 1000 K, 80/20

Ignition_Figures/1200 K_nheptane_heatrelease.pdf

K$_n$*heptane$_h$eatrelease.pdf*

Figure 6.7: Heat release rates, derived from pressure transducer measurements, for the ten repeat studies of n-heptane at 1200 K, 40 atm. The rapid heat released from the primary ignition event is roughly 70 % of the total, with the slow-burning remainder from continued mixing (burn-out period)

% is split between primary and burn-out period, respectively, in similar trend to OH* findings. Continuing to 900 K, with residence times approaching 1 ms, the heat release nears 100 % from the primary ignition event, indicating well-mixed conditions. At residence times greater than 1 ms, combustion efficiency declines due to over-mixing, evidence from reduced OH* in Fig. 6.6a and derived heat release (not depicted).

6.3.2.2   n-heptane/toluene fuels

Within experimental repeatability, the onset of first-stage ignition is nearly the same as the concentration of toluene increases from 0 to 30 % by volume across all temperatures, as seen in Figure 6.8a. Toluene does not participate in first-stage chemistry, so as n-heptane proportions decrease we expect

(a) TRF first stage ignition

(b) TRF second stage ignition
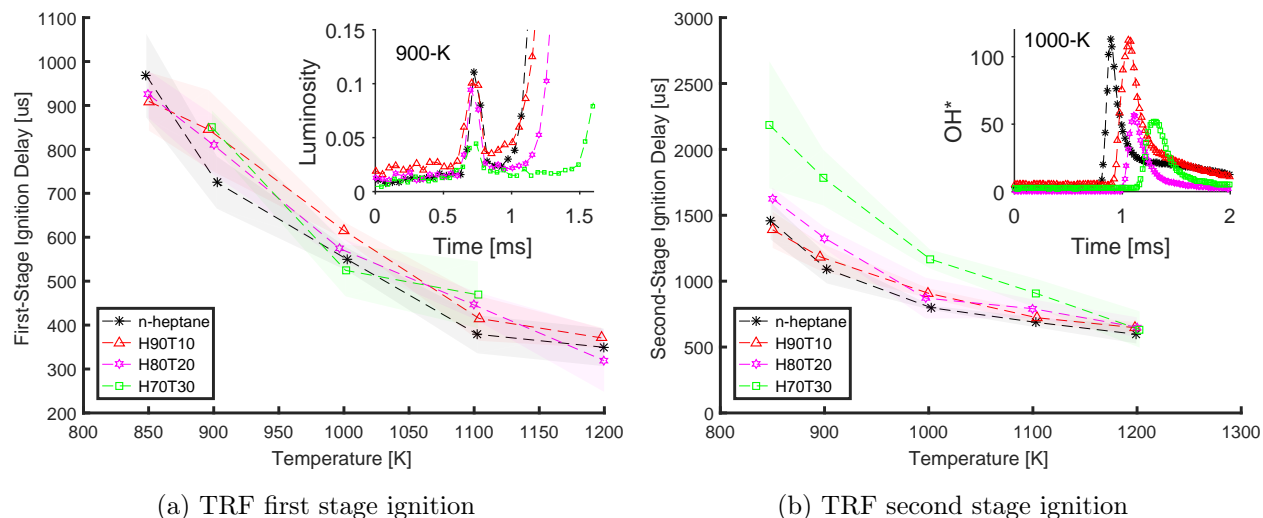
Figure 6.8: Ignition delays for first- and second-stage ignition for n-heptane and TRF fuels. First stage indicated by natural luminosity images, and second stage by OH* chemiluminescence.

the ignition delay to remain the same. Ignoring uncertainty bands, mean values provide unexpected trends. We believe the Ignition delay is very sensitive to mixing processes, varying shot-to-shot, potentially a dominate factor over the 10-30% additions of toluene. Separately, increasing toluene reduces the magnitude of heat release, as pointed out by the inset plot highlighting sequential decreases of luminosity signal. The duration of LTHR is also found to be constant across fuels.

Figure 6.8b shows second-stage ignition delay increases as toluene concentration increases, in agreement with increased octane ratings. Di Sante et al. also observed similar first- and second-stage behavior as toluene was added to n-heptane, in their RCM study at 10 atm, 710—780 K and [143]. They attribute this to the lack of two-stage chemistry for toluene, as to not alter the first-stage ignition delay, but being less reactive in nature caused the second-stage ignition to increase. In our case, the H70T30 second-stage ignition delay is disproportionately longer than the other n-heptane/toluene mixtures. As mentioned with PRF70, the disproportionate ignition delay increase is from prolonged mixing. H70T30 ignition delays are also longer at lower temperatures than PRF40, and vice-versa at higher temperatures. This is surprising since octane ratings are within a few units for H70T30 and PRF40. In addition to mixing and fuel reactivity considerations, toluene requires less oxygen for stoichiometric proportions. As toluene content increases the mixture therefore becomes more fuel-lean holding injection and ambient parameters constant. Because of this, H70T30 being more fuel-lean than PRF40 could explain the further increase in ignition delay

at low temperatures and shorter ignition delays at elevated temperatures from relatively fuel-rich conditions. However, we return to this topic in our discussion of oxygenated fuels which we expect to exacerbate this effect and do not find. As a result, the non-linear kinetics of n-heptane/toluene mixtures may be the sole explanation for observed trends.

Peak OH* signals at 1000 K decrease with octane ratings, in agreement with PRF trends. We note this finding is sensitive to the injection duration, as more fuel mass into the system would cause larger OH* signals and vice-versa. Indeed, H90T10 has cases where the spray plume translates further downstream of the injector prior to ignition at 1000 K relative to n-heptane, indicative of a longer injection event; in these cases, peak OH* signals are larger than n-heptane.

6.3.2.3 n-heptane/ethanol fuels

(a) ERF first stage ignition
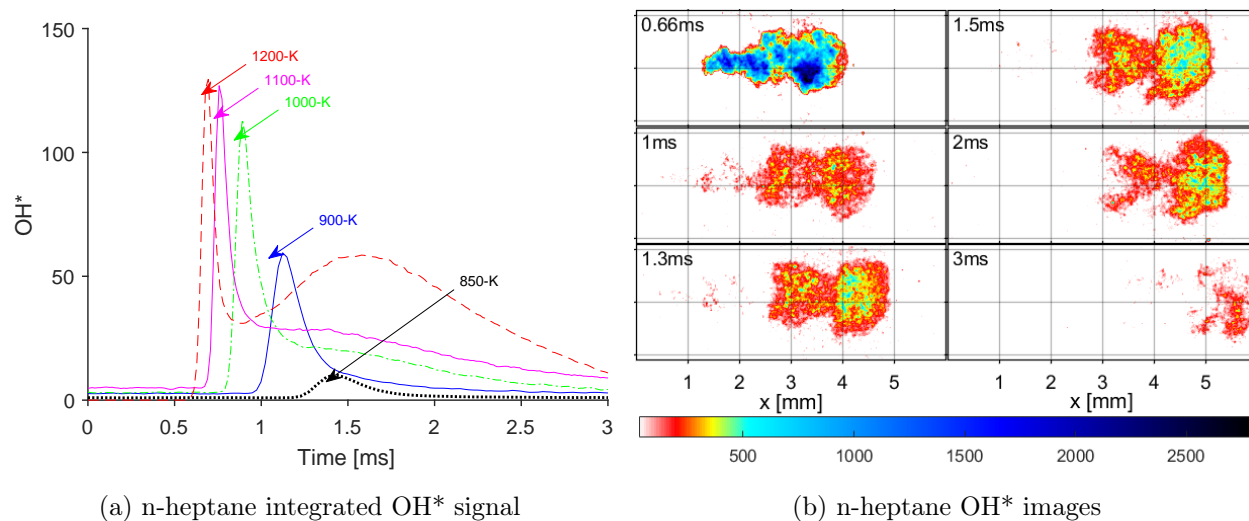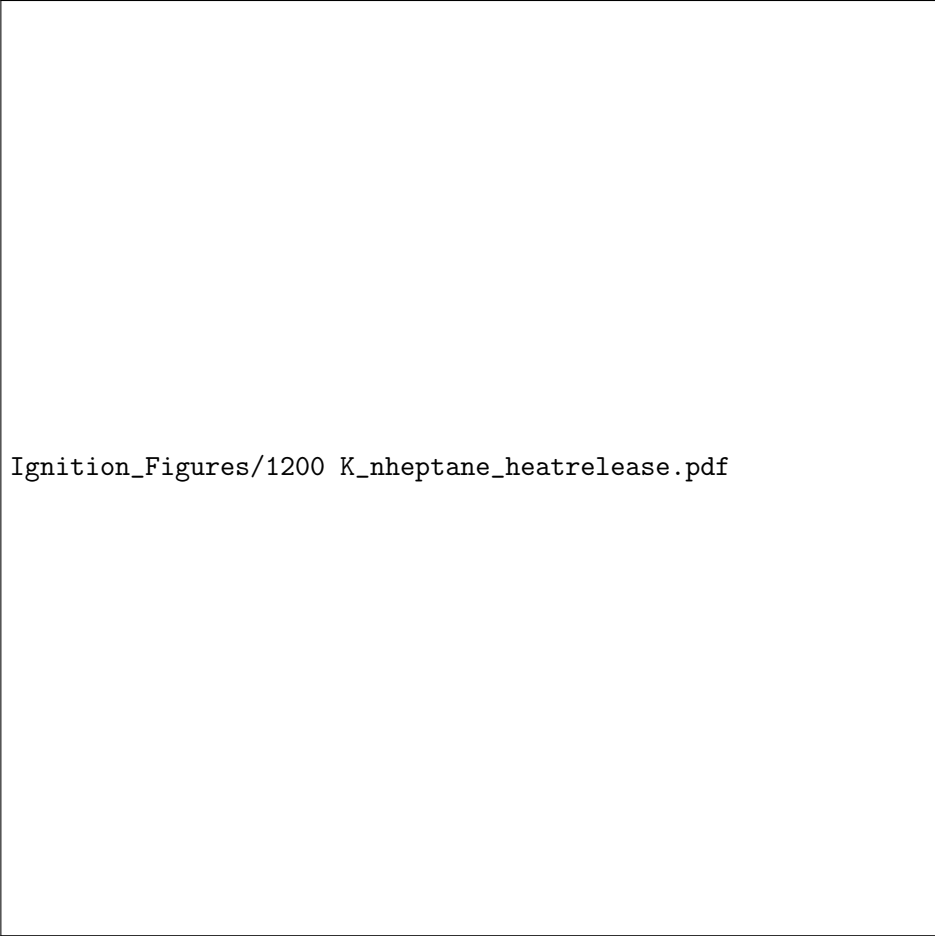
(b) ERF second stage ignition
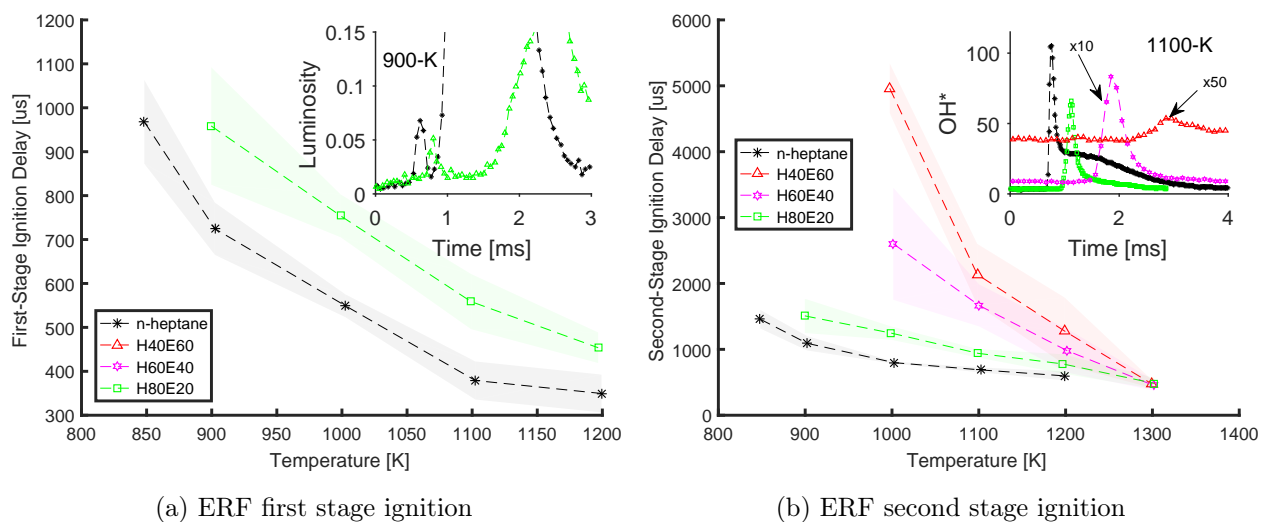
Figure 6.9: Ignition delays for first- and second-stage ignition for n-heptane and ERF fuels. First stage indicated by natural luminosity images, and second stage by OH* chemiluminescence.

Figure 6.9a shows first-stage ignition is delayed between 100 and 200 μs with H80E20 relative to n-heptane, with no detectable first-stage ignition for H60E40 or H40E60. The 20 % by volume addition of ethanol increased the first-stage ignition delay more than the 40 % addition of isooctane or 30 % addition of toluene, evidence of ethanol suppressing first-stage chemistry. This is expected as small additions of ethanol in n-heptane has been shown to delay the onset and significantly reduce the magnitude of LTHR [144]. Our luminosity traces corroborate these trends; as a result, resolving the event optically for H60E40 or H40E60 with the current set-up was not possible.

As the concentration of ethanol increases so does second-stage ignition delay (except for 1300 K), in agreement with octane ratings, as seen in Figure 6.9b. The ignition delays for H60E40 and H40E60 increase significantly past those of PRF70 below 1200 K, expected since octane ratings (71.4 and 94.4) are above 70. Ignition onsets are unclear below 1000 K. Again, the longer ignition delays (or no ignition) is believed to be from over-mixing in conjunction with the unfavorable stoichiometry, causing low fuel to air concentrations relative to the other fuels tested, in turn inhibiting thermal runaway. This is represented in the inset axis, where the OH* rapidly drops at the 1100 K condition with increased ethanol content.

H80E20 and PRF40 have nearly identical second-stage ignition delay trends within certainty, and partially expected from similar octane ratings. Recall the interpreted ignition trends from comparison of H70T30 to PRF40, where lower stoichiometric proportion fuels result in longer ignition delays at lower ambient temperatures, and vice versa. H80E20 has a lower stoichiometric requirement over H70T30, expected to exacerbate perceived trends—albeit was not observed. Fuel stoichiometry may minimally impact ignition trends at residence times below 2 ms; fuel mixture concentrations could be large relative to the decrease from stoichiometric requirements, resulting in a minimal change in kinetic rates. At ignition delays past 2 ms, when the spray is beginning to reach over-mixed conditions, a reduction in stoichiometric requirement becomes a significant factor, evident in the previously discussed H60E40 and H40E60 trends at lower temperatures.

6.3.2.4   Practical Implications

First-stage ignition delay variability proved adequate for the fuels and conditions where optically-resolved. Between all cases (fuels, temperatures) we found an average standard deviation of 75 μs, or error relative to the absolute ignition delay at 13 %. Second-stage ignition delays proved very repeatable across all low fuels and temperatures at residence times below 2 ms. Here, the average standard deviation in ignition delay amounted to 125 μs. On average, the relative error is at an acceptable 12 %. However, for ignition delays at longer residence times we observed a corresponding increase in errors, averaging 541 μs, or 21 % relative. Interestingly, the best-case repeatability was achieved with n-heptane at 1000 K, having a standard deviation of 16 μs, or 2 % relative error; this case had the most repeatable spray penetration profiles up until ignition, suggesting that errors could be correlated to injector performance.

We believe discrepancies in mixing characteristics shot-to-shot are the major cause of the ignition delay repeatability. As the ignition delay increases, and therefore the time allotted for mixing to take place creating low fuel concentrations, the impact on ignition delay is thought to be more dominant. As a result, spray mixing discrepancies for each repeated run is subjecting the fuel to more or less reactive conditions, leading to variance in observed ignition delays. Spray variability is likely caused by our injector being operated at its limits. Alternative injectors or more than ten repeat studies per condition should be considered in future efforts to minimize errors.

The H40E60 case at long residence times (>2 ms) did not demonstrate high ignition delay variability, perhaps from repeated runs randomly being more similar. While penetration trends could be analyzed for repeatability differences, we believe that without quantitative spatiotemporal fuel concentration data we can't make a definitive conclusion. This will be left as an investigation for future efforts.

The high-temperature convergence point observed for the fuels tested in this work, i.e., ignition delays being nearly the same across all fuels around 1300 K, is dictated by a mixing-limited process. At this elevated temperature, chemical reaction rates are sufficiently large relative to convective mixing rates, i.e., a high Damköler number. As a result, the residence time for the spray to adequately mix, reach elevated temperatures and ignitable fuel/air concentrations governs the total ignition delay. In other words, the physical ignition delay is large relative to the chemical. For our injection events at all fuels tested, we find this physical ignition delay is around 500 μs. This datum for all fuels can be used in ensuring reacting spray models, such as that employed in this work or even higher-fidelity CFD models, are accurately representing the physical ignition delay.

High RON and low stoichiometric AFR fuels are more difficult to study with our proposed methodology. For example, H60E40 and H40E60 cannot be studied at temperatures below 1000 K (at 40 atm, 15% O2) because they do not ignite: high octane ratings necessitate long residence times, which prolongs mixing, inhibiting thermal runaway. We expect lower ambient oxygen-concentrations in the vessel to exacerbate this problem regardless of fuel reactivity, and vice-versa. At ignition delays close to the spray physical ignition delay, the spray mixture is fuel rich. This is evident from the burn-out period, where a significant portion of the heat release occurs long after the onset of ignition. To avoid fuel-rich conditions at higher temperature or pressure conditions, shorter injection durations would allow for longer mixing times relative to the onset of ignition. However, shorter

injections would complicate matters with high octane and low stoichiometric AFR fuels at lower temperature and pressure conditions, since prolonged mixing will lead to fuel-lean conditions. Ideal well-mixed conditions appeared to occur at ignition delays around 1 ms for the wide array of fuels, occurring at different ambient temperatures depending on fuel reactivity—again, being specific to the 250 μs injection duration. Future efforts could sweep injection durations to alter spray mixing and therefore bulk mixture concentrations at the time of ignition for a given fuel and ambient condition, providing fuel ignition delay sensitivity versus fuel concentration (in similar fashion to traditional, homogenous investigations). Future efforts aim to provide spatiotemporal measurements of spray fuel concentration at various injection durations to investigate this potential.

6.3.3   Reactive Spray Modeling

To demonstrate the feasibility of using spray-ignition data for chemical mechanism and surrogate fuel validation, we use a simple 1-D fuel spray model coupled with detailed reaction chemistry to predict the experimentally-obtained second-stage ignition delays. The results demonstrate the importance of injector, hydraulic, and control volume boundary conditions specific to our modeling efforts. To assess modeled ignition delay sensitivity to uncertainties in spray physical boundary conditions, we varied discharge coefficient, injection duration, and spreading angle.

(a) Boundary condition sensitivity   (b) Chemical mechanism sensitivity
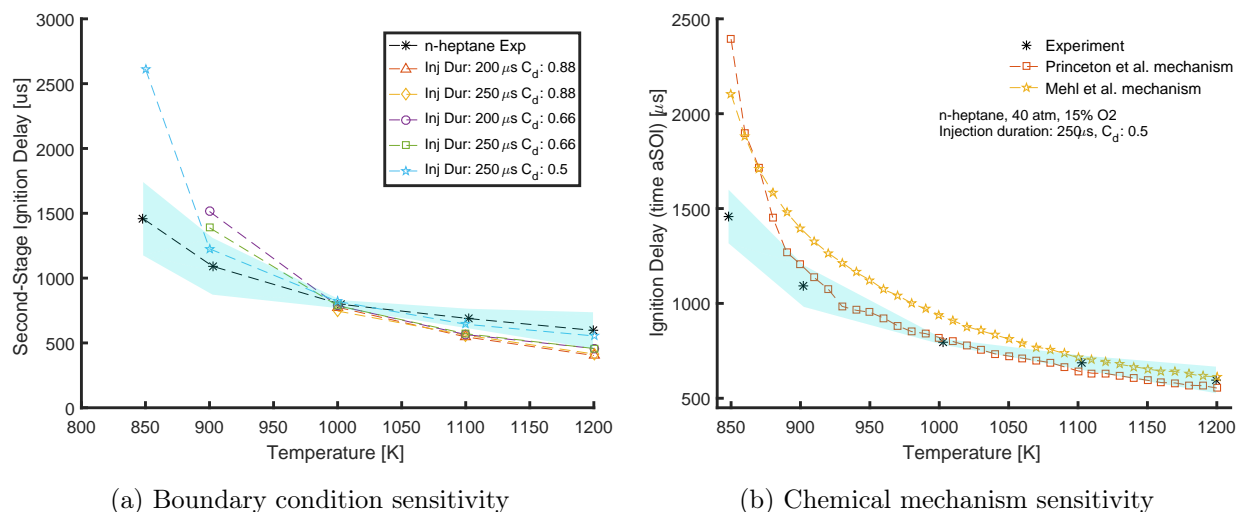
Figure 6.10: Modeled second-stage ignition delay, and sensitivity to the parametric study of imposed boundary conditions and chemical mechanisms.

Figure 6.10a shows modeled second-stage ignition delay for the parametric study of imposed

boundary conditions using the Princeton et al. mechanism. The experimental ignition delays for n-heptane are accompanied with error bands representing one standard deviation about the mean. Modeled values not presented, such as the 0.88 discharge coefficient cases at 900 K, were omitted due to the lack of ignition (simulation limited at 3 ms). We find as injection duration increases and discharge coefficient decreases, the predictive error decreases. The lower discharge coefficient value of 0.5, coupled with the 250 μs injection duration, results in better ignition delay predictions for all temperatures. We attribute this to the increased fuel concentrations as the spray forms, and likely is more representative of experiments. The lower discharge coefficient results in lower injection velocities; this necessitates a reduced spreading angle, constraining the fuel to a smaller control volume at any axial location. The 250 μs injection duration, while requiring a slightly larger spreading angle over the 200 μs injection duration, favorably extends the residence time for high mixture concentrations. At temperatures below 1000 K, this expectedly reduces ignition delays with increased equivalence ratio. At 1100 K and above we find the opposite trend, where 1000 K marks the cross-over points between trends. High Damkholer numbers at elevated temperatures are believed to explain the reversal of modeling trends, i.e., physical ignition delay dictates the modeled ignition. The coarse ignition delay trends are captured, but relative errors do exist. We now present results utilizing the n-heptane-specific chemical mechanism of Mehl et al. [140] and compare with the previous results at a finer simulated resolution in Fig. 6.10b. Here, we use the 250 μs injection duration and discharge coefficient of 0.5, which gave the best results with the Princeton et al. mechanism. As can be seen in Fig. 6.10b, modeled ignition using the Princeton et al. mechanism remarkably matches the experimental data at 900 K and above, demonstrating at most 12 % error with the majority under 5 %. However, at the 850 K condition there is significant error of 79 %. The mechanism of Mehl et al. outperforms at 850 K, overpredicting by only 44 %. Unfortunately, this comes at the cost of increased errors at most other temperatures, but with similar performance between 1100 and 1200 K where physical ignition delays dictate ignition. Spray-model tuning with the Mehl et al. mechanism could potentially reduce errors, as was done previously with the Princeton et al. mechanism, but may not be physically reasonable.

Alfazazi et al. predicted n-heptane ignition delays at 850 K, 50 atm, 21 % O2 ambient conditions with a 0-D spray modeling approach and comprehensive gasoline mechanism of LLNL [145]. They also found large errors in modeled ignition delay of 75 %. Alfazazi et al. attributed this to n-alkanes

not being rigorously tested at 850 K, 50 atm conditions; truly, there are no reference data utilized below 900 K at 50 atm for n-heptane [140]. Albeit, our study is at 40 atm conditions where reference data do exist. If we trust the accuracy of the 1-D physical spray model used, it leads to questioning the chemical mechanism; however, the chemical mechanism is validated at 40 atm—it could be that both simplified spray models are not adequately capturing mixing at residence times greater than 1 ms.

The Princeton and Mehl et al. mechanisms are both founded on the same shock-tube reference data [146] for n-heptane at 40 atm, stoichiometric conditions. Comparing their reference data to shock-tube simulations leveraging each chemical mechanism, at 850 K the Princeton et al. mechanism under-predicts the shock tube reference ignition delays roughly by 25 % [137], but accurately predict temperatures less than 850 K. The Mehl et al. mechanism over-predicts by roughly 25 % [140] at 850 K, featuring much less negative temperature coefficient behavior, and over-predicts at temperatures less than 850 K. Interestingly, this is opposite to our modeled spray-ignition trends at 850 K, but in accordance with spray-ignition trends above 850 K. Investigating the reasoning for this is beyond the scope of this effort, but may be attributed to differences in kinetic sensitivity to fuel concentration. We cannot ascertain that the chemical mechanism or failure of the spray model to adequately represent mixing causes large errors at the 850 K condition. To be certain, future investigation comparing experimental and modeled spray fuel/air mixture fraction distributions are warranted to ensure the 1-D model is adequately representing spray mixture physics. For now, we offer comparisons of experimental and predicted ignition delays for additional fuels, utilizing the comprehensive Princeton et al. mechanism.

Figure 6.11 presents second-stage ignition for PRF40, H70T30, and PRF70, with model results using the same boundary conditions as the n-heptane study to isolate kinetic effects. General trends across all fuels are captured, but large quantitative errors are present at most temperatures, and reasoning behind not simulating the remainder of fuels. Many intricate trends are not captured with the model results: H70T30 ignition being delayed relative to PRF40 at lower temperatures and vice-versa at higher temperatures, PRF40 and PRF70 being delayed at 1100 and 1200 K, among overpredictions for all fuels below 1000 K. Interestingly, ignition for all fuels are reasonably predicted at 1000 K and 1300 K. On the other hand, 1000 K results may be a fortuitous cross-over point between over-predictions of trends at lower temperatures and under-predictions at higher

temperatures. Tailoring model boundary conditions to best match vapor penetration profiles specific to each fuel and case did not improve our results.
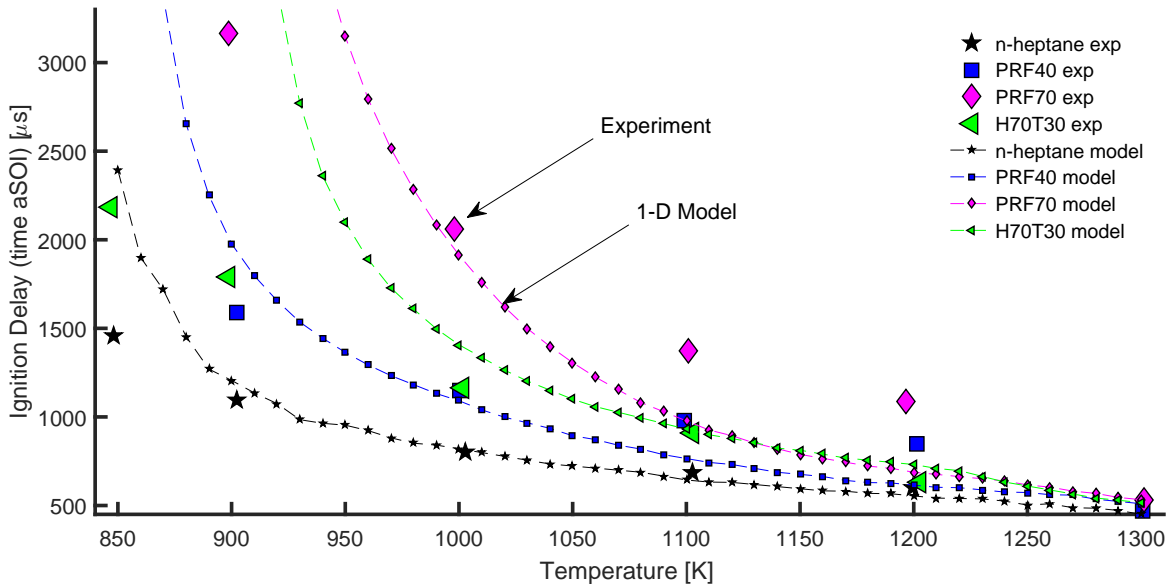
Figure 6.11: Modeled second-stage ignition delay for n-heptane, PRF40, H70T30, and PRF70, overlaid with our experimental results

Observed discrepancies at temperatures below 1300 K lead us to believe the 1-D model is not capturing mixing physics well beyond the physical ignition delay. As previously discussed in the Methodology section, matching experimental vapor penetration—the criterion to ensure relatable mixing between experiments and the model—proved challenging. Neglecting shear stress, axial pressure gradients, and assuming a perfect conical expanding spray profile are potentially the culprits for vapor penetration and mixing discrepancies. It may also be possible that the model boundary conditions, tuned to match n-heptane ignition characteristics, are invalid and should be revisited. Furthermore, in the models' current state, ignition always occurs at the head of the spray, followed by ignition stratification toward the core of the spray nearing up to 500 μs to complete. This may invalidate the ignition delay from the modeling efforts to some degree, defined to occur when any location in the spray exceeds 400 K of the ambient. The definition of ignition delay could be spray-averaged to some degree and delay ignition at all temperatures, but would not alleviate our observed discrepancies. Since the 1-D model is predicting high stratification in the axial direction, not observed in experiments, mixing may be too simplified and could benefit from improvement. Based on our findings, future efforts are warranted to investigate a solution for the 1-D model to

accurately represent true mixing characteristics.

6.4   Conclusions

N-heptane, including binary mixtures of n-heptane/isooctane, n-heptane/toluene, and n-heptane/ethanol were injected into a high pressure (40 atm) and temperature (850 to 1300 K) environment (15% O2) within a constant-volume, pre-burn type combustion vessel, to supplement traditional approaches that study the impact of fuel chemistry on combustion performance. We used high-speed image analysis, simultaneously capturing Schlieren, OH* chemiluminescence, and broadband luminosity. These diagnostics provide temporal- and spatially-resolved spray formation, along with first- and second-stage ignition processes. We employed short-injections ranging between 200–250 μs (subject to repeatability) at 500 atm with a heavy-duty injector with single-hole, axial orifice belonging to the ECN family of "Spray D" injectors. We achieved a quiescent spray mixture after the end of injection within the field of view to optically study autoignition phenomena of low or high reactivity fuels, while avoiding any spray-wall impingement. The long residence times prior to ignition served to enhance mixing, believe to create a more uniform fuel/air distribution—ideal for simplified modeling efforts. We found qualitative ignition delay results were in accordance with established trends in literature derived from traditional, homogenous studies. In most cases, our reported experimental uncertainties are better than those found with homogenous-ignition delay measurements (20 %). Between all cases we found relative error (to the absolute ignition delay) at 13 %. Second-stage ignition delays less than 2 ms are at 12 %, where at longer ignition delays the errors were larger at 21 % relative, thought to be from increased sensitivity to mixing from shot-to-shot variability. Our technique produces repeatable results over a wide range of fuel reactivity and stoichiometric requirements, but the repeatability is subject to injector performance. Future studies should consider a different injector than that used in this work which performs better at ultra-short injections.

The 1-D spray modeling of second-stage ignition delay for n-heptane at 850 to 1200 K, 40 atm, 15 % O2 proved successful. Although, accurate predictions of ignition delay for the 850 K case proved elusive, regardless of the two chemical mechanisms investigated. The ignition delays at ambient temperatures above 850 K are predicted within 13 % of the experimental mean value, lying within experimental repeatability. The ignition delay at 850 K unreasonably matched the experimental mean value regardless of the model boundary conditions, indicating a potential issue

with the chemical mechanism itself. Corroborating our findings, literature suggests reaction kinetics for n-alkanes lack accuracy at high-pressure, low-temperature conditions. In contradistinction, our modeling results for PRF40, H70T30, and PRF70 demonstrated significant quantitative errors across all temperatures. This evidence suggests mixing may not be not well-represented in the 1-D modeling efforts and could benefit from improvement. Incorporating shear stress, axial pressure gradients, or altering the spray boundary in the 1-D model could improve results; that, or leverage a higher-fidelity model. With a computationally efficient model that captures mixing characteristics of short-injection sprays, we believe the methodology outlined in this work demonstrates an attractive method to study two-stage ignition quality for a wide array of fuels, aimed to develop corresponding chemical mechanisms and surrogates.

We encourage the community to leverage and add to this dataset, improve upon our injection technique and simplified modeling efforts, and investigate the other fuels studied. The CVCC in this work rapidly provides fundamental data over most traditional methods, allowing the generation of statistically significant datasets. These fundamental data will serve to supplement ignition delay datasets by which modern combustion models are founded on. Also, surrogate fuels may be rapidly tested in a CVCC and validated against the actual fuel and surrogate-modeled results, as outlined in our methodology. Similarly, as the combustion community begins to target novel alternative fuels and subject them to more extreme operating conditions, a CVCC can do so quickly with minimal fuel sample. As little as 100-ml of fuel sample is required to purge the system and provide hundreds of data-points at ambient conditions potentially ranging 450 to 1400 K, densities from 1 Kg/m3 to 60 Kg/m3, and pressures up to 350 atm—extending the limits of many homogenous facilities. In addition to rapidly providing data for combustion model and surrogate/alternative fuel development, we simultaneously visualize the spray formation process and its impact on the combustion behavior. Short-injection spray formation and its impact on combustion performance has practical implications for engines employing pilot direct injection strategies. Practitioners considering these strategies for commercial applications will benefit from the optical diagnostic findings that are too expensive or difficult to attain themselves. The 1-D modeling techniques adequately predict spray-ignition performance for pilot-like injections of n-heptane—a simple diesel fuel surrogate—and may prove useful in practice for combustion technology optimization.

Chapter 7: Rational LTC Engine Fuel Design

7.1 Introduction

The previous chapter quantified the disagreement between modeled and experimental spray-ignition onsets, concluding the prediction error varied with ambient conditions and the fuel composition. The spray-ignition model, simply put, is made of two components, one representing simplified spray mixing physics and the other detailed reaction chemistry. The body of experimental work in chapters 5, 6, and appendix D demonstrate that the 1-D spray model captures the spray mixing processes well. However, our spray-ignition results and comparisons to literature findings both suggest that mixing may not be not well-represented in the 1-D modeling efforts for some conditions and could benefit from improvement; that, or to leverage a higher fidelity spray model. Since the 1-D spray model is not perfectly representative of the true spray mixing, errors in the modeled spray-ignition results cannot be entirely deduced to be from inaccuracies in the reaction chemistry. With that said, it is possible that the model inaccuracies are partially due to inaccuracies in the reaction chemistry.

The chemical mechanism used in the spray-ignition study was also used for generating the LTC index training/test data set. Assuming the previous study had quantitatively established the ignition timing errors from the chemical mechanism, then LTC index sensitivity to this error could be investigated. Quantifying the sensitivity of LTC index to ignition delay variations would require an exhaustive effort. Potentially, the spray-ignition data set generated in Chapter 6 could be used to update chemical reaction rates to improve model ignition delay predictions. The updated chemical mechanism can then be used to repeat LTC index calculations, allowing a comparison of the updated to previous LTC index values to establish sensitivity. Alternatively, reduced chemical mechanisms could be generated for each fuel, targeted to have global ignition delay errors, then used in the LTC index simulations. Moving forward, the author acknowledges the potential errors present in the LTC index data set and use the IR-to-LTC index predictive models, knowing predictions may not coincide with reality.

This chapter explores thousands of fuel mixtures to find a fuel that provides high LTC engine fuel performance. The computational tools developed in this body of work are all leveraged to automate this process. The LTC index predictive model is used to rapidly evaluate the LTC indices for these fuel mixtures, allowing each case to be evaluated with minimal computational effort; this way, it is possible to efficiently explore the large parameter space to design an optimal fuel. This study demonstrates the process of designing a novel fuel with tailored properties to work with high efficiency LTC engine strategies.

7.1.1   Methodology

This study combines the tools developed in Chapters 2–4 to rationally design high performing fuels for LTC engine applications. Recall in Chapter 3, the author introduced numerically blending hydrocarbon species together into a fuel that emulates the thermochemical attributes of complex refinery grade gasolines. In that effort the IR-RON predictive model from Chapter 2 was embedded into the fuel design algorithm, rapidly determining RON of the hydrocarbon mixtures. The final stage of this work now incorporates the IR-LTC index model into the fuel formulation algorithm.

As detailed in chapter 3, the framework linearly blends hydrocarbon species together to best-match the desired target parameters. At each iteration of fuel composition, the fuel property models are evaluated and return values to the objective function. The optimizer attempts to find a global minimum of the objective function, and in doing so designs a fuel tailored to the user-specified target fuel properties. Recall to use the predictive models for RON or LTC index, knowledge of the fuel IR spectra is required, since The models are a correlation between fuel IR spectra and the fuel engine performance value. Here, fuel IR spectra are estimated by the molar weighted sum of each individual hydrocarbon spectrum. This approximation is used as the input to the IR-RON and IR-LTC index predictive models.

Using linear blened spectra with the IR-LTC index models developed in Ch. 4 is problematic. The IR-LTC index model is trained with hundreds of actual fuel mixture spectra collected by the author. In many cases, real fuel IR spectra are not the same as linearly blended spectra—especially for oxygenated fuel mixtures. As such, inputting an approximated spectrum into the existing IR-LTC index model would yield significant errors for many fuel mixtures. To resolve this issue a new IR-LTC index model is created, trained in the same manner and with the same fuel data as

chapter 4, but instead using linearly blended IR spectra.

A fuel solely designed to maximize LTC index is likely impractical for emerging LTC transportation engines, such as HCCI. For the vehicle parameters studied, as indicated by the LTC index data set, it does not appear technically feasible to have a fuel that can provide the entirety of demanded engine operating conditions. Because of this limitation, in order for HCCI to come to production it would need to be employed with sophisticated engine controls to operate with both spark ignition (SI) and HCCI cycles. This way, portions of the engine operation that can be achieved with HCCI are leveraged for efficiency improvements, and where not possible supplemented with traditional SI. For SI operation, a fuel must have high octane ratings, and for HCCI a high LTC index. Based on this, a fuel is formulated to maximize both parameters. To constrain the optimization problem, a RON of 91.0 and LTC index of 40.0 are selected, both representing large and realistic values to target. Based on the results, some practical directions for hybrid engine cycles are suggested, including the use of direct-injection compression ignition (DICI) engines in lieu of SI for next-generation engine strategies.

7.1.2   Results/Discussion

7.1.2.1   IR-LTC Model

The IR-LTC index model, trained with linearly blended IR spectra, is shown here for performance assessment. General model performance is visualized in Figure 7.1. Perfect LTC index model predictions lie on the linear trend line, below the line indicates the LTC index is under-predicted and above the line over-predicted. The predictions here are the training/test/and validation data set. Here, the validation data set is ten samples randomly pulled from the train/test data set in chapter 4. Model parameters can be found in Appendix E The box-and-whisker plot, shown in Figure 7.2, quantifies the residual (predicted - actual) distributions. As can be seen, The red line indicates the median, red square the mean, the edges of the box the first and third quartiles (25th and 75th percentiles), the whiskers extend to 1.5 times the inter-quartile range (IQR), and potential outliers indicated with plus signs (greater than 1.5 IQR). The mean and median are centered on zero, with the majority of predictions within ± 5, but as worse as ± 10 for outliers. The large errors with some fuels could be attributed to the support vector machine algorithm failing to generalize the

problem. To potentially improve predictive performance, alternative machine learning algorithms such as artificial neural networks should be investigated. Errors could also be an artifact caused by the uncertainty of the "true" values within the LTC index data set, previously discussed to stem from chemical mechanism uncertainty used in the HCCI modeling efforts. Despite the errors in the IR-LTC index model presented here, it predicts most fuels within 6 units (whisker span). The tool should be able to guide the fuel design tool in correct directions.
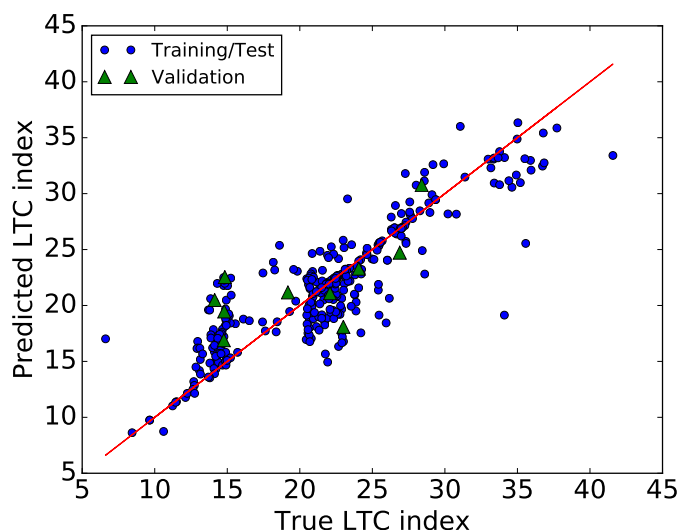
Figure 7.1: True versus predicted LTC index results. The predictive model has a coefficient of fit, R^2, of 0.76 for the complete training/test/validation data set

7.1.2.2   SI-HCCI Fuel

A fuel designed to potentially operate in a hybrid HCCI/SI engine is presented in Table 7.1. The IR-RON and IR-LTC index predictive models are paired with multivariate optimization to design a fuel (linear combination of various hydrocarbons), targeted to have a RON of 92.0 and LTC index of 40.0. As can be seen, the predicted LTC index and RON values match the targeted values well. The algorithm blended the eleven components shown in Table 7.1, and converged to an optimal fuel containing five of them. The fuel comprises roughly 20.5 % 2-methylhexane (paraffin), 15.2 % isooctane (isoparaffin), 11.6 % cyclopentane and 20.4 % cyclohexane (naphthenes), and the remainder aromatic (o-xylene).

To validate the LTC index of this fuel it was directly simulated. The actual LTC index surmounted to 15.5, roughly a factor of two less than desired. The large error between the predicted and
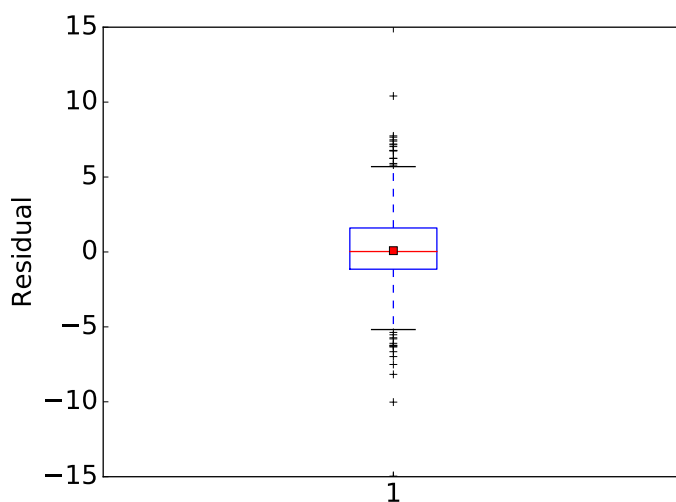
Figure 7.2: Residual (true-predicted) boxplot for LTC index predictions. The red line indicates the median, red square the mean, the edges of the box the first and third quartiles (25th and 75th percentiles), the whiskers extend to 1.5 times the inter-quartile range (IQR), and potential outliers indicated with plus signs (greater than 1.5 IQR).

actual value is likely attributed to the inclusion of cyclopentane and cyclohexane in the fuel palette, which are not within the training data set. The spectral features from these fuels are thought to be inflating the LTC index predictions. Hydrocarbons have many overlapping IR functional groups. In this case, the model is weighting these overlapping features with positive influence towards LTC index as learned from the training data set, when it evidently should be to a lesser extent. To alleviate this issue, the IR-LTC index predictive model should be trained with each fuel present in the fuel formulation algorithm species palette. Moving forward, since the true LTC index value of this fuel is found to be minimal, it is therefore not an attractive option for a hybrid HCCI/SI engine. Because of this, there is little motivation to validate the predicted RON of this fuel through experimental procedures.

The predictive model utility is evidently limited to mixtures of hydrocarbons used to create the model. The fuel formulation procedure is repeated with a species palette only including hydrocarbons present in the training/test/validation data set. The author also removes species that converged to zero in the prior study. The updated results are presented in Table 7.2.

The fuel target values are not achieved, surmounting to a RON of 79.7 and LTC index of 24.6, but the results are expected. For the vehicle and powertrain the LTC index is based on in this work,

Parameter	Target	Predicted	Actual
RON	91.0	89.1	
LTC index	40.0	39.7	15.5
Species		Molar %	
n-heptane		0.0	
2-methylbutane		0.0	
2-methylhexane		20.49	
1-pentene		0.0	
1-hexene		0.0	
2,2,4-trimethylpentane		15.18	
cyclopentane		11.57	
cyclohexane		20.37	
o-xylene		32.39	
1,2,4-trimethylbenzene		0.0	
toluene		0.0	

Table 7.1: Fuel optimization results for a fuel tailored to a SI-HCCI hybrid engine, allowing species not present in the training/test/validation data set. Predicted properties evaluated through IR-fuel property correlations are shown, with comparison to calculated LTC index. Species with "0.0" entries indicates they were included in the optimization species palette, but converged to zero.

Parameter	Target	Predicted
RON	91.0	79.7
LTC index	40.0	24.6
Species		Molar %
n-heptane		15.7
2-methylhexane		7.9
2,2,4-trimethylpentane		75.7
toluene		0.0
ethanol		0.7

Table 7.2: Fuel optimization results for a fuel tailored to a SI-HCCI hybrid engine, removing species not present in the training/test/validation data set. Predicted properties evaluated through IR-fuel property correlations are shown, with comparison to calculated LTC index. Species with "0.0" entries indicates they were included in the optimization species palette, but converged to zero.

higher LTC index fuels can be formulated but the RON value decreases rapidly, and vice-versa. In general, the LTC index training data set show that fuels with a RON less than 80.0 can provide a wide range of LTC index values, depending on fuel composition, but with a RON greater than 85.0 guarantees the LTC index to be at or less than 25.0. Therefore, the RON and LTC index of the formulated fuel are seemingly the best balance for the two metrics to have the highest values. Calculating the actual RON and LTC index values for this fuel is not pursued due to the low predicted LTC index value.

A fuel with a RON of 85.0 or less is going to be knock-prone within most SI engine configurations. Using direct injection strategies could potentially eliminate engine knock with mid-octane fuels (~80-85), due to the latent heat of vaporization acting to reduce in-cylinder temperatures and pressures to decrease chemical reactivity. To investigate further, fuel TRF4 from Truedsson et al. [16, 17], having an LTC index of 34.1 but a RON of 82.8 and MON of 80.7, could be a promising candidate to test in such an engine.

The author suggests investigating LTC index trends at higher compression ratios or boosted (e.g., turbocharged) conditions. It is hypothesized that as in-cylinder pressures and temperatures increase, the fuel reactivity must also decrease to offer successful HCCI combustion phasing. Because of this, high LTC index values could potentially correspond to higher octane ratings. However, further increasing compression ratios past 13.0 and intake charge pressure past atmospheric levels would require increasing the octane requirement near or above 100.0 to combat engine knock. The study should therefore investigate high oxygenate, iso-alkane, and aromatic fuel mixtures that offer large octane ratings to operate at extreme conditions in an SI cycle. The study could potentially reveal a high RON, high LTC index fuel that is not able to be formulated at the CR of 13.0 and atmospheric intake charge pressure. However, it is expected that LTC heat release rates (HRR) will be too rapid causing engine knock, even when favorable ignition onsets occur. An attempt to mitigate accelerated HRR in the simulations will be required. This could entail introducing thermal in-cylinder stratification, shown to reduce HRR [122], but would require moving towards a multi-zone HCCI model.

At the conditions investigated in this work, fuels offering the highest scoring LTC indices have very low RON values (less than 30.0). These fuels are therefore more like a diesel fuel, which are highly reactive in comparison to gasoline. Because of this, it is recommended that the low RON

and high LTC index fuels be paired with direct injection compression ignition (DICI) strategies in lieu of SI.

7.1.2.3 DICI-HCCI Fuel

Of all the fuels investigated to create the LTC index data set, fuel H80T20, having 80 % n-heptane and 20 % toluene by volume, provides the highest LTC index of 41.6. Because of the low octane rating and high LTC index, this fuel could be a candidate for hybrid HCCI/DICI cycle. HCCI could be leveraged at lower engine loads, and DICI to achieve high engine loads. In chapter 6, n-heptane and H80T20 were found to have nearly identical spray-ignition behavior across the conditions tested. Since H80T20 is found to have similar spray-ignition behavior to n-heptane, and n-heptane is often used as a surrogate for diesel in DICI environments, H80T20 could potentially offer similar DICI performance to most diesels.

Again, the LTC index in this work is based on a compression ratio of 13.0, a low value for DICI applications. Despite a low CR of 13.0, operating a DICI cycle with fuel H80T20 should be technically feasible. Chapter 6 investigated conditions emulating a non-boosted engine with a compression ratio of 13.0 at moderate exhaust gas recirculation (15 % O2). The conditions investigated were conducive to low temperature combustion (40 atm, 850 to 900 K) finding H80T20 auto-igniting within 1.0–1.5 ms. This is a short enough residence time to react in a reciprocating engine, even at low RPM. The work also investigated higher temperature conditions mimicking more conventional DICI conditions (40 atm, 1000 to 1200 K), where ignition delays of n-heptane and H80T20 are nearly identical, with both decreasing to 400 ms by 1200 K.

A CR of 13.0 would unfavorably decrease the thermodynamic efficiency over a typical DICI cycle having a much higher CR. However, potentially supplementing much of the DICI cycle with HCCI would serve to increase the overall cycle efficiency and also reduce emissions. In-cylinder temperatures and pressures would be much lower than typical DICI operation at higher CRs, thereby increasing ignition delays. This results in prolonged mixing of the fuel spray, which may in-turn reduce soot emissions for the DICI cycle with a proper injection strategy. Overall, a hybrid HCCI/DICI cycle at a CR of 13.0 with fuel H80T20 could potentially offer reduced emissions and increased fuel economy over traditional SI and CI engines leveraging gasoline and diesel. Future efforts should experimentally investigate this potential.

7.1.2.4 Fuel Design Directions

The fuel design methodology outlined in this work can be extended to other vehicle and powertrain technologies. A new LTC index data set could be generated as a function of vehicle and engine parameters, such as engine CR, to investigate LTC index sensitivity. This information could be used to train, test, and validate new LTC index predictive models. Cloud computing resources are getting significantly faster and less expensive to use, so the time investment for LTC index data set generation could be reduced. Further data generation speed-ups could potentially be achieved as graphics processing units (GPU) become supported for combustion simulation purposes, but at this time is still an active research topic. Strenuous machine learning computations, yet another time investment hurdle, are receiving GPU support not used in this effort. Python tools, such as *Keras* and the *TensorFlow* back-end, provide artificial neural network GPU routines that should be explored. Regardless of the computational burden of creating LTC index predictive models, extending the methodology of this work to new vehicle parameters would reveal changes in optimal fuel compositions and their resulting performance. Through this, the fuel and engine parameters yielding utmost performance can be simultaneously discovered.

7.1.3 Conclusions

Based on the LTC index data set, no single fuel can provide all the necessary engine operating points for a typical vehicle application. As a result, the author attempted to blend a fuel with a high LTC index—for the benefits of increased fuel efficiency and reduced emissions—and also a high RON, such that traditional spark-ignition (SI) could be used where HCCI cannot. As this work showed, the fuel formulation algorithm was not able to do so. The result partly stems from the IR-to-LTC index predictive model being limited in predictive scope to a handful of candidate hydrocarbons, thus being limited in the parameter space to investigate. More-so, the engine parameters used in generating the LTC index data set appears to be the limiting factor, as it does not seem feasible to simultaneously have high RON and LTC index at a compression ratio (CR) of 13.0 with atmospheric intake charge pressure. At these engine parameters, however, there is motivation to further study fuel H80T20 (high LTC index, low RON) in a hybrid low temperature combustion / direct-injection compression ignition engine to achieve significant economy improvements.

To further explore the possibility of tailoring a fuel to HCCI, hybrid HCCI-SI, or hybrid HCCI-DICI applications, the author suggests investigating LTC index trends at alternative engine parameters such as increased compression ratios or boosted conditions. This would entail re-calculating the LTC index data set and developing new IR-LTC index predictive models, then used to repeat the fuel design process outlined in this chapter. An alternative low temperature combustion performance metric could also be used in lieu of the LTC index—the same concept applies to fuel formulation, where the alternative metric and its corresponding "ideal" value would be targeted. In general, a sensitivity study of LTC fuel performance trends versus varying engine parameters could simultaneously reveal an optimal fuel and engine combination.

Chapter 8: Conclusions

This work developed models that can rapidly predict fuel performance metrics for spark ignition (SI) and low temperature combustion (LTC) engines, circumventing the need for costly and time-consuming experiments. Spcifically, the models can predict Research Octane Number (RON), Motor Octane Number (MON), and the OSU-Chevron Low Temperature Combustion Index (LTC index). The models were developed through various supervised machine learning techniques. Fuel infrared absorbance spectra trained these models to predict the fuel performance ratings. In this manner, fuel performance ratings can be determined with only knowledge of a fuels' infrared absorbance spectrum. The fuels used to train the models were neat hydrocarbons and mixtures containing up to six neat hydrocarbon components, yet the models can accurately predict the fuel performance ratings of complex fuel mixtures that contain hundreds of hydrocarbons.

This work contained two significant efforts specifically aimed to validate the LTC index predictive model, the LTC index being a metric that characterizes fuel homogeneous charge compression ignition (HCCI) performance. The first effort outlined a computational tool to formulate specially designed simple fuel mixtures that emulate the thermochemical properties of complex fuels, known as fuel "surrogates". The fuel surrogate is paired with HCCI simulations to determine the LTC index for a complex fuel sample. This was required as the LTC index is a computationally determined metric, posing unmanageable challenges to directly simulate a fuel of high complexity. Creating and simulating these surrogate fuels generated the needed data set to validate the LTC index predictive model.

The LTC index is a simulated metric, so the accuracy of the LTC index data set used to inform the predictive model is subject to the combustion model accuracy. As such, the second validation effort evaluated the performance of simplistic combustion modeling efforts, serving to inform the degree of accuracy of the LTC index data set. Various combustion parameters in a constant volume combustion chamber (CVCC) apparatus were measured for an array of fuels. The author first quantified direct-injection spray mixing with a novel line-of-sight, extinction-based optical diagnostic, developed specifically for this work. The diagnostic showed that using ultra-short

injection durations reduced unfavorable concentration gradients within the fuel spray, serving to reducing physical complexity. With the physical complexity of the spray process reduced, simplistic 1-D modeling efforts proved to accurately represent the spray formation process. Based on this, a short-injection spray ignition study was conducted, optically measuring first- and second-stage ignition onsets. The experimental results are compared to those from a 1-D spray-ignition model. Comparing experimental to modeling spray-ignitions concluded that there are likely errors in the chemical mechanism. The chemical mechanism used for the spray-igntion study was also used for the LTC index simulations. This indicates the LTC index training, test, and validation data-sets must also have errors, but the magnitude of which is unresolved. A more in-depth study is warranted to establish the sensitivity of LTC indices to ignition delay uncertainty. The study would be an exhaustive effort, first requiring updating the chemical mechanism to reflect corrections for simulated ignition delays, then used to re-calculate LTC index trends. This study is left for future efforts. Since all sources of error within the LTC index data set are not yet fully quantified, any predicted LTC index results should be treated with caution.

Moving forward, the RON and LTC index predictive models were paired with multivariate optimization. This combination can design novel fuels tailored to specific vehicle and powertrain applications. The tool produces a single fuel that can potentially operate in a hybrid SI/HCCI engine, having a predicted RON of 89.1 and an LTC index of 39.7. This means the fuel can operate at many engine operating points via HCCI, and at engine operating points not attained by HCCI could be supplemented with traditional SI, offering a 39.7 % savings in burned fuel mass over solely using SI. However, the LTC index of this fuel was directly evaluated and found to be 15.5, indicating the predictive model is not accurate for this fuel composition. The result here stems from the IR-to-LTC index predictive model being limited in scope to predict a handful of hydrocarbons, and in this case was applied to design a fuel containing hydrocarbons not within the training data set. The author removed species from the formulation algorithm to rid of these predictive errors, and designed a fuel with a maximized RON of 79.7 and LTC index of 24.6. This result is expected from trends presents within the LTC index data set, where the highest scoring LTC index fuels have a RON less than 30.0. Therefore the RON of 79.7 and LTC index of 24.6 was the best balance that could be achieved. This result is intrinsic to the compression ratio (CR = 13.0), among other engine and vehicle parameters used in this investigation, which would change if the engine and

vehicle parameters were altered. The result is also influenced by the current state of the LTC index data set and the developed predictive models, which could be improved upon.

Future efforts should extend the fuel design methodology outlined in this work to other vehicle and powertrain technologies. To further explore the possibility of tailoring a fuel to HCCI, hybrid HCCI-SI, or hybrid HCCI-DICI applications, the author suggests investigating LTC index trends at alternative engine parameters such as increased compression ratios or boosted conditions. Investigating the impact of varying compression ratio, or other parameters, would require calculating a new LTC index data set, used to train/test and validate a new LTC index predictive model. Creating this data set was a time-consuming and challenging step in this work. However, with cloud computing resources getting faster and less expensive to use, along with increasing support for using graphic processing units for expedited research calculations, the time investment for LTC index data set generation could be reduced. Extending the LTC index to new vehicle parameters would reveal changes in optimal fuel compositions and their resulting performance. Through this, the fuel and vehicle yielding utmost performance could be simultaneously discovered. Future efforts could also improve upon the LTC index data sets. This could be done by simulating more fuels to add to the training/test/validation data sets, as well as improving the chemical mechanism used in the simulations. Moving towards multi-zone HCCI simulations to account for thermal stratification, a well known parameter to favorably smooth heat release rates in HCCI applications, in turn extending the achievable high load limits and increase LTC index values.

Through engine simulations, developing predictive models, and pairing the efficient models with multivariate optimization techniques provided the means to efficiently explore the huge parameter space demanded by fuel design. The work in this thesis has laid a foundation for a novel approach to fuel design, resulting in a suggested formulation for a specific vehicle and powertrain application. These tools simultaneously point fuel and vehicle technology in a unique direction for designing high efficiency, next-generation combustion systems.

Bibliography

[1] I. for Energy Research, Fossil fuels (2014).
URL "http://instituteforenergyresearch.org/topics/encyclopedia/fossil-fuels/"

[2] U. S. E. P. Agency, Particulate matter (pm)—health (2014).
URL "https://www3.epa.gov/pm/health.html"

[3] J. Riess, Nox: how nitrogen oxides affect the way we live and breathe, US Environmental Protection Agency, Office of Air Quality Planning and Standards, 1998.

[4] J. B. Heywood, O. Z. Welling, Trends in performance characteristics of modern automobile si and diesel engines, SAE International Journal of Engines 2 (1) (2009) 1650–1662.

[5] G. C. Congress, Us diesel car registrations increased by 24% from 2010–2012, hybrids up 33% (2013).
URL http://www.greencarcongress.com/2013/04/diesel-20130426.html

[6] R. D. Reitz, Directions in internal combustion engine research, Combustion and Flame 160 (1) (2013) 1–8. doi:10.1016/j.combustflame.2012.11.002.
URL http://dx.doi.org/10.1016/j.combustflame.2012.11.002

[7] H. Yun, N. Wermuth, P. Najt, Extending the high load operating limit of a naturally-aspirated gasoline hcci combustion engine, SAE international Journal of Engines 3 (1) (2010) 681–699.

[8] M. Yao, Z. Zheng, H. Liu, Progress and recent trends in homogeneous charge compression ignition (hcci) engines, Progress in Energy and Combustion Science 35 (5) (2009) 398–437.

[9] J. B. Heywood, et al., Internal combustion engine fundamentals, Vol. 930, Mcgraw-hill New York, 1988.

[10] ASTM STP225-EB, Knocking Characteristics of Pure Hydrocarbons, ASTM International, Philadelphia, PA, 1958. doi:10.1520/STP225-EB.

[11] A. D2699-13b, Standard Test Method for Research Octane Number of Spark-Ignition Engine Fuel, ASTM International, West Conshohocken, 2014.

[12] A. D613-18, Standard Test Method for Cetane Number of Diesel Fuel Oil, ASTM International, ASTM International, West Conshohocken, PA, 2018.

[13] G. T. Kalghatgi, S. G. S. U. K, Auto-Ignition Quality of Practical Fuels and Implications for Fuel Requirements of Future SI and HCCI Engines Fuel Requirements of Future SI and HCCI Engines (724).

[14] T. Shibata, G., Urushihara, Auto-Ignition Characteristics of Hydrocarbons and Development of HCCI Fuel Index, SAE 2007-01-02.

[15] V. H. Rapp, W. J. Cannella, J.-Y. Chen, R. W. Dibble, Predicting Fuel Performance for Future HCCI Engines, Combustion Science and Technology 185 (5) (2013) 735–748. doi:10.1080/00102202.2012.750309.
URL http://www.tandfonline.com/doi/abs/10.1080/00102202.2012.750309

[16] I. Truedsson, M. Tuner, B. Johansson, W. Cannella, Pressure sensitivity of HCCI auto-ignition temperature for primary reference fuels, SAE Int J Engines 5 (3) (2012) 1089–1108. doi:10.4271/2012-01-1128.

[17] I. Truedsson, M. Tuner, B. Johansson, W. Cannella, Emission formation study of HCCI combustion with gasoline surrogate fuels, SAE Technical Paper 2013-01-2626 (2013). doi:10.4271/2013-01-2626.

[18] I. Truedsson, M. Tuner, B. Johansson, W. Cannella, Pressure sensitivity of HCCI auto-ignition temperature for oxygenated reference fuels, J Eng Gas Turb Power 135 (7) (2013) 072801. doi:10.1115/1.4023614.

[19] I. Truedsson, W. Cannella, B. Johansson, M. Tuner, Development of new test method for evaluating HCCI fuel performance, SAE Technical Paper 2014-01-2667 (Oct. 2014). doi:10.4271/2014-01-2667.

[20] I. Truedsson, The HCCI Fuel Number: Measuring and Describing Auto-ignition for HCCI Combustion Engines, Ph.D. thesis, Lund University (Apr. 2014).

[21] K. E. Niemeyer, S. R. Daly, W. J. Cannella, C. L. Hagen, A novel fuel performance index for low-temperature combustion engines based on operating envelopes in light-duty driving cycle simulations, Journal of Engineering for Gas Turbines and Power 137 (10) (2015) 101601.

[22] ASTM D2699-15, Standard Test Method for Research Octane Number of Spark-Ignition Engine Fuel, ASTM International, West Conshohocken, PA, 2015. doi:10.1520/D2699-15.

[23] U.S. Energy Information Administration, How much gasoline does the United States consume?, http://www.eia.gov/tools/faqs/faq.cfm?id=23t=10, accessed: 2015-11-24 (2015).

[24] J. Kiefer, Recent advances in the characterization of gaseous and liquid fuels by vibrational spectroscopy, Vol. 8, 2015. doi:10.3390/en8043165.

[25] J. J. Kelly, C. H. Barlow, T. M. Jinguji, J. B. Callis, Prediction of gasoline octane numbers from near-infrared spectral features in the range 660–1215 nm, Anal Chem 61 (4) (1989) 313–320. doi:10.1021/ac00179a007.

[26] K. P. J. Williams, R. E. Aries, D. J. Cutler, D. P. Lidiard, Determination of gas oil cetane number and cetane index using near-infrared Fourier-transform Raman spectroscopy, Anal Chem 62 (23) (1990) 2553–2556. doi:10.1021/ac00222a008.

[27] J. B. Cooper, K. L. Wise, J. Groves, W. T. Welch, Determination of octane numbers and Reid vapor pressure of commercial petroleum fuels using FT-Raman spectroscopy and partial least-squares regression analysis, Anal Chem 67 (2) (1995) 4096–4100. doi:10.1021/ac00118a011.

[28] I. Litani-Barzilai, I. Sela, V. Bulatov, I. Zilberman, I. Schechter, On-line remote prediction of gasoline properties by combined optical methods, Anal Chim Acta 339 (1997) 193–199. doi:10.1016/S0003-2670(96)00472-2.

[29] A. A. Kardamakis, N. Pasadakis, Autoregressive modeling of near-IR spectra and MLR to predict RON values of gasolines, Fuel 89 (1) (2010) 158–161. doi:10.1016/j.fuel.2009.08.029.

[30] S. Swarin, C. Drumm, Prediction of gasoline properties with near-infrared spectroscopy and chemometrics, SAE Technical Paper 912390 (1991). doi:10.4271/912390.

[31] S. J. Choquette, S. N. Chesler, D. L. Duewer, S. Wang, T. C. O'Haver, Identification and quantitation of oxygenates in gasoline ampules using Fourier transform near-infrared and fourier transform Raman spectroscopy, Anal Chem 68 (20) (1996) 3525–3533. doi:10.1021/ac960451v.

[32] G. E. Fodor, K. B. Kohl, R. L. Mason, Analysis of gasolines by FT-IR spectroscopy, Anal Chem 68 (1) (1996) 23–30. doi:10.1021/ac9507294.

[33] V. N. Korolev, A. V. Marugin, V. B. Tsaregradskiĭ, Estimation of the petroleum product knock rating by regression analysis of near-infrared absorption spectra, Tech Phys 45 (9) (2000) 1177–1181. doi:10.1134/1.1318105.

[34] R. M. Balabin, R. Z. Safieva, Gasoline classification by source and type based on near infrared (NIR) spectroscopy data, Fuel 87 (7) (2008) 1096–1101. doi:10.1016/j.fuel.2007.07.018.

[35] M. R. Monteiro, A. R. P. Ambrozin, M. da Silva Santos, E. F. Boffo, E. R. Pereira-Filho, L. M. Lião, A. G. Ferreira, Evaluation of biodiesel–diesel blends quality using ^{1}H NMR and chemometrics, Talanta 78 (3) (2009) 660–664. doi:10.1016/j.talanta.2008.12.026.

[36] R. E. Morris, M. H. Hammond, J. A. Cramer, K. J. Johnson, B. C. Giordano, K. E. Kramer, S. L. Rose-Pehrsson, Rapid fuel quality surveillance through chemometric modeling of near-infrared spectra, Energy Fuels 23 (3) (2009) 1610–1618. doi:10.1021/ef800869t.

[37] G. Veras, A. de Araujo Gomes, A. C. da Silva, A. L. B. de Brito, P. B. A. de Almeida, E. P. de Medeiros, Classification of biodiesel using NIR spectrometry and multivariate techniques, Talanta 83 (2) (2010) 565–568. doi:10.1016/j.talanta.2010.09.060.

[38] A. L. Tomren, T. Barth, K. Folgerø, Multivariate analysis of crude oil composition and fluid properties used in multiphase flow metering (MFM), Energy Fuels 26 (9) (2012) 5679–5688. doi:10.1021/ef300620r.

[39] G. N. Merberg, Evaluation of an octane analyzer, American Laboratory 28 (13) (1996) 68–69. URL http://www.zeltex.com/eval.html

[40] IROX 2000 gasoline analyzer, http://www.grabner-instruments.com/Products/FuelAnalysis/irox2000.a Accessed: 2015-11-05.

[41] W. J. Cannella, M. Foster, G. Gunter, W. R. Leppard, , Tech. Rep. CRC Report No. AVFL-24, Coordinating Research Council (Jul. 2014). URL

[42] P. L. Perez, A. L. Boehman, Experimental investigation of the autoignition behavior of surrogate gasoline fuels in a constant-volume combustion bomb apparatus and its relevance to HCCI combustion, Energy Fuels 26 (10) (2012) 6106–6117. doi:10.1021/ef300503b.

[43] T. M. Foong, K. J. Morganti, M. J. Brear, G. da Silva, Y. Yang, F. L. Dryer, The octane numbers of ethanol blended with gasoline and its surrogates, Fuel 115 (2014) 727–739. doi:10.1016/j.fuel.2013.07.105.

[44] I. Hunwartzen, Modification of CFR test engine unit to determine octane numbers of pure alcohols and gasoline-alcohol blends, SAE Technical Paper 820002 (1989). doi:10.4271/820002.

[45] J. E. Anderson, T. G. Leone, M. H. Shelby, T. J. Wallington, J. J. Bizub, M. Foster, M. G. Lynskey, D. Polovina, Octane numbers of ethanol-gasoline blends: Measurements and novel estimation method from molar composition, SAE Technical Paper 2012-04-16 (2012). doi:10.4271/2012-01-1274.

[46] J. Scherzer, Octane-enhancing, zeolitic FCC catalysts: Scientific and technical aspects, Catal Rev: Sci Eng 31 (3) (1989) 215–354. doi:10.1080/01614948909349934.

[47] API data book values—pure component hydrocarbon database, http://inside.mines.edu/ jjechura/Common/PureComponentData.xls, accessed: 2016-04-01 (2016).

[48] F. A. Carey, R. J. Sundberg, Advanced Organic Chemistry, Part A: Structure and Mechanisms, 5th Edition, Springer Science+Business Media, New York, 2007.

[49] K. Owen, T. Coley, Automotive Fuels Handbook, SAE International, Warrendale, PA, 1990.

[50] T. A. Albahri, Structural group contribution method for predicting the octane number of pure hydrocarbon liquids, Ind Eng Chem Res 42 (3) (2003) 657–662. doi:10.1021/ie020306+.

[51] D. Bradley, C. Morley, Autoignition in spark-ignition engines, in: M. J. Pilling (Ed.), Low-temperature Combustion and Autoignition, Vol. 35 of Comprehensive Chemical Kinetics, Elsevier, 1997, Ch. 7, pp. 661–760. doi:10.1016/S0069-8040(97)80022-2.

[52] K. N. Rao, Molecular Spectroscopy: Modern Research, Elsevier, 2012.

[53] J. E. Bertie, C. D. Keefe, R. N. Jones, Infrared intensities of liquids VIII. accurate baseline correction of transmission spectra of liquids for computation of absolute intensities, and the 1036 cm^{-1} band of benzene as a potential intensity standard, Can J Chem 69 (11) (1991) 1609–1618. doi:10.1139/v91-236.

[54] J. E. Bertie, R. N. Jones, Y. Apelblat, C. D. Keefe, Infrared intensities of liquids XIII: Accurate optical constants and molar absorption coefficients between 6500 and 435 cm^{-1} of toluene at 25°C, from spectra recorded in several laboratories, Appl Spectrosc 48 (1) (1994) 127–143.

[55] C. D. Keefe, Computer programs for the determination of optical constants from transmission spectra and the study of absolute absorption intensities, J Mol Struct 641 (2–3) (2002) 165–173. doi:10.1016/S0022-2860(02)00184-9.

[56] J. M. Porter, Laser-based diagnostics for hydrocarbon fuels in the liquid and vapor phases, Ph.D. thesis, Stanford University (2009).

[57] J. M. Porter, J. B. Jeffries, R. K. Hanson, Mid-infrared absorption measurements of liquid hydrocarbon fuels near 3.4 μm, J Quant Spectrosc Radiat Transfer 110 (18) (2009) 2135–2147. doi:10.1016/j.jqsrt.2009.05.017.

[58] I. Jolliffe, Principal component analysis, in: Wiley StatsRef: Statistics Reference Online, John Wiley & Sons, 2014. doi:10.1002/9781118445112.stat06472.

[59] S. Corsetti, F. M. Zehentbauer, D. McGloin, J. Kiefer, Characterization of gasoline/ethanol blends by infrared and excess infrared spectroscopy, Fuel 141 (2015) 136–142. doi:10.1016/j.fuel.2014.10.025.

[60] H. C. Van Ness, J. Van Winkle, H. H. Richtol, H. B. Hollinger, Infrared spectra and the thermodynamics of alcohol-hydrocarbon systems, J. Phys. Chem. 71 (6) (1967) 1483–1494.

[61] J. T. Reilly, A. Thomas, A. R. Gibson, C. Y. Luebehusen, M. D. Donohue, Analysis of the self-association of aliphatic alcohols using Fourier transform infrared (FT-IR) spectroscopy, Ind. Eng. Chem. Res. 52 (2013) 14456–14462. doi:10.1021/ie302174r.

[62] S. M. Sarathy, G. Kukkadapu, M. Mehl, W. Wang, T. Javed, S. Park, M. a. Oehlschlaeger, A. Farooq, W. J. Pitz, C. J. Sung, Ignition of alkane-rich FACE gasoline fuels and their surrogate mixtures, Proceedings of the Combustion Institute 35 (1) (2014) 249–257. doi:10.1016/j.proci.2014.05.122.
URL http://dx.doi.org/10.1016/j.proci.2014.05.122

[63] A. Ahmed, G. Goteng, V. S. B. Shankar, K. Al-Qurashi, W. L. Roberts, S. M. Sarathy, A computational methodology for formulating gasoline surrogate fuels with accurate physical and chemical kinetic properties, Fuel 143 (2015) 290–300. doi:10.1016/j.fuel.2014.11.022.
URL http://dx.doi.org/10.1016/j.fuel.2014.11.022

[64] U.S. Energy Information Administration, Monthly energy review july 2017, DOE/EIA-0035(2017/7), Washington, DC, table 1.3 (2017).

[65] U.S. Energy Information Administration, Annual Energy Outlook 2017, DOE/EIA-0383(2017), Washington, DC, table: Total Energy Supply, Disposition, and Price Summary (2017).

[66] U.S. Energy Information Administration, Annual Energy Outlook 2017, DOE/EIA-0383(2017), Washington, DC, table: Light-Duty Vehicle Stock by Technology Type (2017).

[67] J. E. Dec, M. Sjöberg, Isolating the effects of fuel chemistry on combustion phasing in an hcci engine and the potential of fuel stratification for ignition control, Tech. rep., SAE Technical Paper (2004).

[68] K. E. Niemeyer, S. R. Daly, W. J. Cannella, C. L. Hagen, A novel fuel performance index for low-temperature combustion engines based on operating envelopes in light-duty driving cycle simulations, J. Eng. Gas Turbines Power 137 (10) (2015) 101601. doi:10.1115/1.4029948.

[69] R. C. Costa, J. R. Sodré, Hydrous ethanol vs. gasoline-ethanol blend: Engine performance and emissions, Fuel 89 (2) (2010) 287–293.

[70] W. J. Pitz, N. P. Cernansky, F. L. Dryer, F. Egolfopoulos, J. Farrell, D. G. Friend, H. Pitsch, Development of an experimental database and chemical kinetic models for surrogate gasoline fuels, Tech. rep., SAE Technical Paper (2007).

[71] C. J. Mueller, W. J. Cannella, T. J. Bruno, B. Bunting, H. D. Dettman, J. a. Franz, M. L. Huber, M. Natarajan, W. J. Pitz, M. a. Ratcliff, K. Wright, Methodology for formulating diesel surrogate fuels with accurate compositional, ignition-quality, and volatility characteristics, Energy and Fuels 26 (6) (2012) 3284–3303. doi:10.1021/ef300303e.

[72] A. Ahmed, G. Goteng, V. S. B. Shankar, K. Al-Qurashi, W. L. Roberts, S. M. Sarathy, A computational methodology for formulating gasoline surrogate fuels with accurate physical and chemical kinetic properties, Fuel 143 (2015) 290–300. doi:10.1016/j.fuel.2014.11.022.
URL http://dx.doi.org/10.1016/j.fuel.2014.11.022

[73] S. M. Sarathy, G. Kukkadapu, M. Mehl, T. Javed, A. Ahmed, N. Naser, A. Tekawade, G. Kosiba, M. AlAbbad, E. Singh, S. Park, M. A. Rashidi, S. H. Chung, W. L. Roberts, M. a. Oehlschlaeger, C.-J. Sung, A. Farooq, Compositional effects on the ignition of FACE gasolines, Combustion and Flame 169 (2016) 171–193. doi:10.1016/j.combustflame.2016.04.010.
URL http://linkinghub.elsevier.com/retrieve/pii/S0010218016300591

[74] T. Javed, A. Ahmed, L. Lovisotto, G. Issayev, J. Badra, S. M. Sarathy, A. Farooq, Ignition studies of two low-octane gasolines, Combustion and Flame 185 (2017) 152–159. doi:10.1016/j.combustflame.2017.07.006.
URL http://dx.doi.org/10.1016/j.combustflame.2017.07.006

[75] B. Shankar, V. Shankar, M. B. Sajid, K. Al-Qurashi, N. Atef, I. Al Khesho, A. Ahmed, S.-H. Chung, W. L. Roberts, K. Morganti, et al., Primary reference fuels (prfs) as surrogates for low sensitivity gasoline fuels, SAE Technical Paper Series.

[76] M. Mehl, J. Y. Chen, W. J. Pitz, S. M. Sarathy, C. K. Westbrook, An approach for formulating surrogates for gasoline with application toward a reduced surrogate mechanism for CFD engine modeling, Energy and Fuels 25 (11) (2011) 5215–5223. doi:10.1021/ef201099y.

[77] P. Ghosh, K. J. Hickey, S. B. Jaffe, Development of a detailed gasoline composition-based octane model, Industrial and Engineering Chemistry Research 45 (1) (2006) 337–345. doi:10.1021/ie050811h.

[78] S. M. Sarathy, G. Kukkadapu, M. Mehl, W. Wang, T. Javed, S. Park, M. a. Oehlschlaeger, A. Farooq, W. J. Pitz, C. J. Sung, Ignition of alkane-rich FACE gasoline fuels and their surrogate mixtures, Proceedings of the Combustion Institute 35 (1) (2014) 249–257. doi:10.1016/j.proci.2014.05.122.
URL http://dx.doi.org/10.1016/j.proci.2014.05.122

[79] E. Singh, J. Badra, M. Mehl, S. M. Sarathy, Chemical kinetic insights into the octane number and octane sensitivity of gasoline surrogate mixtures, Energy & Fuels 31 (2) (2017) 1945–1960.

[80] S. R. Daly, K. E. Niemeyer, W. J. Cannella, C. L. Hagen, Predicting fuel research octane number using fourier-transform infrared absorption spectra of neat hydrocarbons, Fuel.

[81] V. Knop, M. Loos, C. Pera, N. Jeuland, A linear-by-mole blending rule for octane numbers of n-heptane/iso-octane/toluene mixtures, Fuel 115 (2014) 666–673. doi:10.1016/j.fuel.2013.07.093.

[82] D. G. Goodwin, H. K. Moffat, R. L. Speth, Cantera: An object-oriented software toolkit for chemical kinetics, thermodynamics, and transport processes, http://www.cantera.org, version 2.3.0 (2017). doi:10.5281/zenodo.170284.

[83] E. W. Lemmon, M. L. Huber, M. O. McLinden, NIST reference fluid thermodynamic and transport properties database—REFPROP: Version 9.1, https://www.nist.gov/refprop (Apr. 2013).

[84] B. J. Thelen, python-refprop, https://github.com/BenThelen/python-refprop, commit a4e58ae (2016).

[85] M. L. Huber, Creating thermodynamic reference files for refprop, Personal communication, title: Theory and Modeling of Fluids Group, NIST (2016).

[86] S. Daly, K. Niemeyer, C. Hagen, REFPROP thermodynamic reference files: 1-hexene, 1-pentene, 1,2,4-trimethylbenzene, 1,3,5-trimethylbenzene, 2-methylexane, https://doi.org/10.6084/m9.figshare.5272411.v4 (2017). doi:10.6084/m9.figshare.5272411.v4.

[87] T. J. Bruno, L. S. Ott, B. L. Smith, T. M. Lovestead, Complex fluid analysis with the advanced distillation curve approach (2009).

[88] T. J. Bruno, L. S. Ott, T. M. Lovestead, M. L. Huber, The composition-explicit distillation curve technique: Relating chemical analysis and physical properties of complex fluids, Journal of Chromatography A 1217 (16) (2010) 2703–2715.

[89] T. J. Bruno, L. S. Ott, T. M. Lovestead, M. L. Huber, Relating complex fluid composition and thermophysical properties with the advanced distillation curve approach, Chemical Engineering & Technology 33 (3) (2010) 363–376.

[90] J. L. Burger, N. Schneider, T. J. Bruno, Application of the advanced distillation curve method to fuels for advanced combustion engine gasolines, Energy and Fuels 29 (7) (2015) 4227–4235. doi:10.1021/acs.energyfuels.5b00749.

[91] E. Jones, T. Oliphant, P. Peterson, others, SciPy: Open source scientific tools for Python, [Online; accessed 2017-01-06] (2001–).
URL http://www.scipy.org/

[92] C. Zhu, R. H. Byrd, P. Lu, J. Nocedal, Algorithm 778: L-bfgs-b: Fortran subroutines for large-scale bound-constrained optimization, ACM Transactions on Mathematical Software (TOMS) 23 (4) (1997) 550–560.

[93] J. E. Dec, Advanced compression-ignition engines - Understanding the in-cylinder processes, Proceedings of the Combustion Institute 32 II (2) (2009) 2727–2742. doi:10.1016/j.proci.2008.08.008.
URL http://dx.doi.org/10.1016/j.proci.2008.08.008

[94] K. E. Niemeyer, S. R. Daly, W. J. Cannella, C. L. Hagen, Investigation of the LTC fuel performance index for oxygenated reference fuel blends, Fuel 155 (x) (2015) 14–24. doi:10.1016/j.fuel.2015.04.010.
URL http://linkinghub.elsevier.com/retrieve/pii/S0016236115003932

[95] F. Pedregosa, G. Varoquaux, A. Gramfort, V. Michel, B. Thirion, O. Grisel, M. Blondel, P. Prettenhofer, R. Weiss, V. Dubourg, J. Vanderplas, A. Passos, D. Cournapeau, M. Brucher, M. Perrot, E. Duchesnay, Scikit-learn: Machine learning in Python, Journal of Machine Learning Research 12 (2011) 2825–2830.

[96] O. Devos, C. Ruckebusch, A. Durand, L. Duponchel, J. P. Huvenne, Support vector machines (SVM) in near infrared (NIR) spectroscopy: Focus on parameters optimization and model interpretation, Chemometrics and Intelligent Laboratory Systems 96 (1) (2009) 27–33. doi:10.1016/j.chemolab.2008.11.005.
URL http://dx.doi.org/10.1016/j.chemolab.2008.11.005

[97] J. Luts, F. Ojeda, R. Van de Plas Raf, B. De Moor, S. Van Huffel, J. a. K. Suykens, A tutorial on support vector machine-based methods for classification problems in chemometrics, Analytica Chimica Acta 665 (2) (2010) 129–145. doi:10.1016/j.aca.2010.03.030.
URL http://dx.doi.org/10.1016/j.aca.2010.03.030

[98] R. Kohavi, A study of cross-validation and bootstrap for accuracy estimation and model selection, in: Ijcai, Vol. 14, Montreal, Canada, 1995, pp. 1137–1145.

[99] R. B. Rao, G. Fung, R. Rosales, On the dangers of cross-validation. an experimental evaluation, in: Proceedings of the 2008 SIAM International Conference on Data Mining, SIAM, 2008, pp. 588–596.

[100] J. D. Rodriguez, A. Perez, J. A. Lozano, Sensitivity analysis of k-fold cross validation in prediction error estimation, IEEE transactions on pattern analysis and machine intelligence 32 (3) (2010) 569–575.

[101] S. R. Daly, K. E. Niemeyer, W. J. Cannella, C. L. Hagen, Face gasoline surrogates formulated by an enhanced multivariate optimization framework, *Fuel*, Submitted (2018).

[102] M. Chaos, A. Kazakov, Z. Zhao, F. L. Dryer, A high-temperature chemical kinetic model for primary reference fuels, International Journal of Chemical Kinetics 39 (7) (2007) 399–414.

[103] M. Chaos, Z. Zhao, A. Kazakov, P. Gokulakrishnan, M. Angioletti, F. Dryer, A prf+ toluene surrogate fuel model for simulating gasoline kinetics, in: 5th US combustion Meeting, 2007, pp. 25–28.

[104] J. Li, A. Kazakov, M. Chaos, F. Dryer, Chemical kinetics of ethanol oxidation, in: 5th US combustion meeting, 2007, pp. 25–28.

[105] F. M. Haas, M. Chaos, F. L. Dryer, Low and intermediate temperature oxidation of ethanol and ethanol–prf blends: An experimental and modeling study, Combustion and flame 156 (12) (2009) 2346–2350.

[106] B. W. Weber, W. J. Pitz, M. Mehl, E. J. Silke, A. C. Davis, C.-J. Sung, Experiments and modeling of the autoignition of methylcyclohexane at high pressure, Combustion and Flame 161 (8) (2014) 1972–1983.

[107] L. S. S. Manin, Julien; Pickett, Measurements of fuel concentration in evaporative diesel sprays at 100 khz, ILASS âĂŞ Europe, 27th Annual Conference on Liquid Atomization and Spray Systems, Brighton, UK.

[108] F. R. Westlye, K. Penney, A. Ivarsson, L. M. Pickett, J. Manin, S. A. Skeen, Diffuse back-illumination setup for high temporally resolved extinction imaging, Applied optics 56 (17) (2017) 5028–5038.

[109] M. P. Musculus, K. Kattke, Entrainment waves in diesel jets, SAE International Journal of Engines 2 (1) (2009) 1170–1193.

[110] N. Sivaraman, R. Dhamodaran, I. Kaliappan, T. Srinivasan, P. Vasudeva Rao, C. Mathews, Solubility of c70 in organic solvents, Fullerenes, Nanotubes, and Carbon Nanostructures 2 (3) (1994) 233–246.

[111] K. N. Semenov, N. A. Charykov, V. A. Keskinov, A. K. Piartman, A. A. Blokhin, A. A. Kopyrin, Solubility of light fullerenes in organic solvents, Journal of Chemical & Engineering Data 55 (1) (2009) 13–36.

[112] D. L. Siebers, Liquid-phase fuel penetration in diesel sprays, Tech. rep., SAE technical paper (1998).

[113] J. Joutsensaari, P. Ahonen, U. Tapper, E. Kauppinen, J. Laurila, V.-T. Kuokkala, Generation of nanophase fullerene particles via aerosol routes, Synthetic metals 77 (1-3) (1996) 85–88.

[114] C. Pan, M. Chandrasekharaiah, D. Agan, R. Hauge, J. Margrave, Determination of sublimation pressures of a fullerene (c60/c70) solid solution, The Journal of Physical Chemistry 96 (16) (1992) 6752–6755.

[115] L. M. Pickett, J. Manin, C. L. Genzale, D. L. Siebers, M. P. Musculus, C. A. Idicheria, Relationship between diesel fuel spray vapor penetration/dispersion and local fuel mixture fraction, SAE International Journal of Engines 4 (2011-01-0686) (2011) 764–799.

[116] I. Renge, Solvent effects on the absorption maxima of fullerenes c60 and c70, The Journal of Physical Chemistry 99 (43) (1995) 15955–15962.

[117] J. P. Hare, H. W. Kroto, R. Taylor, Preparation and uv/visible spectra of fullerenes c60 and c70, Chemical physics letters 177 (4-5) (1991) 394–398.

[118] Q. Gong, Y. Sun, Z. Huang, X. Zhou, Z. Gu, D. Qiang, Optical and thermodynamic properties of isolated fullerene molecules, Journal of Physics B: Atomic, Molecular and Optical Physics 29 (21) (1996) 4981.

[119] F. Cataldo, S. Iglesias-Groth, Y. Hafez, On the molar extinction coefficients of the electronic absorption spectra of c60 and c70 fullerenes radical cation, European Chemical Bulletin 2 (12) (2013) 1013–1018.

[120] H. S. Application Laboratory Team, An ellipsometric study of the optical constants of c60 c70 thin films, Application Note, Material Science SE35 70âĂŞ72.
URL http://www.horiba.com/fileadmin/uploads/Scientific/Documents/TFilm/AN$_S$E35.pdf

[121] P.-F. Coheur, M. Carleer, R. Colin, The absorption cross sections of and in the visible-uv region, Journal of Physics B: Atomic, Molecular and Optical Physics 29 (21) (1996) 4987.

[122] M. Sjöberg, J. E. Dec, N. P. Cernansky, Potential of Thermal Stratification and Combustion Retard for Reducing Pressure-Rise Rates in HCCI Engines, Based on Multi-Zone Modeling and Experiments 2005 (724). doi:10.4271/2005-01-0113.
URL http://papers.sae.org/2005-01-0113/

[123] B. W. Knox, C. L. Genzale, Reduced-order numerical model for transient reacting diesel sprays with detailed kinetics, International Journal of Engine Research 17 (3) (2016) 261–279.

[124] J. Farrell, Co-optimization of fuels engines (co-optima) initiative: Recent progress on light-duty boosted spark-ignition fuels/engines.

[125] B. W. Weber, C.-J. Sung, M. W. Renfro, On the uncertainty of temperature estimation in a rapid compression machine, Combustion and Flame 162 (6) (2015) 2518 – 2528. doi:https://doi.org/10.1016/j.combustflame.2015.03.001.
URL http://www.sciencedirect.com/science/article/pii/S0010218015000760

[126] B. T. Fisher, J. C. Allen, R. L. Hancock, J. A. Bittle, Evaluating the Potential of a Direct-Injection Constant-Volume Combustion Chamber as a Tool to Validate Chemical-Kinetic Models for Liquid Fuels, Combustion Science and Technology 189 (1) (2017) 1–23. doi:10.1080/00102202.2016.1193015.

[127] A. Alfazazi, O. A. Kuti, N. Naser, S. H. Chung, S. M. Sarathy, Two-stage Lagrangian modeling of ignition processes in ignition quality tester and constant volume combustion chambers, Fuel 185 (2016) 589–598. doi:10.1016/j.fuel.2016.08.017.
URL http://dx.doi.org/10.1016/j.fuel.2016.08.017

[128] R. N. Dahms, G. A. Paczko, S. A. Skeen, L. M. Pickett, Understanding the ignition mechanism of high-pressure spray flames, Proceedings of the Combustion Institute 36 (2) (2017) 2615–2623.

[129] D. L. Siebers, Scaling liquid-phase fuel penetration in diesel sprays based on mixing-limited vaporization, Tech. rep., SAE technical paper (1999).

[130] J. V. Pastor, R. Payri, J. M. Garcia-Oliver, J.-G. Nerva, Schlieren Measurements of the ECN-Spray A Penetration under Inert and Reacting Conditionsdoi:10.4271/2012-01-0456.
URL http://papers.sae.org/2012-01-0456/

[131] L. M. Pickett, S. Kook, T. C. Williams, Visualization of Diesel Spray Penetration, Cool-Flame, Ignition, High-Temperature Combustion, and Soot Formation Using High-Speed Imaging, SAE International Journal of Engines 2 (1) (2009) 2009–01–0658. doi:10.4271/2009-01-0658.
URL http://papers.sae.org/2009-01-0658/

[132] J. Abraham, L. M. Pickett, Computed and measured fuel vapor distribution in a diesel spray, Atomization and sprays 20 (3).

[133] S. Som, G. D'Errico, D. Longman, T. Lucchini, Comparison and standardization of numerical approaches for the prediction of non-reacting and reacting diesel sprays. no. 2012-01-1263.

[134] S. Daly, E. Cenker, L. Pickett, S. Skeen, The effects of injector temperature on spray characteristics in heavy-duty diesel sprays. no. 2018-01-0284., SAE Technical Paper.

[135] R. Payri, J. Gimeno, J. Cuisano, J. Arco, Hydraulic characterization of diesel engine single-hole injectors, Fuel 180 (2016) 357–366.

[136] F. L. D. M. Chaos, A. Kazakov, Z. Zhao, A high-temperature chemical kinetic model for primary reference fuels, Int. J. Chem. Kinet (39) (2007) 399–414.

[137] F. L. D. M. Chaos, Z. Zhao, A. Kazakov, P. Gokulakrishnan, M. Angioletti, A PRF+toluene surrogate fuel model for simulating gasoline kinetics, in: Fifth Joint Meeting of the US Sections of the Combustion Institute, Paper E26.

[138] F. L. D. J. Li, A. Kazakov, M. Chaos, Chemical kinetics of ethanol oxidation, in: Fifth Joint Meeting of the US Sections of the Combustion Institute, Paper C28.

[139] F. M. Haas, M. Chaos, F. L. Dryer, Low and intermediate temperature oxidation of ethanol and ethanol-PRF blends: An experimental and modeling study, Combustion and Flame 156 (12) (2009) 2346–2350. doi:10.1016/j.combustflame.2009.08.012.
URL http://dx.doi.org/10.1016/j.combustflame.2009.08.012

[140] M. Mehl, W. J. Pitz, C. K. Westbrook, H. J. Curran, Kinetic modeling of gasoline surrogate components and mixtures under engine conditions, Proceedings of the Combustion Institute 33 (1) (2011) 193–200.

[141] H. J. Curran, P. Gaffuri, W. J. Pitz, C. K. Westbrook, A comprehensive modeling study of n-heptane oxidation, Combustion and flame 114 (1-2) (1998) 149–177.

[142] N. Naser, S. M. Sarathy, S. H. Chung, Estimating fuel octane numbers from homogeneous gas-phase ignition delay times, Combustion and Flame 188 (2018) 307–323.

[143] R. Di Sante, Measurements of the auto-ignition of n-heptane/toluene mixtures using a rapid compression machine, Combustion and flame 159 (1) (2012) 55–63.

[144] X. Lü, Y. Hou, L. Zu, Z. Huang, Experimental study on the auto-ignition and combustion characteristics in the homogeneous charge compression ignition (hcci) combustion operation with ethanol/n-heptane blend fuels by port injection, Fuel 85 (17-18) (2006) 2622–2631.

[145] M. Mehl, W. J. Pitz, C. K. Westbrook, H. J. Curran, Kinetic modeling of gasoline surrogate components and mixtures under engine conditions, Proceedings of the Combustion Institute 33 (1) (2011) 193 – 200. doi:https://doi.org/10.1016/j.proci.2010.05.027.
URL http://www.sciencedirect.com/science/article/pii/S1540748910000787

[146] K. Fieweger, R. Blumenthal, G. Adomeit, Self-ignition of si engine model fuels: a shock tube investigation at high pressure, Combustion and Flame 109 (4) (1997) 599–619.

[147] L. M. Pickett, S. Kook, T. C. Williams, Visualization of diesel spray penetration, cool-flame, ignition, high-temperature combustion, and soot formation using high-speed imaging, SAE International Journal of Engines 2 (2009-01-0658) (2009) 439–459.

APPENDICES

Appendix A: Chapter 2 Supporting Material

A.1   Lists of fuel mixtures

This study considered a total of 134 fuel blends consisting of various mixtures n-heptane, isooctane, methylcyclohexane, toluene, 1-hexene, and ethanol taken from the literature [19, 20, 42, 43]. Tables A.1–A.5 provide the makeup of these mixtures in terms of volume fraction, as well as the RONs measured experimentally by the sources.

ID	n-heptane (vol. %)	isooctane (vol. %)	MCH (vol. %)	toluene (vol. %)	1-hexene (vol. %)	RON
2	60	10	10	10	10	41.0
3	50	50				48.3
4	50		50			43.8
5	50			50		64.1
6	50				50	40.3
7	20	20	20	20	20	75.0
8	10	60	10	10	10	87.1
10	10	10	60	10	10	74.4
11		50	50			86.4
13	10	10	10	60	10	95.7
14		50		50		110.5
15			50	50		91.5
16	10	10	10	10	60	75.8
18		50			50	88.2
19			50		50	74.2
20				50	50	92.5

Table A.1: Blends of n-heptane, isooctane, methylcyclohexane (MCH), toluene, and 1-hexene considered in this work taken from Perez et al. [42].

ID	n-heptane (vol. %)	isooctane (vol. %)	toluene (vol. %)	ethanol (vol. %)	RON
PRF20	80	20			20
PRF40	60	40			40
PRF55	45	55			55
PRF85	15	85			85
H20T10	20	70	10		82.8
H20T20	20	60	20		84.9
H20T40	20	40	40		89.8
H20T60	20	20	60		93.9
PRF80	80	20			80
H20E1	20	79		1	80.5
H20E5	20	75		5	84.4
H20E10	20	70		10	87.9
H20E20	20	60		20	94.1
PRF70	70	30			70
H30E1	30	69		1	70.6
H30E5	30	65		5	73.2
H30E10	30	60		10	78.7
H60E20	30	50		20	85.1
H60E40	60			40	71.4
H55E45	55			45	78
H50E50	50			50	84.7
H45E55	45			55	89.7
H40E60	40			60	94.4
T1	40	45	10	5	67.1
T2	20	50	10	20	94.7
T3	20	30	30	20	97
T4	40	10	30	20	80.8
T5	30	45	20	5	79.6
T6	30	27.5	30	12.5	85.3
T7	30	37.5	20	12.5	83.8
T8	40	25	30	5	71.8
T9	30	47.5	10	12.5	81.6
T10	20	45	30	5	90.2
T11	30	37.5	20	12.5	83.8
T12	40	30	10	20	78.3
T13	20	65	10	5	86.1
T14	40	27.5	20	12.5	74.8
T15	20	47.5	20	12.5	92.3
T16	30	30	20	20	87.9
T17	30	37.5	20	12.5	83.8

Table A.2: Blends of n-heptane/isooctane (PRFs), n-heptane/isooctane/toluene, n-heptane/isooctane/ethanol, n-heptane/ethanol, and n-heptane/isooctane/toluene/ethanol considered in this work taken from Truedsson et al. [19, 20].

ID	n-heptane (vol. %)	isooctane (vol. %)	toluene (vol. %)	ethanol (vol. %)	RON
TE10			90	10	112.8
TE20			80	20	110.9
TE40			60	40	108.6
TE60			40	60	108.1
TE80			20	80	107.9
TRF91-15	12.4	72.6	15		91.0
TRF91-30	17	53.2	29.8		91.3
TRF91-45	20.3	34.7	45		91.1

Table A.3: Blends of toluene/ethanol and n-heptane/isooctane/toluene (TRF) considered in this work taken from Foong et al. [43].

ID	n-heptane (vol. %)	isooctane (vol. %)	ethanol (vol. %)	RON
PRF0-E30	70		30	54.3
PRF0-E40	60		40	69.7
PRF0-E50	50		50	83.8
PRF0-E60	40		60	94.7
PRF0-E70	30		70	101.6
PRF0-E80	20		80	104.7
PRF0-E90	10		90	106.5
PRF10-E20	72	8	20	45.9
PRF10-E30	63	7	30	61.1
PRF10-E40	54	6	40	75.6
PRF10-E50	45	5	50	87.6
PRF10-E60	36	4	60	96.6
PRF20-E20	64	16	20	53.3
PRF20-E30	56	14	30	67.4
PRF20-E40	48	12	40	80.7
PRF20-E50	40	10	50	91.5
PRF20-E60	32	8	60	99.1
PRF20-E80	16	4	80	105.8
PRF30-E10	63	27	10	46.5
PRF30-E20	56	24	20	60.8
PRF30-E30	49	21	30	74.2
PRF30-E40	42	18	40	85.5
PRF30-E50	35	15	50	94.7
PRF40-E10	54	36	10	55
PRF40-E20	48	32	20	68.5
PRF40-E30	42	28	30	80.6
PRF40-E40	36	24	40	90.4
PRF40-E50	30	20	50	97.9
PRF40-E60	24	16	60	102.7
PRF40-E80	12	8	80	106.6
PRF50-E10	45	45	10	63.8
PRF50-E20	40	40	20	75.8
PRF50-E30	35	35	30	86.4
PRF50-E40	30	30	40	94.5
PRF60-E10	36	54	10	72.6
PRF60-E20	32	48	20	83.5
PRF60-E30	28	42	30	92
PRF60-E40	24	36	40	98.9
PRF60-E60	16	24	60	105.5
PRF60-E80	8	12	80	107.6
PRF70-E10	27	63	10	80.9
PRF70-E20	24	56	20	90.3
PRF70-E30	21	49	30	97.4
PRF80-E10	18	72	10	89.5

PRF80-E20	16	64	20	97
PRF80-E40	12	48	40	105.7
PRF80-E60	8	32	60	107.7
PRF80-E80	4	16	80	108.3
PRF90-E5	9.5	85.5	5	94.1
PRF90-E10	9	81	10	97.6
PRF90-E20	8	72	20	103.6
PRF100-E10		90	10	106.8
PRF100-E20		80	20	109.4
PRF100-E40		60	40	110.2
PRF100-E60		40	60	109.6
PRF100-E80		20	80	109

Table A.4: Blends of n-heptane, isooctane, and ethanol considered in this work taken from Foong et al. [43].

| ID	n-heptane (vol. %)	isooctane (vol. %)	toluene (vol. %)	ethanol (vol. %)	RON
TRF91-15-E10	11.16	65.34	13.5	10	97.8
TRF91-15-E20	9.92	58.08	12	20	102.6
TRF91-15-E40	7.44	43.56	9	40	107.1
TRF91-15-E60	4.96	29.04	6	60	107.7
TRF91-15-E80	2.48	14.52	3	80	107.8
TRF91-30-E10	15.3	47.88	26.82	10	97
TRF91-30-E20	13.6	42.56	23.84	20	101.4
TRF91-30-E40	10.2	31.92	17.88	40	106
TRF91-30-E60	6.8	21.28	11.92	60	107.1
TRF91-30-E80	3.4	10.64	5.96	80	107.5
TRF91-45-E10	18.27	31.23	40.5	10	96
TRF91-45-E20	16.24	27.76	36	20	100.2
TRF91-45-E40	12.18	20.82	27	40	104.6
TRF91-45-E60	8.12	13.88	18	60	106.3
TRF91-45-E80	4.06	6.94	9	80	107.1

Table A.5: Blends of n-heptane, isooctane, toluene, and ethanol considered in this work taken from Foong et al. [43].

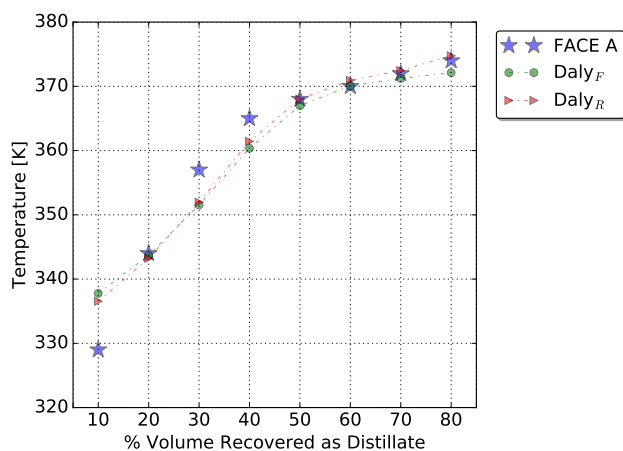# Appendix B: Chapter 3 Supporting Material
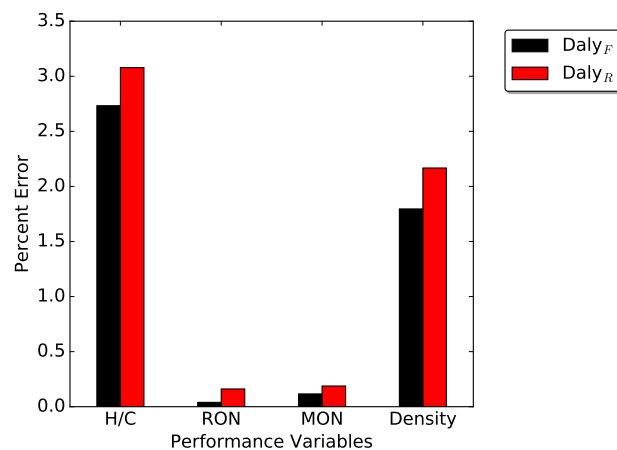
B.1 FACE Gasoline Surrogates
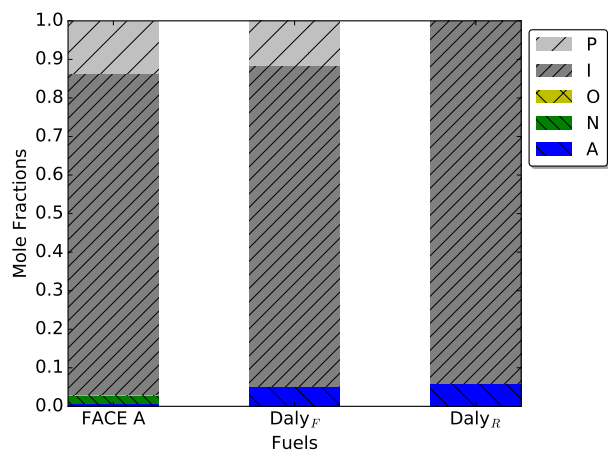
(a) Hydrocarbon class proportions
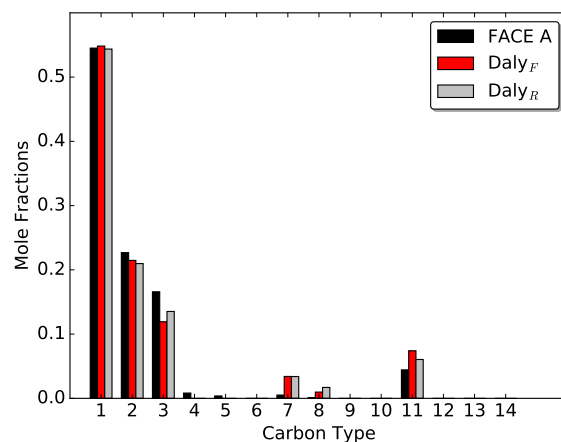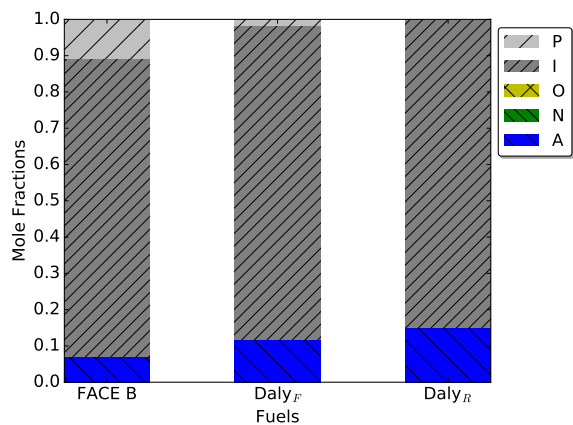
(b) C–C bond type proportions
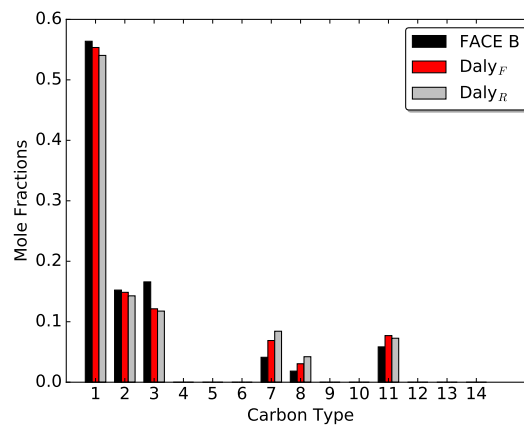
(c) Distillation characteristics

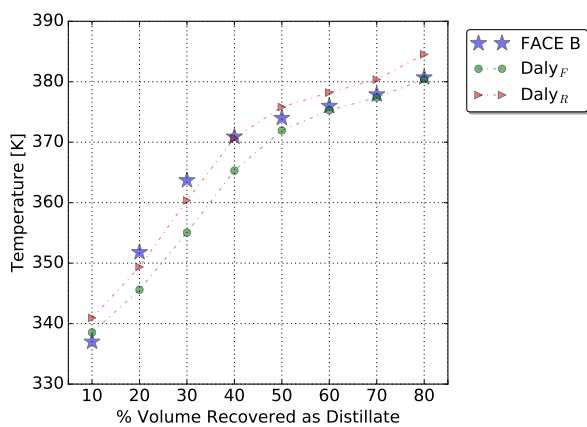(d) Percent error between H/C, RON, MON, and density

Figure B.1: Target property comparisons for FACE A and surrogates developed in this work.
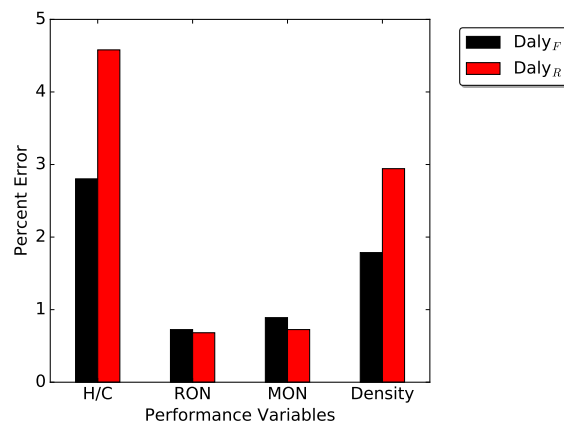
(a) Hydrocarbon class proportions
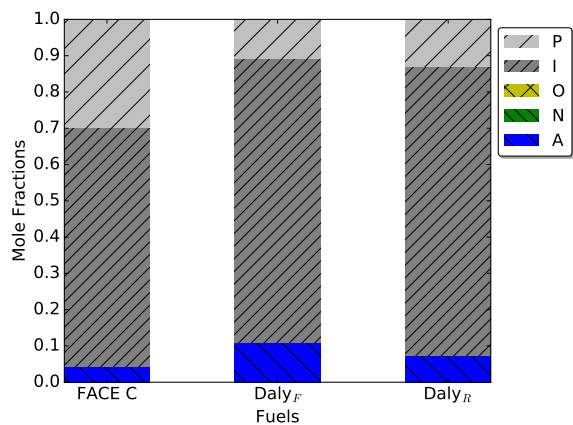
(b) C–C bond type proportions

(c) Distillation characteristics

(d) Percent error between H/C, RON, MON, and density

Figure B.2: Target property comparisons for FACE B and surrogates developed in this work.

(a) Hydrocarbon class proportions

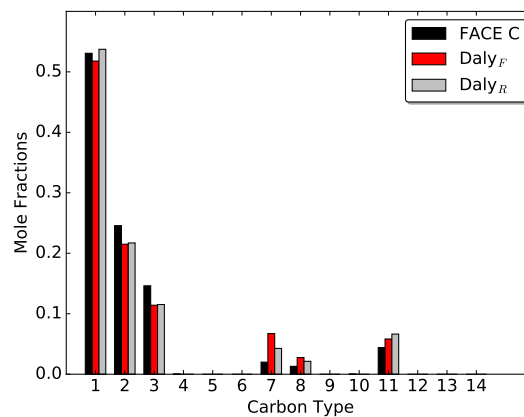(b) C–C bond type proportions

(c) Distillation characteristics

(d) Percent error between H/C, RON, MON, and density

Figure B.3: Target property comparisons for FACE C and surrogates developed in this work.

(a) Hydrocarbon class proportions

(b) C–C bond type proportions

(c) Distillation characteristics

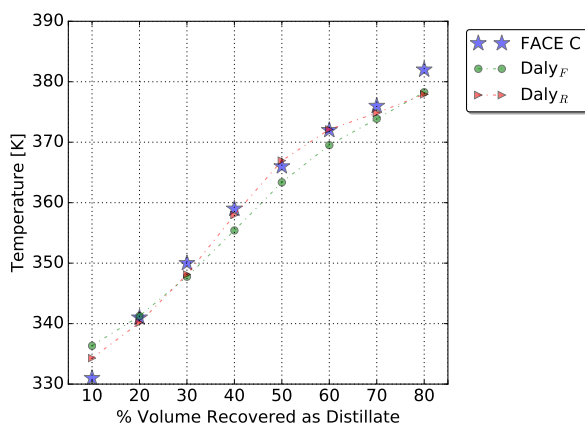(d) Percent error between H/C, RON, MON, and density

Figure B.4: Target property comparisons for FACE D and surrogates developed in this work.
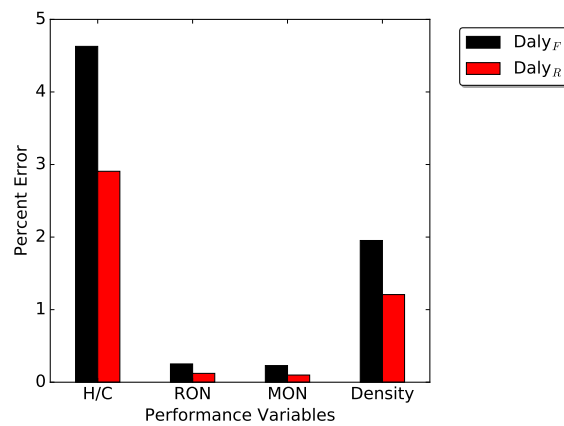
(a) Hydrocarbon class proportions

(b) C–C bond type proportions

(c) Distillation characteristics

(d) Percent error between H/C, RON, MON, and density

Figure B.5: Target property comparisons for FACE E and surrogates developed in this work.

(a) Hydrocarbon class proportions

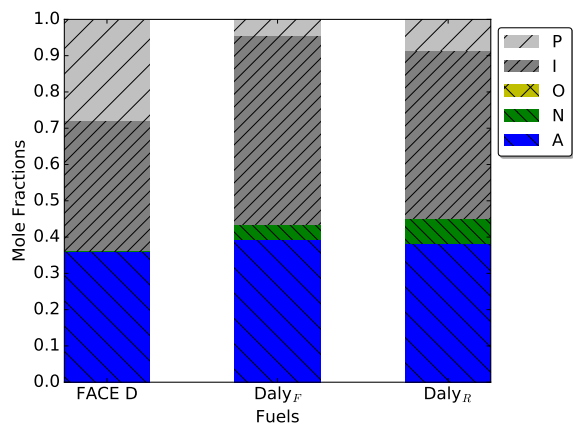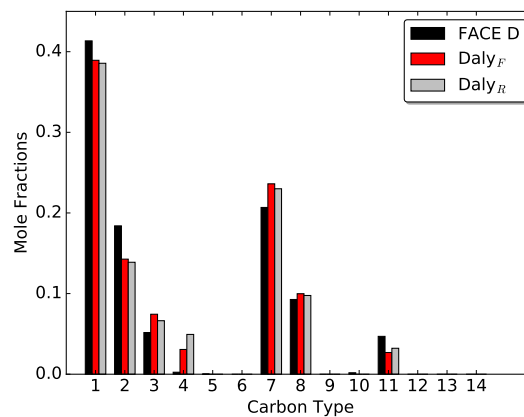(b) C–C bond type proportions

(c) Distillation characteristics

(d) Percent error between H/C, RON, MON, and density

Figure B.6: Target property comparisons for FACE F and surrogates developed in this work.

(a) Hydrocarbon class proportions

(b) C–C bond type proportions

(c) Distillation characteristics

(d) Percent error between H/C, RON, MON, and density

Figure B.7: Target property comparisons for FACE G and surrogates developed in this work.
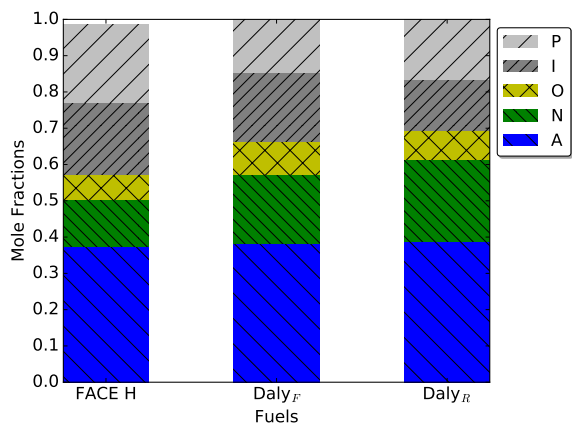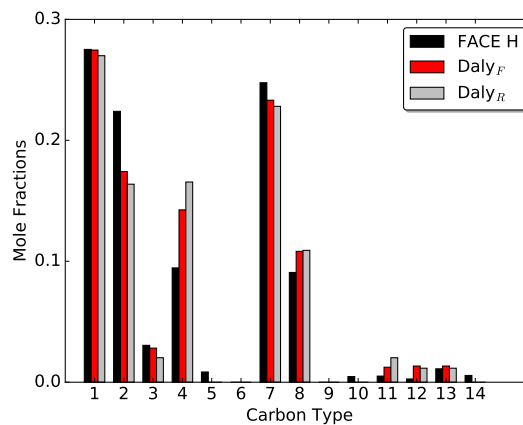
(a) Hydrocarbon class proportions

(b) C–C bond type proportions
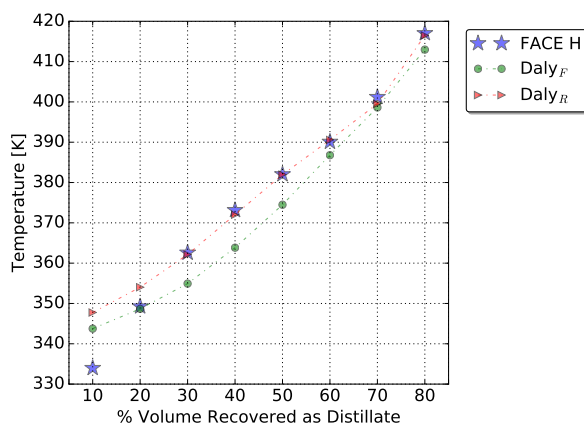
(c) Distillation characteristics
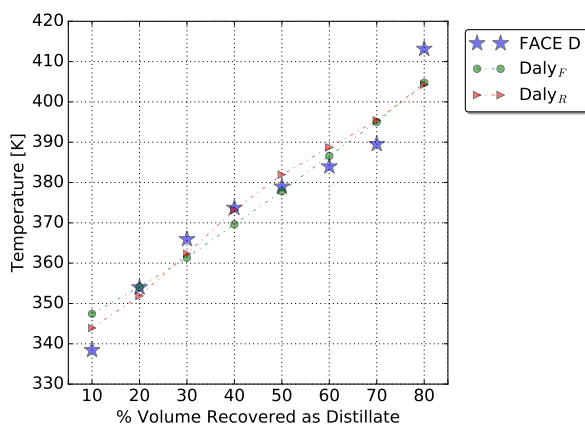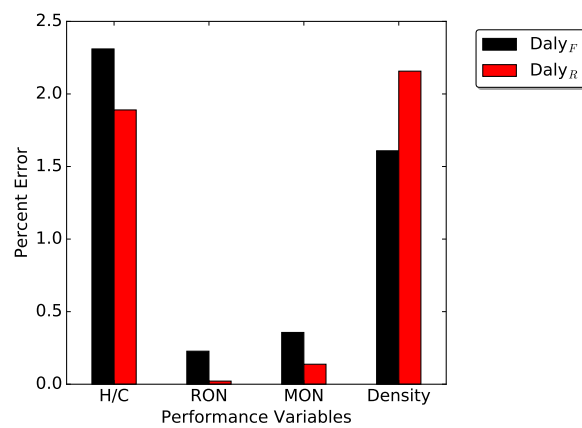

(d) Percent error between H/C, RON, MON, and density

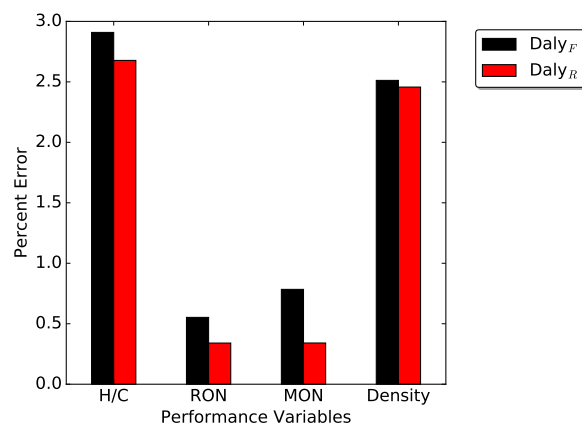Figure B.8: Target property comparisons for FACE H and surrogates developed in this work.
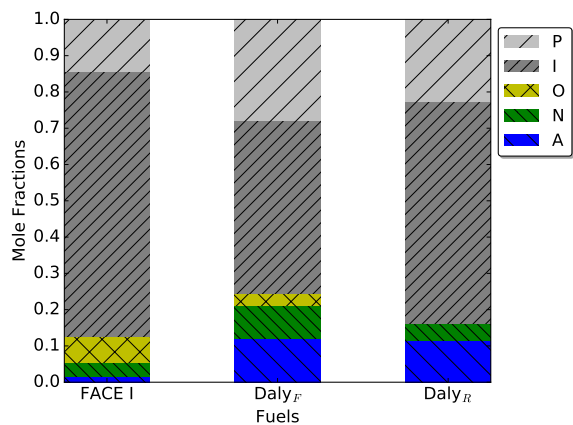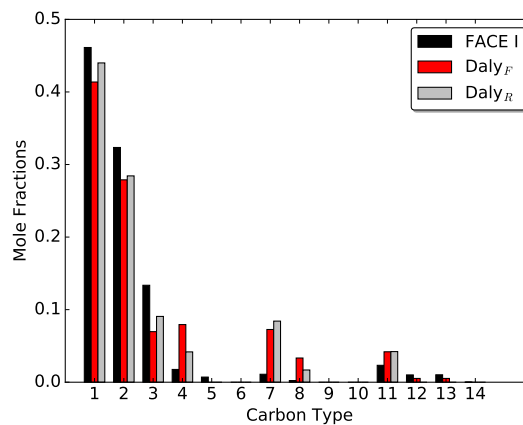
(a) Hydrocarbon class proportions
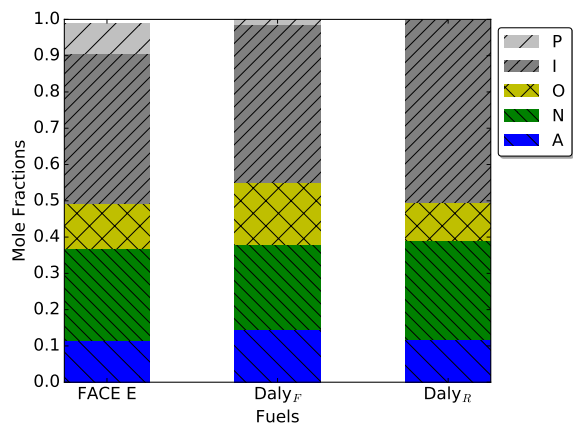
(b) C–C bond type proportions
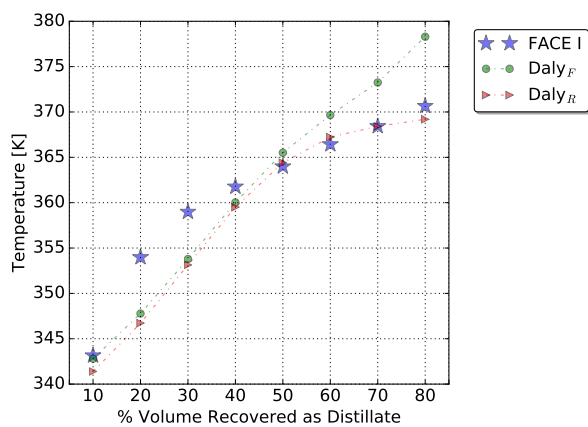
(c) Distillation characteristics
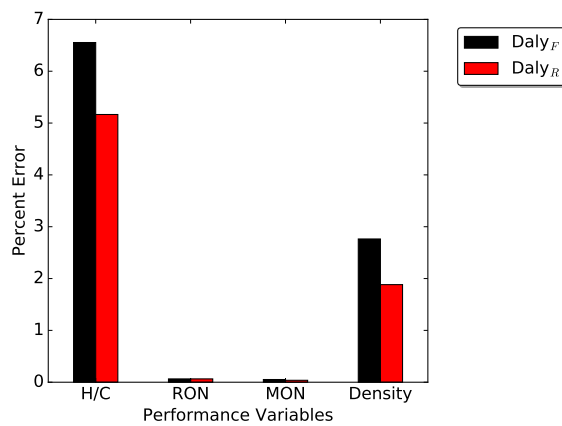
(d) Percent error between H/C, RON, MON, and density

Figure B.9: Target property comparisons for FACE I and surrogates developed in this work.
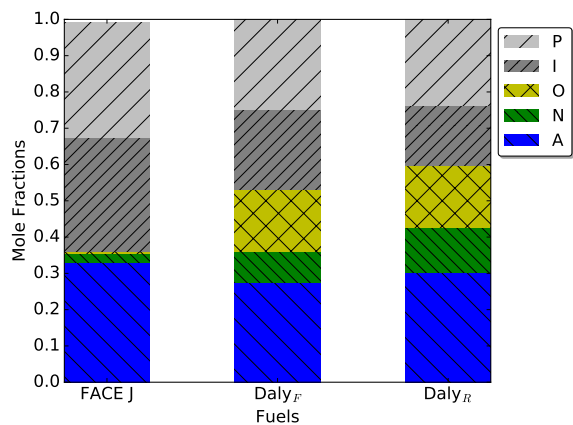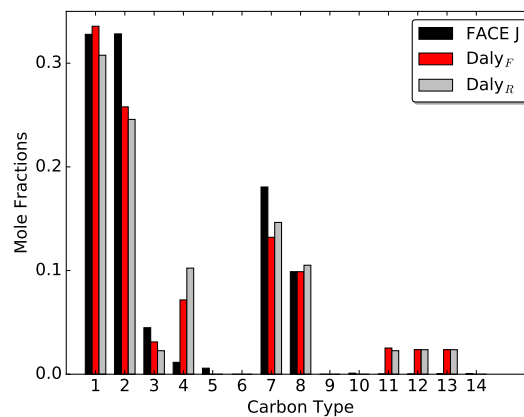
(a) Hydrocarbon class proportions

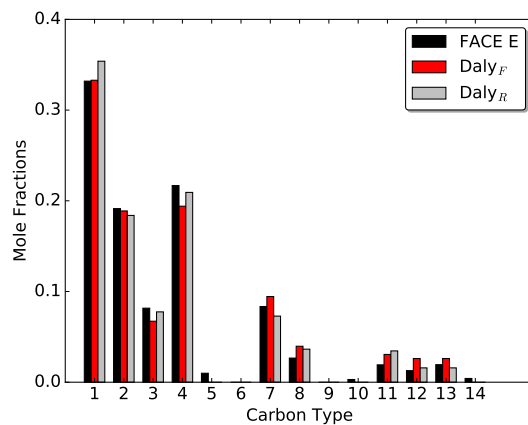(b) C–C bond type proportions
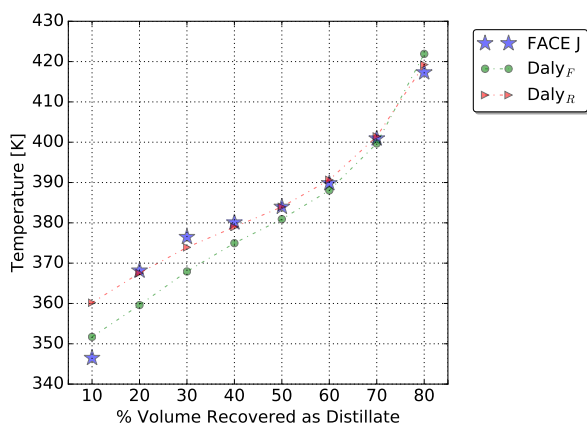
(c) Distillation characteristics

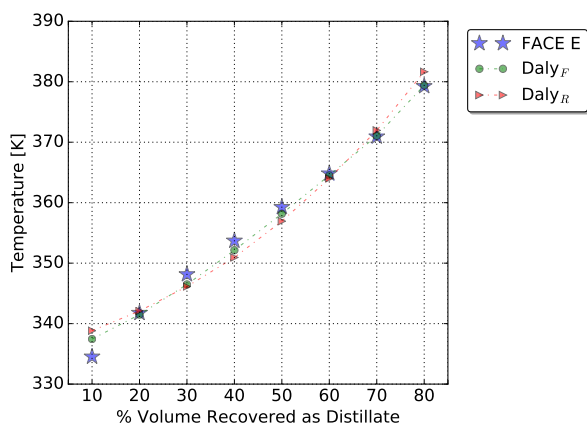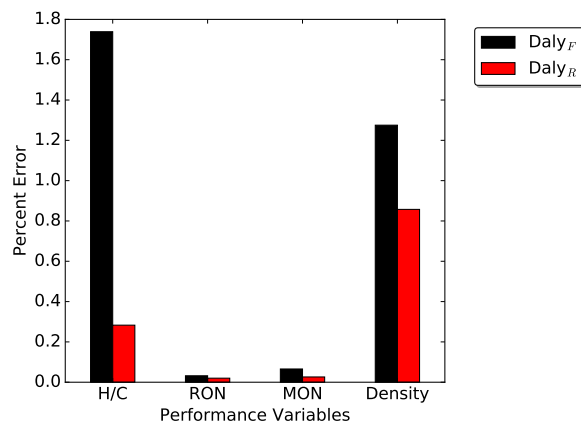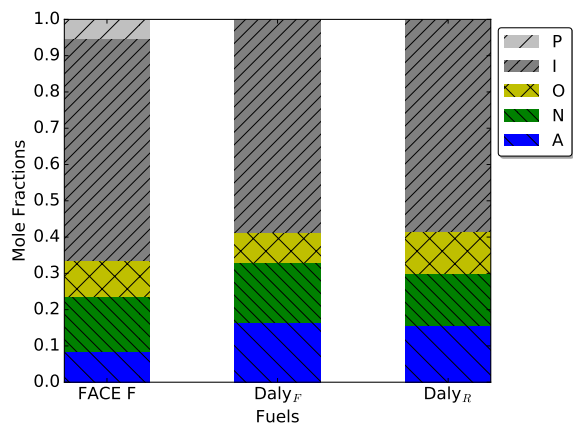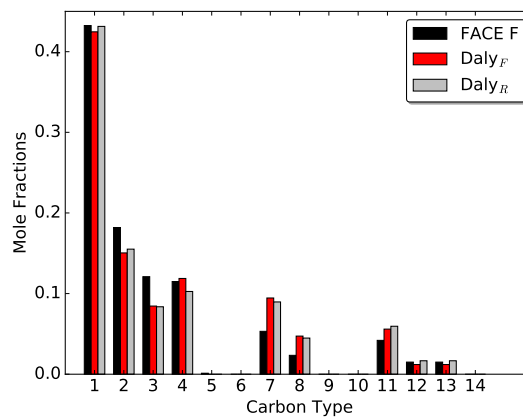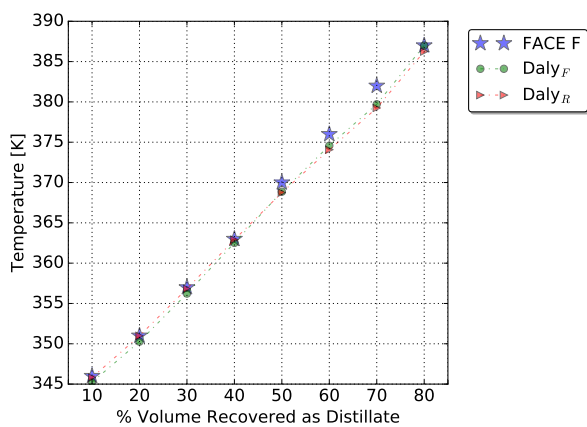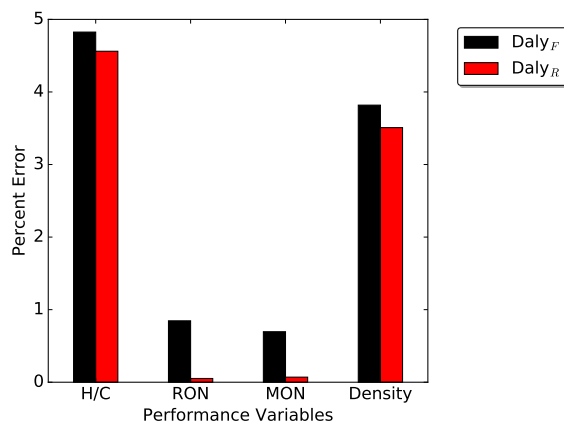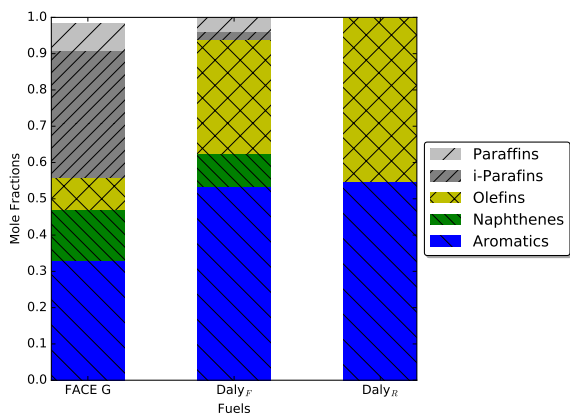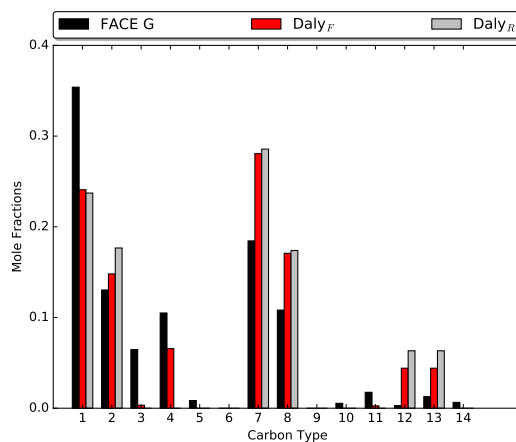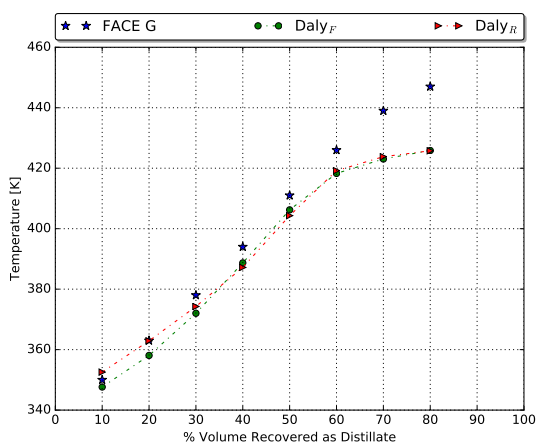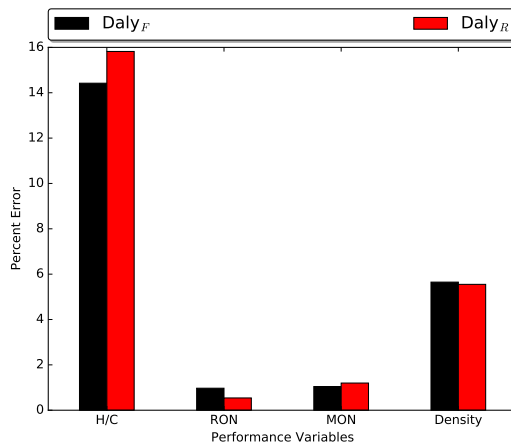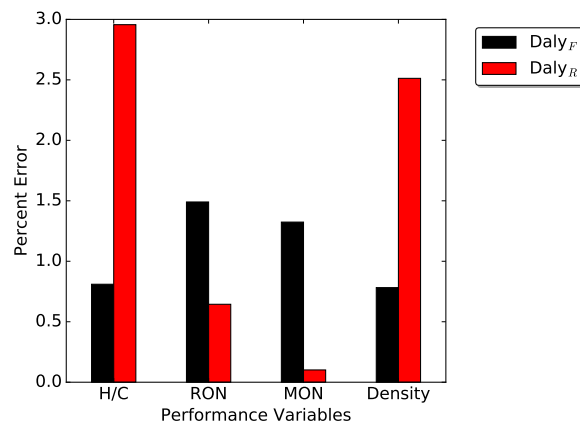(d) Percent error between H/C, RON, MON, and density

Figure B.10: Target property comparisons for FACE J and surrogates developed in this work.

Appendix C: Chapter 4 Supporting Material

Table C.1 presents the FACE gasoline [41] reduced-palette surrogates from Daly et al. [101], with corresponding LTC indices. The 314 fuel blends consist of those from literature [19, 20, 43] and fuels generated in this effort to extend upon those datasets. Tables C.2–**??** provide the makeup of fuel mixtures in terms of volume fraction as well as octane ratings if available. The chemical mechanisms utilized for calculating LTC index depended on the species in the fuel mixture. For mixtures of n-heptane, isooctane, toluene, and ethanol, we used the Chaos et al. [102–105] mechanism; for methylcyclohexane we used the Weber et al. [106] mechanism; for everything else, including the FACE gasoline surrogates, we used the Sarathy et al. [73] mechanism.

C.1 FACE Gasoline Surrogates

Parameter	A	B	C	D	E	F	G	H	I	J
LTC index	14.2	13.4	14.1	14.6	23.2	14.9	13.5	15.4	12.9	14.3
RON	83.8	95.1	84.4	93.9	87.4	94.4	96.3	86.9	70.1	73.2
MON	83.7	93.1	82.9	87.3	81.1	88.9	86.8	79.9	69.5	70.2
Density (kg/m^3)	700	718	698	761	731	732	802	775	710	761
H/C	2.22	2.11	2.20	1.83	2.05	2.03	1.54	1.75	2.15	1.86
Species palette					Molar %					
n-heptane			13.0	8.6				16.5	11.6	23.7
2-methylbutane	26.1	23.3	28.2	16.2	8.8	9.4			12.8	
2-methylpentane			5.5	7.7						
2-methylhexane	25.9	9.1			19.2	7.5			20.0	
2,2,4-trimethylpentane	42.1	52.4	45.9	22.5	22.5	41.5		13.9	28.5	16.4
1-pentene							9.5	8.0		8.5
1-hexene					10.3	11.6	35.7			8.7
cyclopentane				6.9	27.3	14.3		22.8		
cyclohexane									4.7	12.3
toluene				8.1				15.0	11.4	
o-xylene	5.9	15.2	7.4	30.0	11.9	15.7	40.0	11.1		15.0
1,2,4-trimethylbenzene								14.8	12.7	15.4

Table C.1: FACE gasoline surrogates from Daly et al. [101]

C.2 Fuel Mixtures

ID	RON	MON	LTC index
TRF1	39	37	35.2
TRF2	88.8	84.8	15.14
TRF3	76.2	70.9	17.46
TRF4	82.8	80.7	34.1
ERF1	78.7	76.7	23.22
H20T20	84.9	81.8	15.1
H20T40	89.8	82.9	14.93
H20T60	93.9	83.9	13.79
H20E1	80.5	80.4	14.75
H20E5	84.4	83.2	14.93
H20E10	87.9	85.6	14.13
H20E20	94.1	88.2	13.87
H30E1	70.6	70.2	23.05
H30E5	73.2	73.1	23.1
H30E10	78.7	76.7	22.01
H30E20	85.1	81.2	20.56
H40E60	94.4	82.8	21.92
H45E55	89.7	80.4	22.9
H50E50	84.7	76.8	25.46
H55E45	78	71.6	21.54
H90T10	14.1	12.6	37.72
H80T20	27.7	24.8	41.58
H60E40	71.4	65	35.57
TERF1	67.1	63.7	23.12
TERF2	94.7	88.5	14.95
TERF3	97	87.6	14.76
TERF4	80.8	73	24.21
TERF5	79.6	74.5	24.23
TERF6	85.3	78.6	15.24
TERF7	83.8	78.1	22.86
TERF8	71.8	65.8	27.24
TERF9	81.6	77.9	22.34
TERF10	90.2	84.1	14.83
TERF11	83.8	78.2	22.86
TERF12	78.3	74.3	25.95
TERF13	86.1	83.6	14.89
TERF14	74.8	68.9	27.31
TERF15	92.3	86.4	15.27
TERF16	87.9	81.4	23
TERF17	83.8	78.1	22.86

Table C.2: Blends of n-heptane/isooctane/toluene/ethanol taken from Truedsson et al. [19, 20].

ID	RON	MON	LTC index
TERF91-15	91	88.4	14.84
TERF91-15-10	97.8	91.7	6.61
TERF91-15-20	102.6	93.2	14.73
TERF91-15-40	107.1	93.6	14.88
TERF91-15-60	107.7	93.6	14.79
TERF91-15-80	1078	91.7	13.85
TERF91-30	91.3	86.1	14.83
TERF91-30-10	97	89.4	14.78
TERF91-30-20	101.4	91.1	14.92
TERF91-30-40	106	91.2	14.93
TERF91-30-60	107.1	92	14.88
TERF91-80	107.5	91.4	13.7
TERF91-40	91.1	86.5	14.75
TERF91-40-15	96	87.2	14.88
TERF91-40-20	100.2	89.1	14.08
TERF91-45-40	104.6	90.9	14.77

Table C.3: Blends of n-heptane/isooctane/toluene/ethanol taken from Foong et al. [43].

ID	RON	MON	LTC index
n-heptane	0	0	15.02
isooctane	100	100	21.89
2-methylbutane	92	90	15.22
2-methylhexane	42.4	46.3	24.62
methylcyclohexane	74.1	74	11.44

Table C.4: Pure components

ID	n-heptane (vol %)	isooctane (vol %)	LTC Index
n-heptane	100	0	15.02
PRF2	98	2	19.83
PRF4	96	4	21.98
PRF6	94	6	25.39
PRF8	92	8	26.57
PRF10	90	10	27.32
PRF12	88	12	27.57
PRF14	86	14	28.89
PRF16	84	16	29.11
PRF18	82	18	34.62
PRF20	80	20	34.41
PRF22	78	22	34.92
PRF24	76	24	35.94
PRF26	74	26	36.73
PRF28	72	28	36.84
PRF30	70	30	35.9
PRF32	68	32	35.51
PRF34	66	34	33.67
PRF36	64	36	34.11
PRF38	62	38	33.39
PRF40	60	40	32.98
PRF45	55	45	29.18
PRF50	50	50	27.27
PRF55	45	55	28.02
PRF60	40	60	23.29
PRF65	35	65	30.21
PRF70	30	70	26.31
PRF75	25	75	23.57
PRF80	20	80	22.67
PRF85	15	85	23.23
PRF90	10	90	22.55
PRF95	5	95	23.06

Table C.5: n-heptane/isooctane mixtures (primary reference fuels).

ID	n-heptane (vol %)	isooctane (vol %)	toluene (vol %)	2-methylbutane (vol %)	xylene(s) (vol %)	LTC index
S1	50	0	0	50	0	22.38
S2	30	20	0	50	0	28.61
S3	70	0	10	20	0	25.68
S4	50	20	20	10	0	22.08
X1	30	20	0	0	50	21.14
X2	30	20	5	0	45	23.34
X3	30	20	10	0	40	14.31
X4	30	0	20	0	50	19.18
X5	30	5	20	0	45	21.31
X6	30	10	20	0	40	22.00
X7	30	20	20	0	30	22.44
X8	30	10	10	0	50	21.50
X9	30	5	5	0	60	18.67
X10	30	0	0	0	70	9.65
X11	50	0	0	0	50	23.43
X12	50	20	0	0	30	26.99
X13	50	20	5	0	25	28.44
X14	50	20	10	0	20	21.56
X15	50	0	20	0	30	25.45
X16	50	5	20	0	25	26.03
X17	50	10	20	0	20	20.76
X18	50	20	20	0	10	21.80
X19	50	10	10	0	30	26.89
X20	50	5	5	0	40	25.53
X21	70	0	0	0	30	25.55
X22	70	20	0	0	10	29.36
X23	70	0	20	0	10	26.53
X24	70	10	0	0	20	27.05
X25	70	0	10	0	20	27.08
X26	70	10	10	0	10	28.97
X27	70	5	5	0	20	26.92
X28	70	5	0	0	25	26.99
X29	70	0	5	0	25	26.32
X30	90	0	0	0	10	24.06

Table C.6: n-heptane/isooctane /2-methylbutane & n-heptane/isooctane /xylene(s) mixtures.

ID	n-heptane (vol %)	isooctane (vol %)	ethanol (vol %)	RON	LTC Index
PRF0-E10	90	0	10		31.06
PRF0-E20	80	0	20		35.03
PRF0-E30	70	0	30	54.3	28.6
PRF0-E40	60	0	40	69.7	27.32
PRF0-E45	55	0	45		23.46
PRF0-E50	50	0	50	83.8	20.48
PRF0-E55	45	0	55		14.42
PRF10-E10	81	9	10		34.98
PRF10-E20	72	8	20	45.9	33.17
PRF10-E30	63	7	30	61.1	27.77
PRF10-E40	54	6	40	75.6	23.8
PRF10-E50	45	5	50	87.6	14.67
PRF10-E60	36	4	60	96.6	13.98
PRF10-E70	27	3	70		14.22
PRF10-E80	18	2	80		12.96
PRF10-E90	9	1	90		20.52
PRF20-E10	72	18	10		33.36
PRF20-E20	64	16	20	53.3	28.28
PRF20-E30	56	14	30	67.4	25.11
PRF20-E40	48	12	40	80.7	19.72
PRF20-E50	40	10	50	91.5	14.6
PRF20-E60	32	8	60	99.1	13.8
PRF20-E70	24	6	70		14.26
PRF20-E80	16	4	80	105.8	20.69
PRF20-E90	8	2	90		20.64
PRF30-E10	63	27	10	46.5	33.77
PRF30-E20	56	24	20	60.8	25.33
PRF30-E30	49	21	30	74.2	23.76
PRF30-E40	42	18	40	85.5	17.43
PRF30-E50	35	15	50	94.7	22.67
PRF30-E60	28	12	60		14.28
PRF30-E70	21	9	70		14.2
PRF30-E80	14	6	80		20.65
PRF30-E90	7	3	90		20.81
PRF40-E10	54	36	10	55	27
PRF40-E20	48	32	20	68.5	25.42
PRF40-E30	42	28	30	80.6	18.44
PRF40-E40	36	24	40	90.4	22.93
PRF40-E50	30	20	50	97.9	14.52
PRF40-E60	24	16	60	102.7	14.34
PRF40-E70	18	12	70		12.91
PRF40-E80	12	8	80	106.6	20.65
PRF40-E90	6	4	90		20.91

Table C.7: *n*-heptane/isooctane/ethanol mixtures taken from Foong et al.[43], with added resolution mixtures (RON excluded).

ID	n-heptane (vol %)	isooctane (vol %)	ethanol (vol %)	RON	LTC Index
PRF50-E10	45	45	10	63.8	25.47
PRF50-E20	40	40	20	75.8	19.3
PRF50-E30	35	35	30	86.4	23.01
PRF50-E40	30	30	40	94.5	14.12
PRF50-E50	25	25	50		13.99
PRF50-E60	20	20	60		14.37
PRF50-E70	15	15	70		20.44
PRF50-E80	10	10	80		20.65
PRF50-E90	5	5	90		21.03
PRF60-E10	36	54	10	72.6	19.57
PRF60-E20	32	48	20	83.5	22.98
PRF60-E30	28	42	30	92	14.35
PRF60-E40	24	36	40	98.9	14.37
PRF60-E50	20	30	50		14.48
PRF60-E60	16	24	60	105.5	20.79
PRF60-E70	12	18	70		20.57
PRF60-E80	8	12	80	107.6	20.8
PRF60-E90	4	6	90		20.7
PRF70-E10	27	63	10	80.9	23.02
PRF70-E20	24	56	20	90.3	14.34
PRF70-E30	21	49	30	97.4	14.57
PRF70-E40	18	42	40		14.45
PRF70-E50	15	35	50		14.63
PRF70-E60	12	28	60		21.14
PRF70-E70	9	21	70		20.93
PRF80-E10	18	72	10	89.5	14.1
PRF80-E20	16	64	20	97.0	14.48
PRF80-E30	14	56	30		14.41
PRF80-E40	12	48	40	105.7	21.33
PRF80-E50	10	40	50		21.51
PRF80-E60	8	32	60	107.7	22.13
PRF80-E70	6	24	70		20.83
PRF80-E80	4	16	80	108.3	20.87
PRF80-E90	2	8	90		20.53

Table C.8: Continued n-heptane/isooctane/ethanol mixtures taken from Foong et al.[43], with added resolution mixtures (RON excluded).

ID	n-heptane (vol %)	isooctane (vol %)	ethanol (vol %)	RON	LTC Index
PRF90-E5	9.5	85.5	5	94.1	21.52
PRF90-E10	9	81	10	97.6	21.64
PRF90-E20	8	72	20	103.6	21.3
PRF90-E30	7	63	30		21.72
PRF90-E40	6	54	40		22.3
PRF90-E50	5	45	50		22.31
PRF90-E60	4	36	60		22.56
PRF90-E70	3	27	70		20.92
PRF90-E80	2	18	80		20.69
PRF90-E90	1	9	90		20.76
PRF100-E10	0	90	10	106.8	22.01
PRF100-E20	0	80	20	109.4	21.8
PRF100-E30	0	70	30		21.47
PRF100-E40	0	60	40	110.2	21.91
PRF100-E50	0	50	50		22.54
PRF100-E60	0	40	60	109.6	20.94
PRF100-E70	0	30	70		20.83
PRF100-E80	0	20	80	109.0	20.63
PRF100-E90	0	10	90		20.88

Table C.9: Continued n-heptane/isooctane/ethanol mixtures taken from Foong et al.[43], with added resolution mixtures (RON excluded).

ID	n-heptane (vol %)	isooctane (vol %)	toluene (vol %)	LTC Index
H90T10	90	0	10	37.72
H80T20	80	0	20	41.58
H70T30	70	0	30	30.79
H60T40	60	0	40	22.99
H50T50	50	0	50	18.6
H40T60	40	0	60	24.06
H30T70	30	0	70	21.38
H20T80	20	0	80	12.84
H10T90	10	0	90	10.61
H10T10	10	80	10	15.56
H10T20	10	70	20	22.89
H10T30	10	60	30	23.2
H10T40	10	50	40	22.4
H10T50	10	40	50	21.08
H10T60	10	30	60	12.96
H10T70	10	20	70	13.14
H10T80	10	10	80	12.73
H20T2	20	78	2	23.15
H20T4	20	76	4	23.24
H20T6	20	74	6	23.79
H20T8	20	72	8	23.54
H20T10	20	70	10	34.1
H20T12	20	68	12	16.52
H20T14	20	66	14	15.21
H20T16	20	64	16	15
H20T18	20	62	18	16.11
H20T20	20	60	20	15.1
H20T30	20	50	30	22.44
H20T40	20	40	40	14.93
H20T50	20	30	50	22.51
H20T60	20	20	60	13.79
H20T70	20	10	70	14.04
H30T10	30	60	10	25.41
H30T20	30	50	20	23.88
H30T30	30	40	30	23.33
H30T40	30	30	40	23.09
H30T50	30	20	50	22.59
H30T60	30	10	60	22.5
H40T10	40	50	10	21.91
H40T20	40	40	20	20.48
H40T30	40	30	30	18.27
H40T40	40	20	40	18.17
H40T50	40	10	50	24.98
H50T10	50	40	10	26.3
H50T20	50	30	20	24.64
H50T30	50	20	30	24.62

Table C.10: n-heptane/isooctane/toluene mixtures

ID	n-heptane (vol %)	isooctane (vol %)	toluene (vol %)	LTC Index
H50T40	50	10	40	21.39
H60T10	60	30	10	28.58
H60T20	60	20	20	27.62
H60T30	60	10	30	26.68
PRF10-T20	72	8	20	31.38
PRF10-T40	54	6	40	22.17
PRF10-T60	36	4	60	24.26
PRF10-T80	18	2	80	13.08
PRF20-T20	64	16	20	27.58
PRF20-T40	48	12	40	20.85
PRF20-T60	32	8	60	22.46
PRF30-T20	56	24	20	26.99
PRF30-T40	42	18	40	26.04
PRF30-T60	28	12	60	22.43
PRF30-T80	14	6	80	13.8
PRF40-T20	48	32	20	24.62
PRF40-T40	36	24	40	23.96
PRF40-T60	24	16	60	22.02
PRF40-T80	12	8	80	12.69
PRF60-T20	32	48	20	26.17
PRF60-T40	24	36	40	23.15
PRF60-T60	16	24	60	21.72
PRF60-T80	8	12	80	12.63
PRF70-T20	24	56	20	23.87
PRF70-T40	18	42	40	23.26
PRF70-T60	12	28	60	13.87
PRF70-T80	6	14	80	12.24
PRF80-T20	16	64	20	22.77
PRF80-T40	12	48	40	22.41
PRF80-T60	8	32	60	13.11
PRF80-T80	4	16	80	12.12
PRF90-T20	8	72	20	22.81
PRF90-T40	6	54	40	21.88
PRF90-T60	4	36	60	14.39
PRF90-T80	2	18	80	11.5
PRF100-T10	0	90	10	22.08
PRF100-T20	0	80	20	22.1
PRF100-T30	0	70	30	22.33
PRF100-T40	0	60	40	21.16
PRF100-T50	0	50	50	14.23
PRF100-T60	0	40	60	13.7
PRF100-T70	0	30	70	12.75

Table C.11: Continued n-heptane/isooctane/toluene mixtures

ID	n-heptane (vol %)	isooctane (vol %)	toluene (vol %)	ethanol (vol %)	LTC Index
H90T10E20	72	0	8	20	29.92
H90T10E40	54	0	6	40	24.06
H90T10E60	36	0	4	60	14.67
H90T10E80	18	0	2	80	14.47
H80T20E20	64	0	16	20	26.59
H0T10E20	0	72	8	20	21.89
H0T10E40	0	54	6	40	22.21
H0T10E60	0	36	4	60	22.25
H0T10E80	0	18	2	80	20.6
H0T20E20	0	64	16	20	22.89
H0T20E40	0	48	12	40	22.08
H0T20E60	0	32	8	60	22.18
H0T20E80	0	16	4	80	21.69

Table C.12: n-heptane/toluene/ethanol & isooctane/toluene/ethanol mixtures

Appendix D: Short Injection Study

D.1 Introduction

This study determines the efficacy of using ultra-short injection durations to create homogenous conditions throughout the spray prior to chemical ignition, since the fuel will have extendedtime to mix after the end of injection. The end-goal is to then compare ignition characteristics to modeled results. With a more-homogenous fuel/air mixture after the end of injection, it could be possible to use simplified fluid mechanics in modeling the fuel/air mixture. This is a plus as these models are computationally efficient—a basic necessity to use detailed comprehensive chemical mechanisms for large parametric studies. This brief study establishes favorable fuel/air mixture conditions within 650 μs after the end of injection. With mixing characteristics of ultra-short injections quantified, this effort paves the way for fundamental fuel-ignition experiments in Chapter 6

## D.2 Spatiotemporal Mixture Fraction Measurements

This study subjects 350 μs duration fuel sprays into an inert gas ambient at 1000 K, 40 atm. The experimental apparatus and methodology is identical to Ch. 5. Fig. D.1 presents the line-of-sight extinction (Fig. D.1a) and tomographic reconstructed, centerline fuel/air equivalence ratio (Fig. D.1b), both showing 2-D, spray fuel/air mixing. It is apparent in Fig. D.1a that the spray "tail" (close to injector, starting at 5 mm) quickly mixes after the end of injection and has lower signal at all times relative to the downstream portion of the spray, indicating axial signal gradients. Fig. D.1b, the tomographic reconstruction of the spray centerline, resolves radial and axial fuel concentration distributions. In general, both gradually reduce with time. Fig. D.1b also indicates axial concentration gradients in similar fashion to Fig. D.1a, though trends are not easily discernible in the radial.

Radial concentration profiles at select timings and axial positions are shown in Fig. D.2. At 400 μs ASOI, concentration profiles are characteristic of typical long-injection sprays (as shown in Ch. 5), exhibiting large gradients and a bell-shaped distribution. This is expected, where only 50 μs has passed for mixing to take place after the end of injection (350- μs injection duration). As time (and mixing) progresses, radial concentration gradients throughout all axial locations diminish. Radial profiles flatten as early as 1.5 ms ASOI throughout the spray, and are nearly uniform by 2 ms ASOI—indicating well-mixed conditions.

Figure D.3 shows spray-head averaged equivalence ratio for the short-injection toluene spray. Fuel-air ratio is converted to equivalence ratio, ϕ, by diving by the stoichiometric fuel/air ratio, so values less than
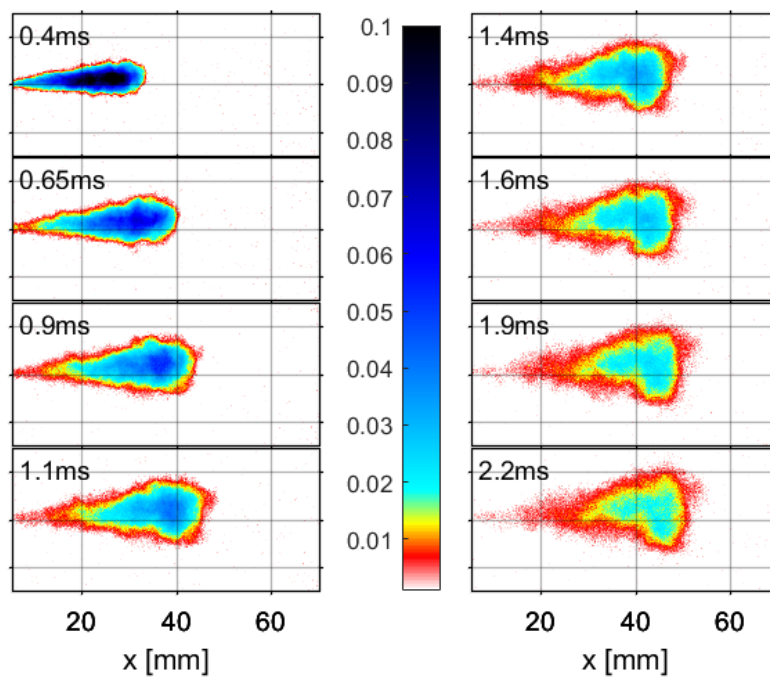
(a) Line-of-sight absorbance
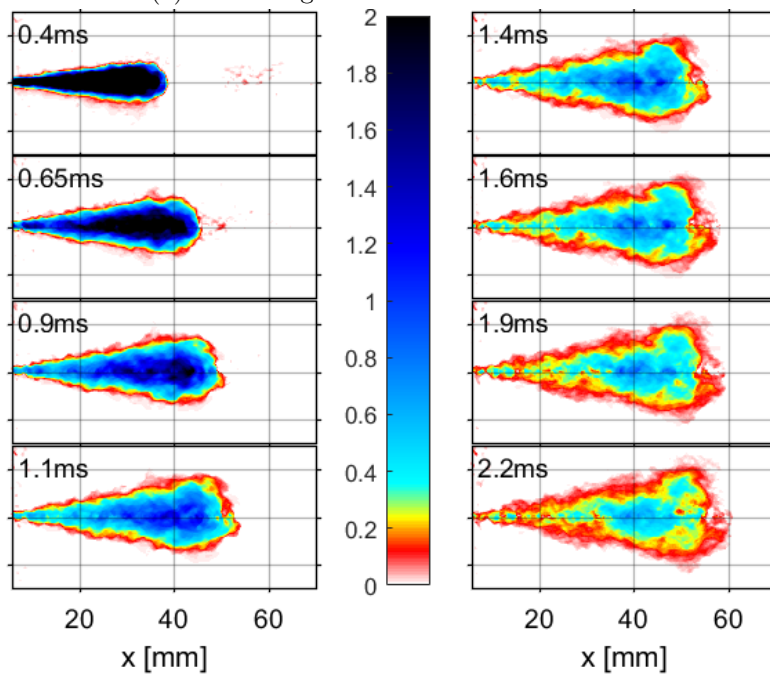
(b) Tomography-resolved centerline equivalence ratio

Figure D.1: Toluene doped with C70-fullerene, directly injected (350 μs at 500 atm) into 1000 K, 40 atm, non-reactive environment.
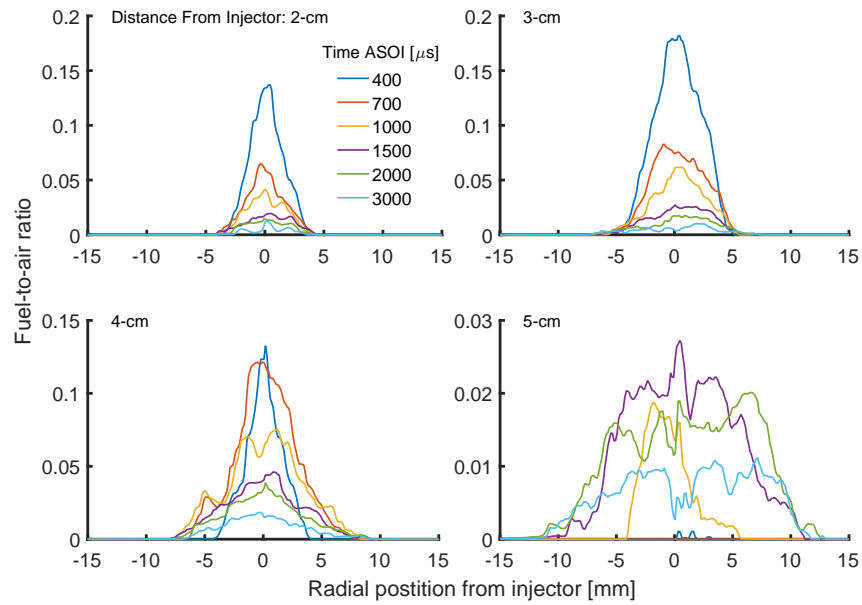
Figure D.2: Radial concentrations at select timings (.4–3 ms, legend) at various axial positions (subplots, 2–5 cm)
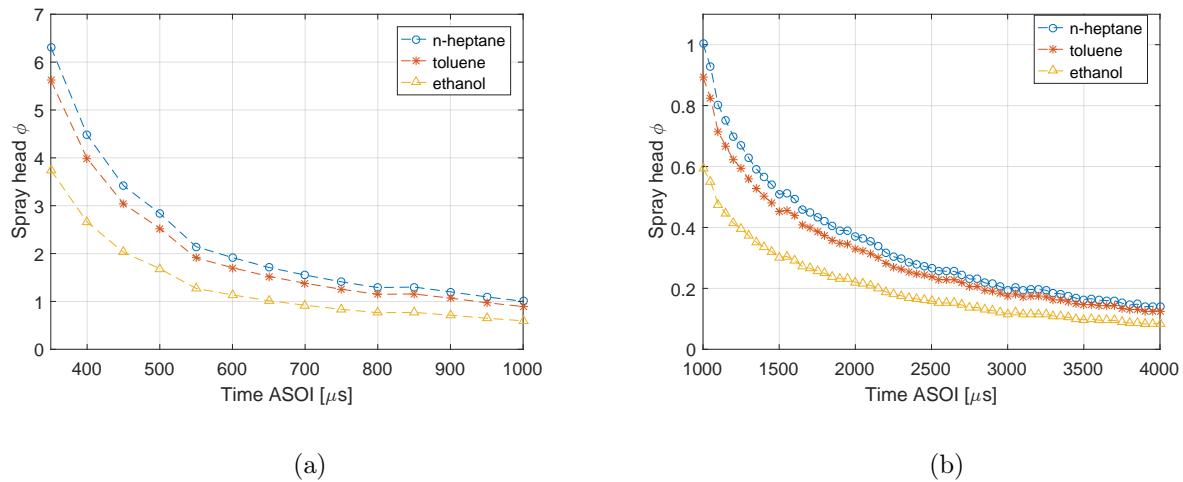

Figure D.3: Spray-head-averaged equivalence ratio of C70-doped toluene. Other fuel trends (n-heptane, ethanol) are estimations based on the fuel/air mixture fractions of the toluene experiment, but instead applying the fuels' respective stoichiometry

one indicate fuel-lean, and greater than one indicates fuel-rich. Toluene mixing results can be re-scaled to show the impact of fuel stoichiometry, by instead using the stoichiometric fuel/air ratio of n-heptane and ethanol as examples. As expected, increased time ASOI and with mixing progressing causes ϕ to decrease; n-heptane and toluene have similar values as their stoichiometric proportions are also similar, with ethanol being distinctly lower. Fig. D.3a shows ϕ reaching stoichiometric conditions for ethanol at 700 μs, toluene at 950 μs, and n-heptane at 1 ms ASOI. Recall the radial profiles indicate well-mixed conditions in the radial around 1.5 ms; at this time, fuels have ϕs of 0.3, 0.42, and 0.46, which are ignitable conditions and relevant to LTC conditions. Eventual over-mixing will govern the maximum residence time a fuel spray can be studied, as fuel-lean conditions ($\phi < 0.2$) will suppress a significant ignition event. For ethanol, this is as early as 2 ms, but toluene and n-heptane are extended to around 3 ms. If the fuel spray has not ignited prior to these timings for respective fuels, significant ignition will not occur, especially as mixing continues to progress (though at a reducing rate).

The findings of the mixing study guides the direction of future spray-ignition modeling efforts. For example, assuming perfectly mixed conditions would omit the axial concentration gradients within the spray, and neglect the fuel spray temperature-concentration dependence. In addition to concentration gradients within the spray, average fuel concentrations decrease with time. Therefore, assuming a static fuel/air concentration with a constant volume 0-D modeling approach would likely result in significant errors, likely to under-predict ignition delays. to summarize, as soon as 1.5 ms, spray radial distributions indicate well-mixed conditions, but axial gradients persist at all timings.

Hereafter, the author investigates using the 1-D spray modeling approach of Knox et al. [123] to predict spray ignition. The model includes 1-D momentum exchange as the spray conically expands downstream, thereby accounting for parameter axial gradients, but assumes radially averaged parameters. The radial-averaged modeling approach should accurately represent the experimental mixing after 1.5 ms ASOI when radial gradients are minimal. Timings before 1.5 ms may result in larger errors since radial concentration gradients are present. In an effort to assess 1-D model performance, the following section compares the experimental radial-averaged profiles as a function of axial position and time to results derived from the 1-D model.

D.3 Model Investigation

The 1-D modeling approach of Knox et al. requires a spray-cone spreading angle boundary condition from the user. This effort first investigates the spreading angle required for the experimental and model penetration trends to best match (with no active chemistry); literature [123, 134, 147] suggests if models match the experimental spray penetration, then the bulk mixing processes are well-represented. As will be shown,

deviating from an ideal conical expansion is required to better-match experimental penetration trends, which lead to improved fuel/air distribution predictions. following, ignition delay is demonstrated to be sensitive to subtle alterations in fuel/air mixing.

D.3.1   Spray Mixing Predictions

Figure D.4 shows select line-of-sight absorbance images, converted to binary based on an absorbency threshold of 0.003, done to emphasize the spray presence. Superimposed is the processed spray border, and an ideal conically expanding spray border of a set spreading angle. The spray border illustrates the assumed conically expanding spray border of knox et al. At 1 ms, when the spray has penetrated around 5 cm downstream, the spray head begins to "plume". This finding is exacerbated as time progresses, where the downstream spray head border extends past the ideal conical expansion, yet the majority of the upstream portion remains inside. The mechanism leading to the spray expanding in non-ideal fashion is believed to be due to axial pressure gradients and shear stresses that become more prominent at low spray velocities. Because of this, modeling spray penetration without accounting for these parameters proves challenging.

Guided by Daly et al. [134], this work uses experimentally derived radial profiles to define spray width as a function of axial position, as opposed to an ideal conically expanding spray width. Again, this was performed to account for the spray "pluming", pseudo-accounting for axial pressure gradients and shear stresses not accounted for. The radial width versus axial position is founded on the experimental spray-width, then hard-coded in the Knox et al. 1-D spray model.

Figure D.5 shows two modelled results for spray penetration, one using the ideal constant spreading angle (18 degrees), and the other with a variable radial width versus axial position. As can be seen, the constant spreading angle approach poorly matches the experimental penetration; as such, errors are expected in predicted mixture distributions. When the model of Knox et al. is modified to implement the variable spray radial width, mixing results are closer to the experimental trends, but by no means perfect.

Fig. D.6 shows full-width half-max (FWHM) radial-averaged experimental fuel/air mass fraction as a function of axial position and time, compared to the modeling results using a constant spreading angle. The FWHM approach increases radial-average values for unmixed conditions (bell-shaped concentration profile), performed to improve ignition delay predictions that are governed by higher (centerline) spray concentrations (if present). The experimental results are overlaid with a shaded region, indicating one standard deviation of the radial concentration about the mean. Surprisingly, great qualitative and quantitative agreement is found between the model and experiment at most axial positions at all times. There is disagreement at the spray head at early and later times, attributed to the model under-predicting spray penetration early, and over-predicting at later times. Over-prediction is due to the model having a smaller spreading angle than
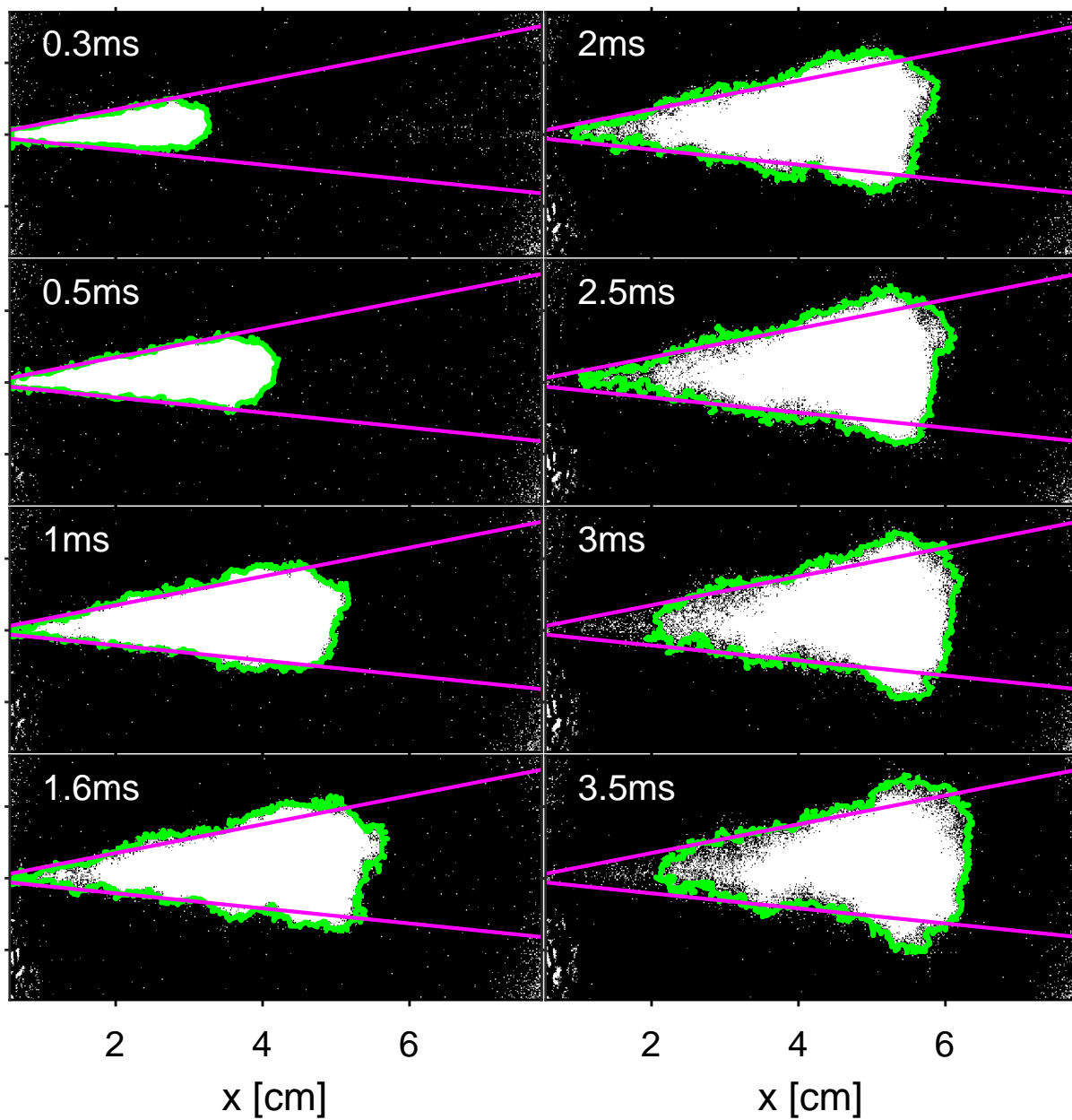
Figure D.4: Saturated line-of-sight absorbance images at select timings, superimposed with the processed spray border (green), and an ideal conically expanding spray border (magenta) of a set spreading angle.
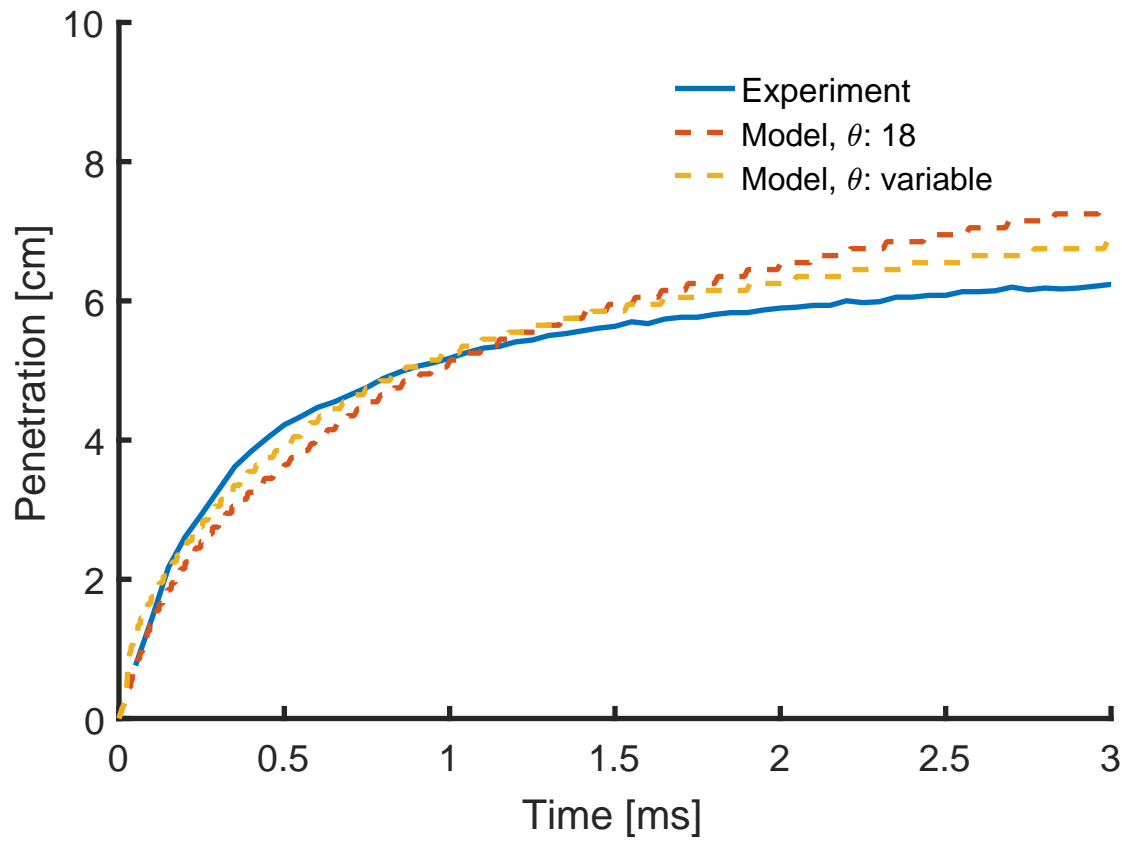
Figure D.5: Spray penetration trends for experimental and modeling results. Using a variable spray width profile in the model, based on the experimentally-observed spray width, converges closer to the true values.

reality after 5 cm axial, causing over-predicions spray penetration, and vice-versa at earlier timings. The high fuel/air mass ratio spike at 500 μs and 8 mm axial position is not predicted.
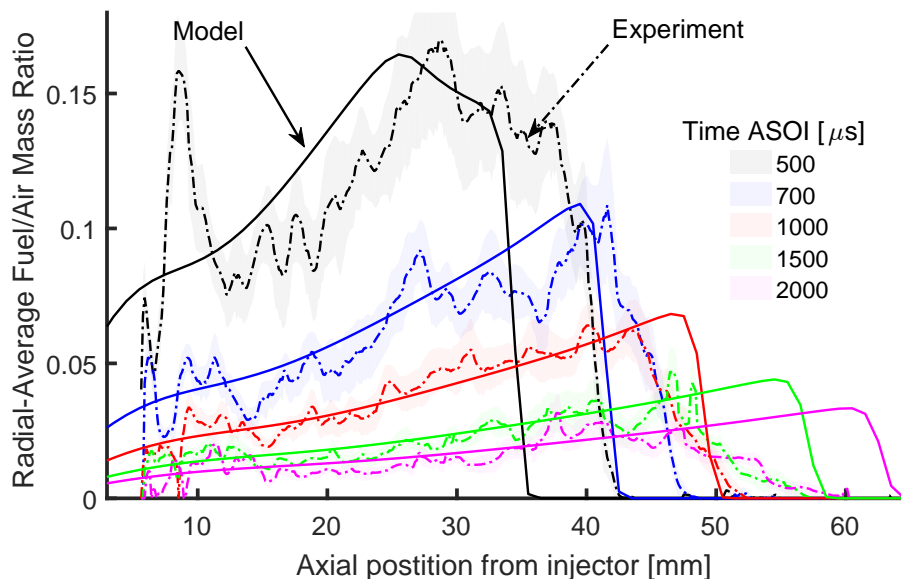

Figure D.6: Radial-averaged fuel/air ratio versus axial position at select timings. Model (constant spreading angle) are compared to experimental results.

Fig. D.7 again shows the experimental results of Fig. D.6, but now compared to the modeling results using a variable spray width versus axial position. Qualitative and quantitative agreement is improved, mostly in the spray head from the better agreement in penetration trends. The spike at 500 μs and 8 mm axial position is now predicted to some degree, but the axial location is shifted closer to the injector. Tuning of the spray width boundary could potentially correct for this. Moving forward, the author investigates whether the slight improvements in fuel/air mixing predictions impact fuel ignition predictions.

D.3.2   Ignition Delay Predictions

With chemistry activated in the simulations, the two models, one having a constant spreading angle boundary condition (model #1) and the other a variable spray width (model #2) are compared. The chemical mechanism of Princeton et al. [136–139] models the fuel in this work, being n-heptane. Following, this work determines the sensitivity of chemical ignition to the subtle alterations of fuel/air mixture profiles between model 1 and 2.

Figure D.8 presents ignition delays from modeling approaches 1 and 2; ignition delay is defined to be the timing when any portion of the spray exceeds 400 K of the initial ambient temperature. At ambient
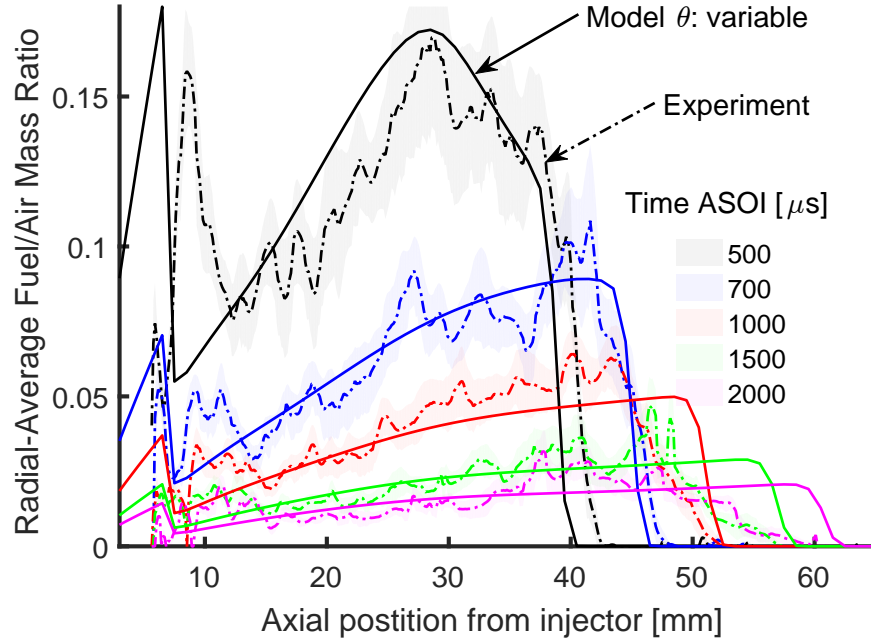
Figure D.7: Radial-averaged fuel/air ratio versus axial position at select timings. Model (variable spreading angle with axial position) are compared to experimental results.

temperatures greater than 1100 K, the two approaches yield similar results. However, as temperature decreases, ignition delays diverge between the two models. For these sprays at all cases investigated, the ignition onsets are exclusively predicted to occur at the leading edge of the spray head. Figure D.9 points out that models 1 and 2 have nearly the same spray-head equivalence ratios prior to 550 μs, but above 550 μs model 2 has significantly lower values. This timing corroborates the point where ignition delays begin to significantly diverge, where the lower equivalence ratio values of model 2 leads to delay the ignition onset. For the 1-D model of Knox et al. [123], ignition delays are governed by the fuel/air mixtures at the leading edge of the spray head. Matching the experimental radial-averaged axial fuel/air distributions may not be needed after all for ignition delay calculations, due to onsets always occurring at the spray head.

D.4 Conclusions

Short-injections were shown to be radially well-mixed at extended residence times, potentially a good candidate for averaging this value to compare to the 1-D modeling efforts. However, this could lead to errors at short residence times where the maximum spray centerline concentrations deviate from the mean. In reality, short injection spray ignition will be mostly governed by the fuel-rich spray centerline. These fuel-rich zones can serve to delay or advance ignition, dependant on being greater or less than stoichiometric proportions. Therefore, even a FWHM radial-average approach on a bell-shaped concentration profile averages-out to a
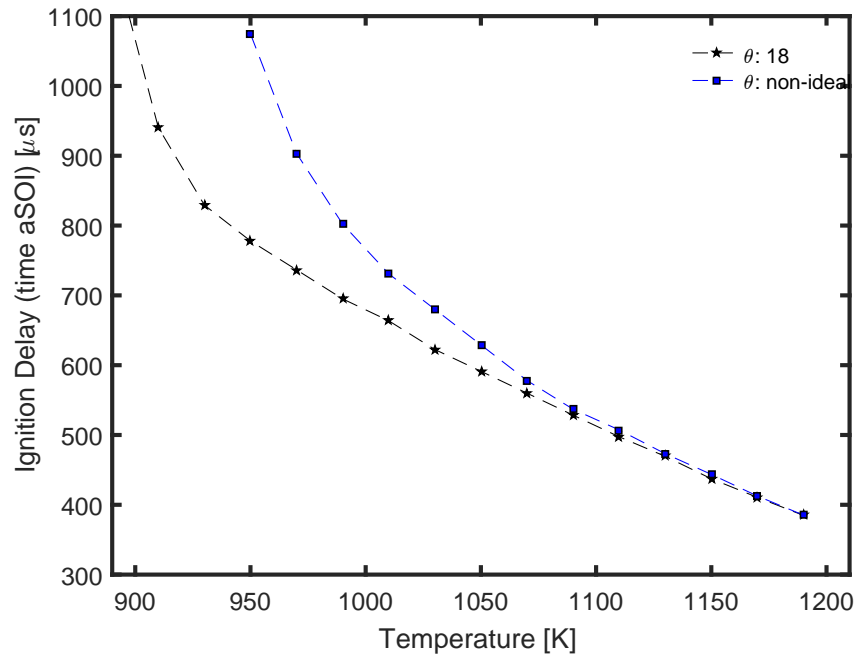
Figure D.8: Spray ignition delay versus temperature at 15 % O2, 40 atm for n-heptane. Model #1 (constant spreading angle) are compared to Model #2 (variable spreading angle with axial position)
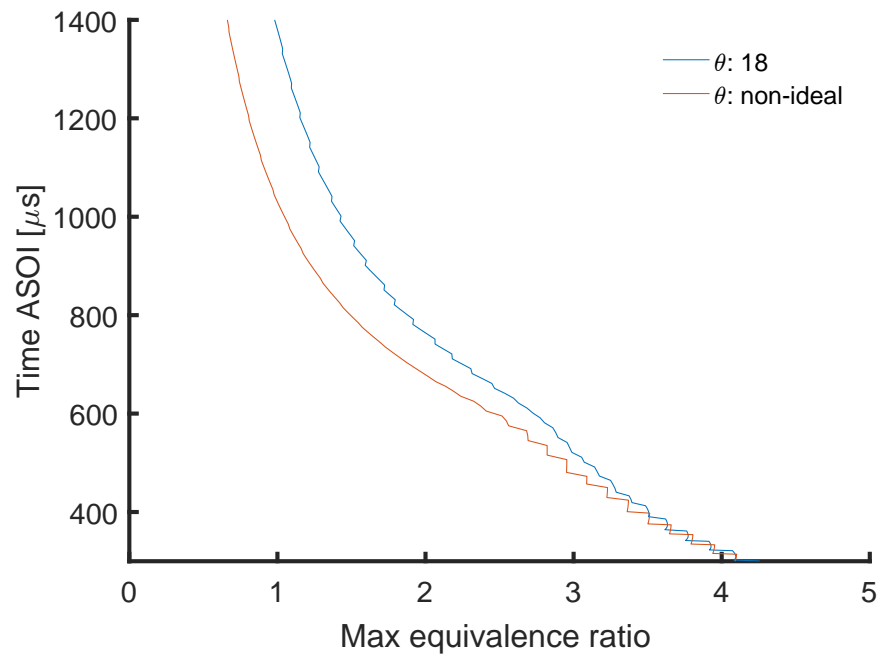

Figure D.9: Maximum spray-head equivalence ratio for model #1 ($\theta : 18$) and model #2 (θ:non-ideal)

leaner fuel/air mixture than the peak centerline value. If this is the case, then spray modeling efforts need to have reduced spreading angles to increase the average fuel/air mixture closer to the centerline values. To also match penetration trends, the injector discharge coefficient would have to be decreased to reduce penetration velocities at the lower spray spreading angles.

Modeled ignition delays were found to be governed by the evolution of the air/fuel mixture at the leading edge of the spray head, with some uncertainty in whether it is best to target the maximum or average of the true radial profile. Moving forward towards accurate ignition delay predictions, the author proposes performing a parametric study of model boundary conditions to best-match experimental ignition trends for a given fuel and condition. Matching the experimental penetration trends could be held constant while model spreading angle and injector discharge coefficient are varied. In this manner, the evolution of the spray head fuel/air ratio can be tailored until the desired ignition trends are observed.

Appendix E: IR-to-LTC Model Parameters

This work explored various kernel functions and corresponding hyperparameter constants for the Support Vector Machine Regression (SVMR). The author investigated linear, polynomial, Sigmoid, and radial-basis kernel functions. The radial-bases kernel yielded the best predictive performance for the IR-LTC index predictive models. The hyperparameter constant, γ, and SVM meta constant, C, are tuned to achieve the best model performance. A great explanation of these variables and how to tune them can be found on the online scitkit-learn documentation, titled: RBF SVM parameters. *Scikit-learn*'s *GridSearchCV()* was used to explore γ and C, exponentially spaced apart:

$\gamma = 1e^{-5} to 1e^{10}$, $C = 1e^{-5} to 1e^{15}$

In addition to the above constants, various data pre-processing and training/test splits were investigated. Data pre-processing involved scaling the IR data to unit variance, and/or performing first or second derivatives. The author found no pre-processing to yield the best performance. Training/test splits were automated within the *GridSearchCV()* routine using k-fold cross-validation. This work investigated k-folds varying between 2 and 20, finding that a k-fold of 3 to be the best value for model robustness.

Recall this work generated two IR-LTC index models. The first IR-LTC index model uses real fuel IR spectra as the input, designed to predict real gasoline samples. The other model uses estimated IR spectra from the linear combination of the fuels individual hydrocarbon species, used for the fuel formulation algorithm.

The tuned values for both IR-LTC index SVMR models are as follows:

Real IR Spectra Model: $\gamma = 0.1$, $C = 100000.0$, $k_{folds} = 3$

Linear IR Spectra Model: $\gamma = 0.1$, $C = 10000.0$, $k_{folds} = 3$